Infrared and Multivariate Studies of a Biopolymer

Author:

Calum D.M. Welsh

Supervisor:

Mike George

Thesis submitted to the University of Nottingham

for the degree of Doctor of Philosophy

September 2016

The University of Nottingham

UNITED KINGDOM · CHINA · MALAYSIA

Declaration

I hereby declare that all work contained in this Thesis has been undertaken by myself, unless acknowledged otherwise.

Calum Welsh

September 2016

Acknowledgements

I would like to thank my supervisor, Mike George for the opportunity to study for my PhD, as well as the advice and support he has provided.

I also thank the members of the entire George Group, past and present who made working within the group very enjoyable. In particular Charlotte Clark, James Calladine, Peter Summers and Raphael Horvath for their continual support, advice and willingness to answer my questions.

Paul Pudney, Julian Bent and Eleanor Bonnist, from Unilever Research provided support and advice whenever needed and I thoroughly enjoyed my time working at Colworth Park with them.

For financial support I thank Unilever UK Ltd and The University of Nottingham. I would also like to thank Rich Wilson, Pete Fields and Dave Litchfield in the Workshop for their help with the modification of the ATR system.

Finally, a huge thank you to my family for their unconditional love and support. Their willingness to help me with my numerous maths and science questions from a young age is ultimately what inspired me to become a scientist. I dedicate this Thesis to them.

Abbreviations

2DCOS	Two-Dimensional Correlation Spectroscopy
ATR	Attenuated Total Reflection
AWGM	Additive White Gaussian Noise
FTIR	Fourier Transform Infrared Spectroscopy
FWHM	Full Width Half Maximum
IR	Infrared
MCR	Multivariate Curve Resolution
MW2D	Moving Window Two-Dimensional Correlation Spectroscopy
PC	Principal Component
PCA	Principal Component Analysis
PCMW2D	Perturbation Correlation Moving Window Two-Dimensional Correlation Spectroscopy
PID	Proportional Integral Derivative
RMSEC	Root Mean Square Error of Calibration
RMSECV	Root Mean Square Error of Cross-Validation
SNR	Signal to Noise Ratio

Abstract

This Thesis utilises vibrational spectroscopy in combination with multivariate and two-dimensional analytical techniques to probe the interactions of a biopolymer in water-based systems.

Chapter 1

This Chapter gives an introduction to the Thesis and briefly outlines the experimental techniques used to study biopolymeric systems before covering the theory and implementation of the multivariate and two-dimensional methods used. A brief introduction to carrageenan, the biopolymer of interest, is then given.

Chapter 2

The general experimental procedures are discussed together with the development of a new low-temperature ATR system, which allows very precise control and variation of sample temperature. The latter is key to many of the measurements and analyses reported in this thesis. The ATR system is stable to 0.01 °C over a temperature range of -30 to 80 °C. Many of the techniques used within this thesis rely on the MATLAB environment. Analysis methods that are not commercially available have been programmed as part of my work. The theoretical background is discussed and the scripts for these functions are included in the Appendix.

Chapter 3

Three commercially available carrageenans, κ-, ι- and λ-carrageenan are studied with infrared spectroscopy. The carrageenan solutions are cooled from *ca.* 80 to 10 °C. κ- and ι-carrageenan undergo a gelation transition during the cooling and this is investigated with a variety of analysis methods. The gelation transition can be monitored with FTIR allowing insight into the structural rearrangement of the biopolymer as a function of temperature. The spectral transitions are probed with multivariate (PCA & MCR) and two-dimensional (2DCOS, MW2D & PCMW2D) techniques. Structural rearrangement for κ- and ι-carrageenan is observed, with various sulfate based modes showing the most intense changes to temperature. As cooled from 80 to 10 °C, κ- and ι-carrageenan showed sulfate vibrational modes changing predominantly before vibrations associated with the backbone of the polyelectrolyte (C-O-C), indicating a sequential order to the molecular rearrangement occurring during the gelation transition.

Chapter 4

Investigation of a 2 % ι-carrageenan in H_2O is frozen and probed with infrared spectroscopy using a modified low-temperature ATR accessory. The sample is cooled past its freezing point and is then subjected to short term, constant temperature storage. Changes in structure of the water and carrageenan are observed as a function of time post-freezing. Analysis by multivariate, two-dimensional and band fitting routines is applied, allowing the post freezing spectral perturbations to be monitored. Several spectral changes within the fingerprint region occur at a different rate, these have been proposed as vibrations associated with the backbone and protruding groups of ι-carrageenan showing different processes in response to being frozen. Initially post-freezing, large changes in the O-H stretch region for H_2O are observed, before subsiding and followed by changes in the structure of carrageenan. These effects suggest an interaction between ι-carrageenan and ice.

Chapter 5

A confocal Raman microscope, installed at Unilevers Colworth facility, has been used to investigate frozen -carrageenan and water samples. A gradient temperature stage allows formation of ice-fronts and a variety of these type of systems are probed. Changes in the concentration of carrageenan are seen to be dependant on the movement of the ice-front. Progressing an ice front into a gelled (unfrozen) section of the sample results in a large increase in carrageenan concentration at the ice-front. This indicates that the slow growth of the ice crystal is excluding the carrageenan and causing a freeze-concentration effect at the ice-front.

Contents

Chapter 1

Introduction

This Thesis uses infrared spectroscopy coupled with a modified low-temperature ATR accessory to investigate a biopolymer in water. Introduction to the techniques and methods used is presented within the first two Chapters before results are discussed in later Chapters.

1.1 Vibrational Spectroscopy

The study of fundamental molecular vibrations within the mid-infrared wavelength region (2.5 - 25 μm or 4000 - 400 cm^{-1}) allows not only the identification of molecules and materials through their characteristic vibrations, but can also indicate finer structural geometry. Infrared (and in general, optical) spectroscopy is a powerful technique for probing molecular structure, utilising the interaction of electromagnetic radiation with matter. The vibrations of various bonds show absorption patterns that are highly characteristic of a substance, particularly in the fingerprint region (*ca.* 1200 - 400 cm^{-1}). As such, IR spectroscopy can be used to determine the chemical content and/or molecular structure of an analyte. The introduction does not aim to give an extensive overview of vibrational spectroscopy but rather an insight into a few areas that are central to this Thesis.

1.1.1 ATR-FTIR

ATR-FTIR is the combination of attenuated total internal reflection (ATR) and Fourier transform infrared spectroscopy (FTIR). An FTIR spectrometer uses radiation from a single infrared source split into two paths by a beamsplitter and passed into an interferometer. One beam travels a fixed distance and the other is reflected off of a moving mirror. These two beams interfere, due to their phase difference, at the beamsplitter before passing through the sample.[1] The detector records the interferogram as a function of the moving mirror position. The interferogram contains information about every frequency emitted from the source. This is very useful as it allows collection of the entire spectral range very quickly and, in comparison to dispersion spectrometers, allows a much larger throughput of light. The interferogram then undergoes a Fourier transform from the time domain into the frequency domain and a ratio is taken between spectra with and without a sample in place to produce an IR transmission spectrum.

ATR was pioneered independently by Fahrenfort[2] and Harrick[3] during the 1960's and is now an important technique in analytical chemistry. ATR-FTIR is particularly useful, combining the simplicity of sample preparation of ATR with the analytical capabilities of FTIR spectroscopy.

Electromagnetic radiation striking an interface between two media with different refractive indices causes reflection and refraction to occur. The refractive index, n, is the factor by which the speed of light, c and wavelength, λ, are reduced compared to their vacuum values. The wavelength dependence of the refractive index causes dispersion; the splitting of polychromatic light into its constituent spectrum.

Simple treatment of the incident light as a ray or wavefront, rather than quantised radiation (photon) allows simple geometrical calculations to be performed using Snell's equations, Figure - 1.1. The critical angle, θ_c, is the angle of incidence above which total reflection occurs, as depicted in Figure - 1.1. Reflection between an interface can be described as internal or external, the former being a case where the incident beam originates from the optically denser medium

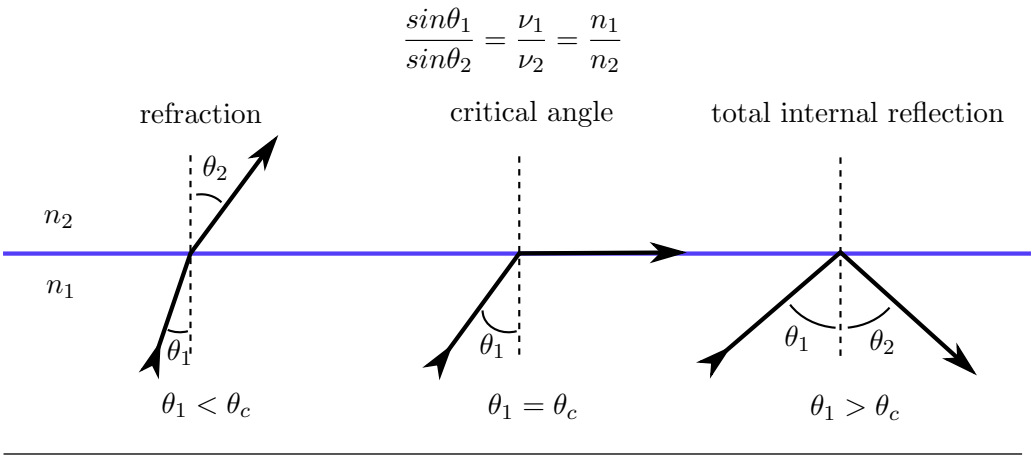

Figure 1.1: Snell's equation; θ is the angle of incidence measured from the normal of the boundary, ν is the velocity of light and n_1 and n_2 are the refractive indices of the respective media. The diagram shows the approach to critical angle, θ_c as θ_1 is increased until total internal reflection occurs.

(higher refractive index) and is then reflected from the interface with the rarer medium, and the later being where the light is reflected within the rarer medium.

Upon total internal reflection, where no light propagates into the rarer medium, a standing evanescent wave propagates across the boundary between the two media. Since the incident and reflected wave have equal intensity the evanescent wave cannot be sinusoidal, as energy transfer into the rarer medium would violate conservation of energy. The electric field of the non-transverse evanescent wave decays exponentially with distance from the boundary, as shown in Figure 1.2.[3]

It is possible to calculate the penetration of the evanescent field (d_p) into the rarer medium and this is dependant upon the angle of the incident ray and the refractive index matching of the two media. It is defined as the distance required for the electric field amplitude to fall to e^{-1} of its initial value at the surface.[3] As the refractive index is wavelength dependent, d_p is also wavelength dependent. As the angle of incidence approaches the critical angle, d_p tends to infinity. Interaction of the evanescent field with the rarer medium not only depends on the depth of penetration but also the electric field, sampling area, index matching and the type of

$$d_p = \frac{\lambda_1}{2\pi(sin^2\theta - n_{21}^2)^{1/2}}$$

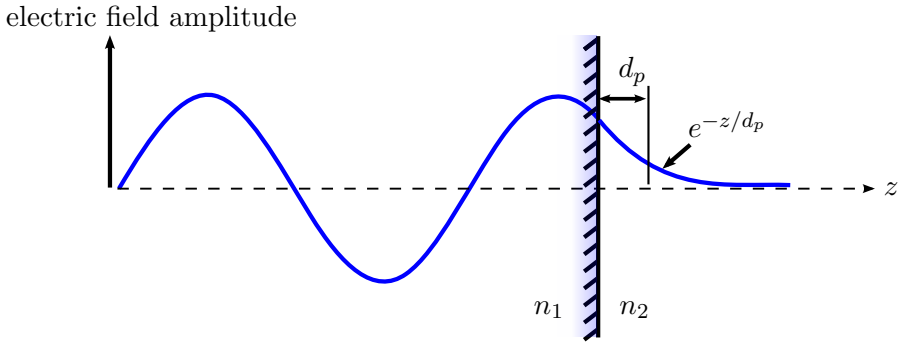

Figure 1.2: A schematic diagram of an evanescent wave amplitude near a totally internally reflected interface. In the denser medium, n_1, there is a sinusoidal variation in the electric field amplitude and an exponentially decaying amplitude in the rarer medium, n_2, associated with the standing wave. Equation shows penetration depth; λ_1 is the wavelength in the denser medium and $n_{21} = n_2/n_1$ is the ratio of the refractive indices.

interaction with the medium.

Although there is no energy flow into the rarer medium *via* the evanescent wave, interactions with the evanescent wave producing a change in the reflected wave can be observed. Coupling to the evanescent wave forms the basis for Internal Reflection Spectroscopy. Coupling to the evanescent standing wave, referred to as attenuated total reflection (ATR), is the phenomenon in which the evanescent field interacts with an absorbing medium, which produces attenuation at specific wavelengths of the reflection, generating an absorption spectrum.

When comparing ATR to transmission spectroscopy it is possible to calculate the (polarisation dependant) effective depth of penetration (d_e), defined as the equivalent path length of a transmission experiment that would lead to an absorption band of the same intensity.[3] Although the effective depth oaf penetration varies for each reflection element, sample and system setup, for most experiments ATR spectroscopy has an equivalent penetration to a pathlength of around a micron (0.5-5 μm).[4,5] The small "pathlength" of ATR, means that samples do not usually have to be diluted prior to data collection, and the ease of preparation has lead ATR to

become the most popular sampling technique for infrared spectroscopy of the condensed phase. [4]

1.2 Multivariate Analysis

The interpretation of infrared spectra in complex systems can often be aided by multivariate analysis. [6] The key concept behind multivariate analysis is the observation and subsequent analysis of multiple statistical variables simultaneously. This allows spectroscopists to analyse the change in intensity of multiple wavelengths simultaneously, compared to more traditional univariate analyses, whereby the intensity of a single wavelength, *i.e.* height of a peak, is monitored.

MATLAB, an acronym for MATrix LABoratory, is a product of Mathworks Inc. It is a computational environment especially suited for problems in matrix algebra. All analyses within this Thesis were performed within MATLAB, making use of its ability to perform complex matrix computations in a command language with a similar notation to matrix algebra. Although some toolboxes and scripts (obtained through MATLAB's File Exchange [7], or third party websites, referenced accordingly) were used during analysis. This Thesis also makes extensive use of PLS Toolbox, produced by Eigenvector. [8] PLS Toolbox is a collection of essential and advanced chemometric routines built within MATLAB's computational environment.

1.2.1 Principal Component Analysis

Principal Component Analysis (PCA) is widely used for data compression and feature extraction. [6] PCA finds combinations of variables, or factors, that describe major trends in the data. [8] If dataset X is a data matrix with m rows and n columns, in which each variable is a column and each sample is a row, PCA decomposes X as the sum of r, t_i and p_i, where r is the rank of the matrix (number of linearly independent rows), $r \leq min\{m, n\}$.

$$X = t_1 p_1^T + t_2 p_2^T + \cdots + t_i p_i^T + \cdots + t_r p_r^T \tag{1.1}$$

The t_i vectors are known as *scores*, containing information of how the samples are related. The p_i vectors are known as *loadings* and contain information of how the variables relate to one another. The t_i and p_i pairs are arrange in descending order of variance captured. For example: if X was a collection of absorbance spectra, then t_i would resemble concentrations and p_i would resemble pure component spectra.

Computationally the principal components are found by calculating the eigenvectors and eigenvalues of the data covariance matrix, equivalent to finding the axis system in which the covariance matrix is diagonal. Equation 1.2 shows calculation of the covariance matrix of X.

$$cov(X) = \frac{X^T X}{m-1} \tag{1.2}$$

Within the PCA decomposition, the p_i vectors are eigenvectors of the covariance matrix, as shown in Equation 1.3, where λ_i is the eigenvalue associated with eigenvector p_i. The eigenvector, p_i, with the largest eigenvalue, λ_i is the direction of greatest variation. p_i with the second largest λ_i is the orthonormal ($p_i^T p_j = 0$ for $i \neq j$, $p_i^T p_j = 1$ for $i = j$) direction with the next highest variation.

$$cov(X)p_i = \lambda_i p_i \tag{1.3}$$

Finally, the score vector, t_i also forming an orthogonal set ($t_i^T t_j = 0$ for $i \neq j$), is the linear combination of the original X variables defined by p_i, depicted in Equation 1.4. t_i are the projections of X onto p_i.

$$Xp_i = t_i \tag{1.4}$$

Practically, p_i with the largest λ_i can be considered to be the loading that contains the most information about the system. It is generally found that the data can be adequately described using many fewer factors, p_i, that the original variables. Herein lies the power of PCA, by observing and monitoring far fewer scores (weighted sums of the original variables) than original variables, with no significant loss of information, the data overload problem can be solved.[6] It is also found that PCA finds combinations of variables that are useful descriptors, or predictors of events.

1.2.2 Multivariate Curve Resolution

Principal component analysis is probably the most commonly used factor analysis technique,[6] however it is not the only one. PCA extracts information based on properties of the data such as capturing maximum variance and orthogonality, these factors are often difficult to interpret as they are generally not related to the chemical properties of a system. Typically PCA loadings are linear combinations of pure analyte spectra that have positive and negative intensities. Multivariate Curve Resolution (MCR) attempts to decompose a matrix into non-negative factors, *i.e.* pure analyte spectra. This approach is based on an "un-mixing" method in an attempt to decompose the data and MCR is part of a collection of techniques referred to as self-modelling curve resolution. The result of this is that concentrations and pure component spectra (equivalent to PCA's scores and loadings respectively) can be extracted.

$$X = CS^T + E \tag{1.5}$$

A real $m*n$ data matrix, X, can be decomposed into a product of an $m*k$ matrix of concen-

tration profiles, C, and an $n * k$ matrix of pure component spectra S, where k is the number of analytes, and a residual error term, E. This bilinear deconvolution is referred to as Multivariate Curve Resolution and is shown in Equation 1.5. This is particularly suited to spectroscopy as chemical systems adhere to an analytical bilinear model known as the Beer-Lambert law.[9]

1.2.3 Interpretation of PCA and MCR

To demonstrate the applicability and interpretation of Principal Component Analysis and Multivariate Curve Resolution to systems monitored with vibrational spectroscopy, simulated spectra with noise have been created and subsequently analysed with PCA and MCR. A pseudo-chemical system with two components, A and B, has been created. Over the course of the experiment, A is converted to B at a linear rate. In this artificial example the system is monitored by FTIR spectroscopy.

Generation of the pseudo-spectra is given in Section 5.5. Both species, A and B, are modelled using Gaussian profiles. Chemical A has peak maxima at 1200, 1175 and 1100 cm^{-1}, with relative intensites of 1, 0.6 and 0.8, respectively, and FWHMs (full width at half maximum) of 10, 15 and 5 cm^{-1}, respectively. Chemical B has peak maxima at 1150, 1090 and 1075 cm^{-1}, with relative intensities of 0.7, 0.2 and 0.3, respectively, and FWHMs of 12.5, 20 and 7.5 cm^{-1}. A spectrum is collected every second and the experiment lasts 1000 seconds. From $t = 0$ to $t = 1000$ seconds, A is consumed, with its concentration falling from 100 % to 0 % and B is produced, its concentration increasing from 0 % to 100 % at a linear rate. Each spectrum is augmented with additive white Gaussian Noise (AWGN) to a level that corresponds to a signal to noise ratio (SNR) of 20. Figure 1.3 shows simulated spectra at 4 different time delays over the course of the experiment. The different time delays; $t = 0, 250, 500$ and 1000 correspond to ratios of components A to B (A:B) as 1:0, 0.75:0.25, 0.25:0.75 and 0:1, respectively.

The spectra displayed in Figure 1.3 are very noisy (simulated AWGN to SNR of 20) and

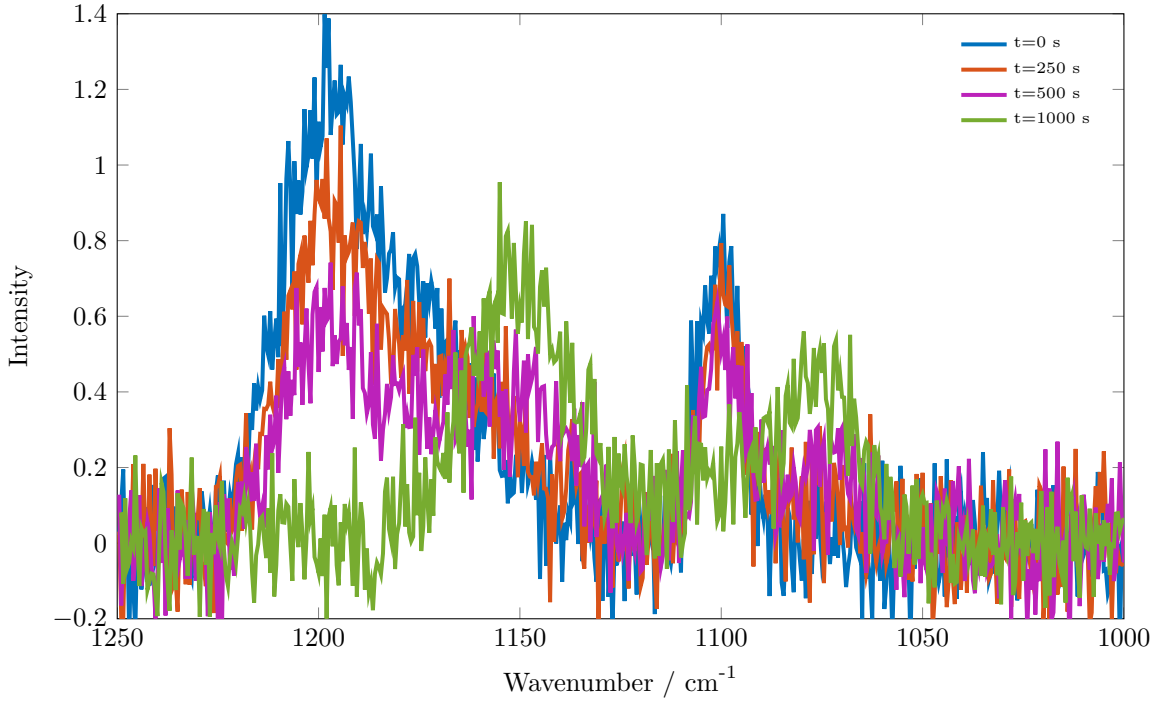

Figure 1.3: Simulated spectra (with added AWGN, to a SNR of 20) of a pseudo-chemical system comprised of two species; A and B, over the course of a 1000 second experiment. $t = 0$ and $t = 1000$ represent pure component A and B species respectively

although interpretation using classical univariate methods is possible, a multivariate approach can yield superior noise reduction and interpretation. Principal Component Analysis was performed on the data utilising the command line interface of PLSToolbox.[8] The eigenvalues, λ_i, or root-mean-square error of calibration / cross-validation (RMSEC / RMSECV) can be inspected to determine how many principal components are needed to describe the system.

The first principal component (PC1) contained 78 % of the system's variance, PC2 contained 11 % and subsequent PCs captured 0.3 % or less each. The RMSECV (effectively the ability to predict the model) increased after PC2, and continues to do so indefinitely. This indicates that two principal components can best model the data and the data becomes more difficult to predict (and explain) when more than two are included within the model.

The loadings and scores (p_i and t_i respectively) for the first two principal components of the experiment are shown in Figure 1.4. The principal components (often referred to as loadings) are shown in the top panel, and indicate how the spectra change (as a function of wavenumber). The bottom panel shows the scores of each PC and how these relate to each loading changes as a function of time after the start of the experiment. In relation to classical univariate analysis of a set of spectra, the scores are similar to observing how a peak height changes in intensity during the experiment. However, instead of describing how peak height changes with each time delay, the scores describe how the loadings change per time delay.

As shown in Figure 1.4, the loadings appear to show a large resolution enhancement compared to the raw data seen in Figure 1.3. Multivariate techniques are able to provide a noise reducing (sometimes called resolution enhancement) effect due to the simultaneous processing of the entire spectral set. The extent of noise reduction is directly related to the number of individual spectra within the set, and the SNR increase achieved by multivariate techniques is similar to averaging all the spectra collected, *i.e.* the mean of 1000 spectra within this experiment. It is also worth pointing out here, that this noise can effectively be removed as it is random (Gaussian, AWGN)

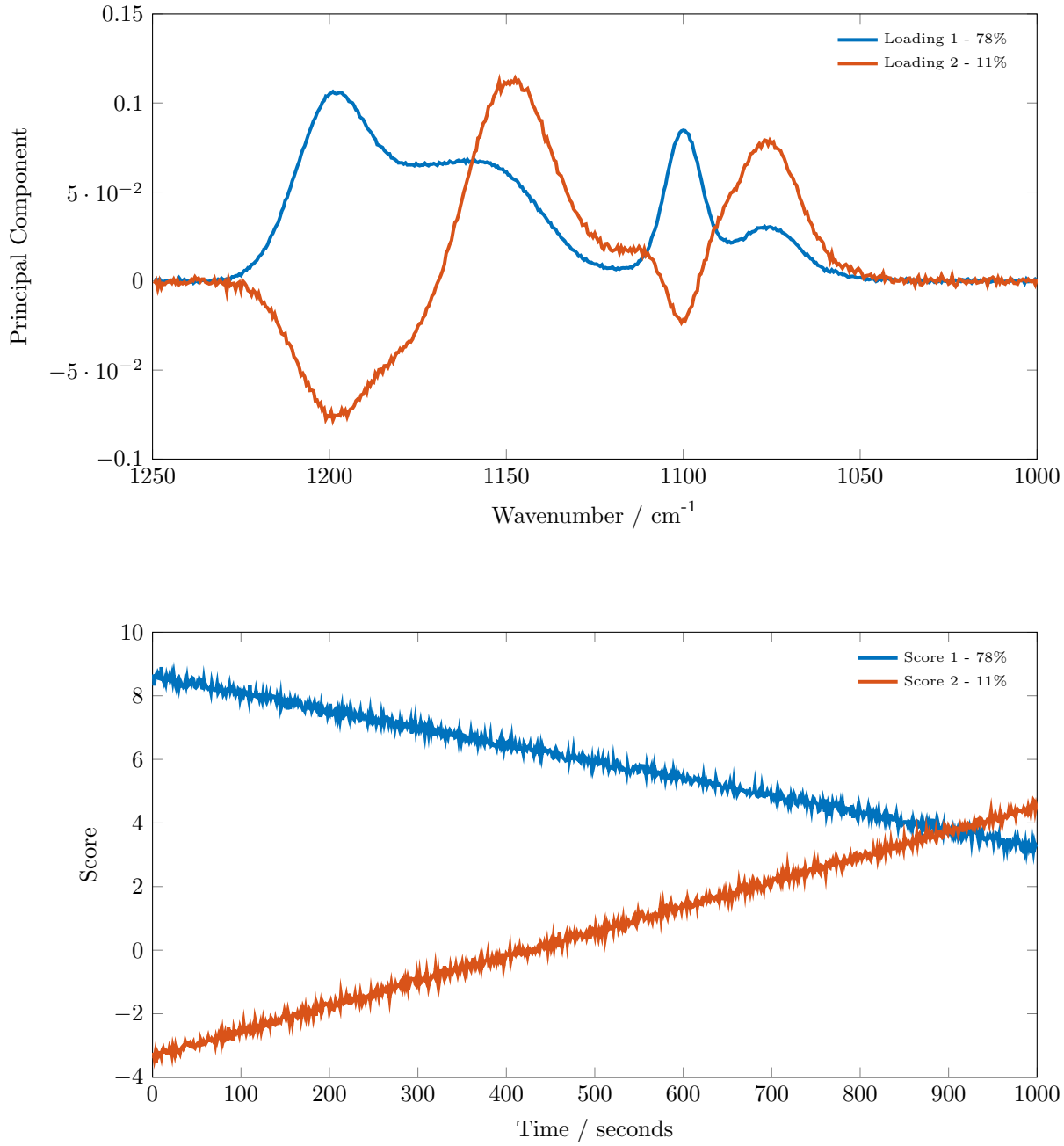

Figure 1.4: PCA results from the analysis of the pseudo-spectra. Top: loadings 1 and 2. Bottom: scores 1 and 2

and not systematic.

Analysis using PCA during this Thesis will always mean-center the data prior to processing, however within this example this has not been done to enable slightly easier interpretation and reference back to the original spectra. Without the mean-centering of data prior to analysis, the first PC mostly shows the mean of the data. This can be useful for spectroscopic applications where values of 0 have an absolute meaning (*i.e.* an absorbance of 0, meaning a 0 % concentration). Many applications however require mean-centering, such as where zero values are arbitrary, temperatures measured in °C for example.

The first loading shows features analogous to the mean of the original data, with only positive features, as expected. The second loading shows both positive and negative features. Positive bands at 1150 and 1075 $cm^{-1}$and negative features at 1200 (with a lower energy shoulder) and 1100 cm^{-1}. These features correspond to chemicals A and B within the system. The fact that they are both represented within a single loading suggests that they are not orthogonal to each other, *i.e* they change with near-identical rates. The combination of negative and positive features suggest that they change in opposite directions.

The Scores plot (bottom panel of Figure 1.4) shows that both the PCs change linearly over the duration of the experiment. The score of loading 1 decreases, while the score of loading 2 increases. When both the scores and loadings plot are analysed together a description of the system can be achieved. A decrease of loading 1 as time is progressed indicates that all the bands present a decrease as a function of time. For loading 2, which sees increase over time, some bands are positive and others are negative, representing an increase and decrease over time, respectively. Over the course of the experiment, the 1200 cm^{-1} feature diminishes completely, and the feature at 1150 cm^{-1} increases in intensity. The 1200 and 1150 cm^{-1} features can be attributed to chemicals A and B respectively. Figure 1.4 suggests that as chemical A is consumed, chemical B is formed at the same rate, which remains linear over the course of the

experiment, *i.e.* A $\rightarrow$ B.

The analysis from PCA (Figure 1.4) indeed demonstrates the expected change over the course of the experiment, A $\rightarrow$ B. However the interpretation of the loadings and scores can sometimes be difficult as both positive and negative features exist, and since A decays at the same rate B grows, their spectral features cannot be separated by PCA. This is because their spectral features change in a mathematically identical way, and PCA separates variance based on orthogonality.

Due to the confusion of chemicals A and B within one PC, their relative concentrations at a given time of the experiment cannot be extracted easily. Multivariate Curve Resolution (MCR) attempts to extract pure component spectra, with scores that are closely related to concentrations. MCR was performed on the same data (shown in Figure 1.3). The model was based on a 2 component system, and the components (the MCR terminology analogous to PCA's loadings) and scores are shown in Figure 1.5.

The top panel of Figure 1.5 shows the two components from the MCR decomposition of the data. It is immediately obvious, in contrast to the PCA loadings that the MCR components more closely resemble real chemical spectra. These components exactly replicate the chemical species A and B as described at the beginning of this section. Also apparent is a large reduction in noise, similar to that observed for PCA. The scores show that at the start of the experiment, component 1 accounts for 100 % of the mixture and there is no evidence of component 2. As the experiment progresses, score 1 decreases at a linear rate, and score 2 increases at a linear rate. At the end of the experiment the system is comprised solely of component 2. The interpretation of MCR results is much more straight forward than PCA analysis.

Although Multivariate Curve Resolution is hugely powerful and can be more useful than Principal Component Analysis when applied to spectroscopy, there are also problems associated with it. Within the PCA, it was clear that species A and B changed at the same rate because

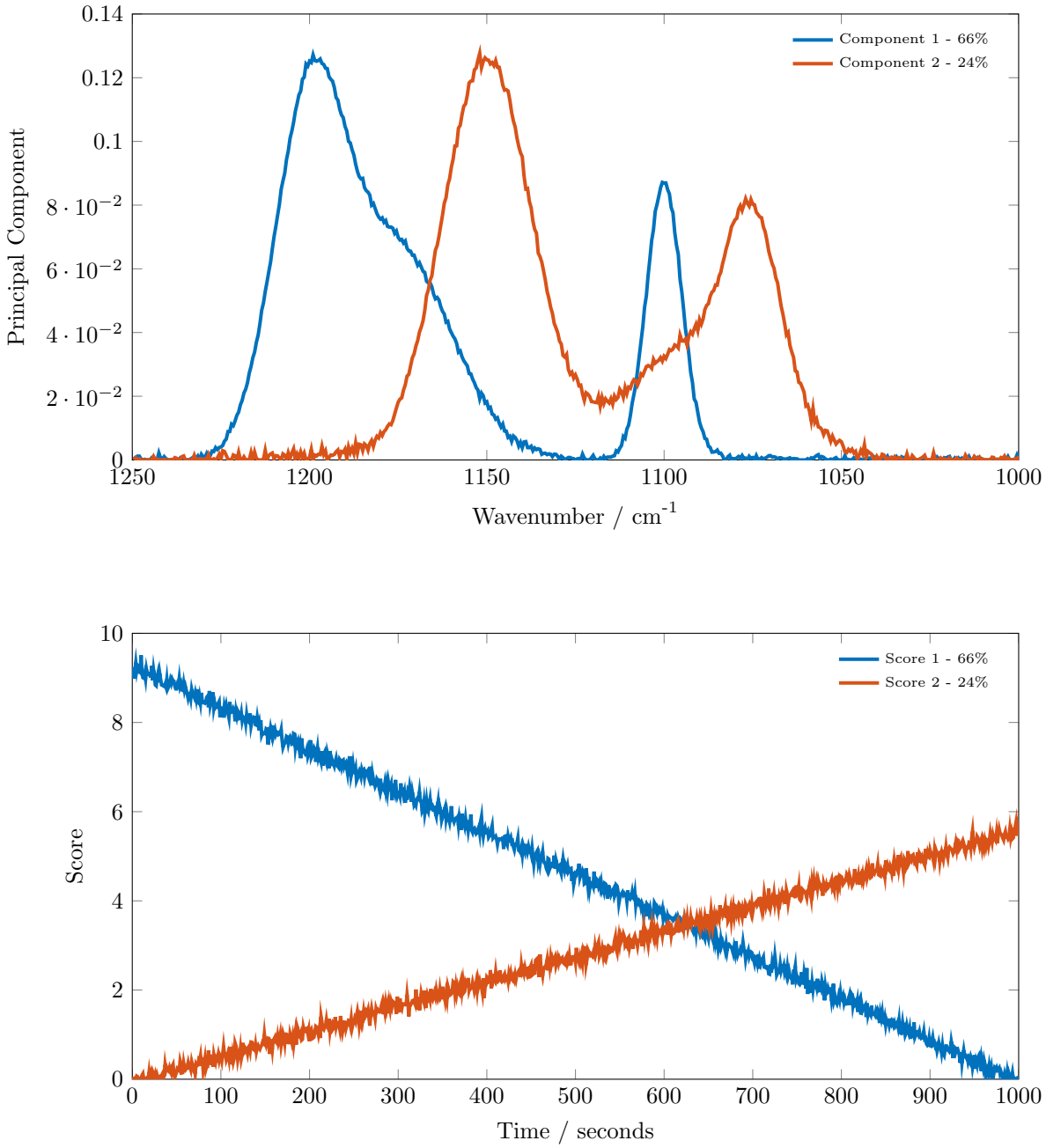

Figure 1.5: MCR results from the analysis of the pseudo-spectra. Top: components 1 and 2. Bottom: scores 1 and 2

spectral features from the two chemicals were present within one loading. The scores of the MCR analysis however do not have the same gradient and therefore it is easy to assume that their rate is different. However, at $t = 0$ MCR scores show 100 % component 1 and 0 % component 2, at $t = 100 =$ the scores show 0 % component 1 and 100 % component 1. As they both have linear rates, the system must be an exact A $\rightarrow$ B linear transition. The scores of MCR analysis, are related to the component "concentration", and this changes depending on the total absorbance of its spectral features, *i.e.* the score is dependant on the area of the components, in the same way the concentration of a species is dependant on the area under its absorbance profile.

Both PCA and MCR capture 89.7 % of total variance, within two components / loadings. Reconstruction of the original data is possible *via.* a linear combination of the scores and loading / components. Figure 1.6 shows 4 spectral traces: the raw data (blue dashed), raw data with no noise (AWGN removed) (orange), the PCA reconstruction (purple) and the MCR reconstruction (green) for $t = 500$ seconds. The PCA and MCR reconstructed spectra show near-perfect agreement to the raw simulated spectra, without the noise. The level of noise reduction gained with these multivariate techniques is clear when compared with the original spectrum (blue trace).

Multivariate Curve resolution has the added benefit of extracting components with the aim of matching the pure chemical spectra to species changing during an experiment. Figure 1.7 shows the pure chemical simulated spectra that were used to create the pseudo spectra (blue and orange traces) overlaid with the Components 1 and 2 (blue and orange dashed traces, offset for clarity). It is clear that the MCR components replicate the original chemical spectra very closely. This is one of the most useful aspects of MCR; without knowing the original spectra of chemicals A and B, MCR can be used to calculate them and significantly reduce the noise level compared to the simulated, raw spectra.

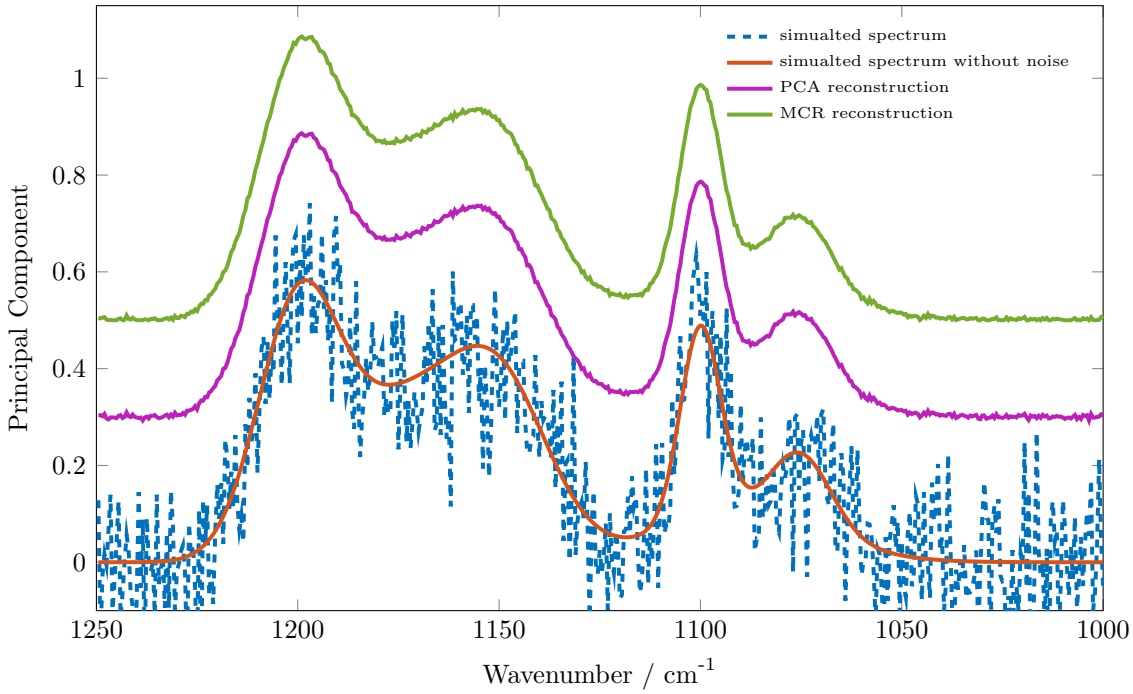

Figure 1.6: For $t = 500$ seconds, of the simulated spectra, the raw data (blue dashed trace), raw data without AWGN (orange trace) PCA reconstructed data (purple trace) and MCR reconstructed data (green trace)

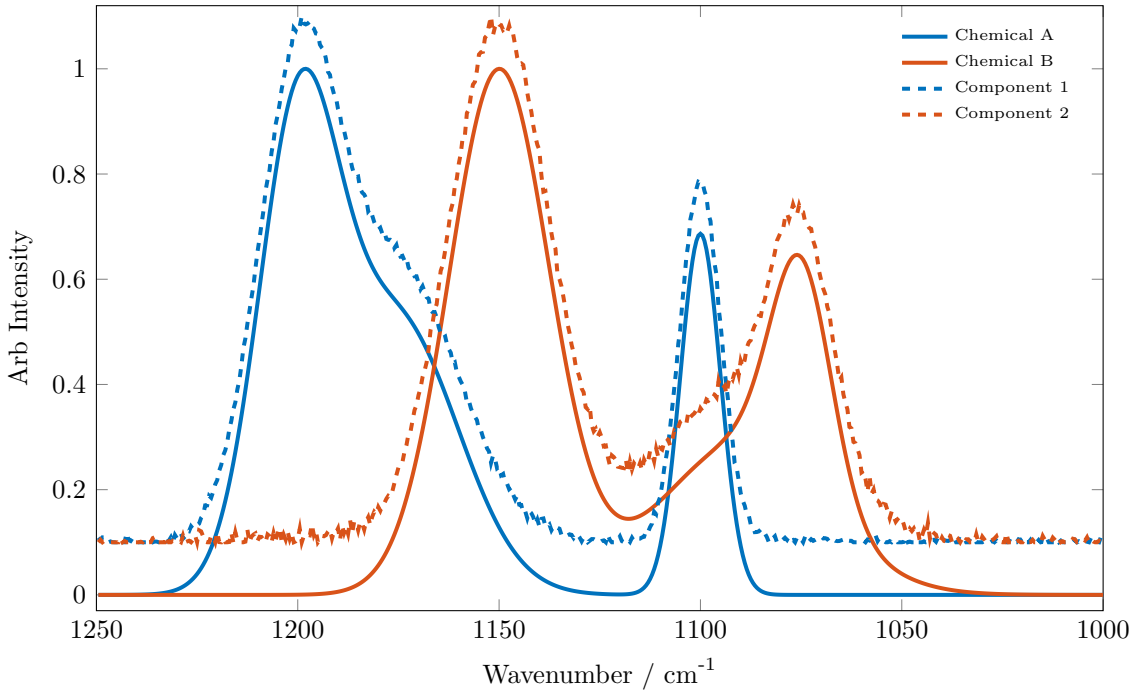

Figure 1.7: Pure component spectra for chemicals A and B (blue and orange traces, no noise), and MCR Components 1 and 2 (blue and orange dashed traces, offset for clarity)

1.3 Two-Dimensional Correlation Spectroscopy

Generalised two-dimensional correlation analysis was developed in the early-1990s by Isoa Noda.[10,11] By spreading overlapping spectral features over a second dimension it is possible to improve visualisation of the data, which can aid interpretation. Two-dimensional correlation spectroscopy (2DCOS) also aids in visualising the relationships among multivariate data by means of a complex cross-correlation function. The application of 2DCOS to infrared spectroscopy is not to be confused with 2D-IR spectroscopy, which is a separate, unrelated, non-linear pump-probe technique.[12]

Large datasets, such as those obtained from modern analytical techniques often exhibit high dimensionality, whereby many of the variables are mutually dependant and exhibit collinearity. Identifying and understanding the correlation within signals is of the upmost importance in developing knowledge of physiochemical relationships. Utilising correlation and/or covariance tables as a way to visualise these changes often aids in their interpretation. Two-dimensional correlation spectroscopy is an extension of this visualisation, implementing a complex cross-correlation. Additionally, if the system is subjected to systematic perturbation, cross-correlation techniques may lock-in to the modulated signal, enhancing information obtained from measurements.

To perform 2DCOS on a set of data a series of perturbation induced dynamic spectra must first be collected systematically, *i.e.* in a sequential order during the perturbation. The set of dynamic data is then transformed, *via* a specific mathematical procedure, into a set of 2D correlation spectra by cross-correlation analysis. Various studies have utilised a wide range of external perturbations: mechanical, electrical, chemical, magnetic and thermal, for example.[10]

1.3.1 Generalised Two-Dimensional Correlations Spectroscopy

For a spectral dataset $y(\nu, t)$ where ν and t ($T_{min} \leq t \leq T_{max}$) are respectively, the spectral variable (wavelength or wavenumber) and the external variable (here chronological time is used, however any physical perturbation can be used), dynamic spectra must first be generated.

The dynamic spectrum, $\tilde{y}(\nu, t)$, of a system is formally defined in Equation 1.6. The reference spectrum, $\bar{y}(\nu)$, Equation 1.7, is chosen to be the mean spectrum inline with convention, however, the selection of a spectrum at a fixed point in time ($t = T_{ref}$, so that $\bar{y}(\nu) = y(\nu, T_{ref})$) can be made.

$$\tilde{y}(\nu, t) = \begin{cases} \tilde{y}(\nu, t) - \bar{y}(\nu) & \text{for } T_{min} \leq t \leq T_{max}, \\ 0 & \text{otherwise.} \end{cases} \tag{1.6}$$

$$\bar{y}(\nu) = \frac{1}{T_{max} - T_{min}} \int_{T_{min}}^{T_{max}} y(\nu, t)\, \mathrm{d}t \tag{1.7}$$

2D correlation spectroscopy is the quantitative comparison of patterns of change in spectral intensity variations with respect to the external variable t. These changes in spectral intensities are examined at two different spectral variables, ν_1 and ν_2, over a finite interval, t ($T_{min} \leq t \leq T_{max}$). The intensity of the cross-correlation, $X(\nu_1, \nu_2)$, shown in Equation 1.8, represents the similarity or dissimilarity of spectral intensity variations at two separate spectral variables. Owing to the complex cross correlation function used the product of the cross correlation is treated as a complex number function, Equation 1.9.

$$X(\nu_1, \nu_2) = \langle \tilde{y}(\nu_1, t) \cdot \tilde{y}(\nu_2, t') \rangle \tag{1.8}$$

$$X(\nu_1, \nu_2) = \Phi(\nu_1, \nu_2) + i\Psi(\nu_1, \nu_2) \tag{1.9}$$

Generalised 2D correlation yields two orthogonal (real and imaginary) components, called the synchronous, $\Phi(\nu_1, \nu 2)$, and asynchronous, $\Psi(\nu_1, \nu_2)$, spectra. The exact form of the complex cross correlation can take many different forms, yielding different information contained within the 2D correlation intensities. For the generalised case, the synchronous 2D correlation intensity $\Phi(\nu_1, \nu_2)$ represents coincidental trends between two separate intensity variations measured at different spectral variables, as t varies from T_{min} to T_{max}. The asynchronous $\Psi(\nu_1, \nu_2)$ is the out of phase character of the spectral intensity variations.

$$\Phi(\nu_1, \nu_2) + i\Psi(\nu_1, \nu_2) = \frac{1}{\pi(T_{max} - T_{min})} \int_0^\infty \tilde{Y}_1(\omega) \cdot \tilde{Y}_2^*(\omega) \mathrm{d}\omega \tag{1.10}$$

Equation 1.10 shows the synchronous and asynchronous correlation intensities. Here term $\tilde{Y}_1(\omega)$ is the forward Fourier transform of the spectral intensity variations, $\tilde{y}(\nu_1, t)$, observed at a given spectral variable, ν_1, with respect to external variable t and where $\tilde{Y}_2^*(\omega)$ is the complex conjugate. $\tilde{Y}_1(\omega)$ and $\tilde{Y}_2^*(\omega)$ are expressed in Equations 1.11 and 1.12.

$$\begin{aligned} \tilde{Y}_1(\omega) &= \int_{-\infty}^{\infty} \tilde{y}(\nu_1, t) e^{-i\omega t} \mathrm{d}t \\ &= \tilde{Y}_1^{Re}(\omega) + i\tilde{Y}_1^{Im}(\omega) \end{aligned} \tag{1.11}$$

$$\begin{aligned} \tilde{Y}_2^*(\omega) &= \int_{-\infty}^{\infty} \tilde{y}(\nu_2, t) e^{+i\omega t} \mathrm{d}t \\ &= \tilde{Y}_2^{Re}(\omega) - i\tilde{Y}_2^{Im}(\omega) \end{aligned} \tag{1.12}$$

Equations 1.11 and 1.12 demonstrate the components of the cross correlation. In short, $\Phi(\nu_1, \nu_2)$ and $\Psi(\nu_1, \nu_2)$ correspond respectively to the real and imaginary parts of the Fourier

frequency domain spectral correlation, *i.e.* in phase and quadrature components of the spectral intensity variations of ν_1 and ν_2.

Since the differences between $\tilde{Y}_1(\omega)$ and $\tilde{Y}_2^*(\omega)$ lie solely within the imaginary component, the synchronous spectrum $\Phi(\nu_1, \nu_2)$ can be directly calculated without Fourier transforming the dynamic spectra. Equation 1.13 indicates that the synchronous correlation intensity is the time average of the product of spectral intensity variations occurring at different spectral variables, ν_1 and ν_2. This has important implications upon the use of 2DCOS, discussed more in Section 1.3.4, in particular time-windows that contain multiple spectra variation patterns will yield the convolution of these features. This can be both an advantage and a hinderance during analysis.

$$\Phi(\nu_1, \nu_2) = \frac{1}{(T_{max} - T_{min})} \int_{T_{min}}^{T_{max}} \tilde{y}(\nu_1, t) \cdot \tilde{y}(\nu_2, t) \mathrm{d}t \tag{1.13}$$

This realisation allows direct computation of the synchronous spectrum, however the asynchronous spectrum must be calculated by other means. As evident from Equation 1.10, it is possible one can obtain the asynchronous spectrum by performing a correlation within the forward Fourier frequency domain. However, as real and imaginary components are related orthogonally, one may use a time-domain Hilbert transformation to equate the orthogonal components needed for the asynchronous spectrum. The Hilbert Transform $h(t)$ for a given analytic function $g(t)$ is given by:

$$h(t) = \frac{1}{\pi} \int_{-\infty}^{\infty} \frac{g(t')}{t' - t} \mathrm{d}t' \tag{1.14}$$

The Hilbert transform is associated with Kramers-Kronig analysis and transformations [13], whereby orthogonal dispersion relationships due to anomalous dispersion are observed. The transformation function shifts the phase of each Fourier components backwards or forwards by $\pi/2$ if $\omega < 0$ or $\omega > 0$ respectively, producing a function $h(t)$ orthogonal to $g(t)$. Using the

Hilbert transform to generate an orthogonal spectrum, $\tilde{z}(\nu_2, t)$ shown in Equation 1.15, allows computation of the asynchronous spectrum through the product of the dynamic spectrum and the orthogonal spectrum, as shown in Equation 1.16.

$$\tilde{z}(\nu_2, t) = \frac{1}{\pi} \int_{-\infty}^{\infty} \frac{y(\nu_2, t')}{t' - t} \mathrm{d}t' \tag{1.15}$$

$$\Psi(\nu_1, \nu_2) = \frac{1}{(T_{max} - T_{min})} \int_{T_{min}}^{T_{max}} \tilde{y}(\nu_1, t) \cdot \tilde{z}(\nu_2, t) \mathrm{d}t \tag{1.16}$$

1.3.2 Practical Computation of Two-Dimensional Correlation Spectroscopy

Although computation of 2DCOS spectra can be achieved through the Fast Fourier Transform (FFT),[14] use of the discreet Hilbert transform has proved to be a valuable method for practical computation.[15] The Hilbert transform algorithm carries out the time-domain orthogonal transformation of the dynamic spectra and provides a computational advantage over FFT methods, as long as the number of discreet spectra does not greatly exceed 40.[15]

$$\tilde{y}(\nu) = \tilde{y}(\nu_1, t_j) \quad \text{for } j = 1, 2, ..., m, \tag{1.17}$$

A discreet set of dymanic spectra, measured at m equally spaced points in time t between T_{min} and T_{max}, can be described as Equation 1.17.

Equation 1.18 expresses the dynamic vector in matrix notation as a discreet column vector. With this notation, the synchronous 2D correlation spectrum can be calculated as the inner product of the dynamic spectrum vectors; Equation 1.20.

$$\tilde{\boldsymbol{y}}(\nu) = \begin{bmatrix} \tilde{y}(\nu_1, t_1) \\ \tilde{y}(\nu_1, t_2) \\ \vdots \\ \tilde{y}(\nu_1, t_) \end{bmatrix} \tag{1.18}$$

$$\boldsymbol{\Phi}(\nu_1, \nu_2) = \frac{1}{m-1} \tilde{\boldsymbol{y}}(\nu_1)^T \tilde{\boldsymbol{y}}(\nu_2) \tag{1.19}$$

The orthogonal spectrum $\tilde{z}_j(\nu_2)$ for a fixed time period between T_{min} and T_{max} can be achieved through the use of the Hilbert-Noda transformation matrix, $\boldsymbol{N}$.[16]

$$\tilde{z}_j(\nu_2) = \sum_{k=1}^{m} N_{jk} \cdot \tilde{y}_k(\nu_2) \tag{1.20}$$

where

$$N_{jk} = \begin{cases} 0 & \text{if } j = k, \\ \frac{1}{\pi}(k-j) & \text{otherwise.} \end{cases} \tag{1.21}$$

The MATLAB code for the computation of the 2DCOS spectra is included in the Section 5.6.

1.3.3 Interpretation and Implementation of Two-Dimensional Correlation Spectroscopy

To demonstrate the use of two-dimensional correlation spectroscopy, some sample data is presented. The data has been adapted from the work of Noda.[17,18] Four spectral features, A, B, C and D, with gaussian profiles have been submitted to different perturbations as a function of

time. The generation of this data is shown in the appendix, Section 5.7. During the perturbation from $t = 0$ to $t = 50$, band A increases in intensity at the same time and same rate as that at which band C decreases in intensity. Bands B and D both increase intensity from $t = 10$ to $t = 40$.

The intensity of a synchronous 2D correlation spectrum, $\Phi(\nu_1, \nu_2)$, represents the coincidental or simultaneous changes of spectral intensity variations at ν_1 and ν_2 between T_{min} and T_{max} of the external perturbation, t. Figure 1.8 shows the synchronous map of the sample data. Along the top and left axes the mean of the sample data is shown, this aids with interpretation. The colourmap used for the 2DCOS contour plots is 'bluewhitered' (included in the Appendix), which is a modified version of 'BLUEWHITERED', obtained from the MATLAB File Exchange.[19] Negative values are shown in blue, white indicates values close to 0, and red shows positive values. The function used to display two-dimensional maps within this thesis is given in Section 5.10 and allows dynamic zooming within the MATLAB environment.

Synchronous spectra are symmetrical along the diagonal $\nu_1 = \nu_2$, with correlation peaks appearing at both on-diagonal and off-diagonal positions. The intensity of peaks located along the diagonal mathematically corresponds to the autocorrelation function of spectral intensity variations during the perturbation. The magnitude of these peaks, referred to as autopeaks, represents the overall extent of the intensity variation at spectral variable ν. It can be seen from figure 1.8 that bands A, B, C and D all show strong autopeaks, indicating intensity variations during the perturbation. The use of autopeaks in assessing a systems susceptibility to change over the course of a perturbation is a useful tool to investigate the spectral regions of interest.

The cross peaks, located at off-diagonal positions, develop if the change in spectral intensity variation at two different variables(ν_1 and ν_2) is simultaneous or coincidental. A synchronised change between two variables suggests that these two processes are coupled or have a common origin. The intensity of the cross peaks show the extent of coupling between the two variables,

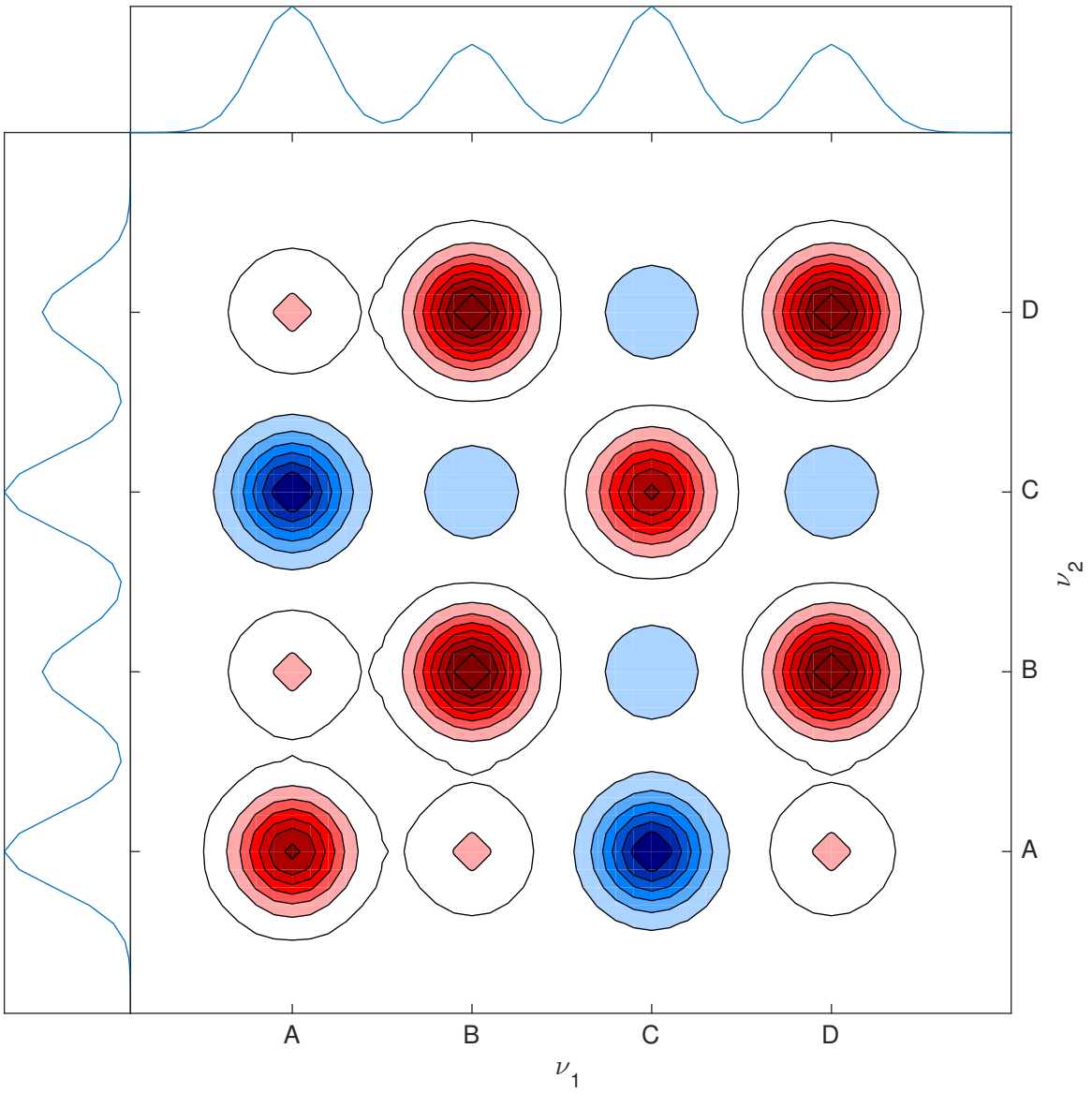

Figure 1.8: 2DCOS synchronous correlation map of sample data; colourmap: blue-white-red; negative-0-positive

relative to other changes within the system. Cross peaks can be either positive or negative. A positive cross peak will develop if the direction of change between the two spectral variables is the same, *i.e.* spectral intensities increasing or decreasing simultaneously. A negative cross peak indicates that changes in intensity occur with opposite signs between the two variables. More specifically this could be one increasing and one decreasing or *vice versa*, as a function of the perturbation.

Figure 1.8 shows multiple cross peaks. The four most intense peaks are those that are of most interest. These peaks are located between bands A and C, and bands B and D. The two A-C cross peaks (at $\Phi(A, C)$ and $\Phi(C, A)$) are negative, indicating that the change in spectral intensities of bands A and C is synchronous, however they are in an opposite directions. The B-D cross peaks (at $\Phi(B, D)$ and $\Phi(D, B)$) are positive, showing that the bands not only change at the same rate, but with the same sign.

Figure 1.9 shows the asynchronous spectral map for the sample data. Asynchronous spectral features represent sequential or successive changes of spectral intensity variation measured at ν_1 and ν_2. The asynchronous spectrum, unlike the synchronous, is antisymmetrical about the diagonal, with no autopeaks and only cross peaks. Peaks only develop if the intensity variation at two spectral variables change out of phase with each other, *i.e.* at a different rate. The sign of the asynchronous cross peak is positive only if the intensity change at ν_1 occurs predominately before ν_2, and the peaks are negative if ν_1 occurs after ν_2. These rules are referred to as Noda's rules. However, the rules are reversed if the corresponding position in the synchronous spectrum is negative, $\Phi(\nu_1, \nu_2) < 0$.

When interpreting the asynchronous spectrum it is important to always refer back to the synchronous spectrum so that a misassignment is not made due to reversal of Noda's rules when $\Phi(\nu_1, \nu_2) < 0$. To ease interpretation without the need to refer to multiple figures, it is possible to display half of the synchronous data and half of the asynchronous data (along the diagonal)

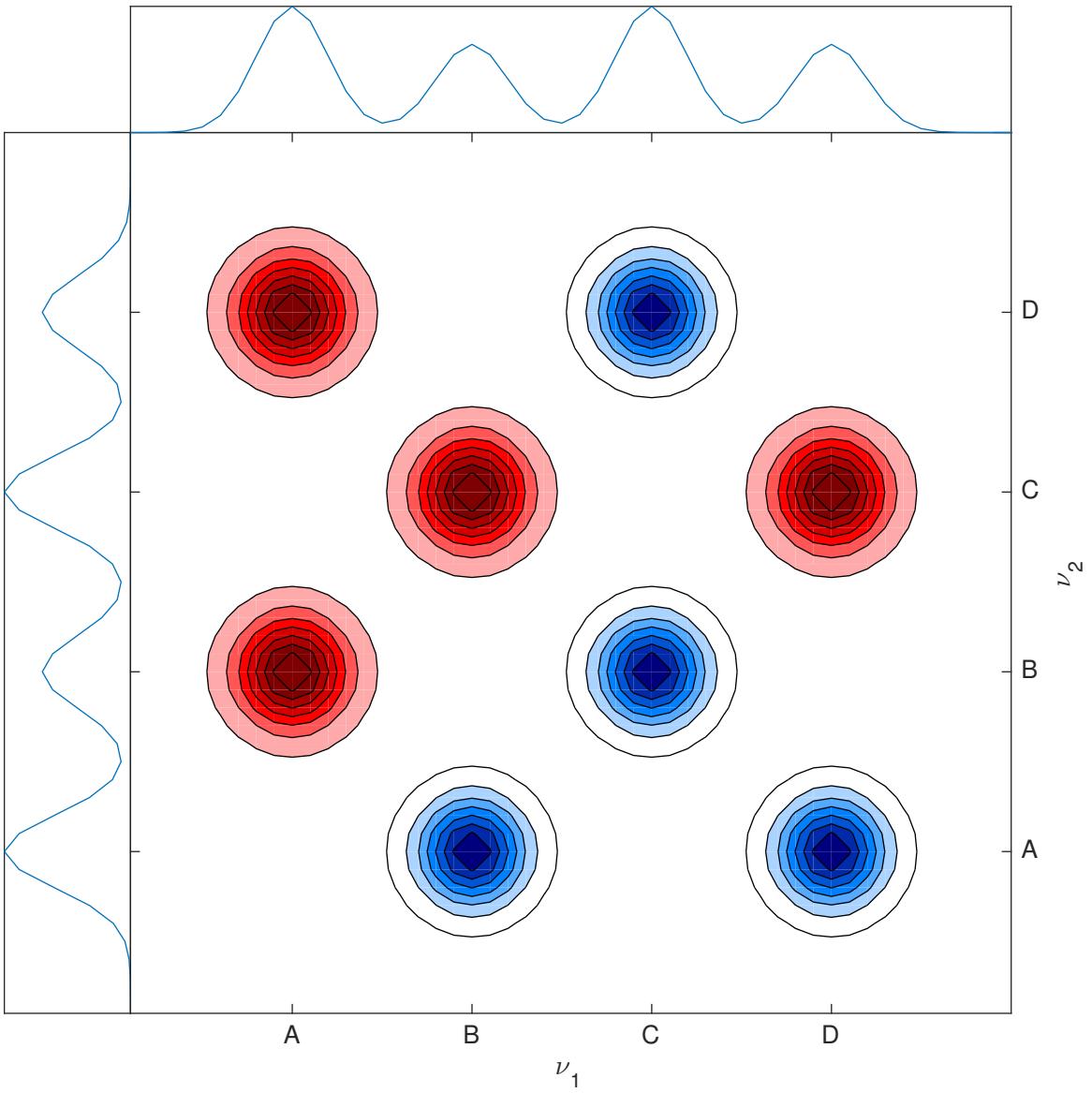

Figure 1.9: 2DCOS asynchronous correlation map of sample data; colourmap: blue-white-red; negative-0-positive

on the same figure, as the synchronous and asynchronous are symmetrical / antisymmetrical along the diagonal respectively.

Modified Noda's rules allow simplification of the asynchronous spectrum, without the need to apply the rule reversal, when $\Phi(\nu_1, \nu_2) < 0$.[20] The modified rule states that if the sign of both the synchronous and asynchronous spectra are the same, at a particular position, then ν_1 occurs predominately before ν_2. If the sign of $\Phi(\nu_1, \nu_2)$ and $\Psi(\nu_1, \nu_2)$ is different then ν_2 varies before ν_1.

Figure 1.10 shows the asynchronous (Modified Noda's rules) spectrum. This is the asynchronous spectrum in which every datapoint has been multiplied by the sign of the corresponding synchronous datapoint. The consequence of this mathematical manipulation is the implementation of modified Noda's rules which can subsequently be presented in a graphical format. Equation 1.22 shows the Hadamard product (element-wise multiplication) of the asynchronous spectrum with the sign of the synchronous.

$$\Psi_{mod}(\nu_1, \nu_2) = \Psi(\nu_1, \nu_2) \circ sgn(\Phi(\nu_1, \nu_2)) \tag{1.22}$$

If a peak is positive (red) then ν_1 occurs before ν_2. However a negative, blue peak indicates that ν_1 changes after ν_2. By utilising this graphical format the sequential order of changes in intensity can be readily determined, in this example, A and C change before B and D. This is correct, as the sample data gave the spectral intensities of A and C changing at $t = 0$, whilst the spectral intensities of B and D were constant until $t = 10$.

Within this example another major difference as to how data is displayed for the modified Noda's rules asynchronous spectra is that the autocorrelation of the perturbation is displayed along the top and left of the spectrum. This is in contrast to the synchronous spectrum figures, where the mean of the input data is displayed. Often when dealing with complex systems it

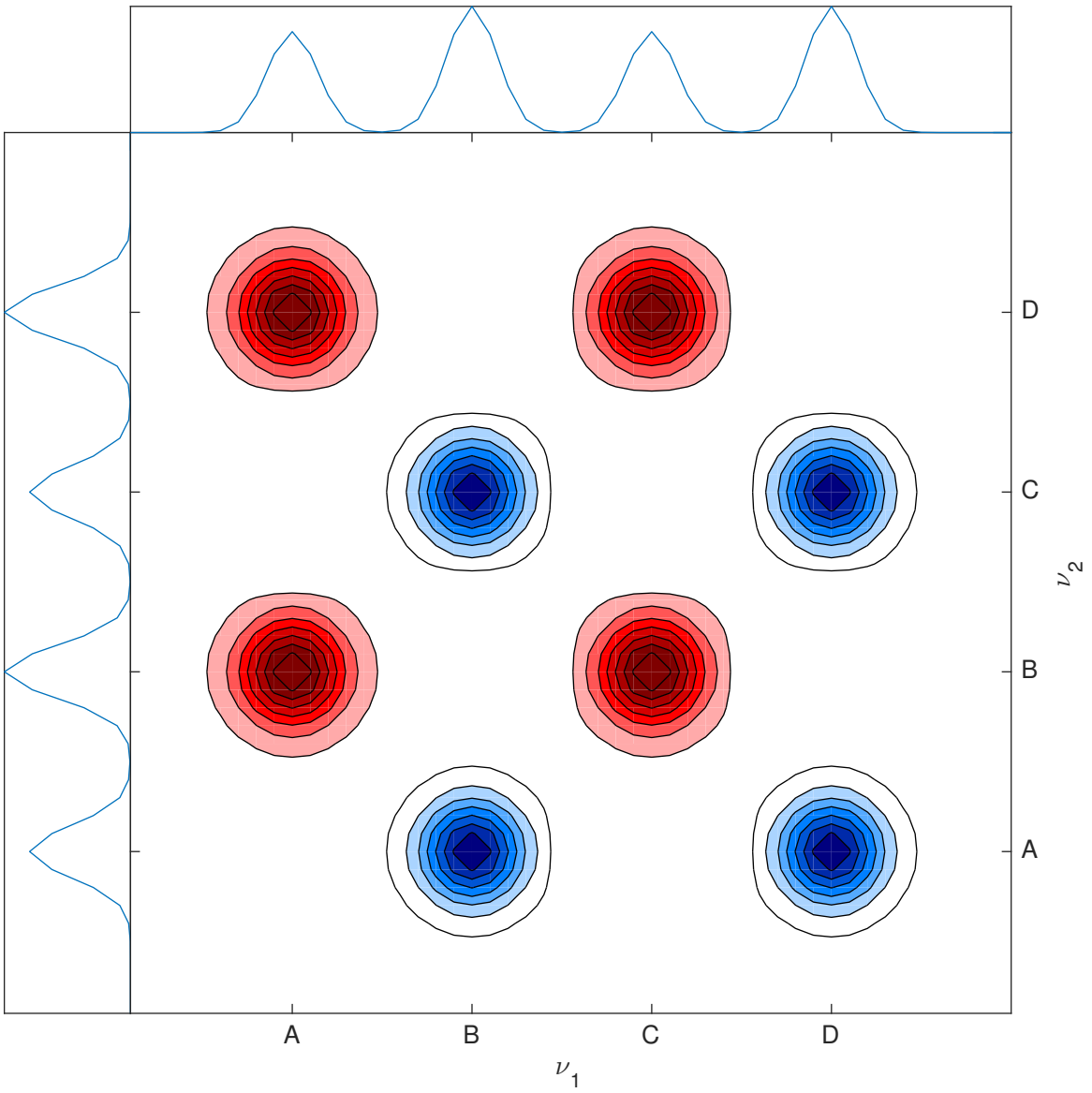

Figure 1.10: 2DCOS asynchronous (Modified Noda's rules) correlation map of sample data; colourmap: blue-white-red; negative-0-positive

can be easier to pick out changing spectral features within the modified asynchronous map if the reference spectra already highlight the regions of the spectrum that are most susceptible to changes in spectral intensity.

1.3.4 Moving-Window Two-Dimensional Correlation Spectroscopy

Although hugely powerful, the interpretation of 2DCOS can sometimes be complex due to the inclusion of many underlying processes that can influence spectral changes. A variation of the base technique was proposed using systematic subdivision of the spectral dataset, called Moving-Window Two-Dimensional (MW2D) Correlation Analysis.[21] Subdivision of the spectra is produced through a moving window of an arbitrarily fixed width. For each window the autocorrelation is selected and plotted against the local average of the perturbation variable within the moving window.

The autocorrelation spectrum is extracted as the diagonal line between ν_1 and ν_2 of the synchronous spectrum ($\Phi(\nu,\nu)$ *i.e.* when $\nu_1 = \nu_2$), first used by Thomas and Richardson while investigating phase transitions using FTIR.[21] Given a spectral dataset, $y(\nu,p)$, where each column p represents a perturbation variable, a sub-matrix is constructed by taking $2m+1$ rows around the jth row of data.[i] Equations 1.23, 1.24 and 1.25 show the sub-matrix selection, reference spectrum and dynamic spectrum in the jth windows respectively.

[i] Up until now, the external perturbation applied onto the system was expressed as chronological time t, to ease interpretation. Here onwards the external perturbation is refered to as p due to convention within moving-window two-dimensional techniques.

$$y_j(\nu, p_j) = \begin{bmatrix} y(\nu, p_{j-m}) \\ y(\nu, p_{j-m+1}) \\ \vdots \\ y(\nu, p_j) \\ \vdots \\ y(\nu_1, p_{j+m}) \end{bmatrix} \tag{1.23}$$

$$\bar{y}_j(\nu) = \frac{1}{2m+1} \sum_{J=j-m}^{j+m} y_j(\nu, p_j) \tag{1.24}$$

$$\tilde{y}_j(\nu, p_j) = y_j(\nu, p_j) - \bar{y}_j(\nu) \tag{1.25}$$

The MW2D correlation spectrum, based on an autocorrelation spectrum $\Omega_A(\nu, p)$ (Equation 1.26) is calculated by incrementally sweeping the window position across the entire dataset and recalculating $\Omega_A(\nu, p)$ at each position. These vectors are then stacked to generate a three-dimensional plot.

$$\Omega_A, j(\nu, p_j) = \frac{1}{2m} \sum_{J=j-m}^{j+m} \tilde{y}_j^2(\nu, p_j) \tag{1.26}$$

The MW2D autocorrelation spectrum has been previously reported to be proportional to a squared perturbation derivative,[22] which is a useful comparison to make while interpreting MW2D spectra, shown in Equation 1.27.

$$\Omega(\nu, p) \sim \left[\frac{\partial y(\nu, p)}{\partial p} \right]_v^2 \tag{1.27}$$

The MW2D spectra allow inspection of how the system changes as a function of the pertur-

bation. The MATLAB code for the computation of such moving window analyses is included in the appendix, Section 5.8. The code also allows computation of slices of the asynchronous spectrum as well as the autocorrelation spectrum moving window analysis.

1.3.5 Perturbation-Correlation Moving-Window Two-Dimensional Correlation Spectroscopy

Perturbation-Correlation Moving-Window Two-Dimensional Correlation Spectroscopy (PCMW2D) is based on the correlation between a spectral intensity change and a change in perturbation, developed by Morita *et al.*.[23] Unlike MW2D, PCMW2D requires no constant variable, such as the autocorrelation spectrum or arbitrary slice. The following explanation utilises the same nomenclature as those contained in the 2DCOS and MW2D sections (1.3.1 and 1.3.4), some definitions are therefore not repeated.

For a spectral dataset, $y(\nu, p)$, where ν and p are the spectral variable (wavelength or wavenumber) and the external variable (*i.e.* perturbation), respectively, dynamic spectra must first be generated. The dynamic spectra, $\tilde{y}(\nu)$, are generated in the same way as described in the 2DCOS and MW2D. The dynamic perturbation is calculated in a similar manner to the dynamic spectra, shown in Equations 1.28 and 1.29

$$\bar{p}_j = \frac{1}{2m+1} \sum_{J=j-m}^{j+m} p_j \tag{1.28}$$

$$\tilde{p}_j = p_j - \bar{p}_j \tag{1.29}$$

For the jth window of the analysis, the synchronous and asynchronous PCMW2D spectra are calculated according to Equations 1.30 and 1.31. In the same manor as for the MW2D analysis, these vectors are then stacked accordingly.

$$\Pi_{\Phi}, j(\nu, p_j) = \frac{1}{2m} \sum_{J=j-m}^{j+m} \tilde{y}_j^2(\nu, p_j) \cdot \tilde{p}_J \tag{1.30}$$

$$\Pi_{\Psi}, j(\nu, p_j) = \frac{1}{2m} \sum_{J=j-m}^{j+m} \tilde{y}_j^2(\nu, p_j) \cdot \sum_{K=j-m}^{j+m} M_{JK} \cdot \tilde{p}_K \tag{1.31}$$

The synchronous and asynchronous PCMW2D spectra have been shown to be similar to the first and second order derivative, respectively, of the spectral intensity variations along the perturbation direction. The PCMW2D spectra are less susceptible to noise than the perturbation derivative spectra however.

1.4 Carrageenan

Carrageenans are high molecular weight sulfated polysaccharides that are extracted from a variety of red seaweeds. Depending on the position and number of sulfate groups they are classified into different types, giving the commercially important *kappa*, *iota* and *lambda*-carrageenan (κ-, ι- and λ-carrageenan). The commercial interest in these compounds stems from their gelling, thickening and stabilising abilities and they have seen subsequent application in the food (labelled as E407), pharmaceutical and cosmetics industries. Together with alginates and agars, carrageenans are part of complex biopolymeric substances termed phycocolloids. A larger variety of naturally occurring carrageenans are found in seaweed, with more sulfate groups. However the alkaline extraction process mostly yields the three forms of carrageenan mentioned above due to cleavage of the sulfate half-esters.[24]

In Europe, the use of carrageenan started over 600 years ago and originated in Ireland. Irish moss stewed in milk was used to produce flans in the village of Carraghen.[25] Today the annual sales of carrageenan exceed £350 million,[26] *ca.* 90% of which is food grade.[27] Food grade

carrageenans have a weight average molecular mass (M_w) of between 400-600 kDa.

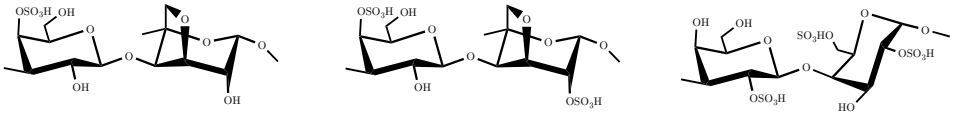

Figure 1.11: Repeating units of *kappa*, *iota* and *lambda*-carrageenan, from left to right

As natural carrageenans are a mixture of non-homogeneous residues, the disaccharide repeating unit shown in Figure 1.11 is that of an idealised structure. To accurately describe the full features of the biopolymer a revised nomenclature specific to carrageenans was devised.[28] In the idealised situation, carrageenans are composed of alternating 3-linked β-D-galactopyranose (G-units) and 4-linked α-D-galactopyranose (D-units), both of which are monosaccharide sugar units, with sulfate half-ester and anhydride bridge groups in varying positions. The primary deviation from the idealised structure is the absence of the anhydride bridge of the D-unit inducing a conformational change in the chain.[29] Alkali treatment (part of the extraction process) increases structural regularity, with most extracted carrageenans having a greater than 95% idealised structure. Carrageenans often contain fractions of their biosynthetic and extraction precursors.[30]

The most important (commercially exploited) property of carrageenan is its gelling capacity. As the sulfate content rises (*kappa* < *iota* < *lambda*), the gelling capacity of the carrageenan declines. This is due to the resulting increase in negative charge associated with the sulfate ester groups, although it has been suggested that this is due to the position of the sulfate groups rather than the quantity per repeating unit.[31] As such κ-carrageenan forms strong/brittle gels, ι-carrageenan forms elastic gels (both ion dependent) and λ-carrageenan only forms high viscosity solutions. Interestingly, λ-carrageenan has been seen to form a gel in the presence of trivalent iron ions,[32] however only viscous solutions are formed with mono- and divalent cations.

The ability for dilute aqueous solutions to transform into solids encompasses a fascination

for many people due to an observed phase change with such a low concentration of a gelling agent (*ca.* 1% w/w). Gels can be classified due to the strength of their cross-linkages. Some gels form covalent bonds, these are usually thermosetting gels and gelation is irreversible as they cannot be dissolved. Others are cross-linked physically, by intermolecular interactions. In the physically linked case, whether that be hydrogen bonding, ionic interactions or entanglement of chains, application of heat can reverse the gelation process. Polysaccharides are by their composition a type of polyelectrolyte, a charged polymer chain. This results in the formation of physically linked chains and thermo-reversible gelation.[33,34]

Polysaccharide gelation falls into two classifications for the type of network formed; associative and particulate networks.[33] The latter arises through globular association to form aggregates (*e.g.* association of casein micelles). Associative gel networks form when random coils of biopolymers undergo a coil to helix transition giving rise to a network. Both classifications show varying levels of heterogeneity on the micro and macro scale, controlled by various factors (concentration, pH, ionic strength, thermal history etc). Micro-phase separation between the solute and gelling agents can represent a form of micro-cystallisation if the aggregates are dense enough. On a larger scale, even when networks can be considered molecular in their association, heterogeneity can arise through long range network density fluctuations giving the gel a translucent or opaque nature.

More recently, carrageenans have been used within the pharmaceutical industry as excipients for pills and tablets.[35,36] Use as a polymer matrix in oral extended-release tablets, a novel extrusion aid for the production of pellets, and as a stabiliser in micro/nano-particle systems have been presented.[37] Matrices of carrageenan have also been used for tissue regeneration, with the inclusion of therapeutic macromolecules, and carrageenans may exhibit anticoagulant, anticancer, antihyperlipidemic, and immunomodulatory activities.[38] There are also indications that inclusion of carrageenans into sexual lubricants can reduce the transmission of HPV (human papillomavirus) due to antiviral properties of these biopolymers.[39,40]

Wavenumber / cm^{-1}	Functional Group	κ	ι	λ	References
3400-3000	O-H (stretching)	+	+	+	47
2920	C-H (stretching)	+	+	+	48
1380-1355	Sulfates	+	+	+	48
1250-1230	O=S=O (antisymmetric stretching)	+	+	+	49–52
1190	S=O (antisymmetric stretching)	+	+	-	47
1160-1155	C-O-C (antisymmetric stretching)	+	+	+	49
1125	Glycosidic bonds (antisymmetric stretching)	+	+	+	47
1090	S-O (symmetric stretching)	+	+	+	49, 51, 53
1080-1040	C-O and C-OH	+	+	+	47, 51, 53
1045	C-OH and S=O	+	+	+	47, 53
1026	S=O in C2 (pseudo-symmetric stretching)	-	+	+	47
1012	S=O in C6 (pseudo-symmetric stretching)	-	-	+	47
1002	Glycosidic bonds	+	+	+	47
970-965	Glycosidic bonds	+	+	+	47
930	C-O-C (3,6-anhydrogalactose)	+	+	+	47, 48, 50, 52
900-890	C6 group in β-D-galactose	+	+	+	47, 54
850-840	C4-O-S group in galactose (stretching)	+	+	-	47, 50, 52
830-825	C2-O-S galactose	-	-	+	50
820-810	C6-O-S (stretching)	-	-	+	47, 50
805-800	C2-O-S in 3,6anhydrogalactose	-	+	-	47, 48, 50, 52
740-725	C-O-C α(1,3) (stretching)	+	+	-	47
615-608	O=S=O (bending)	+	+	+	47
580	O=S=O (bending)	+	+	+	47

Table 1.1: Typical infrared vibrational bands of carrageenan and their correspondence to the κ-, ι- and λ-forms, designated as +/- for observed/not-observed

1.4.1 Vibrational Spectroscopy of carrageenans

Vibrational spectroscopy is a powerful tool for the study of natural polymers and can be used to monitor changes of state, whether that be a sol to gel transition or crystallisation.[41] Analysis of the spectra, using statistical techniques such as Principal Component Analysis, has been applied and developed so that quantification of various polysaccharides can be achieved allowing authentication of various foods.[42,43] The 500 to 1500 cm^{-1}region of the infrared spectrum has attracted considerable interest due to the presence of multiple vibrational modes that are sensitive to the type of polysaccharide and glycosidic linkage joining the repeating units.[44–46]

Table 1.1 shows the main spectral features for the commercially important carrageenans in the region of interest, reproduced in part.[55] The structure of the various carrageenans is determined by the number and position of sulfate groups, along with the presence of anhydride bridges. The varying environments of the sulfate groups leads to specific stretching frequencies, as seen at 1012, 1026 and 1045 cm^{-1}in Table - 1.1. Various other methods for quantification of carrageenans have been employed,[56] however FTIR spectroscopy has become the fastest and most efficient way to determine the percentage content of carrageenans. Although this is mostly down to the power of FTIR as a spectroscopic technique, the ease of sample preparation by the use of ATR has facilitated the migration towards infrared spectroscopy.[46]

Figure 1.12 shows the three commercially important carrageenans, κ-, ι- and λ-carrageenan, at 20 °C, with the main spectral regions identified (see Figure 1.11 for the repeating units of the carrageenans). A more detailed assignment of the vibrational bands of carrageenan from the literature can be found in Table 1.1.

Raman spectroscopy has received recent attention for the identification and classification of various seaweed phycocolloids.[44–46] As a vibrational technique, Raman spectroscopy can also aid in the understanding of the molecular interactions within the biopolymers.[57,58] Until more recently however, Raman spectroscopy has been limited in the study of biopolymeric systems due to the need for a visible laser; often producing a large laser induced fluorescence from the biological samples and sometimes degradation of the sample.[45,59] The development of near infrared FT-Raman spectroscopy has greatly reduced these limitations.[54] Combinations of FTIR and FT-Raman techniques have shown to be very useful for the understanding the nature of various phycocolloids.[60] Although usually an unwanted side effect of Raman spectroscopy, the fluorescence of polysaccharides has also been positively exploited to monitor the thermal phase changes occurring within ι-carrageenan.[61,62]

Various other techniques have been applied to aid in the understanding of the wide array

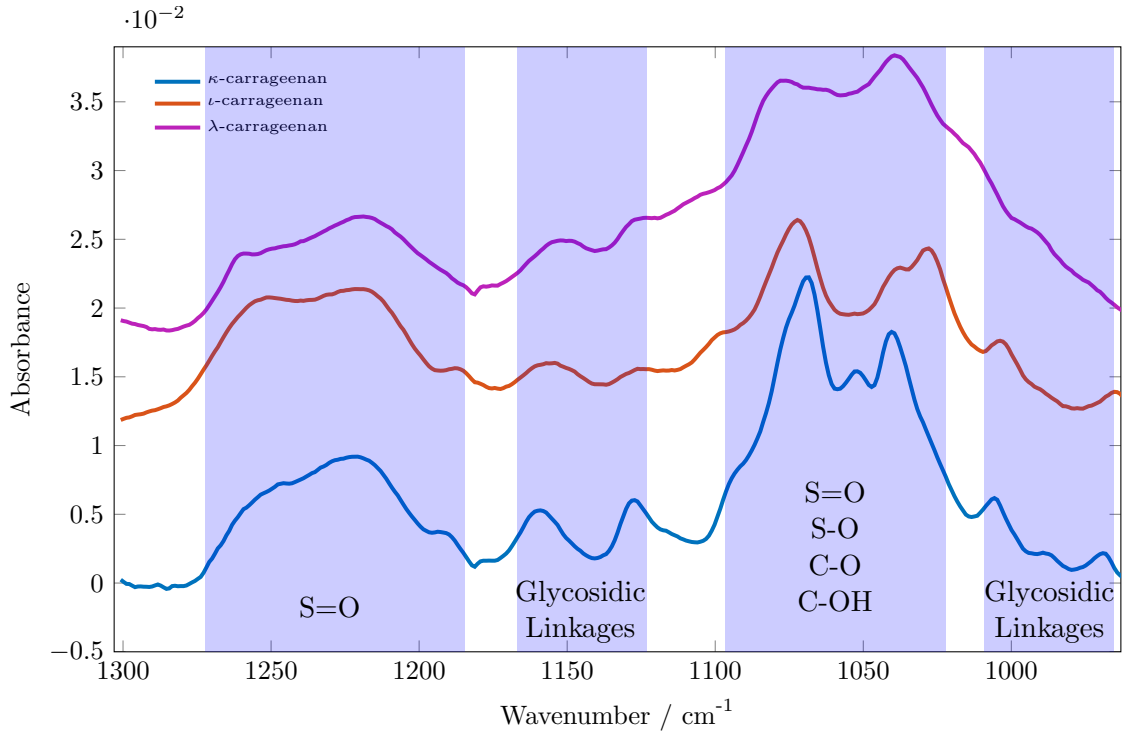

Figure 1.12: FTIR spectra of κ-, ι- and λ-carrageenan, at 20 °C, with the main spectral regions identified and labeled. Spectra are offset for clarity and collected with the modified low-temperature ATR system described in Chapter 2

of properties of polysaccharides. The basis of a lot of the research is to gain understanding of the sol-gel and gel-sol transitions, using a variety of variables.[33,61,63–65] The majority of other techniques used are techniques that afford structural or mechanistic insights into the interaction involved during polysaccharide gelation.

Nuclear magnetic resonance (NMR) is a powerful technique for both the qualitative and quantitative analysis of multiple compounds, particularly when investigating the primary structure of biopolymers.[66–68] At present however, the study of polysaccharides using NMR spectroscopy receives less attention than in the past.[45] Mostly due to the increased success of vibrational techniques and the problems associated with producing an NMR spectrum of viscous fluids, giving a spectral resolution insufficient to allow fine detailed structural characterisation of the polysaccharides.[45,69–71] NMR experiments are usually carried out at higher temperatures to reduce the viscosity of the solution,[35] which minimises line broadening. NMR spectroscopy has proven to be useful in the quantification of carrageenans (percentage κ, ι or λ), however at the conditions needed for successful analysis, high temperatures and/or high concentrations (10% w/w for ^{13}C NMR), the analysis is outside the bounds by which carrageenan is used within industry.[35,72] The requirement of NMR spectroscopy to use deuterated (or non-hydrogen containing) solvents in the collection of spectra also presents differences in the real-world and experimental techniques as heavy water interactions with carrageenan have been shown to afford differences in the rheological properties of the resultant gel.[73]

It is also possible to investigate the gelation of phycocolloids using atomic force microscopy (AFM).[74–79] Figure 1.13 shows a thin film of ι-carrageenan solution (0.5% w/v) that has been dried with varying ion concentration.[75] Image b) contains an increase in calcium chloride concentration compared to image a) and image d) contains an increase in sodium chloride concentration compared to image c). As can be seen, the increase in respective cation concentration results in a larger aggregation of the strands in the images. This is consistent with previous rheological studies showing an increase in gel strength as cation concentration increases, attributed to a

larger extent of helical aggregation.[63,80] AFM has also been used to fingerprint polysaccharides allowing individual polysaccharides to be identified in complex mixtures at a single molecule level, using a library of force spectrograms.[81]

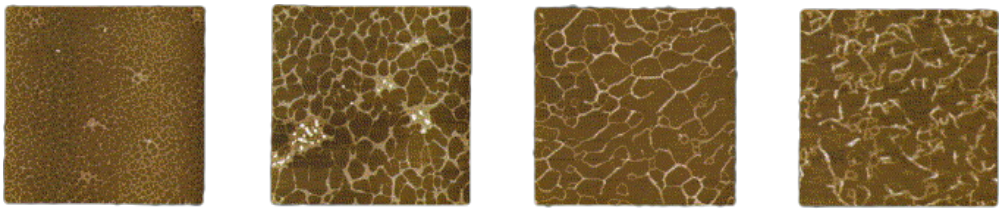

Figure 1.13: Topographical AFM images of ι-carrageenan prepared at 0.5% w/v, deposited onto a surface and dried; a) 0.01M $CaCl_2$, b) 0.05M $CaCl_2$, c) 0.1M NaCl and d) 0.5M NaCl. Reproduced from Funami *et al.*[75]

This Thesis uses vibrational spectroscopy to investigate a selection of carrageenans as they are cooled from 80 to 10 °C, as well as their subsequent freezing. The variety of vibrations present within a large biopolymeric system such as carrageenan can lead to a very complex fingerprint region of the mid-infrared and the use of multivariate techniques is employed to gain insight and understanding. The following Chapter details the experimental setup and modification of a low temperature ATR system that is used in the later Chapters.

Chapter 2

Experimental

This Chapter deals with the setup of equipment and the basic spectral acquisition and processing used for all data within this thesis. Many MATLAB routines have been used as part of the analysis of data and these were covered in the Introduction (Sections 1.2 and 1.3). Additional MATLAB scripts of relevance are included in the appendix (Chapter 5.4).

2.1 ATR system developement

A Specac low temp Golden Gate ATR-FTIR accessory was provided by Unilever. The system was comprised of 3 parts; a Golden Gate single bounce ATR bottom mounting, a heated top plate and a low temperature dewar. The thermally insulated copper and stainless steel dewar is mounted onto the modified heated top plate with 4 screws. The heated top plate houses the diamond ATR crystal that is bound to a tungsten carbide support disk. During operation a thermal gasket (usually a graphite disk) ensures good heat transfer between the dewar and diamond. This assembly is then mounted onto the ATR accessory that sits in the IR beam path of the spectrometer.

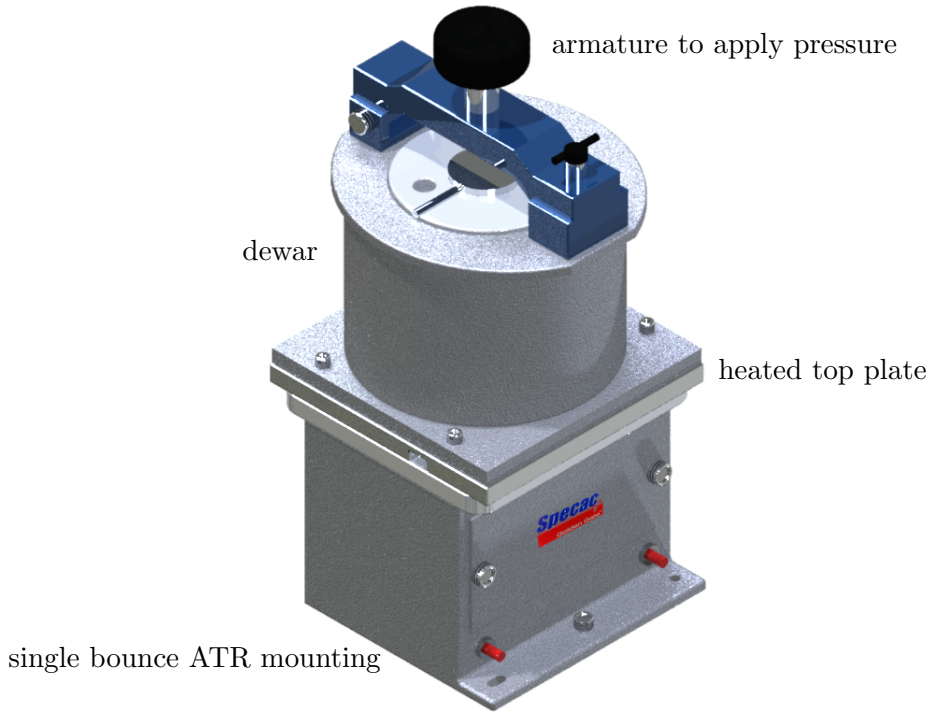

Figure 2.1: 3D modelled Specac Low-Temperature ATR system, showing the golden gate accessory, heated top plate and thermally insulated dewar

In order to evaluate the Specac apparatus for our proposed experiments, a simple experiment was devised to show temperature dependent spectra of a substance in the -150 °C to 80 °C range. Very few compounds show dramatic temperature dependent IR behaviour that is simple to interpret and that could be used as a "test" sample. A protein, for example, will show structural changes upon folding/unfolding that can be visualised by the change in IR bands.[82,83] But ideally a simpler compound with a more decipherable temperature dependent nature should be analysed. Iron tricarbonyl cyclobutadiene is one such compound that show a very precise temperature dependent infrared band change.

2.1.1 Iron tricarbonyl cyclobutadiene

Iron tricarbonyl cyclobutadiene, $Fe(CO)_3$(cyclobutadiene), has three carbonyl ligands attached to the iron center, allowing the metal center to be probed using the ν(CO) bands. Due to the C_{3v} symmetry of the complex it is readily predictable that the compound shows 2 carbonyl bands. However studies showed that although $Fe(CO)_3$(cyclobutadiene), along with $Fe(CO)_3$(norbornadiene), show two ν(CO) bands at room temperature, three ν(CO) bands were observed at lower temperatures.[84,85]

Figure 2.2: $Fe(CO)_3$(cyclobutadiene), left; below -80 °C and right; above -80 °C

At temperatures higher than *ca.* -80 °C the three CO ligands rapidly interconvert, producing degeneracy of the CO groups on the IR timescale. This gives an overall C_{3v} symmetry, with only two bands being observed in the IR spectra, Figure 2.2. At temperatures lower than *ca.* -80 °C it has been suggested that the CO groups do not rapidly interconvert; producing one unique axial CO and two equivalent CO groups on the infrared timescale. This results in a C_s

symmetry, showing three separate ν(CO) bands.

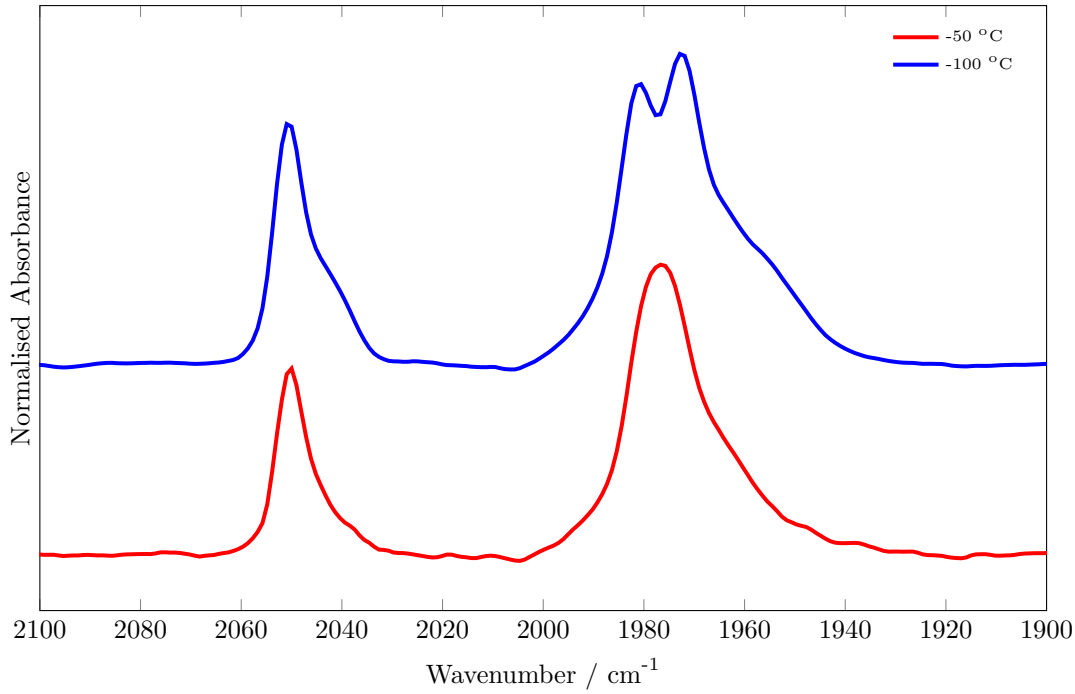

Figure 2.3: Variable temperature iron tricabonyl cyclobutadiene, red -50 °C and blue; -100 °C

$Fe(CO)_3$(cyclobutadiene) was impregnated into a polyethylene disk and the system cooled with liquid N_2. Figure 2.3 shows the the change in absorbance between -50 °C (red) and -100 °C (blue). The traces are offset for clarity. On cooling, the band at 1975 cm^{-1} was seen to split into two separate peaks; this was shown to be reversible (and repeatable) over several experiments. The evidence from this experiment is in agreement with that stated by Turner and coworkers, with the splitting / coalescing of the carbonyl bands occurring between -50 °C and -100 °C.[84,85]

Inspection of Figure 2.3 shows shoulders, to lower energy, of the bands observed. These shoulders are deviations from the idealised ν(CO) vibration of $Fe(CO)_3$(cyclobutadiene) and should not be present, suggesting that they could be attributed to an impurity. It is also possible that the $Fe(CO)_3$(cyclobutadiene) concentration in the polyethylene disk is too high and at lower temperatures the sample precipitates out of the disk.

2.1.2 Problems and solutions

Unfortunately, it was not possible to obtain spectra with more precise temperatures (ideally -75 °C to -85 °C in 1 °C increments), due to experimental limitations. For low temperature measurements, the Specac system is intended to be cooled, beyond the temperature required and the heated top plate (below the dewar in Figure 2.1) used to "fine tune" the temperature. Fine temperature control, within the 0 °C to -150 °C range is not possible with liquid N_2, as the system is not sufficiently thermally insulated to accommodate liquid N_2 (-196 °C). This causes the entire assembly to be cooled to near liquid N_2 temperatures forcing a large driving current from the temperature controller to reach temperatures in this range.

Despite the use of a PID temperature controller to maintain to steady temperature, it was found that for the sample within the system to reach the desired temperatures the coolant had to be boiled off before the system was allowed heat up. Although this demonstrated good thermal conductivity from the dewar to the sample, this was not what was required for controlling the temperature. The inefficiency of the system to maintain a reservoir of coolant whilst keeping the sample above the temperature of the coolant was attributed to the poor thermal insulation provided by the dewar. The dewar's insulation consists of foam padding between the layers of the jacket, when working at near liquid N_2 temperatures a vacuum shroud would be preferable.

The project aims were to study the features of several compounds in ice, as such the minimum temperature required is around -10 °C. Using liquid N_2 as a coolant to reach these temperatures would be inefficient. Control of the coolant temperature would enable the system to be taken to a specific temperature with the coolant and any fine adjustment done with the temperature controller. The temperature required is well within the range of a typical vapour compression refrigeration unit. It was suggested that using a water/ethylene glycol mixture as a coolant to be cooled by a refrigeration unit and circulated through the dewar would provide adequate cooling and temperature control.

Figure 2.4 shows an approximate schematic of the proposed modifications to the low temperature ATR system attached to the Golden Gate ATR accessory. Instead of a liquid N_2 reservoir and heating element, a coolant jacket allows heating and cooling of the sample.

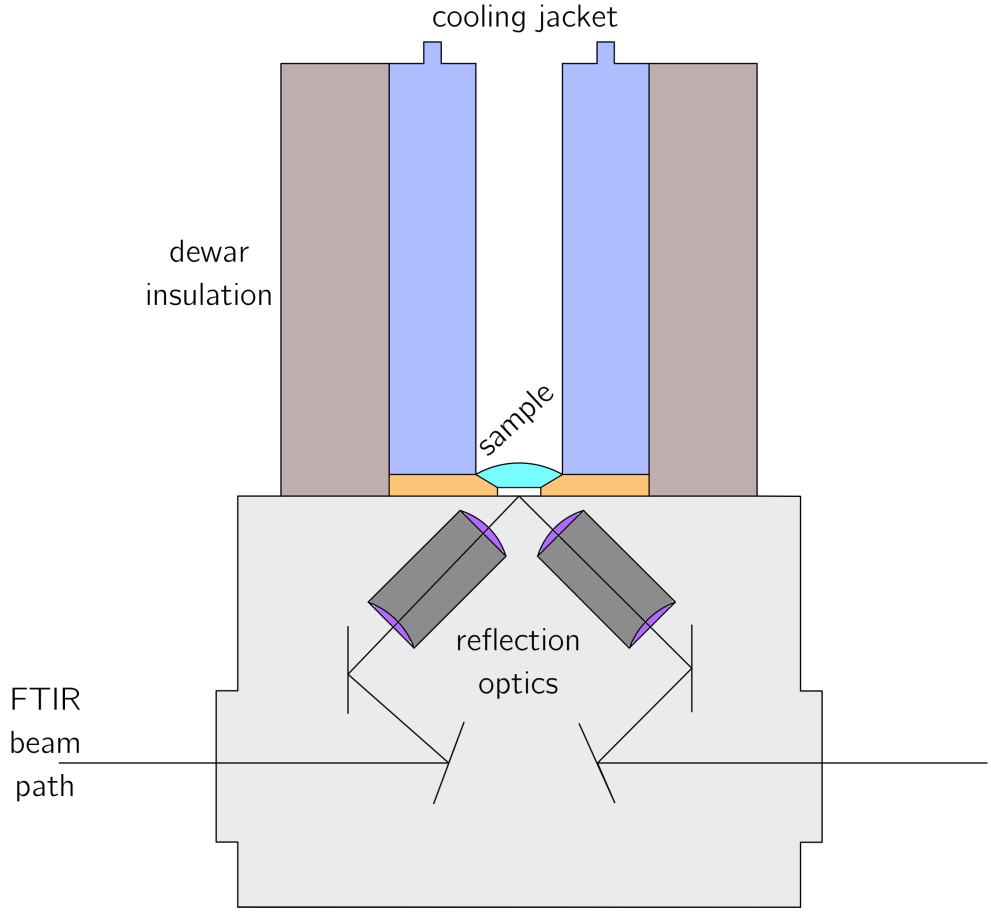

Figure 2.4: Modified Specac low temperature ATR system setup

Figure 2.5 shows the copper heat exchanger and the heat exchanger forms part of a sealed system with the pump assembly attached to the refrigeration unit. The heat exchanger is placed inside the dewar in a bath of ethylene glycol and water to facilitate heat transfer.

Initially the refrigeration unit used was not able to initially provide sub 0 °C temperatures to the sample, due to the poor thermal insulation of the dewar. Additional insulation of the

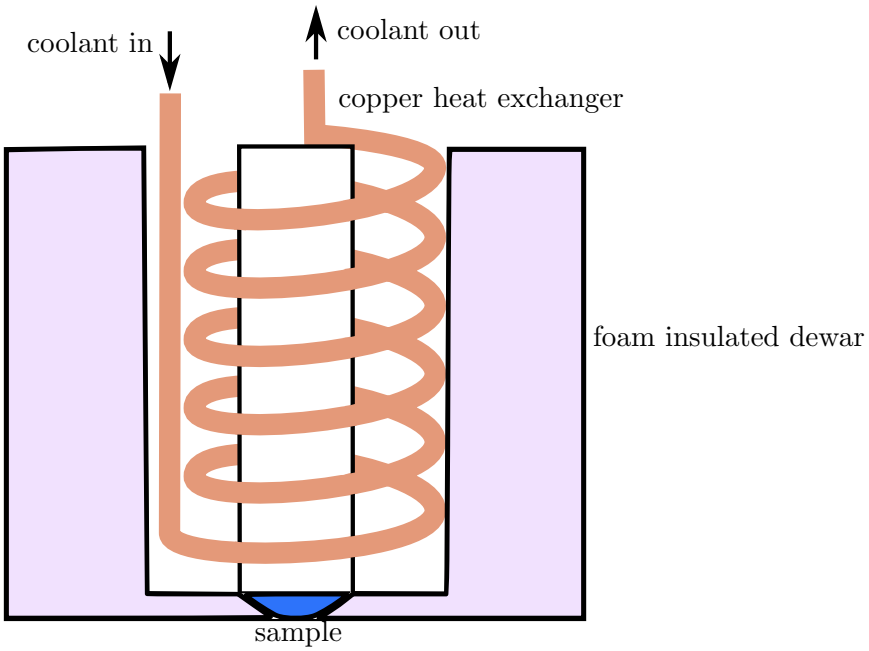

Figure 2.5: Diagram of the copper heat exchanger in place in the Specac dewar

system, as shown in Figure 2.6, enabled the new setup to reach sample temperatures of *ca.* -10 °C. This is more than sufficient to study the water to ice transition. The system depicted within Figure 2.6 shows the first working prototype that was used to study low temperature biopolymer systems, providing reproducibility in results. The Specac ATR setup along with external foam insulation, coolant pipes off to the refrigeration unit and thermocouples monitoring various temperatures across the system is visible, housed in an FTIR spectrometer can be seen.

It was also reported that studying the water to ice transition of the carrageenan gels was problematic due to freeze concentration that took place when the gel froze.[86] This is because cooling the gel rapidly forced the outer parts of the gel (away from the diamond ATR and close to the dewar walls) to crystallise and the carrageenan to migrate towards the centre of the sample and the diamond ATR element. This effect was replicated with the modified ATR system when using liquid nitrogen as a coolant, causing an unpredictable concentration increase resulting in unreliable results and a large freezing point depression of the area of the sample undergoing

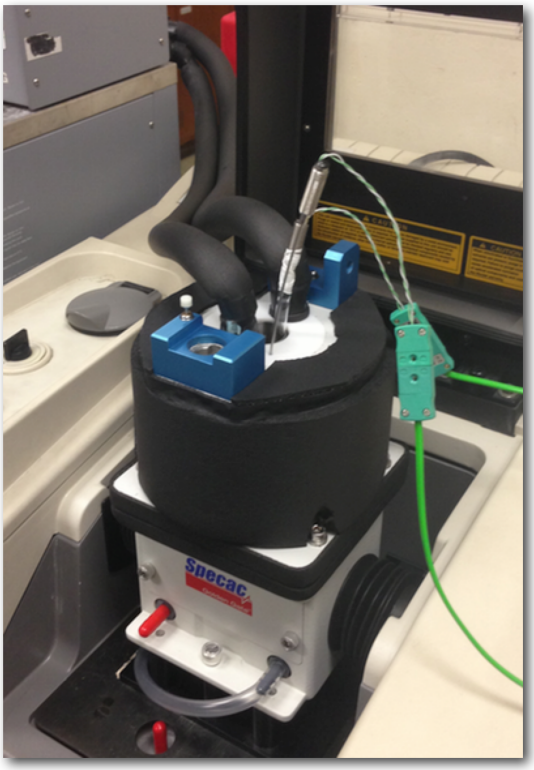

Figure 2.6: First working prototype of the modifications of the Specac low temperature ATR system for use of water/ice systems

analysis. It is expected that a more controlled cooling rate will limit the freeze concentration allowing successful analysis of the water to ice transition occurring within the carrageenan gel.

2.1.3 Final system setup

A powerful oil chiller / circulator (Julabo FP50) was integrated into the low temperature ATR system allowing fine temperature control and a greater thermal range. This refrigerator is a high end chiller capable of large cooling capacities even at low temperatures and can heat / cool from +200 to -50 °C. This unit replaced the old ethylene glycol chiller and utilises a silicone based oil allowing a -50 to +120 °C range within this application. Simple coupling to the Specac ATR system with improved insulation allowed sample temperatures from -35 to +90 °C to be achieved. The large temperature range enabled the homogenised hot carrageenan samples to be placed into the sample compartment at their preparation temperatures, in contrast to the ethylene glycol based system which could only reach *ca.* 50 °C. This allowed the cooling of the samples to be controlled and infrared spectra collected at any temperature desired.

Figure 2.7 shows images of the final system setup used to collect all data within this Thesis. The Specac ATR unit contains the copper heat exchanger (shown in Figure 2.5) linked to the chiller. As the experiments needed within this work can often run for long periods of time at sub-zero temperatures the entire ATR unit becomes cold. Although additional insulation was wrapped around the ATR unit to aid in the less-than-effective foam walled insulation on the original dewar, the entire block reaches close to coolant temperature after *ca.* 10 minutes (depending on gradient and rate of cooling / heating). For low temperature experiments this initially caused condensation to form on the unit, and for this reason a purge box was implemented that incased the entire ATR system. The purge box utilised the same purge gas that feeds into the FTIR system and is more or less void of water vapour, to minimise the condensation that occurs.

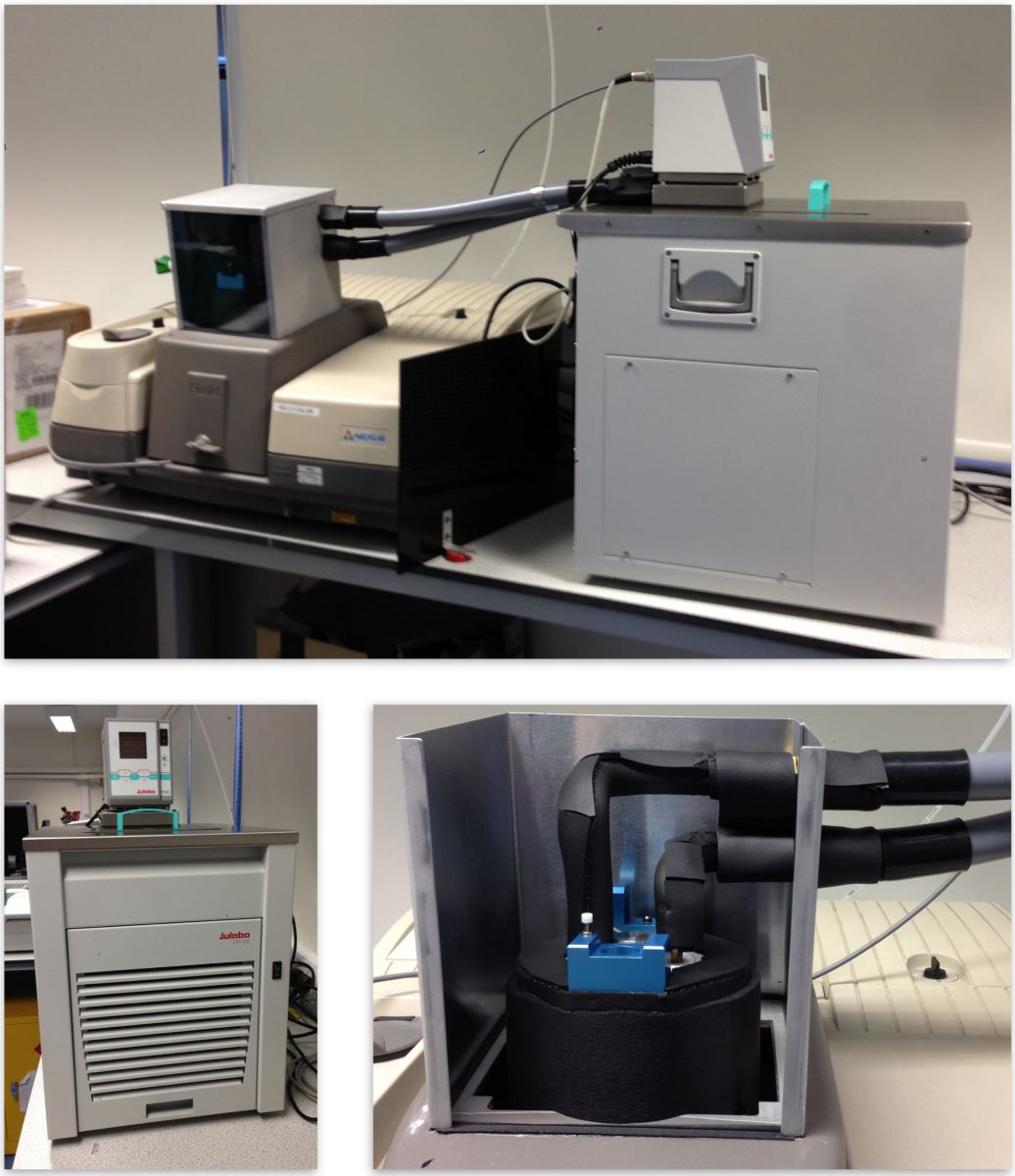

Figure 2.7: Final system setup. Top: Showing beige Nicolet Nexus 670 FTIR spectrometer with custom fitted mount to house the modified low temperature ATR system, grey coolant pipes connected to a Julabo FP50ME oil chiller on the right. Bottom left: front view of Julabo FP50ME chiller. Bottom Right: coolant pipe arrangement passing into top of Specac low temperature ATR system on top of FTIR spectrometer

Heavily insulated coolant pipes were utilised for the feed and return of oil from the Julabo chiller. The chiller has a computer interface allowing control of set temperatures, rate of cooling / heating and temperature logging. The PID system runs from a PT100 sensor that is mounted just below the ATR crystal, which enables the sample temperature to be logged and temperature adjustments to be made relative to the sample compartment, rather than the coolant.

The system allows investigation of additives used in a variety of industrial processes across the temperature ranges in which they are normally subjected. [32,87]

Table 2.1.3 shows the experimental conditions used for the collection of vibrational data during this thesis

2.1.4 Sample preparation and cooling regimes

2 % carrageenan solutions (by weight) were prepared in 10 ml of water and stirred at 80 °C for 30 minutes prior to being transferred into the ATR chamber. The ATR chamber was pre-heated to 80 °C as well, so that no sample cooling / change of temperature occurred as it was placed against the sampling medium (diamond crystal). This protocol was used because it hopefully minimised any change in structure of the carrageenan as it cooled onto a cold diamond ATR. The ATR chamber was cooled at a rate of 0.2 °C per minute in most cases, unless otherwise stated. Table 2.1.4 shows information regarding the samples used in this thesis.

2.2 Spectral Processing

During a typical experiment the temperature of the sample (as well as other temperatures related to the chiller) are logged every 3 seconds and spectra are continuously collected every second. For a fixed cooling rate this protocol allows the optimisation of temperature resolution and spectral signal to noise ratio (SNR) required. For example, if we select a 1 °C per minute cooling rate

Parameter	Condition
Chiller	Julabo FP50-ME
Temperature Control	external PT-100 sensor mounted under ATR puck
FTIR Spectrometer	Nicolet Nexus 670 FTIR
Source	MIR glowbar
Detector	MCT/A
Beamsplitter	KBr
Digitizer bits	20
Mirror velocity	1.8988 cm/sec
Aperture	69
Gain	1.0
High pass filter	200
Low pass filter	2000
No. of scans	16
Collection time	11.8 sec
Resoultion	2 cm^{-1}
No. of data points	3734
Start wavenumber	400.1635
End wavenumber	399.7058
Zero filling	0
No. of scan points	16672
No. of FFT points	16384
Laser frequency	15798.3 cm^{-1}
Interferrogram position	8192
Apodization	Happ-Genzel
Phase correction	Mertz
Raman spectrometer	WiTec Alpha300
Raman engine	Witec UHTS 300 spectrometer
Detector	Witec TE cooled EMCCD
Laser excitation	532nm
Objective	Olympus 20x/0.35 LWD
Exposure time	10 secs
Co-additions	6
Microscope stage	Linkam GS350 liquid N_2 cooled gradient stage

Table 2.1: Equipment specifications and parameters used during this thesis. Top section shows the chiller and FTIR specifications used at Nottingham University, bottom shows Raman spectrometer used at Colworth

Parameter	Condition
Carrageenan mass	0.2 g
Carrageenan supplier	Sigma Aldrich
κ-carrageenan	CAS:1114-20-8 LOT:0001432063
ι-carrageenan(Type II)	CAS:9062-07-1 BATCH:020M1307
λ-carrageenan	CAS:9064-57-7 LOT:0001480463
Volume of water	10 ml
Water type	deionised water, 15 MΩ·cm

Table 2.2: Sample Conditions

and run the experiment for 10 minutes, our sample temperature will change by 10 °C. During this time we will collect 600 individual spectra and, assuming a linear temperature change, this will result in each spectrum will being 0.017 °C apart. However running only several scans at a 2 cm^{-1} resolution (1 second averaging time) using an FTIR spectrometer can give rather noisy spectra. We can choose to average 60 spectra together (giving a 1 minute time averaging on the spectrometer) and achieve much better SNR, allowing easier interpretation of the spectra. The result of this is that instead of our spectra being spaced 0.017 °C apart, they are now spaced 0.17 °C apart, with each spectrum being a moving average of the samples change during that 0.17 °C temperature gradient. In other words, we can sacrifice a order of magnitude in temperature resolution for an order of magnitude in spectral averaging time.

Experimental results showed that continually collecting spectra whilst allowing the temperature to change (at a near linear rate) was a much more efficient use of experimental time that waiting for the apparatus to reach a set temperature and then collect a spectrum. This is probably a result of the PID (proportional–integral–derivative) controller algorithms used by the Julabo chiller. Although variation of the main PID parameters was performed to optimise the control of the chiller with the thermal mass of the ATR cell, approach to a set temperature was somewhat asymptotic and took a comparatively large amount of time to reach desired temperatures.

As with all FTIR techniques a ratio of the sample power spectrum against a background

must be taken in the correct manner before interpretation. In the case of our carrageenan solutions this gives us 3 options: process against another carrageenan solution from with the same experiment (provides a difference spectrum), process against a water background of the correct temperature (showing only carrageenan without solvent), or process against a diamond background of the correct temperature (giving water and carrageenan absorbances). Standard experimental procedure for ATR systems is to take a background spectrum just prior to sample spectrum, as this minimises the possible change in experimental differences leading to undesirable spectral features. However this cannot be done with these experiments as the system can take hours to reach the desired temperature, thermal hysteresis of biopolymers can be present (altering their behaviour), and fine temperature resolution is needed to observe conformational changes within biopolymers. The result of this is that an entire background dataset must be collected prior to a sample dataset, with their temperatures correctly aligned to the Julabo's PT100 sensor, then processed against the correct temperature of each set of data. The timestamps on both the spectra and temperature data is used to correlate the two data sources before the background and sample spectrum for each temperature are processed.

Section 5.12 shows the MATLAB script utilised for importing the ".txt" file produced by the EasyTemp software that controls the Julabo chiller. The Julabo EasyTemp software was setup to record three temperatures; the set-point (desired temperature), the internal temperature of the oil bath, and the external temperature as read by the PT100 sensor placed next to the ATR diamond. The date and time of each datapoint is also converted into MATLAB's "datenum" format for ease of manipulation when matching correct temperatures to spectral files.

All of the spectra within the Gelation Chapter (Chapter 3) are displayed as carrageenan spectra that have, in effect, been processed against water, so no O-H stretch or H-O-H bend modes can be observed. Initially a spectrum of 2 % carrageenan was processed against a pure water spectrum of the correct temperature, however it was apparent that bands associated with H_2O were still present within the sample spectrum following processing. There was also

significant baseline offset as well. This is because the ATR crystal is sampling a different number of H_2O molecules when a pure water sample is compared with a 2 % carrageenan in water sample. Apart from the obvious difference of 2 % water between the samples (pure water is 100 %, carrageenan samples are 98 % water), the density of the samples has changed as well as the refractive index. For this reason both the background spectra (pure water) and sample spectra (2 % carrageenan) were processed against diamond of the correct temperature, then the water spectra were dynamically subtracted away from the carrageenan spectra.

Each carrageenan spectrum has the "best" water spectrum subtracted from it, giving a carrageenan spectrum with no H_2O bands present. This is done by dynamically allowing a MATLAB algorithm to search for the best-matching water spectrum that is then subtracted away in the correct ratio. An example of the MATLAB minimisation routine is shown in Section 5.13. Initially the correct water spectrum for subtraction was chosen by matching the closest temperature, however better results were found by allowing an algorithm to search for the best spectrum. Analysis of the temperatures chose by the minimisation function shown in Section 5.13 indicated that the water spectrum chosen (*via.* matching of the IR spectrum alone, independent of temperature information) was within $\pm$ 0.1 °C. Interestingly this minimisation algorithm can therefore also be used to determine the temperature of water to within 0.1 °C utilising only the O-H stretch band of the Mid-IR.

Figure 2.2 shows a schematic representation of the spectral collection and processing described above. A possible improvement to this approach would be to search for the best diamond single beam to ratio against the spectra, similar to the carrageenan / water subtraction, instead of simply selecting the diamond background of correct temperature. This approach could also be used to minimise atmospheric contributions *via* selection of diamond backgrounds from a large spectra library. This method, although producing very clear carrageenan spectra, with regards to the baseline in the fingerprint region does not allow investigation into the ν(OH) stretch region (3000 - 3500 cm^{-1}) as little information is left here following the spectral subtraction.

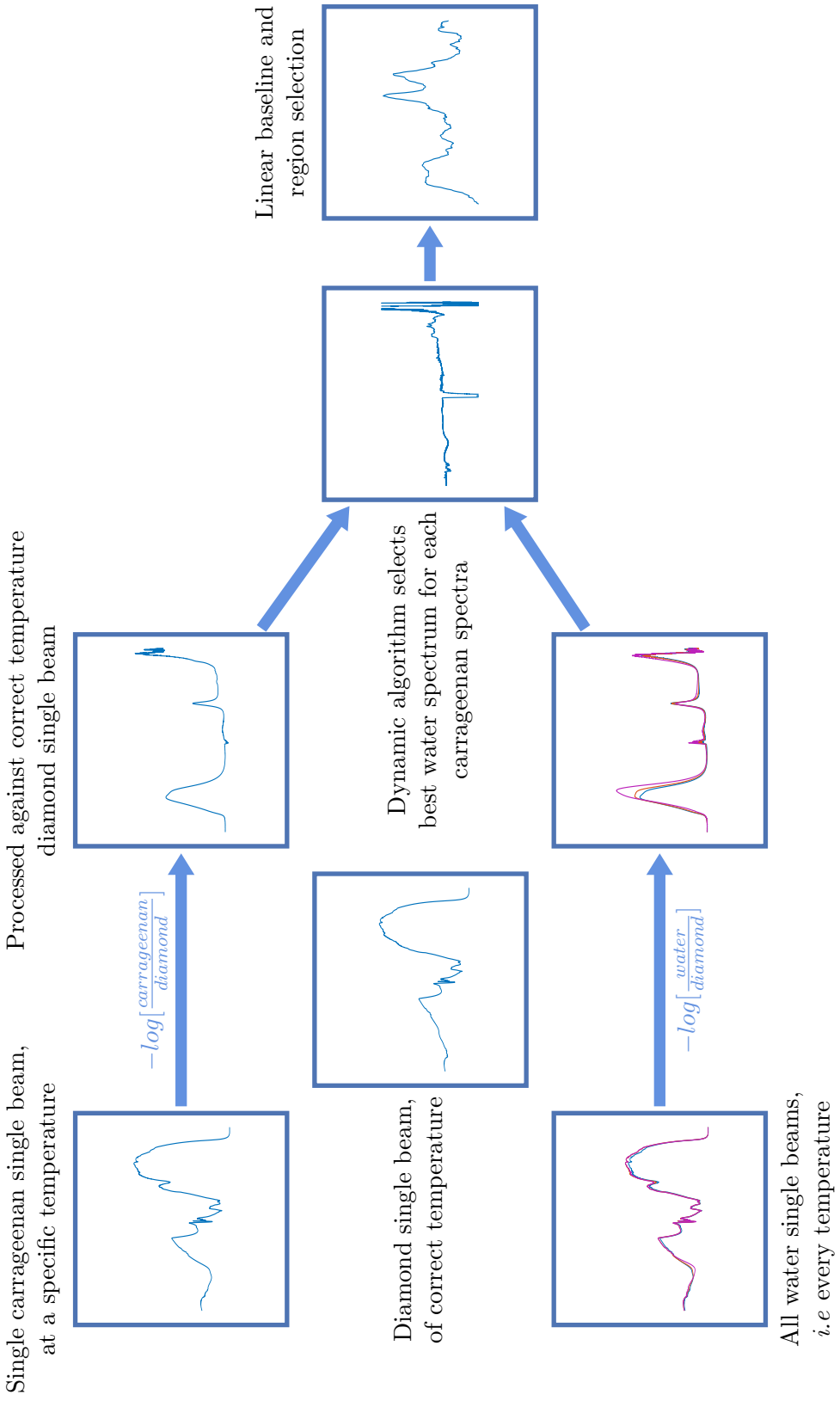

Figure 2.8: Schematic showing the general routine used for processing of raw data within this thesis

Each set of data displayed within this thesis underwent multiple repeats to demonstrate the reproducibility of these results. In particular the post-freezing changes as these have previously not been demonstrated before. Pure water underwent *ca.* 15 separate low-temperature / post-freezing experiments during the course of the experiments, with every single experiment (of the final methodology) showing no post-freezing spectral perturbations. Early experiments with ι-carrageenan showed freeze concentration, observed spectrally as an exponential increase of carrageenan absorbencies, when the sample underwent cooling at too fast a rate. The post-freezing growth within the fingerprint region for ι-carrageenan was demonstrated *ca.* 10 times, with each experiment exhibiting different rates for the two component growth (highlighted in Section 4.2.4). κ- and λ-carrageenan experiments were also performed with the same methodology that gave the post-freezing changes for ι-carrageenan, however these systems appeared to be steady state post-freezing, with no spectral changes within the O-H stretch or fingerprint regions, this was verified through 5 repeats.

Within the appendix is also included a MATLAB script for the setup and calculation of the band-fitting routine used within the 3-component fit procedure for the fingerprint region of ι-carrageenan post-freezing, explained within Section 5.14. Following fitting of the components, the MATLAB code also demonstrates the manual extraction of the fit variables and component reconstruction required to examine the residuals and reconstructed spectra that are the result of the fitting routines. This script will work "as-is", however careful attention to the over / under fitting of spectra must be taken. Examination of the residuals and component bands overlaid with reconstructed spectra (such as in Figures 4.29 and 4.30, respectively) is highly recommended.

Chapter 3

Gelation of Carrageenans

3.1 Introduction

This Chapter focuses on the use of FTIR to probe the gelation transition of carrageenans. The work in this Chapter uses three commercially available carrageenans. Two of these, κ-carrageenan and ι-carrageenan, have been shown to form gels. The other, λ-carrageenan does not demonstrate gelling behaviour. The gelling, thickening and stabilising properties of these biopolymers are widely used as texture modifiers within the food industry.[88] As explained in Section 1.4, the main difference in structure between these carrageenans is the number and position of sulfate groups per repeating unit within the biopolymer (see Figure 1.11).

At high temperatures the gelling carrageenans (κ and ι) are thought to exist in solution as disordered coils, which upon cooling associate *via* the formation of double helices.[89–97] The structure of the helical form of ι-carrageenan polysaccharide is show in Figure 3.1. At sufficiently high concentrations these helices can aggregate together further, forming a network and possibly a gel.[87,98] It is the extent of aggregation of the helices that determines the strength of the gel. Figure 3.2 was reproduced from Cardoso *et al.* showing a schematic representation of

κ-carrageenan chains during the sol-gel transition.[73] Many factors influence the gelling nature and the temperature of the sol-gel transition, however, carrageenans are widely known as room temperature gels.

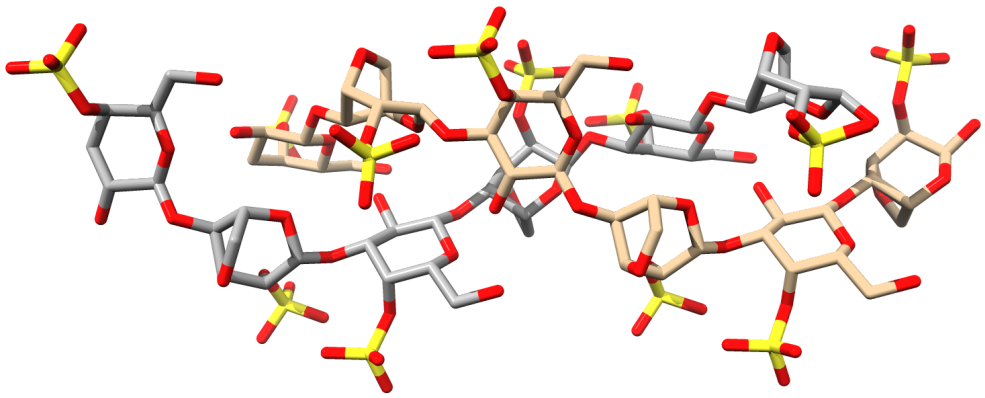

Figure 3.1: Double helix visualisation of ι-carrageenan, from PDB: 1CAR

The addition of cations can affect the extent and strength of gelation.[90] This is due to the decrease in effective negative charge density of the polysaccharide.[99] Cations, specifically Na^+, K^+ and Ca^{2+}, have been shown to improve the gel strength through enhancing conformational ordering and subsequent aggregation of the helices to form gels.[89,91,94,97,100–104] Matching the counter-ion concentration, stoichiometrically, to the sulfate content of carrageenan can lead to gels with a high elastic modulus, high optical clarity and a fine network structure.[98]

Although there was some early deliberation as to whether the helices that were formed were either single or double stranded, it is now generally accepted that the double stranded helix theory is correct.[105,106] Gel formation is contingent on reaching the gelation temperature and correct ionic concentration, as this decreases the negative charge of the carrageenan strands allowing them to become more ordered.

Figure 3.3 shows the phase diagram for the sol-gel transition of κ-carrageenan. This diagram

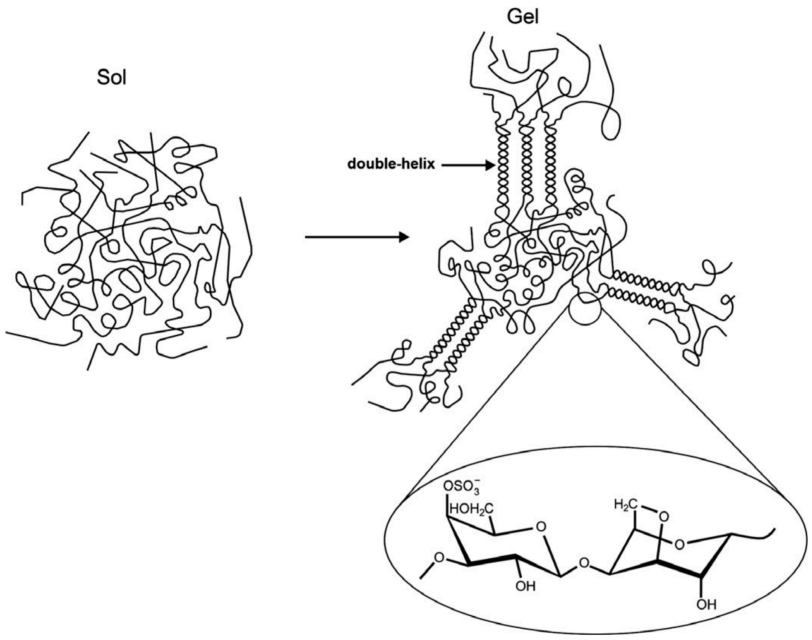

Figure 3.2: Schematic representation of κ-carrageenan chains in sol-gel (solution to gel) transition, due to the aggregation of double helices, reproduced from ref[73]

concisely shows the gelling regime and various conformations observed during the process. The formation of κ-carrageenan gels are thermodynamically reversible. They can be formed upon cooling hot solutions and melted upon heating ("o" and "x" data points of Figure 3.3 respectively). Figure 3.3 is split into three domains. In domain I the biopolymer is in a disordered conformation (random coil) for temperatures above T_m (melting temperature). In domain II the biopolymer is in an ordered conformation where double helices are formed. Aggregation is not observed for temperatures below T_{gel} (gelation temperature) and for values of C_T (total ionic concentration) lower than C^* (the critical concentration). In domain III the biopolymer is in a ordered helical conformation and also gelled, that is to say that the helices have aggregated to form a three-dimensional network with C_T greater than C^*. C^T is a factor containing both the cation concentration (potassium (K^+) in this case) and the biopolymer concentration, as well as the average activity coefficient (γ); $C_T = C_{potassium} + \gamma C_{biopolymer}$. The transition diagram shows the gels can be formed from low concentrations of κ-carrageenan and high concentra-

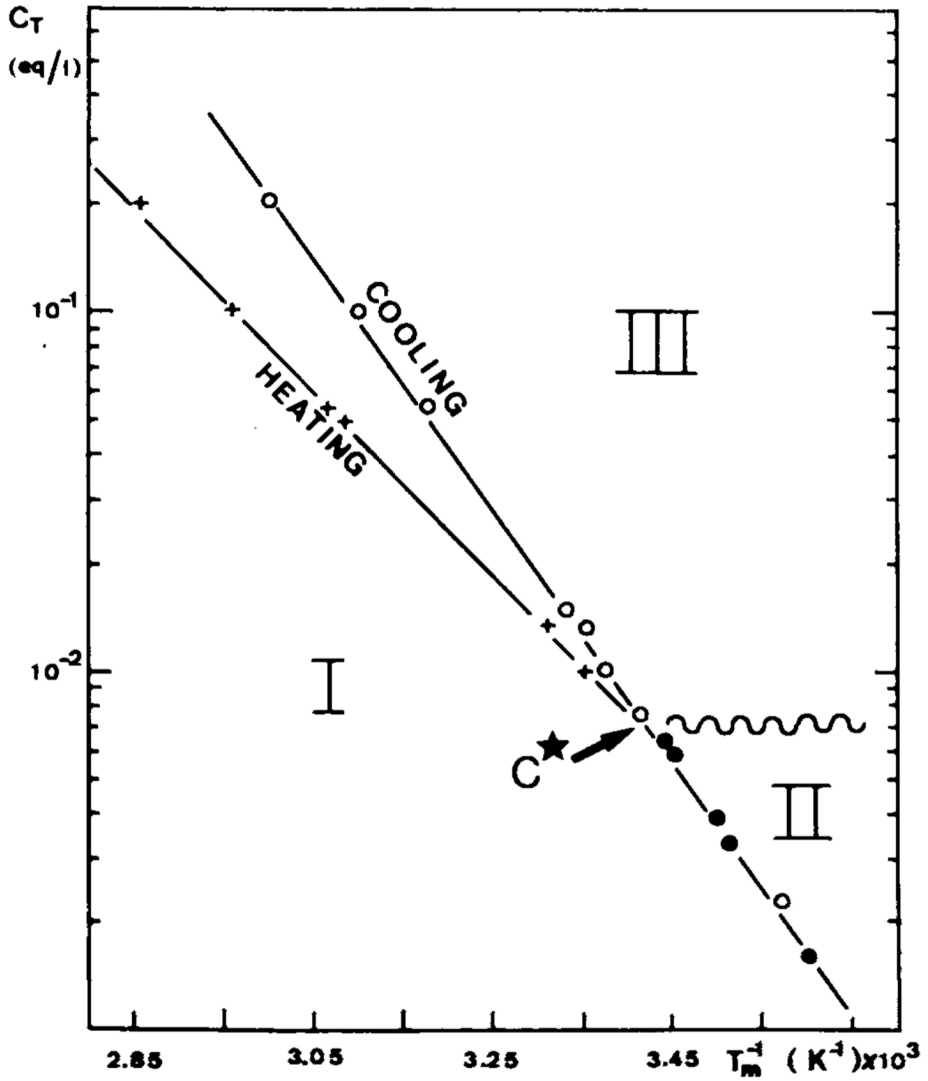

Figure 3.3: Phase diagram for the sol-gel transiton of κ-carrageenan, based on the melting temperature, T_{melt}, and total free potassium concentration C_T, reproduced from Rochas *et al.* (1984),[94] which was based on previous work.[107] The data points 'x' and 'o' show the results based on heating of the gel to form a solution, or cooling of a solution to form a gel respectively.

tions of K^+ and *viceversa*. However, the gels formed under different conditions exhibit different rheological behaviours.

Gelation of a solution suggests the formation of a continuous network of biopolymer chains.[33] Deviations from a rod-like shape of aggregated double helices is thought to be essential for the strands to form a network.[108] This network formation takes place at either a superhelical or helical level ('A' and 'B' of Figure 3.4 respectively).[89] 'A' shows superhelical aggregation where helical strands or their (multiple) aggregates form a network. 'B' shows the network formation on a helical level, where each chain joins in multiple double helices due to incomplete helical formation and single strands are responsible for the branching and association.

Many techniques have been used to study the random coil to double helix transition of biopolymers, κ-carrageenan has been studied by rheology,[105,109] light scattering and polarimetry,[110] spectrophotometry,[98] photon transmission,[63] X-ray scattering,[111] and laser dispersion to measure the strain optical coefficient.[105] These studies helped confirm the mechanism of gelation *via* association of two linear κ-carrageenan strands forming a double helix during gelation, *i.e.* 'B' from Figure 3.4

As stated above, the gelation of κ-carrageenan is promoted by monovalent cations (K^+, Rb^+, Cs^+, and NH_4^+).[112,113] These cations promote the aggregation of κ-carrageenan double helices into "aggregated domains". Viebke *et al.* concluded that the gelation of κ-carrageenan occurs at the superhelical level,[89] and this also explains the hysteresis observed for κ-carrageenan.[63,108]

Conversely, for ι-carrageenan the coil-to helix transition does not appear to be monovalent cation specific and the lack of thermal hysteresis suggests that there is little or no inter-helical aggregation. The formation of ι-carrageenan gels is assumed to take place at the helical level.[89] For such gel formation to occur at the helical level it is thought that ι-carrageenan chains must contain kinks, caused by the occurrence of disaccharide units without the 3,6-anhydro ring.[114]

This Chapter uses infrared spectroscopy to probe the gelling of carrageenans. A summary

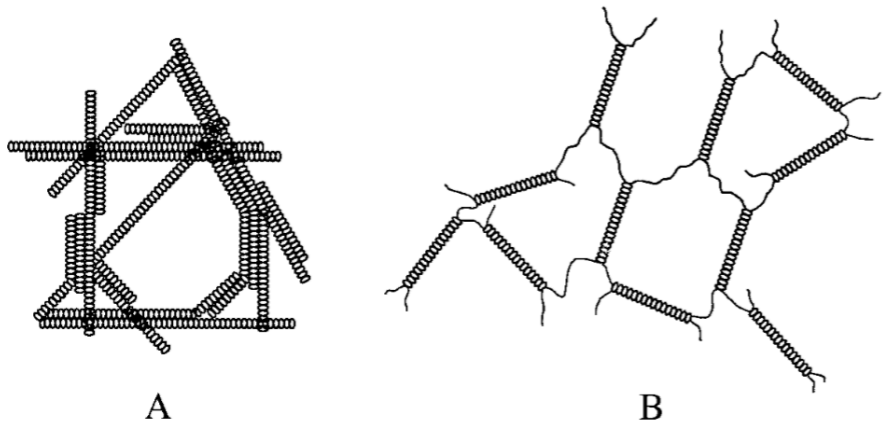

Figure 3.4: Schematic drawing of two mechanisms of network formation in carrageenan: A - gelation on the superhelical level; B - gelation on the helical level. Reproduced from van de Velde *et al.*,[108] originally adapted from Viebke *et al.*[89]

of infrared features and their assignment of κ, ι and λ-carrageenans is given in Table 1.1. The infrared spectra of carrageenans allow quantification of the type of carrageenan present and the more recent studies have focused on this, rather than the conformational aspects during transitions.[41,44,60,115]

The infrared spectra of carrageenans was seen to vary significantly depending on the cation concentration. This unsurprising due to the cations' role during gelation and the overall rheological properties that cations effect.[75] Spectral changes within sulfate based vibrations were observed as a function of cation concentration, suggesting that the sulfate groups interact directly with the cations present.[104] However, it was subsequently concluded that the observed spectral changes were due to conformational reordering during the sol-gel transition and no correlation was found with ion interactions.[51]

Infrared spectroscopy showed early promise for the study of these transitions. The ease of sample preparation, compared to optical rotation techniques which require long path lengths (10 cm) and dilute solutions (1%), enabled study of viscous solutions. However the complexity of biopolymeric systems within the fingerprint region of the spectra makes analysis difficult to interpret.[51,116]

Unlike κ- and ι-carrageenan, λ-carrageenan does not gel with mono or divalent cations, and only show viscous behaviour. This is due to the additional (compared to κ- and ι-carrageenan) sulfate group at the 2-position of the galactopyranose unit, facing inwards and preventing cross-linking and formation of an ordered network.[35] λ-carrageenan has three negatively charged sulfate groups per repeating unit, compared to κ-'s and ι-carrageenan's one and two sulfate groups respectively. However it is the position of the sulfate groups as well as the number that influences the λ-carrageenan's lack of gelation ability.[35] Interestingly, Running *et al.* recently demonstrated λ-carrageenan gelation through the use of Fe^{3+} as a trivalent cation. Most carrageenan research has been focused on κ- and ι-carrageenan due to their gelling abilities, however

Running *et al.*'s study could promote the use of λ-carrageenan beyond a viscosity modifier in coming years.

3.2 FTIR Results

The work shown in this section is based around the analysis and interpretation of three sets of IR spectra that were obtained during cooling of solutions of κ-, ι- and λ-carrageenan. These are investigated using the ATR-FTIR system described in the experimental section (Section 2). Figures 3.5, 3.6 and 3.7 show the IR spectral changes observed in the fingerprint region for the κ-, ι- and λ-carrageenan carrageenan systems as they are cooled from 80 to 10 °C. The results for each carrageenan are reported in turn and we first discuss the experiment performed on κ-carrageenan.

Rheological studies of carrageenans defined the gelation transition by the midpoint of change of the rigidity or shear moduli,[112,117] or more commonly the crossover of the shear storage modulus (G') and the shear loss modulus (G").[118] Previous IR spectroscopic studies have also been used to monitor the gelation transition.[51] Due to the subtraction algorithms used to remove the water content from the spectra, described in Chapter 2, data above 1300 cm^{-1} is not shown. The subtraction routines selected the "best-fitting" water spectrum (that was always within 0.1 °C of the sample) and therefore all O-H stretch and bend bands are subtracted out to the point where they cannot be examined.

3.2.1 Raw data

3.2.1.1 κ-carrageenan

κ-carrageenan has the strongest gelling capacity, with only one sulfate ester group per repeating unit, amongst the carrageenans studied. Figure 3.5 shows the IR spectral changes observed upon cooling of a solution of κ-carrageenan which has allowed the gelation process to be probed. Section 3.1 detailed the mechanism of gelation for carrageenans; coil-helix-aggregation, and during this process we expect a change in the conformation of the biopolymer's backbone. It

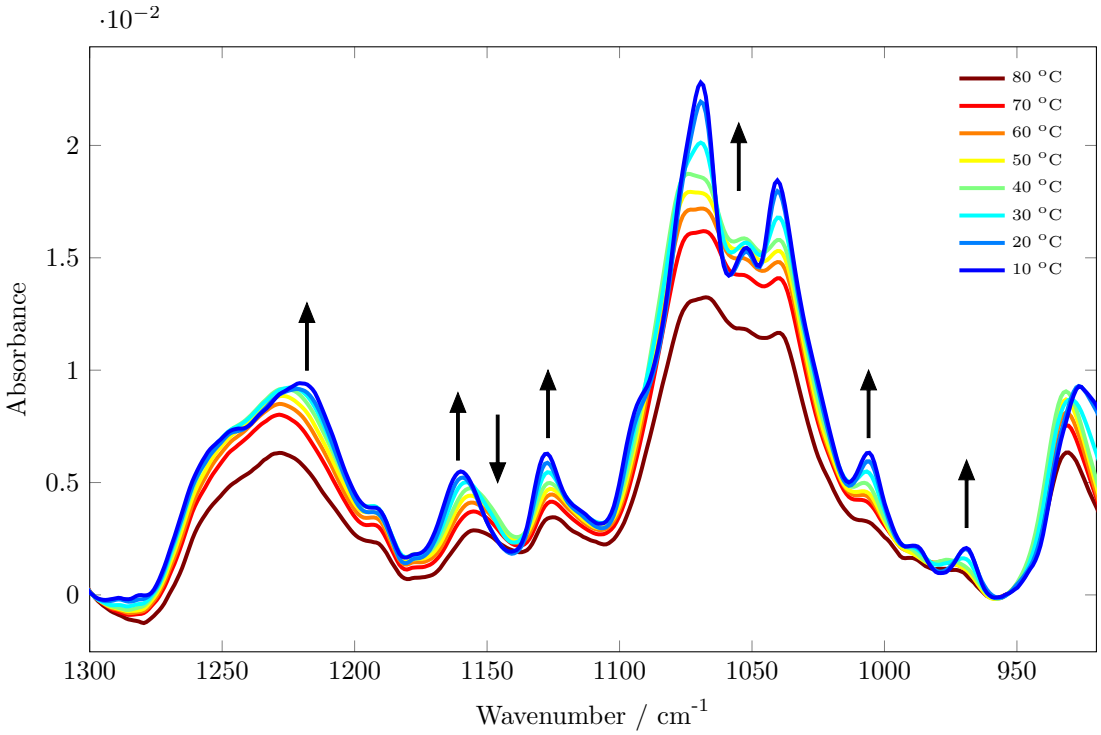

Figure 3.5: FTIR-ATR spectra of 2% κ-carrageenan in H_2O, cooled from 80 to 10 °C, which covers temperatures passing through the gelation transition. In these spectra the baselines have been corrected with a 1st order polynomial

is also to be expected that species protruding from the backbone will undergo a perturbation as they come into closer contact with other polymer strands and aggregate together during the sol-gel transition.

Figure 3.5 shows the IR spectra obtained during the cooling of κ-carrageenan. A sharpening of many bands, consistent with a reduction in anisotropy expected as a system transitions to a more ordered structure, expressed here as gelation. Some of the more prominent changes can be identified as vibrations bands belonging to sulfate (i.e. 1012 cm^{-1}) or ether (i.e. 1040-1080 cm^{-1}) vibrations, see Table 1.1. The perturbation of these bands is consistent with a change of both the backbone of the biopolymer (glycosidic linkages and ring C-O modes) and the biopolymer's surroundings (S-O and S=O groups protruding from the chain).

3.2.1.2 ι-carrageenan

The cooling of ι-carrageenan shows similar IR spectral changes to those seen within κ-carrageenan, these are depicted in Figure 3.6. There is a very obvious wavenumber shift of the S=O band at *ca.* 1225 cm^{-1}, along with changes to various backbone based vibrations (1040 to 1080 cm^{-1}). Similar to the features previously observed, the change in vibrational nature of the sulfate bands suggests interaction of the biopolymer chain, and the backbone and glycosidic linkage vibrations are consistent with a change of overall confirmation.

Within the IR spectra, both the κ and ι-forms show a shoulder appearing at *ca.* 1090 cm^{-1} as the samples are cooled, assigned to a ν(S-O) band. The appearance of this band suggests a change in the nature of the S-O stretch that occurs as a function of gelation in both carrageenans. This observation has been noted previously with FTIR,[53] with initial interpretation assigned to a sulfate-cation interaction, subsequently confirmed by NMR studies.[119] Although this assignment fitted well with gelation understandings at the time, where the sulfate groups are stabilised by cations within the helical structure, the cation specificity of this interaction

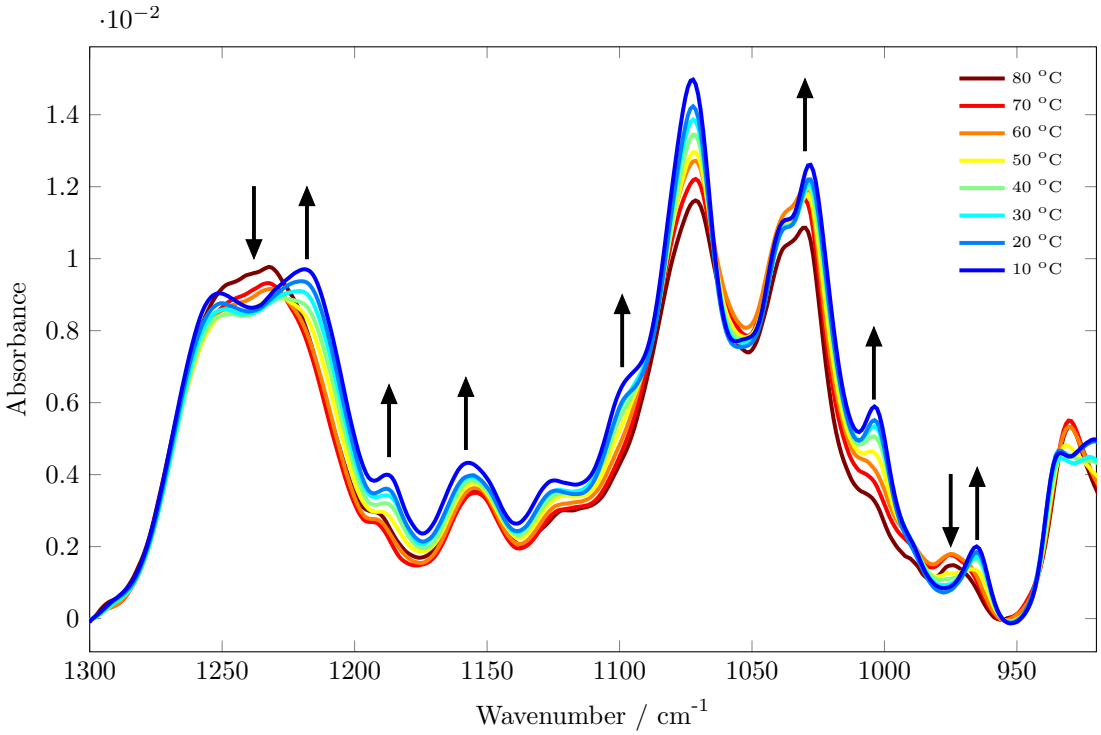

Figure 3.6: FTIR-ATR spectra of 2% ι-carrageenanin H_2O, cooled from 80 to 10 °C, which covers temperatures passing through the gelation transition. In these spectra the baselines have been corrected with a 1st order polynomial

was later revoked. The band at 1090 cm^{-1} can be observed in high temperature, solution state carrageenans following deconvolution (using Fourier self-deconvolution) and it becomes more prominent as temperature is decreased as the large band to lower energy (*ca.* 1070 cm^{-1}) sharpens.[51]

The variable temperature IR spectral changes for κ and ι-carrageenan samples are similar; the peak maxima associated with the S=O band (*ca.* 1230 cm^{-1}) moves to lower energy, S-O and S=O growth at 1090 and 1010 cm^{-1} respectively, and a shift to lower energy of modes associated with glycosidic linkages at *ca.* 970 cm^{-1}. Frequency shifts of IR bands indicated a perturbation in the molecules vibrational nature. For the glycosidic linkages this could be due to a change in conformation and for the sulfate moieties electron density withdrawn from the S=O bond due to interactions with the lone electron pairs on the oxygen, from other species along the chain, or possibly metal cations. Although similar changes to the spectra of both κ- and ι-carrageenan are observed, the κ- and ι-forms have been shown to have slightly different gelation structures, especially in the presence of metal cations.[31]

3.2.1.3 λ-carrageenan

In contrast to the κ and ι-forms, λ-carrageenan does not gel upon cooling, however the solution increases in viscosity at low temperatures.[31] Unlike the spectral changes present within the gelling carrageenans, λ-carrageenan does not show significant relative change in absorbances of bands as the temperature is decreased, nor is there peak maxima shift or apparent band sharpening. There is a general increase in absorbance across the entire wavenumber range, the magnitude of the increase at each wavenumber is proportional to the initial absorbance value. Although an increase in viscosity of the sample occurs as a function of temperature there is no IR spectral evidence within Figure 3.7 to suggest that λ-carrageenan undergoes a significant change of structure.

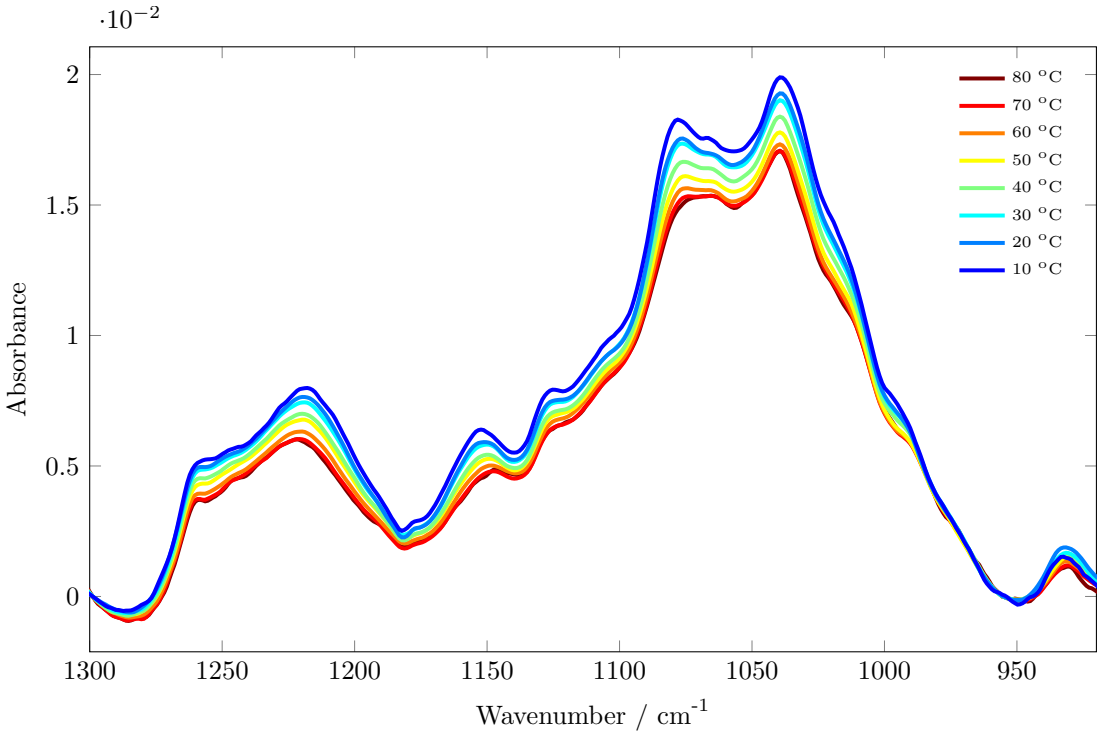

Figure 3.7: FTIR-ATR spectra of 2% λ-carrageenanin H_2O, cooled from 80 to 10 °C, which covers temperatures passing through the gelation transition. In these spectra the baselines have been corrected with a 1st order polynomial

3.2.1.4 Univariate Analysis of FTIR results

By taking a univariate approach to the data analysis, there are several common analytics that can be used to monitor changes of power spectra; peak position and peak intensity, however reconciling all of these changes together can often be difficult. Figure 3.8 shows the normalised absorbance of the C-O band at 1070 cm^{-1} (left axis, blue trace), for κ (dashed) and ι-carrageenan (solid), and the peak maxima of the ν(O=S=O) stretch at 1225 cm^{-1} (right axis, orange trace), as a function of temperature. As these systems transition from the solution to gelled state, we would expect to see large changes around the gelation temperature; *ca.* 45 °C. There is no such clear transition, for ι-carrageenan, although it might be possible to discern some change in the ν(O=S=O) between 50 and 30 °C (orange solid trace). For both the normalised absorbance at 70 $cm^{-1}$and the ν(O=S=O) maxima, κ-carrageenan shows a distinct change at *ca.* 35 °C. This temperature closely matches the expected range for the gelation of κ-carrageenan.

The growths/shifts of multiple bands for the gelling carrageenans were probed in this way in an attempt to find spectral markers that correlated with the rheological measurements of the gelation transition. It was not possible to find reliable indicators for ι-carrageenan using the univariate approach, however several spectral features showed temperature dependant changes for κ-carrageenan. In an attempt to understand and monitor the transitions of the carrageenan systems, various multivariate analyses are employed in the following sections.

3.2.2 Principal Component Analysis

It can be seen above that the univariate analysis of the IR spectra obtained during the cooling of the carrageenan solutions did not produce concrete spectral relationships capable of monitoring the gelation transition. We have analysed these data further using various multivariate approaches. The most commonly used method that provides a starting point to many types of multivariate analyses is Principal Component Analysis.

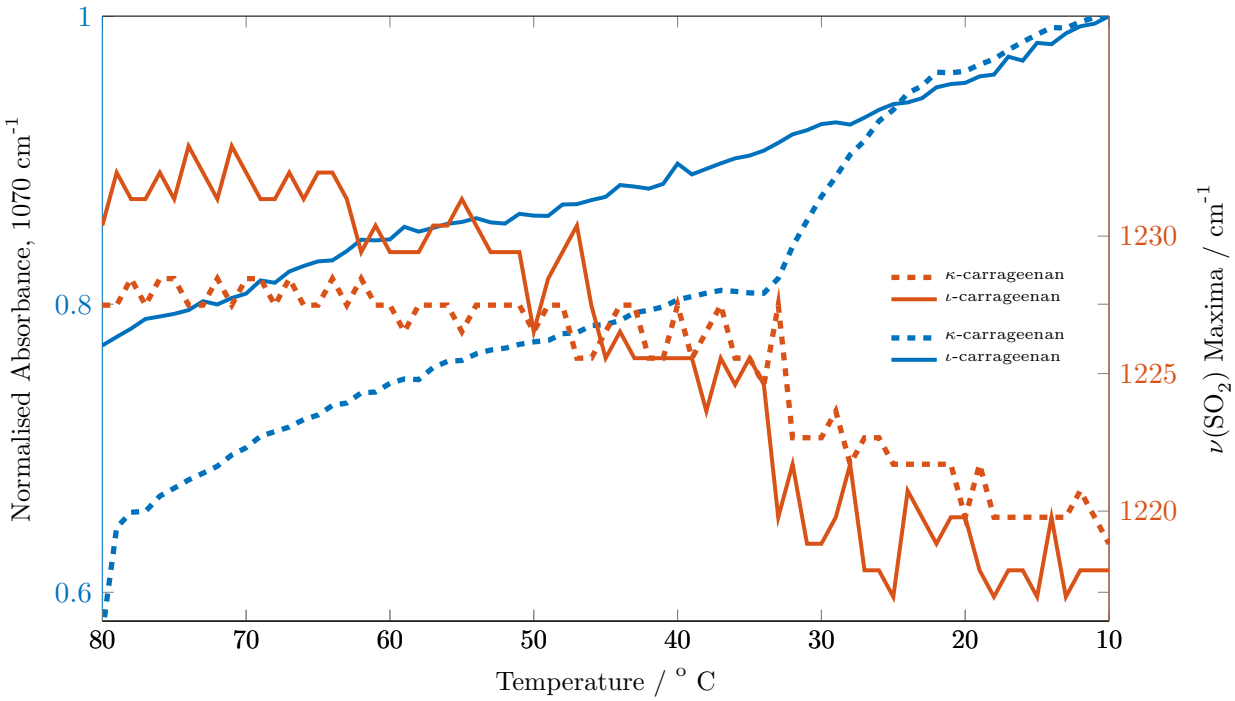

Figure 3.8: FTIR-ATR normalised absorbance at 1070 cm^{-1} (left, blue axis and blue traces) and $\nu(SO_2)$ band position (right, orange axis and orange traces), for 2 % κ-carrageenan (dashed traces) and 2 % ι-carrageenan (solid traces) in H_2O, as they are cooled from 80 to 10 °C. In these spectra the baselines have been corrected with a 1st order polynomial

Section 1.2.1 describes the theory and application of Principal Component Analysis. This multivariate technique has been used in this work to probe spectral variation within the gelation systems. Figures 3.10, 3.11 and 3.12 show the Scores and Loadings obtained from the PCA analysis of the infrared spectra κ, ι and λ-carrageenan, respectively, as they are cooled from 80 to 10 °C. For each analysis, the appropriate number of components has been chosen.

A useful method in determining the number of principal components needed to completely model the system is to analyse the root mean square error of cross validation (RMSECV) per principal component number. When a system is modelled by PCA, the entire dataset is rearranged into a set of linearly uncorrelated variables, ordered by decreasing variance captured. Mathematically the number of principal components (PCs) equals the number of original variables. The key power of PCA is that these PCs are ordered such that the first PC contains the most amount of information, allowing the system to be described in fewer variables. The RMSECV is calculated by removing a percentage of the data and, per number of principal components, estimating the removed data and then comparing it with the original. Therefore the RMSECV is a measure of how well the real system is modelled by a particular number of PCs.

Figure 3.9 shows the RMSECV values for the κ, ι and λ-carrageenan systems for a different number of principal components included in the model. The RMSECVs here have been calculated by removing 10 % of the original data, constructing a PCA model of the remaining 90 %, then attempting to estimate the missing 10 %. There are multiple different ways to exclude data, for example one could remove the first 10 % of the data, or the last 10 %. This is referred to as data removal by contiguous blocks and is one of the most simple approaches. However if the majority of the variation occurs within the first (or last) few spectra the RMSECV would not provide a true error of prediction within the data. Values within Figure 3.9 have been calculated in a venetian blind fashion, where 1 % of the data is excluded at 10 regularly spaced intervals within the dataset, starting at the the beginning. For a dataset containing 100 samples this means that samples numbers $[0, 10, 20, 30, 40, 50, 60, 70, 80, 90, 100]$ are excluded. The

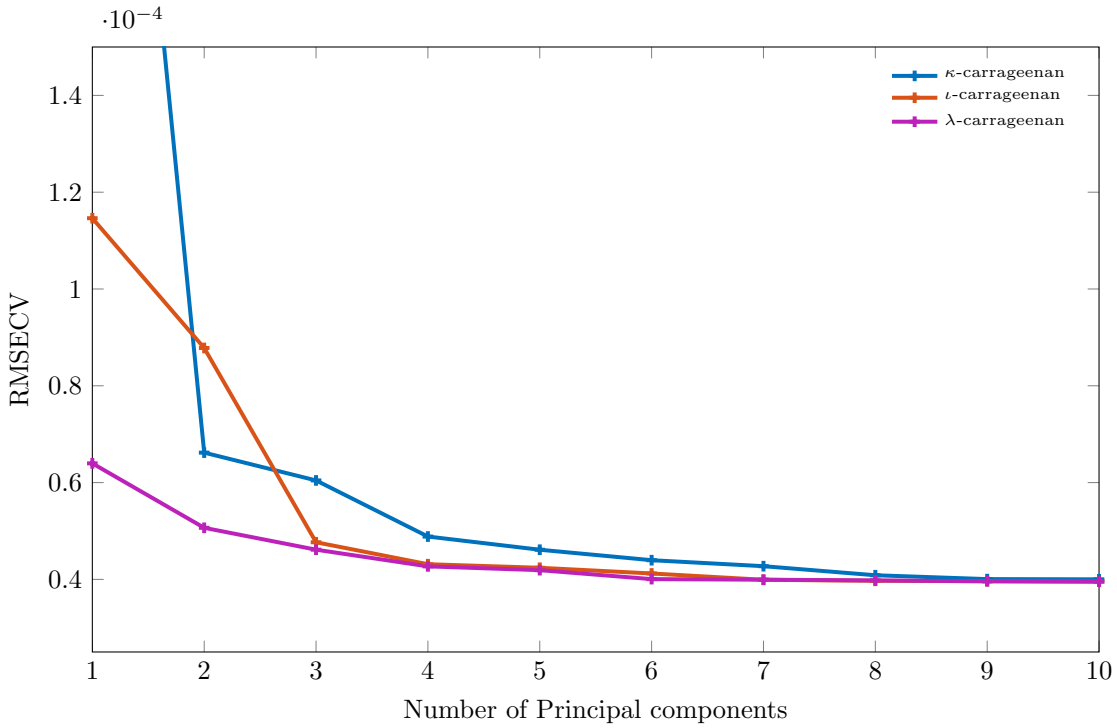

Figure 3.9: RMSECV for PCA analysis per number of principal components for PCA of κ, ι and λ-carrageenan systems as they are cooled from 80 to 10 °C, monitored by ATR-FTIR spectroscopy, RMSECV calculated using a venetian blind type data exclusion

RMSECV algorithm then steps through the next available spectra removing these in the same venetian blind manor and recalculating the RMSECV, *i.e.* $[1, 11, 21, 31, 41, 51, 61, 71, 81, 91]$, until RMSECVs have been calculated for all excluded spectra, these are then averaged together.

Figure 3.9 shows the RMSECV decrease as the number of principal components increases. For most datasets this is generally the case, as the number of components increase, the model includes more of the systems variation, allowing for a better prediction of the excluded data. However, at a higher number of principal components, where the components include no real information and only noise, the RMSECV can actually increase. If a system contains only two orthogonal and real variations, and a lot of noise, the RMSECV vs PC number plot would show a no further decrease in the RMSECV above 2 components; *i.e.* including more loadings that contain only noise do not aid in the model's predictive capability.

The blue trace (κ-carrageenan) shows plateauing of the RMSECV at 2 and 4 principal components. Examination of the 3rd and 4th loadings and scores for this system did not show any significance in the spectral or perturbational dimensions, hence only two components have been shown in Figure 3.10 as these are sufficient to describe the variation within the system. ι-carrageenan (orange trace) showed no significant change in the RMSECV after 3 principal components and examination of the later loadings was consistent with this interpretation. Finally the purple trace, λ-carrageenan, does not appear to show any significant plateauing in RMSECV, suggesting that the system can be described by only one principal component. This was also confirmed by the later components displaying only noise and including a very small percentage of the data's total variance.

The legends for Figures 3.10, 3.11 and 3.12 show the number of components displayed and also their associated total variance captured by each principal component. Utilising the number of components outlined above, it can be seen that they account for 99.4 %, 99.3 % and 98.8 % of the total variance within the κ, ι and λ-carrageenan systems respectively. The cross-validation

method described above is only used to generate RMSECV values (and allow cross-validated inspection of the model's robustness), 100 % of the data is included during the analysis.

As explained in Section - 1.2.1, the Loadings and Scores can be analysed to give insight into systems undergoing a perturbation. In relation to the real spectra, each Loading represents a aggregate of spectral variation derived from the PCA algorithm, allowing parallels between the loadings and real spectra to be drawn. The Scores represent the likeness of each spectra, at a specific temperature, to the loadings, giving an indication to the overall changes occurring during the perturbation.

3.2.2.1 κ-carrageenan

Figure 3.10, κ-carrageenan, shows a distinct change of the score plot at *ca.* 30-35 °C. The scores relate to the particular contribution of each loading. The score of the first principal component (blue trace) shows a steady increase as the system is cooled from 80 to 10 °C, whereas the second component (orange) has a large gradient change *ca.* 30-35 °C. As the system is cooled down, the κ-carrageenan not only cools but forms a gel structure. The score of PC1 changing linearly with temperature and score 2 having a non-linear temperature dependance, suggests that PC1 is following the a spectral response that changes linearly with temperature and PC2 is probing the gelation transition.

The observation of a distinct change within the PCA scores at *ca.* 30-35 °C is also in line with the gelation transition of κ-carrageenan.[94] However, as discussed in in Section 3.1 the gelation process is complicated and the gelation transition temperature (normally defined as the midpoint of the transition[120]) can vary tremendously depending on counterion valency and concentration.[94]

To provide further evidence on this initial assignment of the principal components, one must look towards the loading, attempting to assign some spectral significance to the mathemati-

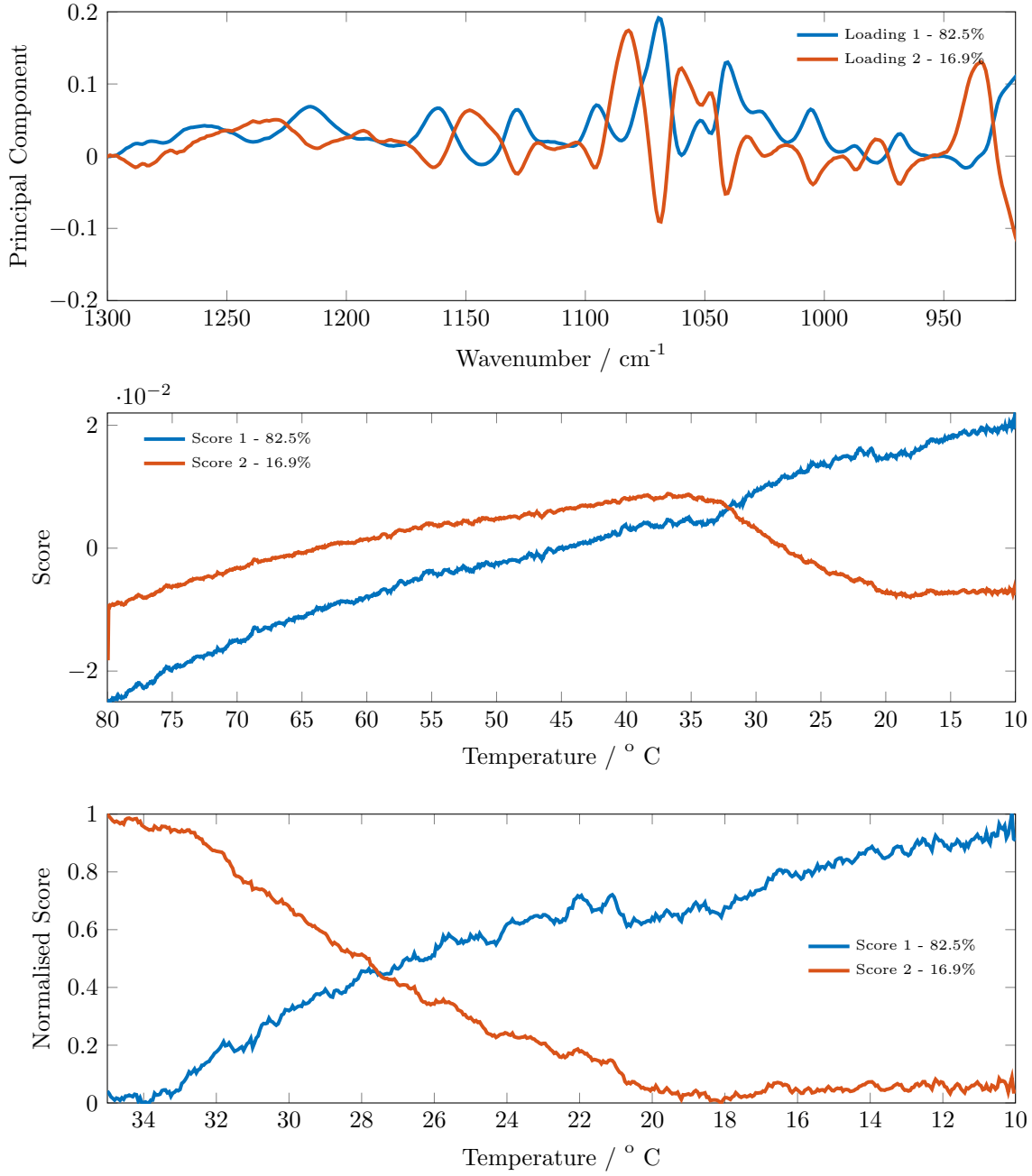

Figure 3.10: Top: PCA Loadings, Middle: PCA Scores, and Bottom: normalised PCA scores between 35 and 10 °C, of the 2 % κ-carrageenan system in H_2O, cooled from 80 to 10 °C. The spectra have had their baselines corrected with a 1st order polynomial prior to PCA analysis, data has been mean-centered

cal variation that PCA elucidates. This approach can be difficult, as the systems orthogonal variation represented as the principal components can bear little spectral meaning.[6]

Although there is evidence of mathematical confusion between the principal components resulting in artefacts; where loading 1 and loading 2 contain positive and negative contributions, several variables can be picked out and uniquely assigned to bands within the real system. Loading 2 shows a large band at 930 cm^{-1}, associated with a C-O-C vibration, a unique trace at 1080 cm^{-1}, another C-O band. Many other changes can be picked out, however they are mimicked by loading 1, with an associated change of sign, suggesting a mathematical artefact rather than unique spectral change.

3.2.2.2 ι-carrageenan

The ι-carrageenan PCA deconvolution, Figure 3.11, indicates three orthogonal components that have a significant contribution on the total variance of the system. The scores of PC1 and PC2 (blue and orange trace) both show significant changes at 60-65 °C. Score 1 has a distinctive change in the gradient of it's score with respect to temperature between 60 and 65 °C, then continues to show a linear change over the remaining cooling period, similar to that of PC1 from κ-carrageenan in Figure 3.10. Score 2 shows a maximum at 60 - 65 °C, decaying to an almost flat line by 50 °C. From the scores plot, PC3 (purple) does not appear to show any major change, changing steadily over the temperature range and therefore suggesting that this particular loading is following a general change in spectral features with respect to temperature, rather than a gelation transition. It is generally accepted that the gelation of ι-carrageenan occurs at roughly 35 °C,[61] with the gelation process starting at temperatures around 50 °C.[121] Monitoring the gelation process by FTIR spectroscopy does not allow for a definition of the gelation temperature, as this is a rheological phenomenon, merely that we can monitor the start, end and midpoints of the molecular rearrangements, which these data appears to follow previously stated temperatures. Rheological studies of ι-carrageenan systems gives the critical

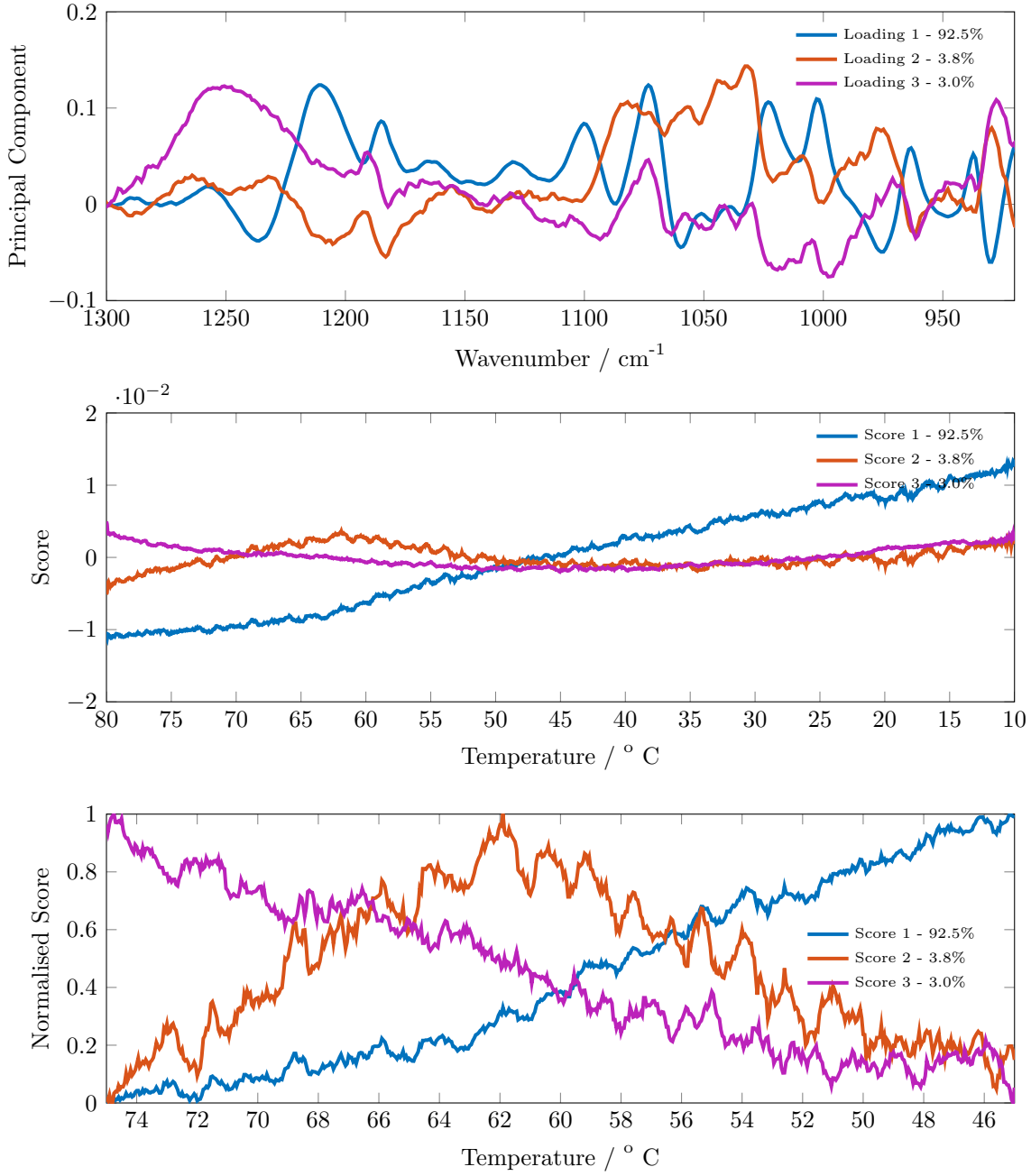

Figure 3.11: Top: PCA Loadings, Middle: PCA Scores, and Bottom: normalised PCA scores between 75 and 45 °C, of the 2 % ι-carrageenan system in H_2O, cooled from 80 to 10 °C. The spectra have had their baselines corrected with a 1st order polynomial prior to PCA analysis, data has been mean-centered

gelation point *ca.* 10 to 20 °C lower than that observed here. This could be an effect of the ionic concentration of the carrageenan samples used within this study, more likely however is that the molecular rearrangement, as monitored by vibrational spectroscopy, occurs *ca.* 10 to 20 °C before the rheologically defined gelation transition.

In contrast to the κ-carrageenan, 3 components were shown for the ι-carrageenan. The third component (purple trace, top plot, Figure 3.11) does contain some spectral information, such as the bands at 1080 and 1250 cm^{-1}, however a main feature within the loading plot is a sloping baseline, suggesting that PC3 is a persistence of the baselining routines, described in Section 2.2. Although the variation contribution for PC3 is 3 %, which is very close to the contribution of PC2 at 3.8 %, the lack of spectral features and sloping nature of the loading suggest that it is mostly artificial, or at the very least not monitoring the gelation transition.

3.2.2.3 λ-carrageenan

Figure 3.12 shows only one component for the PCA analysis of λ-carrageenan. This component contains the majority of the variation within the cooling of λ-carrageenan, 98.8 %. Along with evidence from the RMSECV plot (Figure 3.9) the loading (top plot, Figure 3.12) closely resembles that of raw carrageenan spectra, with the score showing a steady increase over time. This was exactly what was suggested from Figure 3.7, where the spectral intensities increased proportionally to their original absorbance values. λ-carrageenan does not gel (under the conditions used here,[32]), rather just increase the solution's viscosity as the temperature is reduced. It is of no surprise, therefore that PCA only identifies a single component displaying real spectral variation and the associated score shows a steady increase. In contrast to the sudden change in gradient of the scores extracted from the component analysis of κ-carrageenan and ι-carrageenan, indicating their gelation transitions.

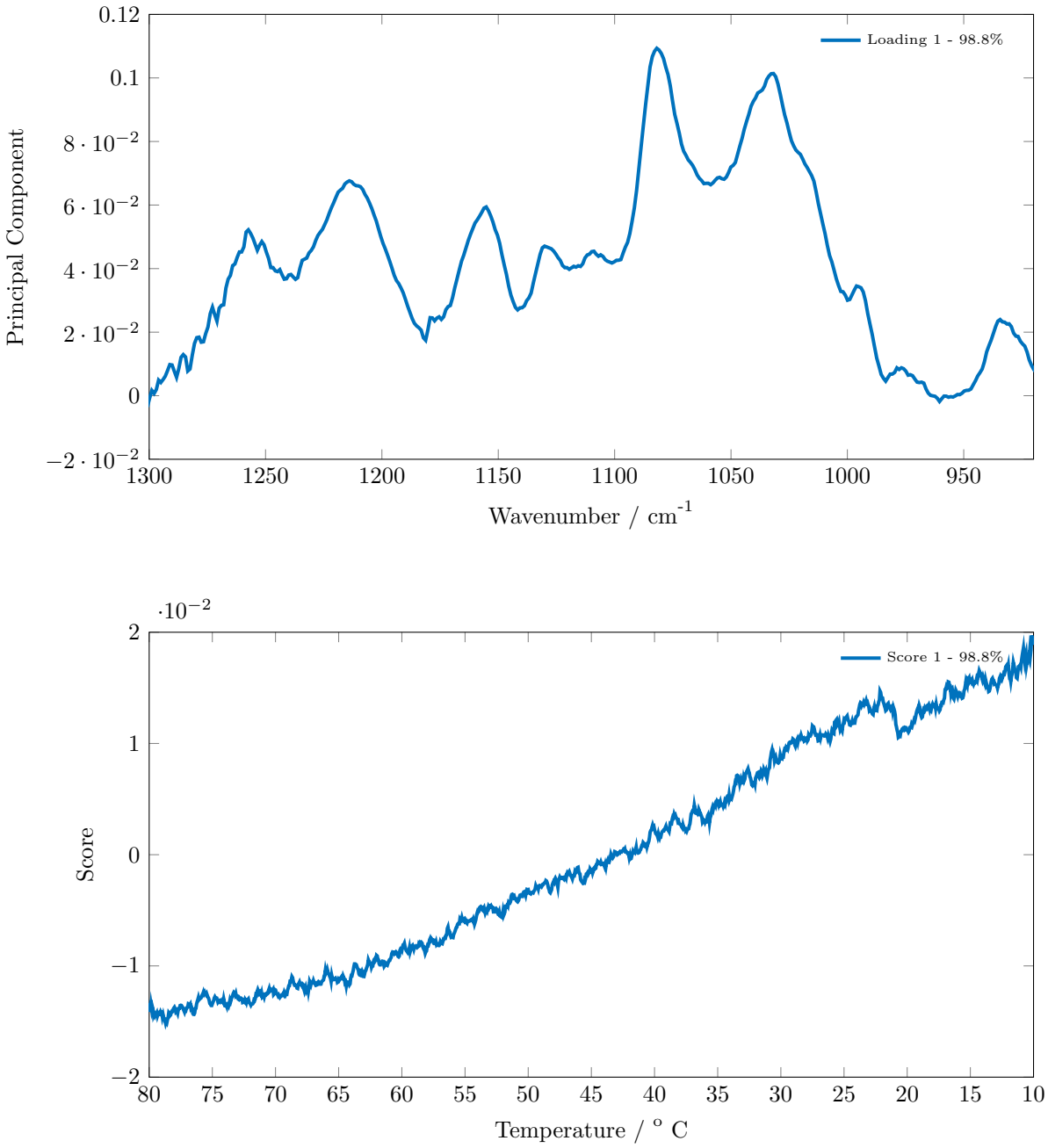

Figure 3.12: PCA Loadings and Scores (top and bottom) of the λ-carrageenan system, cooled from 80 to 10 °C as monitored by ATR-FTIR, preprocessing: linear baseline and mean-centering

3.2.3 Multivariate Curve Resolution

Multivariate Curve Resolution is described in Section 1.2.2, it is a particularly useful tool for mixture analysis.[122] The objectives of MCR are similar to that of PCA's, however the resulting component loadings are generally more spectrally significant due to the non-negativity constraints applied during the optimisation phase of the modelling.

Figures 3.13, 3.15 and 3.17 show the MCR components and scores for the κ-, ι- and λ-carrageenan systems as they cooled from 80 to 10 °C. Unlike PCA analysis, the number of components is predefined. The number of components modelled was chosen based on evidence from Section 1.2.1; RMSECV plots, evaluation of the loadings, and evaluation of the fitting of the MCR model.Two components were chosen for the κ- and ι-carrageenan systems, one component for λ-carrageenan.

Initial analysis of the FTIR data and subsequent principal Component Analyses indicated that the gelation of (κ and ι) carrageenan showed a system that transitions from a solution to gel state, at some point over the temperature range. Although the mechanism of gelation has several steps (Section 3.1), FTIR data suggest and "A goes to B" type system. Modelling A $\rightarrow$ B systems by MCR highlights the purity of the A $\rightarrow$ B nature. Modelling two components will identify the pure spectral components and their associated concentrations including 100 % of the variation within the model. To ensure the correct number of components was chosen for each system, MCR models with $n + 1$ components were calculated (where n is the assigned number of components). For each of the systems the extra component contained a very small amount of total system variance (< 5 %). This final component was a combination of the two components in the two component model, and the score showed little to no change over the temperature range. All of these factors suggest mathematical artefacts introduced by forcing the MCR model to fit a higher number of components than the real system contained - indicating the correct number of components was originally chosen.

3.2.3.1 κ-carrageenan

Figure 3.13 shows the two component MCR deconvolution of the gelation of κ-carrageenan. Component one (blue trace, top plot) is almost identical to the low temperature, gelled κ-carrageenan that can be seen in Figure 3.5 (10 °C, dark blue trace), while component two (orange trace, top plot) bears a strong similarity to the high temperature, solution state κ-carrageenan seen within the FTIR data; Figure 3.5 (80 °C, dark red trace).

The scores of Figure 3.13 (which can be considered concentrations with respect to the components)[9] show little change as the system is cooled from 80 °C to to *ca.* 35 °C. The mixture analysis reveals that during this initial temperature decrease the κ-carrageenan system is comprised mainly of component two with little component one characteristic; *i.e.* the mixture resembles hot, solution state κ-carrageenan during the 80 to 35 °C cooling. At *ca.* 35 °C, there is sudden change in the scores plot and over the next 20 °C decrease the system moves towards resembling component one with no component two contribution.

In contrast to the PCA analysis (Section 3.2.2, Figure 3.10) the components of the MCR much closer resemble the untreated dataset, allowing for easier interpretation. The sudden change in gradient of the scores plot is seen at 33 °C in both the PCA analysis (Figure 3.10) and the MCR analysis (Figure 3.13) indicating that it is at this point that κ-carrageenan begins its gelling transition. Visualising the contribution of the solution-state and gelled-state system in this manner allows for a very easy method to follow the extent of gelation, possibly useful in monitoring gelation-like conformational changes in low concentration systems that do not contain enough carrageenan to fully gel.

Figure 3.14 shows the comparison between the gelled and solution state raw spectra of κ-carrageenan and the MCR loading obtained by modelling the gelation process. The low and high temperature raw spectra, and MCR 1 and MCR 2 component couples are offset for clarity. The dashed spectra at the bottom of the plot, show the similarity of the first MCR loading at

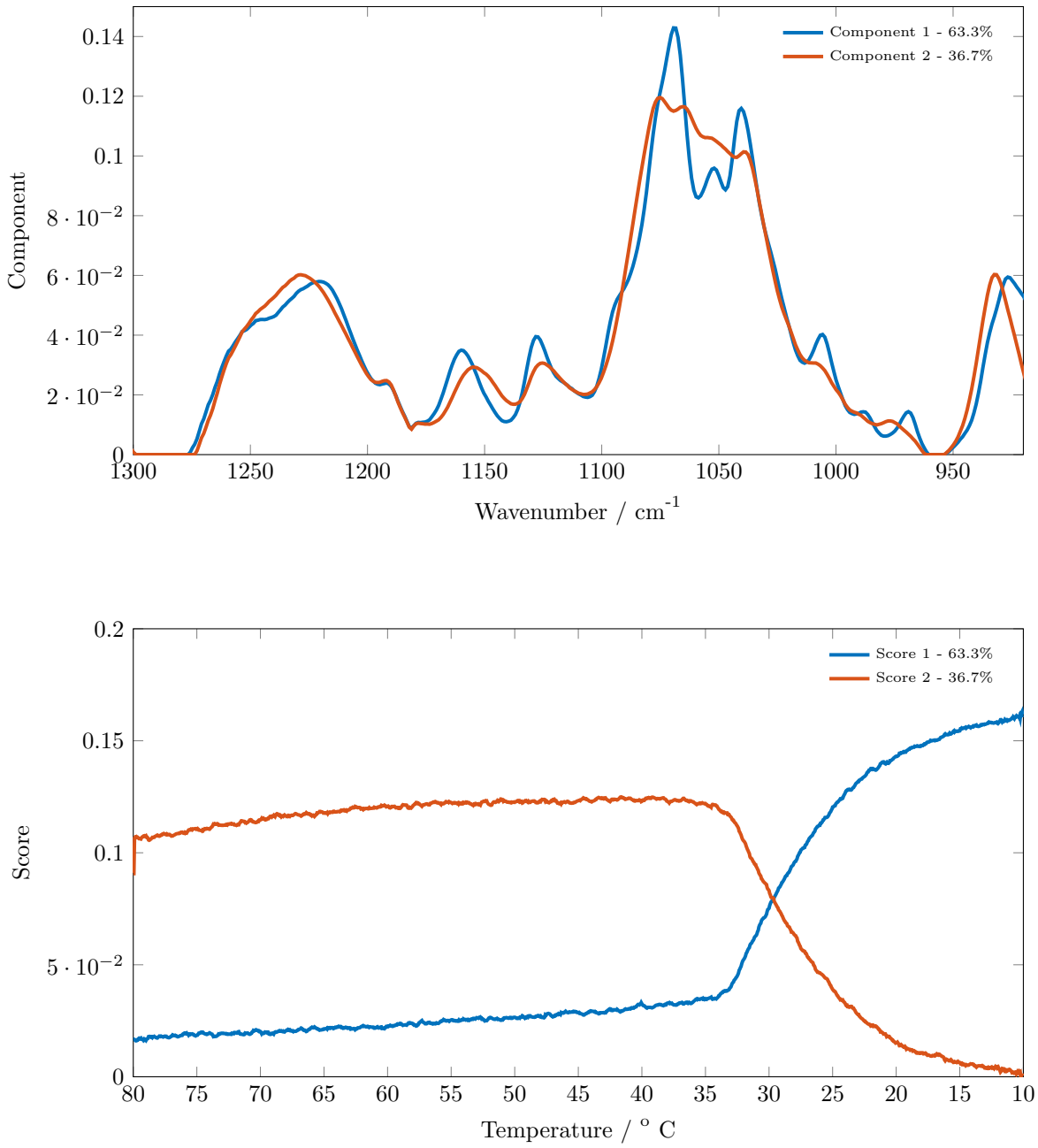

Figure 3.13: MCR Components and Scores (top and bottom) of the κ-carrageenan system, cooled from 80 to 10 °C as monitored by ATR FTIR, preprocessing: linear baseline

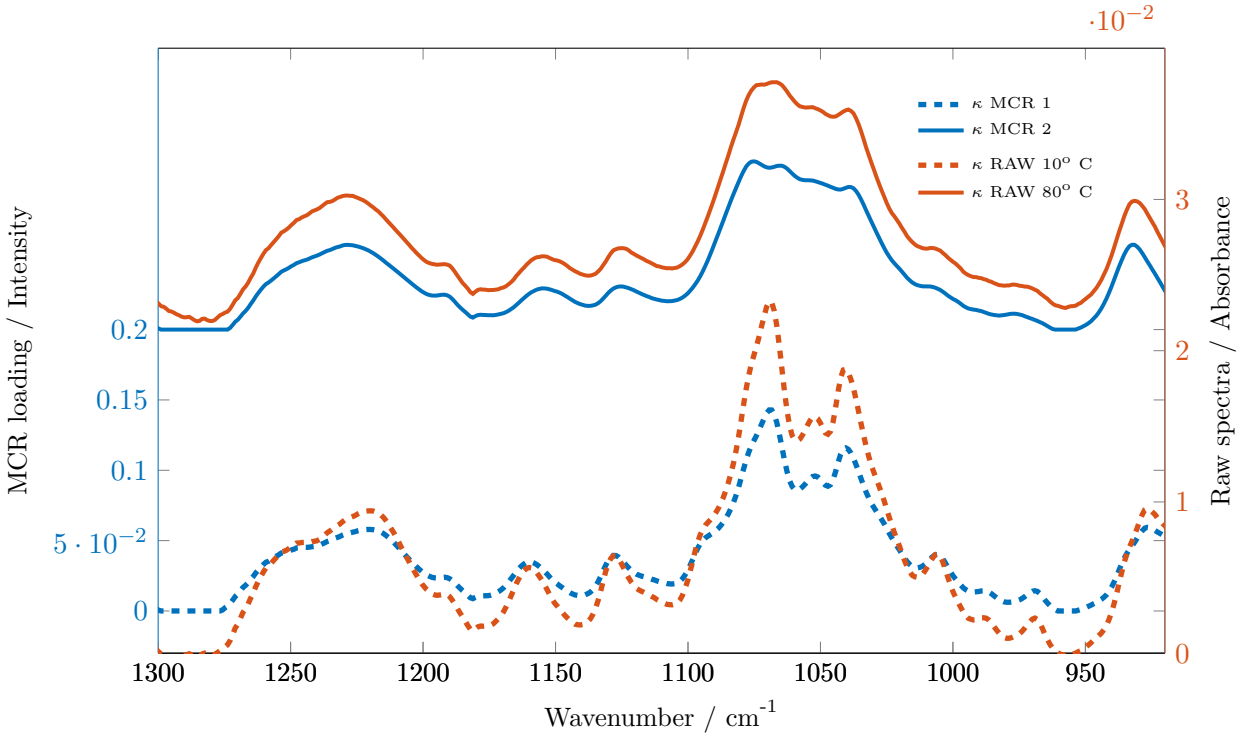

Figure 3.14: Comparison of raw spectra and MCR loadings, showing similarity, of κ-carrageenan, at low; 10 °C and high; 80 °C, temperatures - *i.e.* gelled and solution state carrageenan

the low temperature raw spectra. Although there are slight baseline differences between them, all main spectral features are replicated within the MCR loading. The spectra to the top of the plot, high temperature raw spectra and the second loading also match up very well. The only significant difference between the two top traces is the high wavenumber deviation (1300 - 1270 cm^{-1}), a baseline routine introduced difference due to curvature of the baseline just above the spectral window displayed. Although the raw spectra of the temperature run, Figures 3.5, 3.6 & 3.7, appeared to be correctly baselined. The difference between the MCR loadings suggests that the baselining routine requires further research. The similarities between the MCR components and raw gelled and solution state spectra of κ-carrageenan gives evidence to the assignment of the MCR components representing the gelled and solution state carrageenan systems.

3.2.3.2 ι-carrageenan

Figure 3.15 shows the MCR decomposition of the gelation of ι-carrageenan from 80 to 10 °C. Similar to that of the κ-carrageenan system, there is little change in the score plot at the start of the experiment when the solution is being cooled. At *ca.* 63 °C change is observed for the scores of both components. The top plot shows the loadings for the MCR, with components one and two almost exactly matching that of the hot and cold (solution and gelled state) ι-carrageenan FTIR spectra, as seen in Figure 3.16. As with the MCR deconvolution of the κ-carrageenan system, the match between the raw spectra and MCR loadings is very good, indicating that a combination of FTIR and MCR and be used for monitoring of the transition from a solution to gelled state within these systems.

In agreement with the PCA analysis of ι-carrageenan, Figure 3.11, there is a change in the scores between 65 and 60 °C, suggesting physical change in the biopolymer. At 63 °C there is substantial change, as the system converts from component 1 to component 2. The rate of change decreases as the temperature is lowered, suggesting that the gelation process, as monitored by IR, continues past the temperature of the gelation transition monitored by rheological methods,

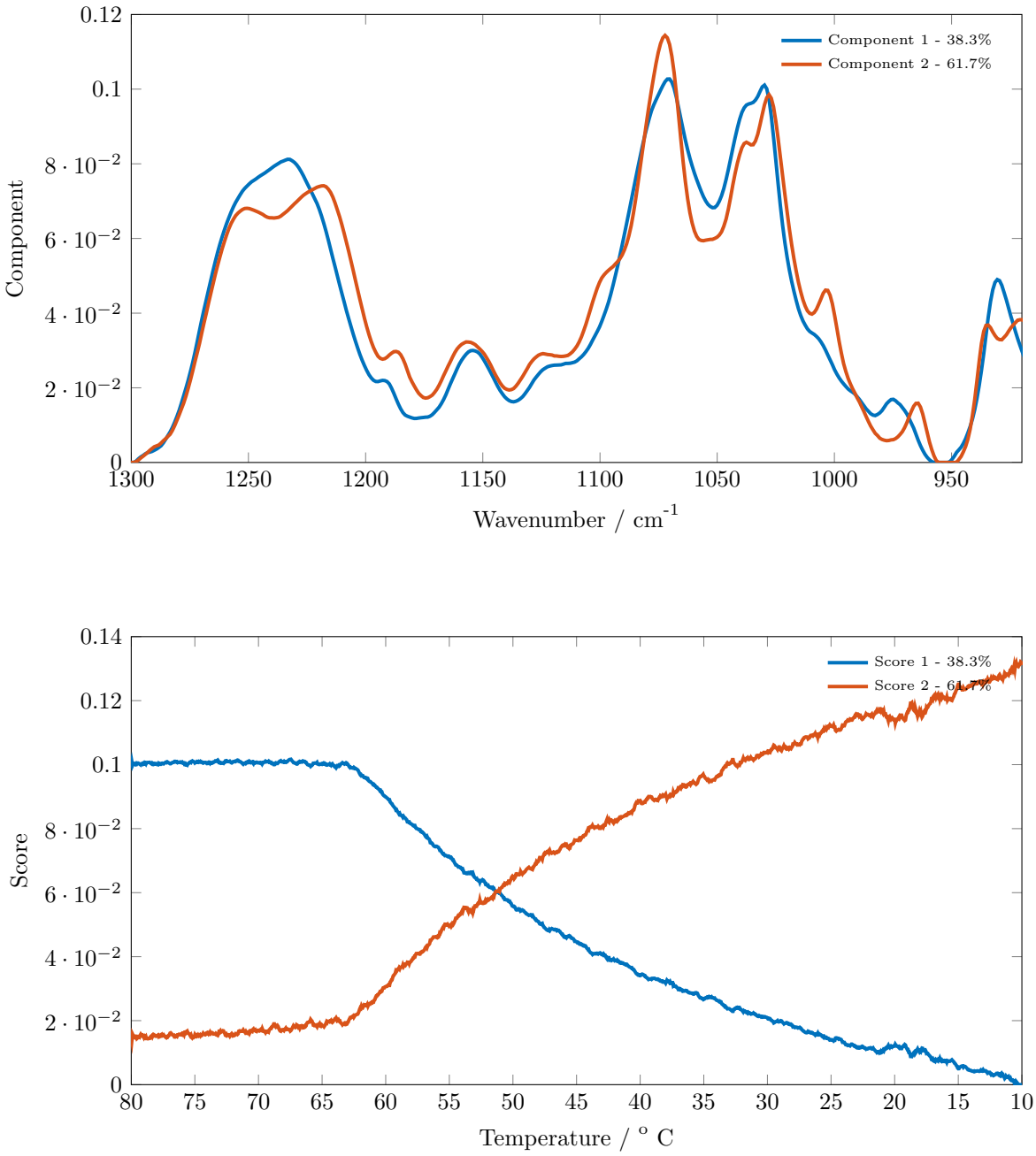

Figure 3.15: MCR Components and Scores (top and bottom) of the ι-carrageenan system, cooled from 80 to 10 °C as monitored by ATR FTIR, preprocessing: linear baseline

slowing down as it does so.[51,117] Although it is difficult to give an exact transition midpoint, as measured by rheological methods for this sample of carrageenan, the temperature window of transition monitored by IR is much wider than that of the rheological window.[51,112,117]

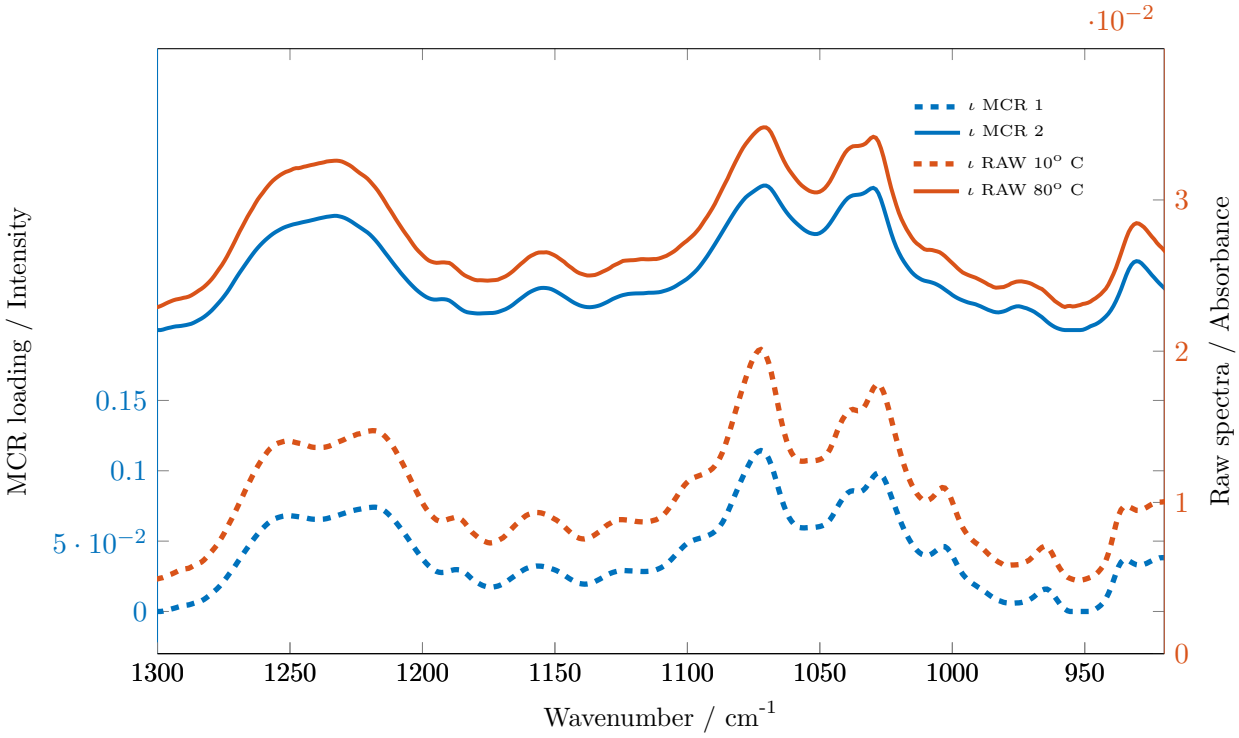

Figure 3.16: Comparison of raw spectra and MCR loadings, showing similarity, of ι-carrageenan, at low, 10 °C and high, 80 °C, temperatures - *i.e.* gelled and solution state carrageenan

3.2.3.3 λ-carrageenan

Figure 3.17 shows the MCR results for the λ-carrageenan samples as they are cooled from 80 to 10 °C. Unlike the κ- and ι-forms, λ-carrageenan does not form a gel, under these conditions.[32] Also, in contrast to κ- and ι-carrageenan, only one MCR component was used to model the λ-carrageenan system. The spectral agreement between the MCR component and the raw spectra is very high - Figure 3.18. It can be seen from the scores (bottom plot, Figure 3.17) that a gradual increase with respect to temperature is observed. Similar to the PCA analysis of the λ-carrageenan system there is no indication that a significant change in the IR spectra are wit-

nessed, as expected for a system that does not undergo a temperature dependant rearrangement, *i.e.* gelation.

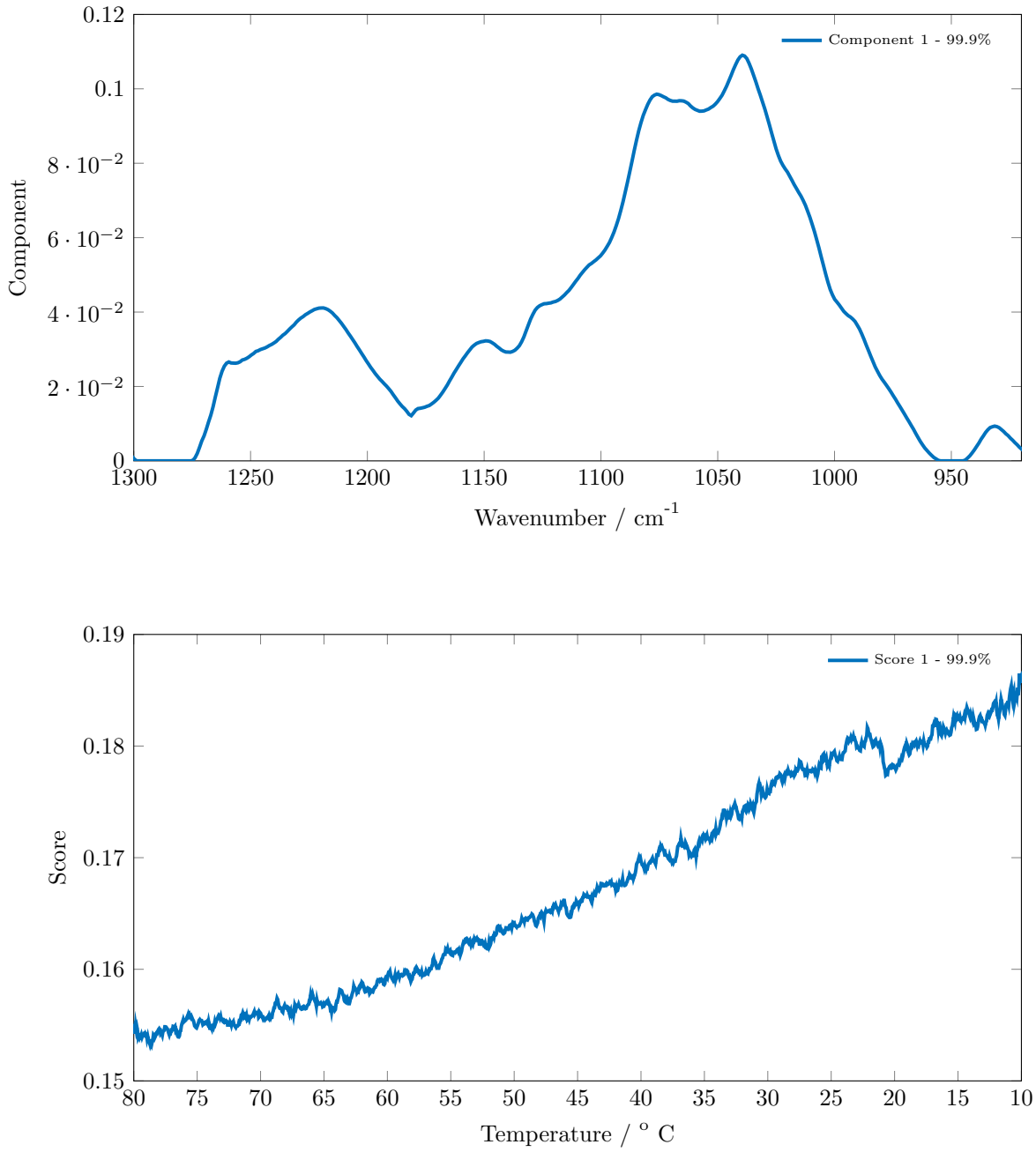

Figure 3.17: MCR Components and Scores (top and bottom) of the λ-carrageenan system, cooled from 80 to 10 °C as monitored by ATR FTIR, preprocessing: linear baseline

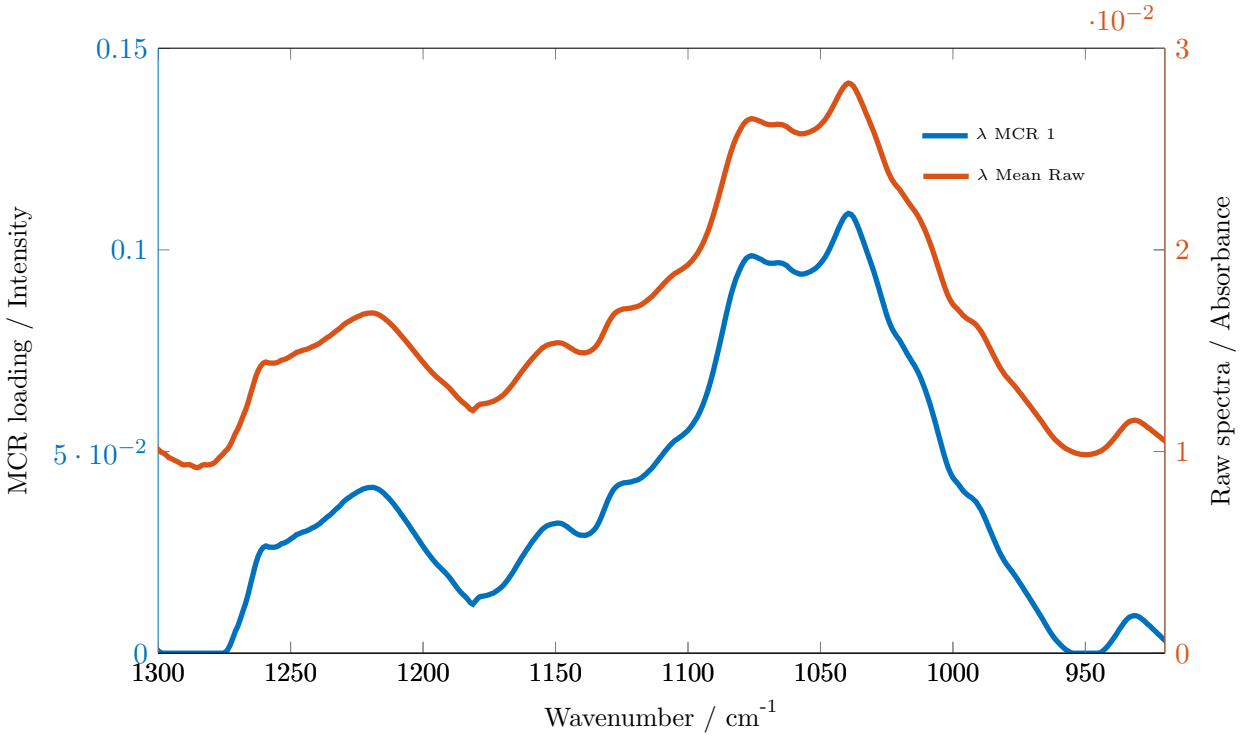

Figure 3.18: Comparison of the mean of the raw spectra and MCR loading, showing similarity, for λ-carrageenan

3.2.4 Two-Dimensional Correlation Spectroscopy

Two-dimensional correlation spectroscopy (2DCOS) was described in Section 1.3.1, along with the computational methods used. The techniques use complex correlation methods to spread data over an additional dimension, this can often aid in visual interpretation and help to simplify the data. 2DCOS highlights regions of the spectra which are susceptible to change, often proving a resolution enhancement of features which show intensity variations. The complex part of the correlation (referred to as the asynchronous/imaginary spectrum) identifies spectral regions changing out of phase, *i.e.* at a different rate to one and another, this is particularly useful at separating overlapping bands assigned to different vibrations, if they change independent of each other.

Data from the gelation of the κ, ι and λ-carrageenan systems, with a constant temperature offset (every 0.05 °C), were passed into the 2DCOS algorithm. As previously discussed, this gives two spectral cross-correlation maps; synchronous and asynchronous. The former representing simultaneous or coincidental change of the spectral intensity variation, and the latter identifying sequential changes.

Within the synchronous correlation, the intensity of peaks located along the diagonal axis ($\nu_1 = \nu_2$) mathematically correspond to the autocorrelation function of spectral intensity variations during the perturbation. At a particular ν the magnitude of the autopeak represents the extent of the variation. As such this autocorrelation spectrum can be used to identify spectral bands that change, with a resolution enhancement over simply viewing the dynamic spectra ($y(\nu, t) - \bar{y}(\nu)$), referred to as mean centered data within multivariate terminology.[123]

3.2.4.1 Autocorrelation Spectra

Figure 3.19 shows the normalised autocorrelation spectrum (orange trace) overlaid with the mean spectrum (blue trace) observed as κ-carrageenan is cooled from 80 to 10 °C. It is imme-

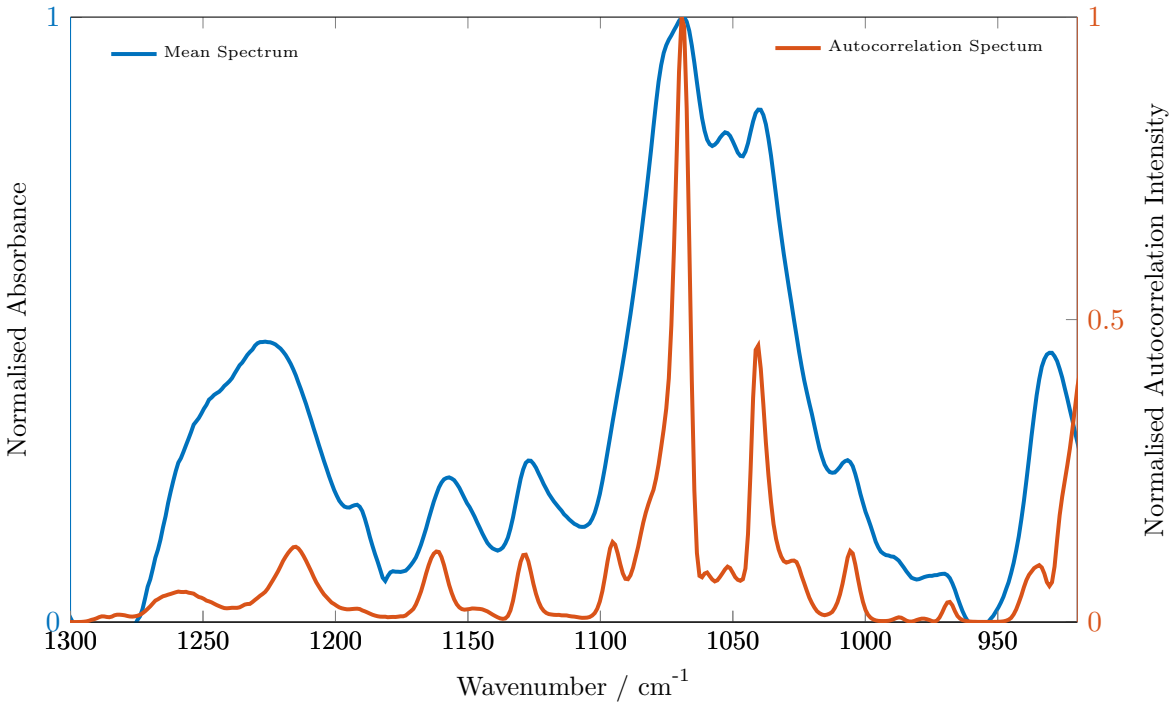

Figure 3.19: Autocorrelation Spectrum calculated from FTIR data of κ-carrageenan, cooled from 80 to 10 °C

diately obvious that there is some resolution enhancement within the autocorrelation spectrum compared to that of the the mean spectrum. This is however, not an absolute tool for resolution enhancement. Comparison of the bands at 1250 and 1070 cm^{-1} show a different degree of resolution enhancement between the mean and autocorrelation spectrum. This is because the autocorrelation function is able to provide a resolution enhancement through a mathematical function that is describing change to a system, *i.e.* bands that change more will show a larger enhancement. The autocorrelation spectrum is not an overall resolution enhancement, solely an enhancement of the intensity variation of each particular datapoint along the perturbation axis.

The ability to monitor a region's susceptibility to change in spectral intensity as a function gelation allows a comparative resolution enhancement of the observable bands that change the most during gelation. The immediate feature that stands out is the band at 1070 cm^{-1} (C-O and C-OH modes), this was seen to change greatly during gelation (Figure 3.5). During the initial look at the gelation of κ-carrageenan a shoulder appeared at *ca.* 1090 cm^{-1}, and a much more obvious band at 1010 cm^{-1}, due to S=O and S-O stretching respectively (Section 3.2). Both of these features are very obvious within the autocorrelation spectrum, confirming that the bands associated with sulfate groups change during gelation. The increased resolution also allows for more accurate determination of wavenumber; 1095 and 1005 cm^{-1}.

The O=S=O antisymmetric stretch of the large band at 1230 to 1250 cm^{-1} has also been deconvoluted with respect to the gelation; a single band at 1215 cm^{-1}appearing within the autocorrelation spectrum, indicating this is the region most susceptible to change.

The autocorrelation of ι-carrageenan is shown along with the mean spectrum over the gelation transition (80 to 10 °C) in Figure - 3.20. The autocorrelation spectrum of ι-carrageenan appears somewhat more complex than that of κ-carrageenan. Similarities between the C-O and C-OH combination modes at 1073 cm^{-1}, the O=S=O stretching at 1011 cm^{-1}, and the S-O and S=O stretches 1100 and 1002 cm^{-1} respectively, exist between the κ- and ι-systems. Bands

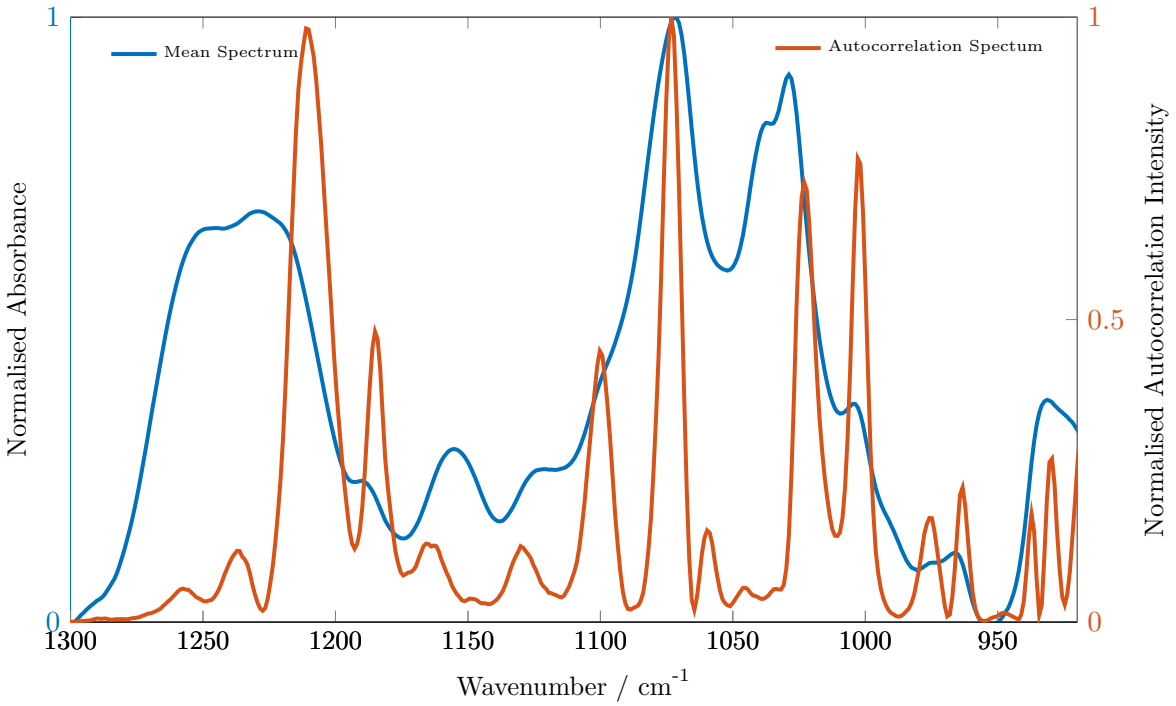

Figure 3.20: Autocorrelation Spectrum calculated from FTIR data of ι-carrageenan, cooled from 80 to 10 °C

associated with the sulfate vibrations are much more intense for the ι-carrageenan sample. Two sulfate vibrations are made significantly clearer; at 1023 and 1185 cm^{-1} (only appearing as slight shoulders within Figure 3.19).

Initial interpretation of the increased spectral intensity variations associated with sulfate bands for ι-carrageenan compared to κ-carrageenancould indicate increased sulfate group interactions for the ι-system. ι-carrageenan has two sulfate groups per repeating unit, compared to κ-carrageenan's one, purely on the observed absorbance, one would expect a higher intensity change of the perturbed sulfate groups during gelation. However these systems are independent, so the reason for the increased intensity variation of the sulfate modes is likely to be much more complex than a simple concentration increase. The different number of sulfate groups per repeating unit between κ- and ι-carrageenan have previously been investigated with respect to different counter ions; K^+, Na^+, Cs^+, Ca^{2+}, and Mg^{2+}.[101,124–127] κ-carrageenan with one sulfate group per repeating unit forms stronger gels with monovalent counter ions, while ι-carrageenan, with two sulfates per chain, shows increased specificity and gel strength towards divalent counter ions. The carrageenan samples used will have varying counter ion concentrations, which is related to the preparation methods used by the manufacturers.

It is also worth noting that the two bands between 1100 and 1200 cm^{-1}, associated with C-O-C and glycosidic linkage modes remain stable in wavenumber and relative intensity compared with the C-O & C-OH band at *ca.* 1070 cm^{-1} for both samples; κ-carrageenan: 1162 and 1129 cm^{-1}, ι-carrageenan: 1164 and 1130 cm^{-1} for the C-O-C antisymmetric stretch and the band of the glycosidic linages respectively.

Figure 3.21 shows the autocorrelation and mean spectrum for λ-carrageenan. Although similar features are observed when compared with κ-carrageenan and ι-carrageenan, the most notable difference is that the autocorrelation spectrum of λ-carrageenan does not appear to enhance some bands compared to others. The autocorrelation spectrum in Figure 3.21 looks like

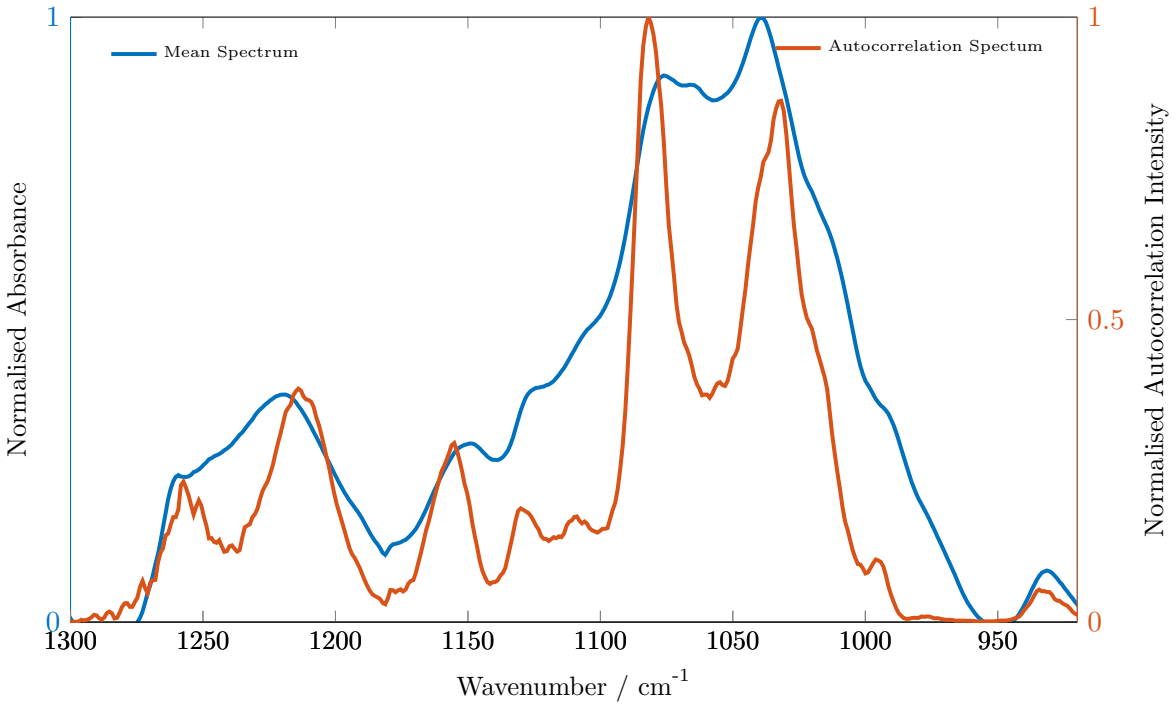

Figure 3.21: Autocorrelation Spectrum calculated from FTIR data of λ-carrageenan, cooled from 80 to 10 °C

a classical resolution enhancement, similar to something that might be observed when performing Fourier Self-Deconvolution.[128] This can be attributed to the lack of gelation of λ-carrageenan, no structural changes are occurring from 80 to 10 °C, as highlighted in Section 3.2 where the λ-carrageenan spectra were seen to increase absorbance across all wavenumbers as cooled.

With κ-carrageenan and ι-carrageenan a conformation change was observed, the autocorrelation function can be used to study regions of the spectra that are most susceptible to intensity changes, highlighting bands responsible for the gelation transition of the carrageenans. The λ-carrageenan system also demonstrates the usefulness of an autocorrelation spectrum to sharpen bands, providing a resolution enhancement with systems that are perturbed, assuming an intensity change.

3.2.4.2 κ-carrageenan

The full synchronous and asynchronous correlation maps can also be analysed in an attempt to understand whether the change of intensities of different bands as the sample undergoes gelation occur in phase or out of phase with each other. Figures 3.22 and 3.23 show the synchronous and asynchronous 2DCOS filled contour maps for κ-carrageenan, as the sample is cooled from 80 to 10 °C. Data passed into the 2DCOS algorithm was separated by 0.05 °C, the figures show dark blue to white for values from the most negative to 0, and white to dark red for datapoint values from 0 to the most positive within the map.

The synchronous map, Figure 3.22, from the majority red peaks, indicates that most of the spectral intensity changes within the κ-carrageenan gelation change in the same direction, this can be seen by the increased absorbance across the spectral range within Figure 3.5. Although some areas do indicate a different direction of change, the wavenumbers at which this is seen relate to positions between spectral features, such as 1145 cm^{-1}, directly between the two C-O-C backbone vibrations (1125 and 1170 cm^{-1}). This suggests that the difference in intensity changes

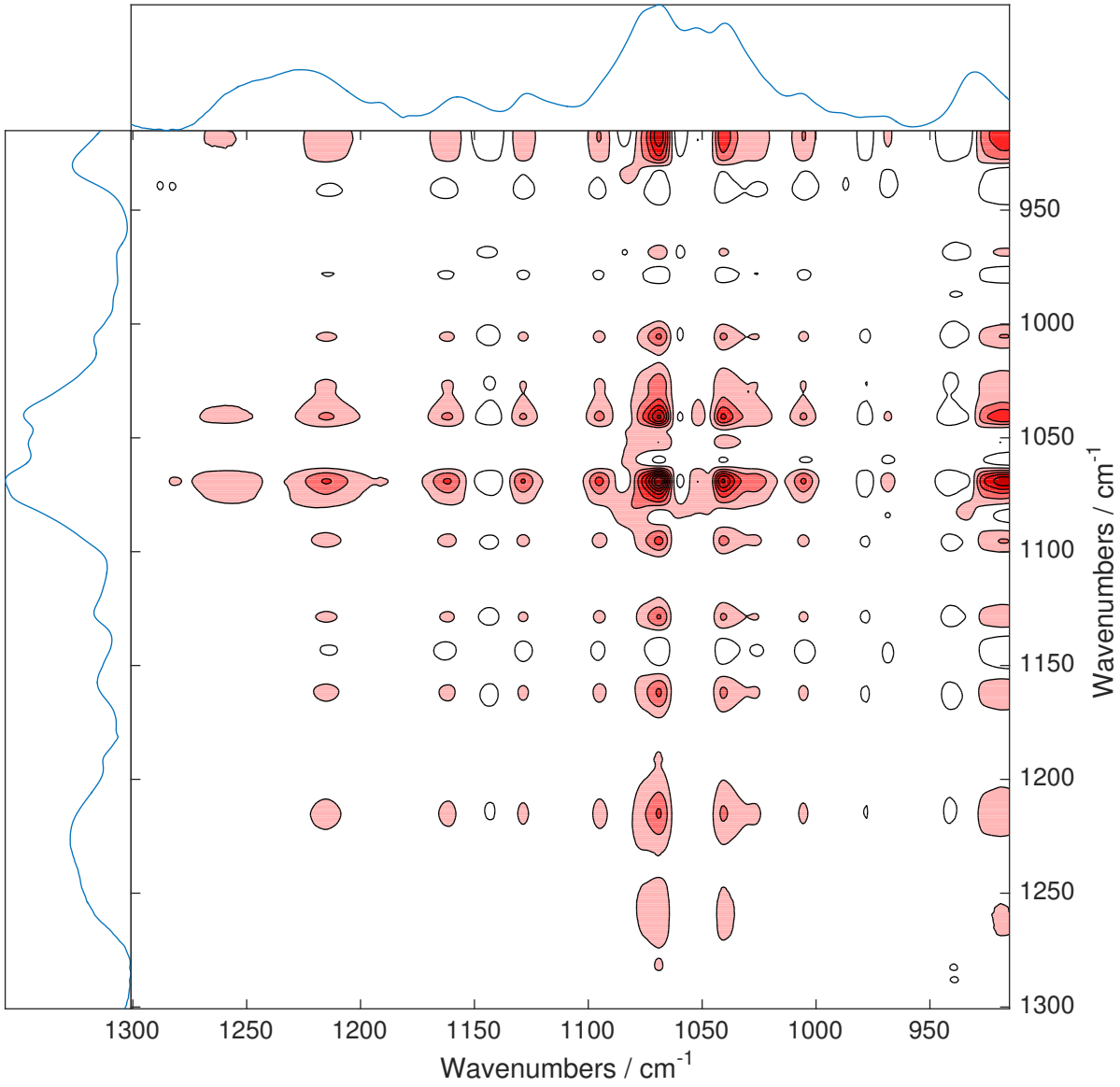

Figure 3.22: 2DCOS synchronous correlation map of κ-carrageenan, from 80 to 10 °C, colourmap: blue-white-red; negative-0-positive

compared with the rest of the spectra (especially considering the evidence from Figure 3.5), that this is either artificially introduced during the baseline procedures, or the sharpening of discrete bands either side of the features results in a decrease in absorbance.

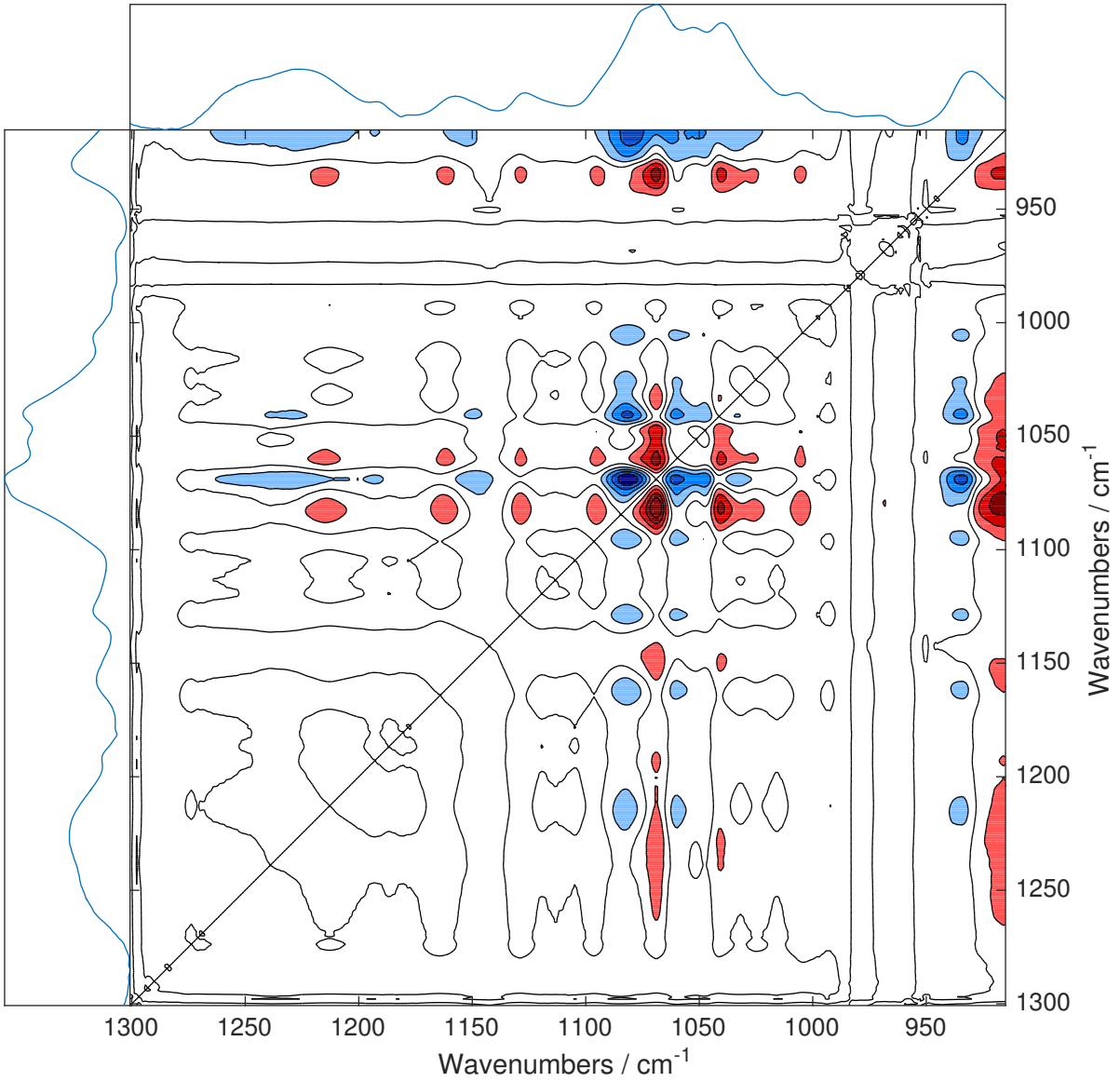

Figure 3.23: 2DCOS asynchronous correlation map of κ-carrageenan, from 80 to 10 °C, colourmap: blue-white-red; negative-0-positive

The asynchronous map, Figure 3.23, shows multiple negative and positive bands, indicating not only spectral changes that occur out of phase, but also that there is a predominant order

to their change. Noda's rules[17] allow interpretation of these changes. ν_1 at 1070 cm^{-1} (x-axis) shows a red positive band across almost all ν_2 (y axis) wavenumbers. The positive nature of the correlation map suggests that the intensity changes at 1070 cm^{-1} occur predominately before those of other wavenumbers. Fortunately, for this analysis, the majority of the synchronous map (Figure 3.22) is positive. However, Noda's rules state that if the sign of the the corresponding datapoint within the synchronous map is negative then the order rules (for ν_1 occurring before/after ν_2) are reversed.

Modified Noda's Rules allow a simplification of this rule reversal. If the datapoint under investigation has the same sign within the synchronous and asynchronous (i.e. $sign(syn)$ & $sign(asyn)$ is + or $sign(syn)$ & $sign(asyn)$ is −) then ν_1 changes before ν_2. For this reason further asynchronous plots (title as "modified Noda's rules") have been multiplied, point by point, by the sign of their corresponding synchronous map. This is explained in section 1.3.1. This means that a positive (red) area indicates ν_1 changing before ν_2 and negative (blue) areas show ν_2 before ν_1. Figure 3.24 shows the mathematical modified Noda's rules applied to the κ-carrageenan asynchronous map. As was mentioned previously, as there are few negative areas within κ-carrageenan's synchronous map, Noda's rules do not need inverting, therefore the modified asynchronous map, Figure 3.24, looks rather similar to the original map, Figure 3.23. As is also mentioned in section 1.3.1, to make interpretation of the modified asynchronous maps even simpler, instead of displaying the mean of the input data across the top and left axes, the autocorrelation spectrum (from Figures 3.19 to 3.21) is displayed, allowing comparison to spectral regions that undergo largest changes in intensity.

The 1070 cm^{-1} band of Figure 3.24 (of ν_1, x axis, along ν_2, the y axis) shows mostly positive red peaks, suggesting that the spectral feature at 1070 cm^{-1} changes predominately before that of other features. The inverse in true for the 1085 cm^{-1} band, with the analysis suggesting that it changes after most spectral features. Within Figure 3.19 it can be seen that the 1070 cm^{-1} feature has a shoulder to higher wavenumber; 1085 cm^{-1}. 2DCOS has long

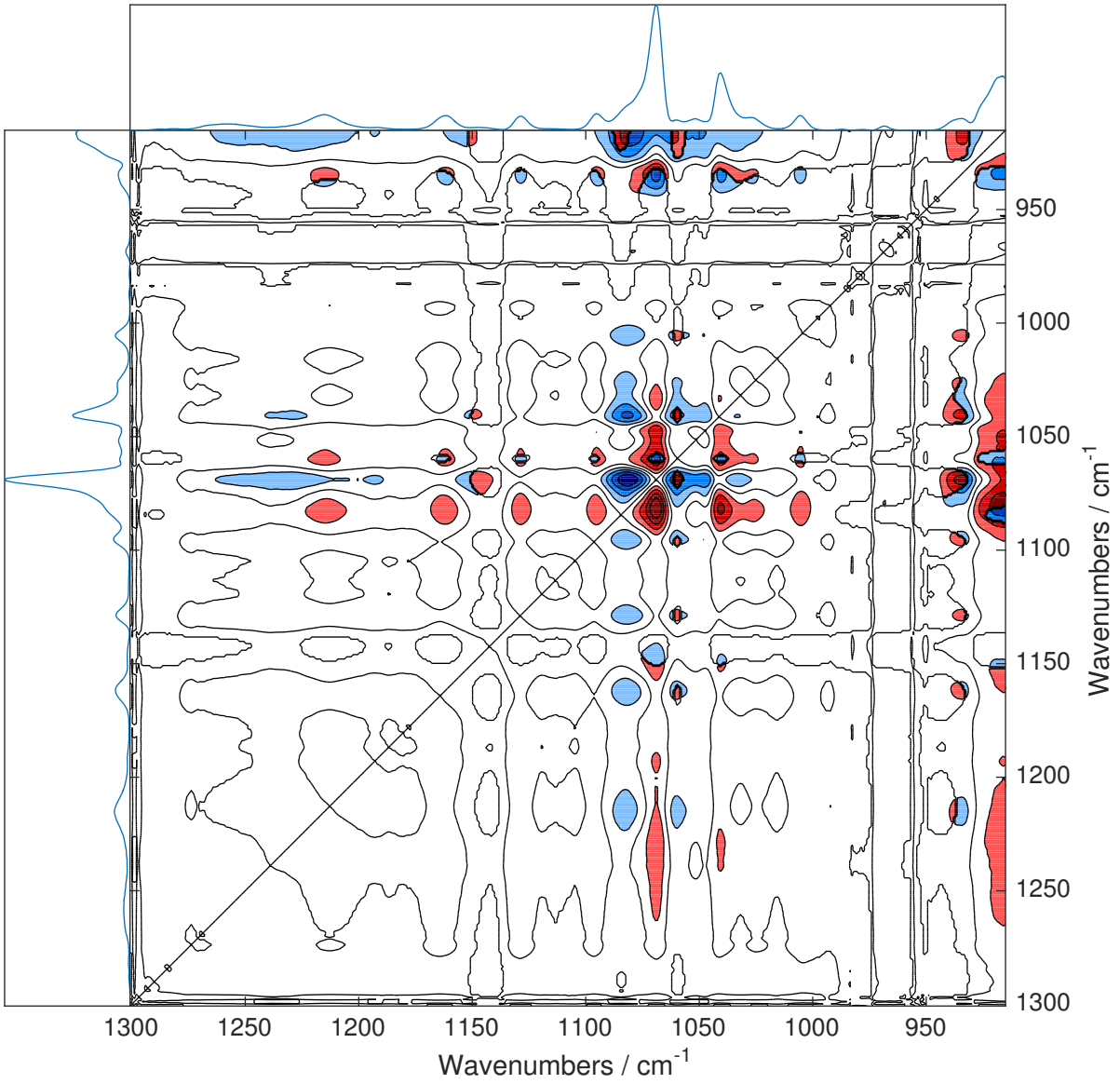

Figure 3.24: 2DCOS asynchronous (Modified Noda's rules) correlation map of κ-carrageenan, from 80 to 10 °C, colourmap: blue-white-red; negative-0-positive

been used to separate overlapping bands, especially when perturbation causes out of phase changes.[10] However as this region of the IR spectra is attributed to multiple C-O and C-OH modes of a complex bio-polymeric system, attempting to differentiate modes or assign meaning to this observation without further investigation is difficult. Other areas of the map that show strong positive or negative intensities are those below 925 cm^{-1}, although there are multiple absorbencies for carrageenan within this range, signal to noise ration rapidly drop off below *ca.* 925 cm^{-1} with the spectrometer in use.

3.2.4.3 ι-carrageenan

The synchronous spectrum of ι-carrageenan is shown in Figure 3.25, multiple positive and negative areas are present, suggesting that the spectral features of the gelation of ι-carrageenan change in different directions to one and another. The majority of the cross peaks are positive, changing the same direction 1220 to 1070, and 1030 to 995 cm^{-1}. The sulfate $\nu(SO_2)$ band (1235 cm^{-1}) changes in a different direction to the other spectral features as does a band at 1059 cm^{-1}, possibly a C-O or C-OH mode, however this could also be associated with an S=O stretch as it is on the lower side of the main C-O and C-OH vibrations. Towards the lower end of the wavenumber range displayed there are two negative areas, 975 and 930 cm^{-1} respectively. Although the latter is starting to get into a higher noise area, the band appears quite distinct within the synchronous map. This area of the spectrum is due to C-O-C and glycosidic linkage vibrations (table -1.1).

The modified Noda's rules, asynchronous spectrum is shown in Figure 3.26, with the autocorrelation spectrum displayed in the reference panels; top and left. Perhaps the most striking feature of this correlation map are the large blue/red bands at *ca.* 1250 cm^{-1}, it can be seen (from the autocorrelation reference spectrum) however, that these out of phase changes are due to bands that are not that particularly susceptible to spectral intensity variations. The 1259 cm^{-1} band is seen to change before almost every other spectral feature, interestingly this was

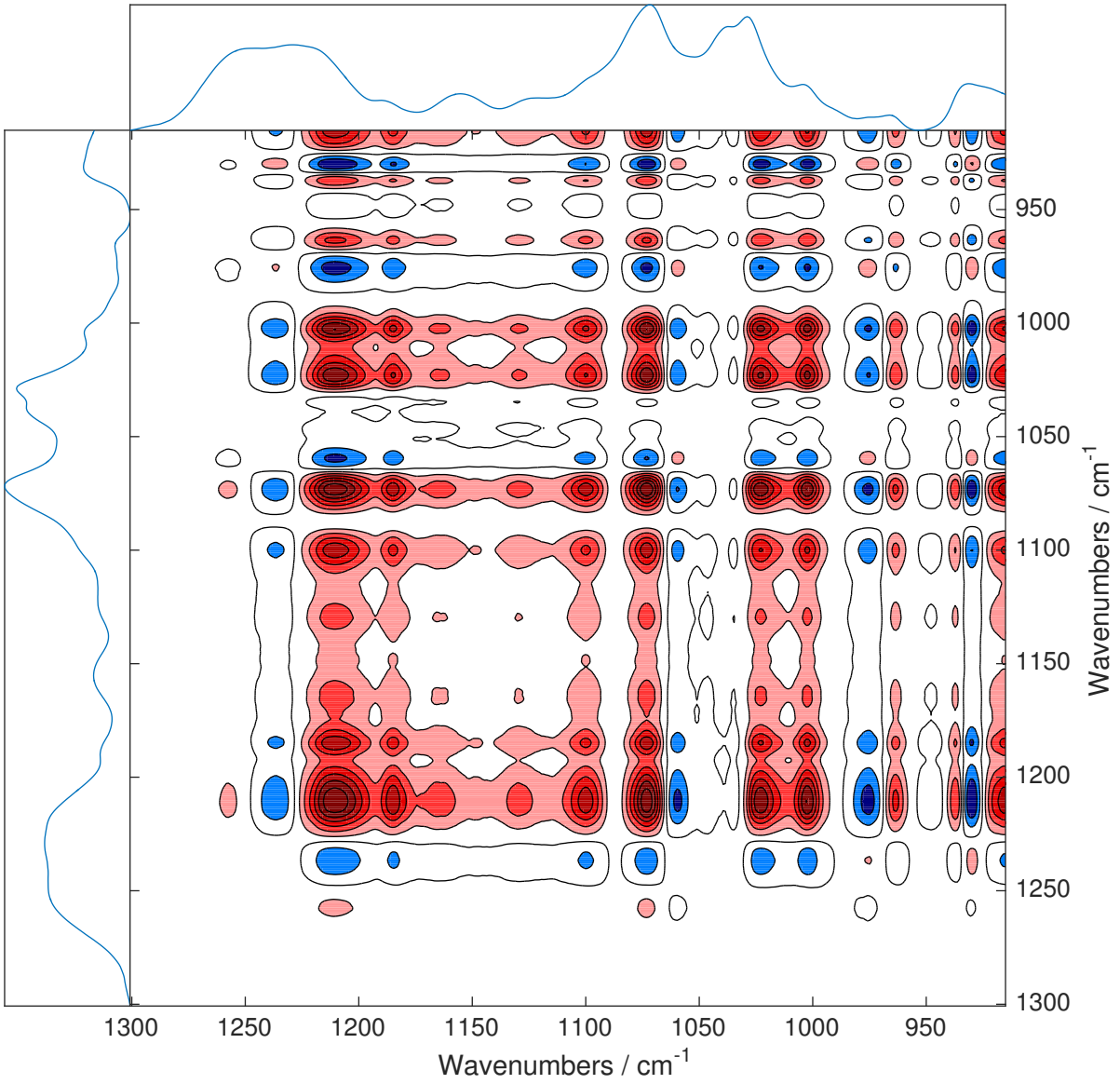

Figure 3.25: 2DCOS synchronous correlation map of ι-carrageenan, from 80 to 10 °C, colourmap: blue-white-red; negative-0-positive

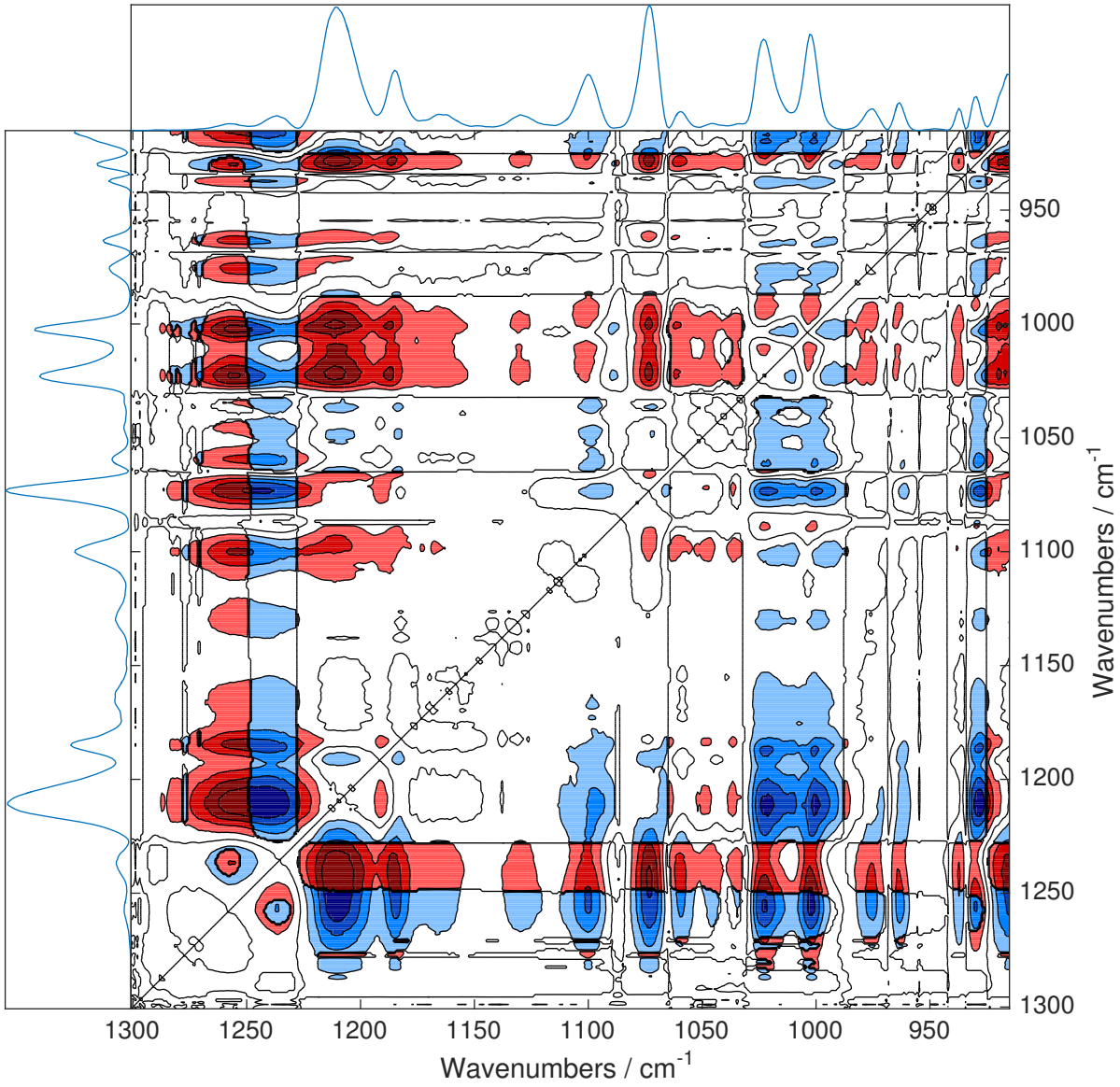

Figure 3.26: 2DCOS asynchronous (Modified Noda's rules) correlation map of ι-carrageenan, from 80 to 10 °C, colourmap: blue-white-red; negative-0-positive

also the band that was identified as changing in a different direction to the majority of the spectrum within the synchronous spectrum. A band to slightly lower wavenumber, 1238 cm^{-1}, still associated with a ν(S=O) band changes predominately after every other spectral feature. The clear separation of two bands that are associated with similar vibrations suggest at least two separate interactions that cause these spectral features to change. The intensity of the asynchronous cross-peaks is relatively large, even thought the variation at these wavenumbers is small, suggesting a large out of phase nature. It is know that gelation of ι-carrageenan proceeds via a multistep route; sol-coil-helix-gel.[129] The sulfate group protrudes from the polymer backbone and play a crucial role in the ordering of the system, to produce coil and helix based arrangements, as a precursor to the helices aggregating together resulting in gel formation. The sulfate based interactions, and therefore the vibrational nature of the S=O bands are expected to change during different stages of the gelation. 2DCOS could be locking in to this change.

The two bands associated with ν(S=O), between 1025 and 1000 cm^{-1}, also change predominately after most other spectral features, apart from the 1238 cm^{-1} S=O band, where they change before. Apart from strong asynchronous correlation of these two S=O bands (between 1025 and 1000 cm^{-1}) with sulfate based features in the higher wavenumber range (1190 - 1260 cm^{-1}), there is also significant correlation with the C-O / C-OH mode at 1074 cm^{-1}, with the S=O bands again changing after.

3.2.4.4 λ-carrageenan

λ-carrageenan, with the synchronous and asynchronous spectra shown in Figures - 3.27 and 3.28 respectively shows less interesting features than those observed for κ- or ι-carrageenan. The synchronous spectrum is entirely positive, as expected for a steady increase in overall spectral intensity that was observed (Figure 3.5).

The asynchronous spectrum (modified Noda's rules), Figure 3.28, shows large features with

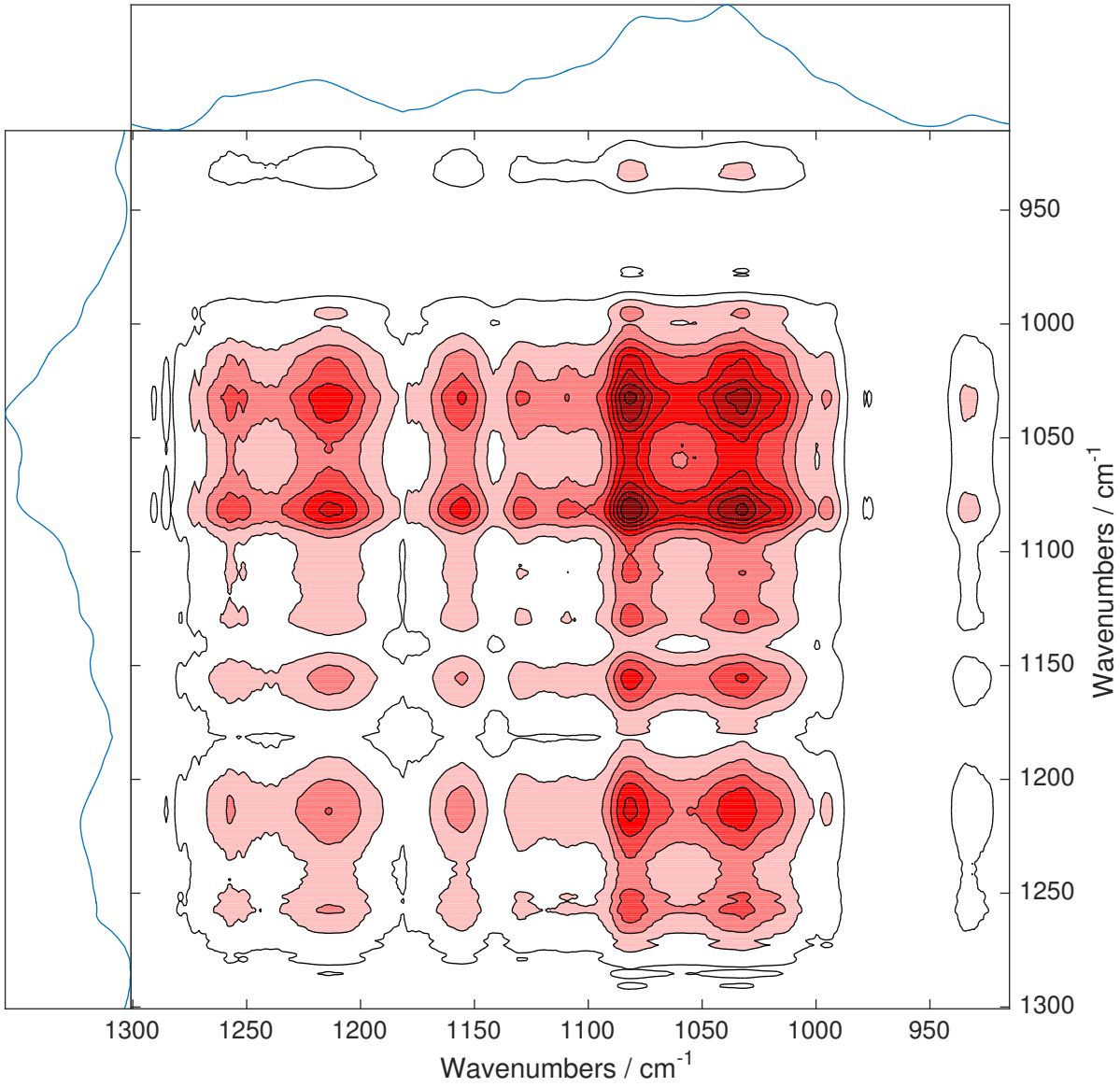

Figure 3.27: 2DCOS synchronous correlation map of λ-carrageenan, from 80 to 10 °C, colourmap: blue-white-red; negative-0-positive

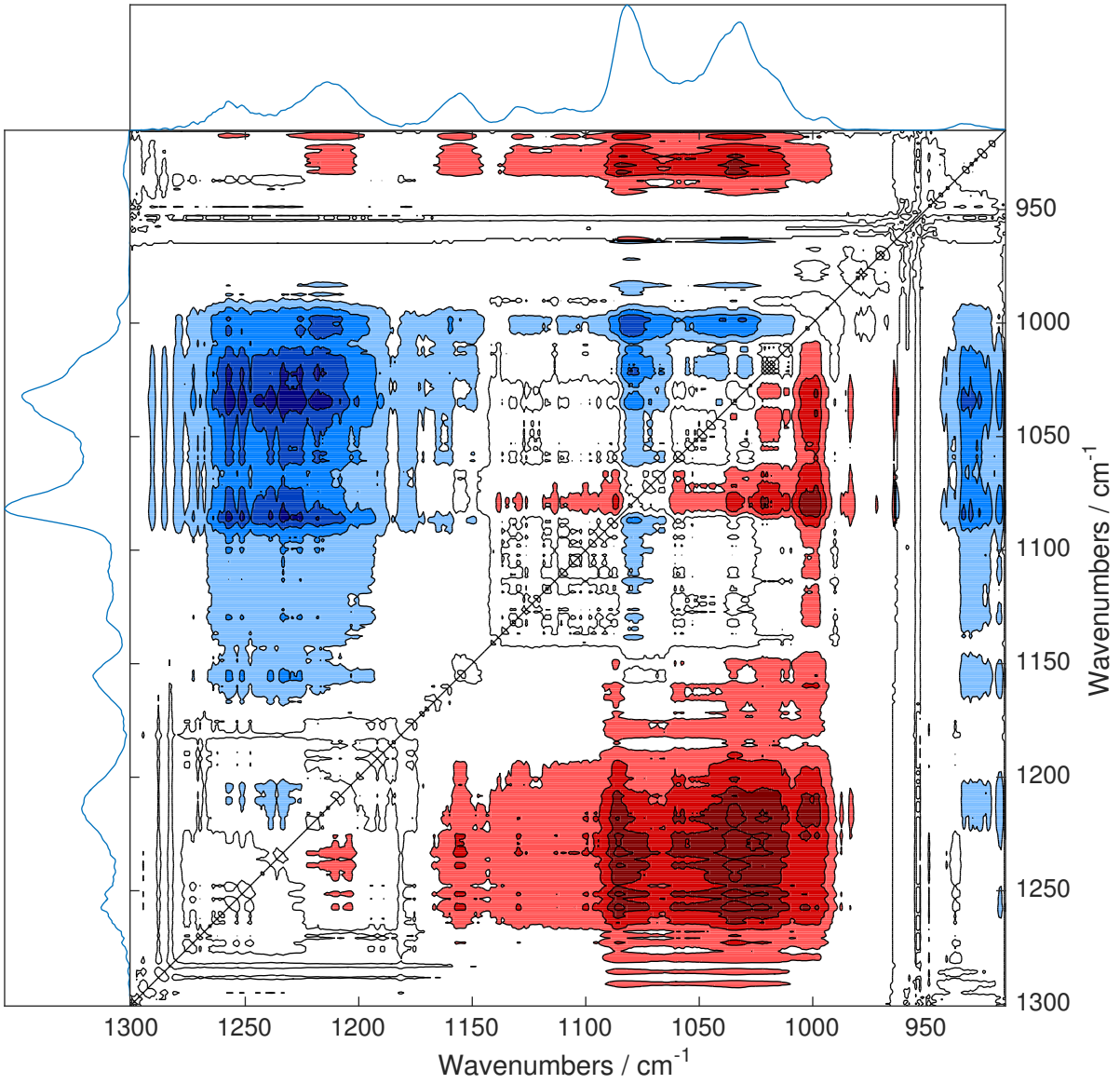

Figure 3.28: 2DCOS asynchronous (Modified Noda's rules) correlation map of λ-carrageenan, from 80 to 10 °C, colourmap: blue-white-red; negative-0-positive

little asynchronicity observed. The out of phase changes are observed between the main spectral bulk, 1250 - 950 cm^{-1} and the high noise area below 950 cm^{-1}, suggesting that 2DCOS is locking onto an artefact. However, there is an asynchronous change of the C-O / C-OH band at 1078 cm^{-1} with respect to the rest of the fingerprint region. This feature was also observed with κ- and ι-carrageenan. This band is perhaps the most intense spectral feature that directly relates to the skeletal structure of the carrageenans. Even though λ-carrageenan does not gel, there is some possible reordering occurring as the solution cools and thickens. The observed difference in rate between most other spectral features and the most intense C-O / C-OH modes could point to an "action - reaction" interaction, whereby the skeletal conformation of the biopolymer changes after interactions with protruding species, such as the sulfate groups. If this were entirely true however, we would expect to see bands associated with the glycosidic linkages changing out of phase with the sulfate bands, which is not observed, even when a higher resolution contour plot and zooming features are implemented.

3.2.5 Moving Window Two-Dimensional Correlation Analysis

Moving window two-dimensional correlation analysis (MW2D, section 1.3.4) was carried out utilising the autocorrelation function, with a window size of *ca.* 10 °C (200 spectra) for cooling experiments of the κ, ι, and λ-carrageenan systems. This analysis will identify not only regions of the spectra that are most susceptible to spectral intensity variations (*i.e.* the autocorrelation spectra), but will also indicate the temperature at which these spectral intensity variations occur.

The output of the analyses is displayed in the same manor as the 2DCOS spectra, a contour map with a blue-white-red colour scheme and reference panels to the top and left. Along the y-axis the wavenumbers are displayed, with autocorrelation spectrum of the 2DCOS analysis in the left panel. The x-axis shows the temperature, with the top panel showing the sum of the autocorrelation along the wavenumber axis. Simply put, at each temperature, t along the x-axis, the autocorrelation spectrum has been calculated for the sub-dataset of $t-5$ to $t+5$ °C, and displayed in a contour format.

3.2.5.1 κ-carrageenan

Figure 3.29 shows the MW2D autocorrelation for κ-carrageenan as the system cools from 80 to 10 °C and undergoes gelation. It is immediately obvious that the majority of spectral intensity variations occur at 30 °C (the same temperature that was previously identified by PCA and MCR), *i.e.* the gelation transition midpoint as monitored by FTIR. The spectral regions showing the most variation at this temperature are fairly similar to those identified during the 2DCOS analysis, however the band at 1082 cm^{-1} was only apparent as a shoulder when the autocorrelation spectrum was calculated for the entire temperature range. By calculating the autocorrelation spectra for just the 35 to 25 °C region of the transition, the analysis will be locking on to only spectral variation occurring within this temperature range.

Figure 3.30 shows the comparison of the autocorrelation spectrum for the entire temperature

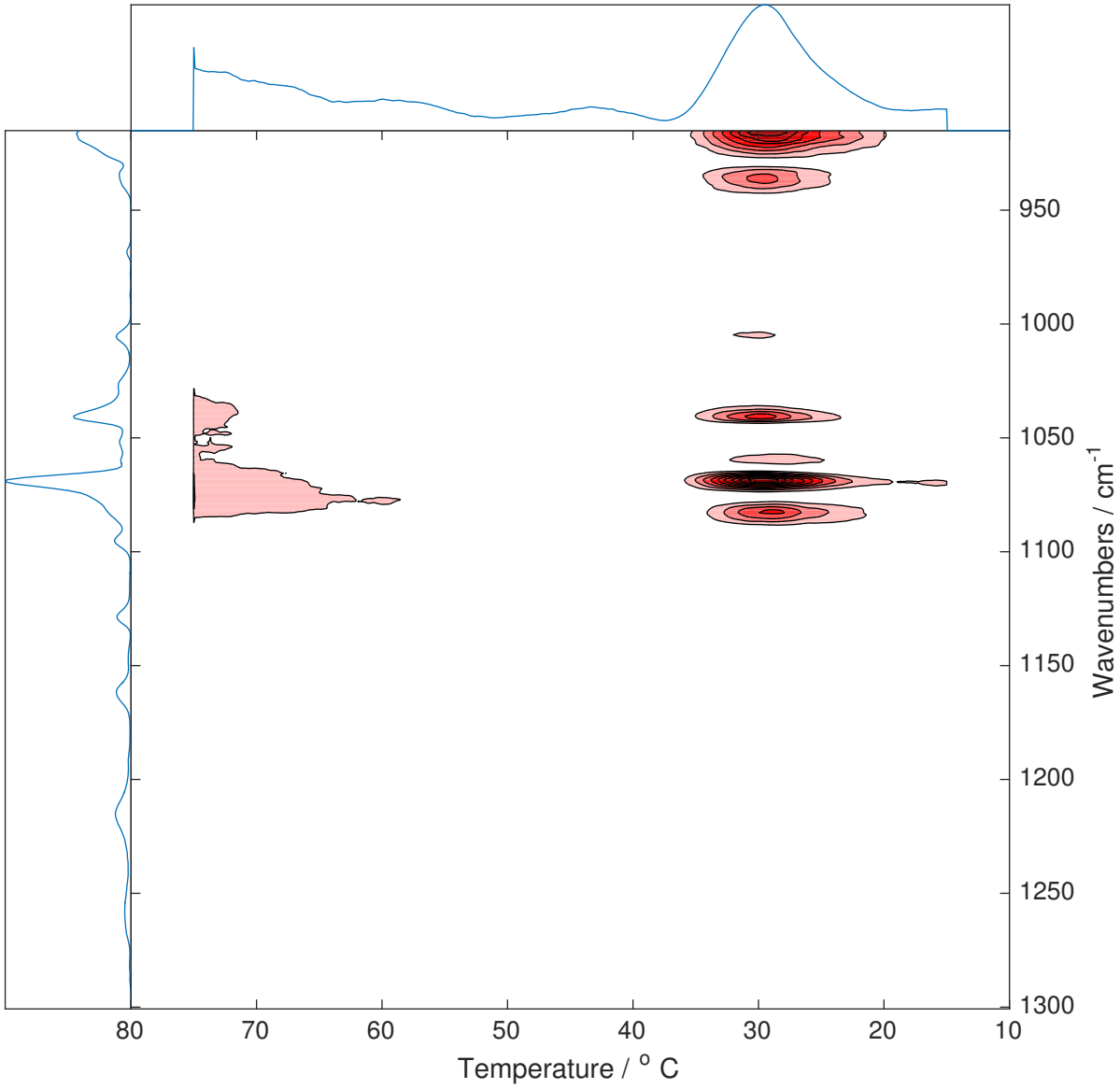

Figure 3.29: MW2D correlation map of κ-carrageenan, from 80 to 10 °C, window-size: 10 °C, colourmap: blue-white-red; negative-0-positive

range (same as Figure 3.19) with the autocorrelation of the spectra between the temperatures of 35 and 25 °C. As it can be seen, the band at 1084 cm^{-1}, is much sharper for the 35 to 25 °C spectrum. The band to slightly higher wavenumber, 1092 cm^{-1}, is an S-O (previously deconvoluted from a shoulder in the raw spectra: Figure 3.19) and to lower wavenumber is a C-O / C-OH combination mode. The sulfate bands between 1200 and 1270 cm^{-1}show little spectral intensity variation during the gelation transition, compared to their variation across the entire temperature range. There are also emphasised features at 1145 cm^{-1}, most probably a C-O-C, skeletal vibration and at 1059 cm^{-1}, within C-O and C-OH mode assignments.

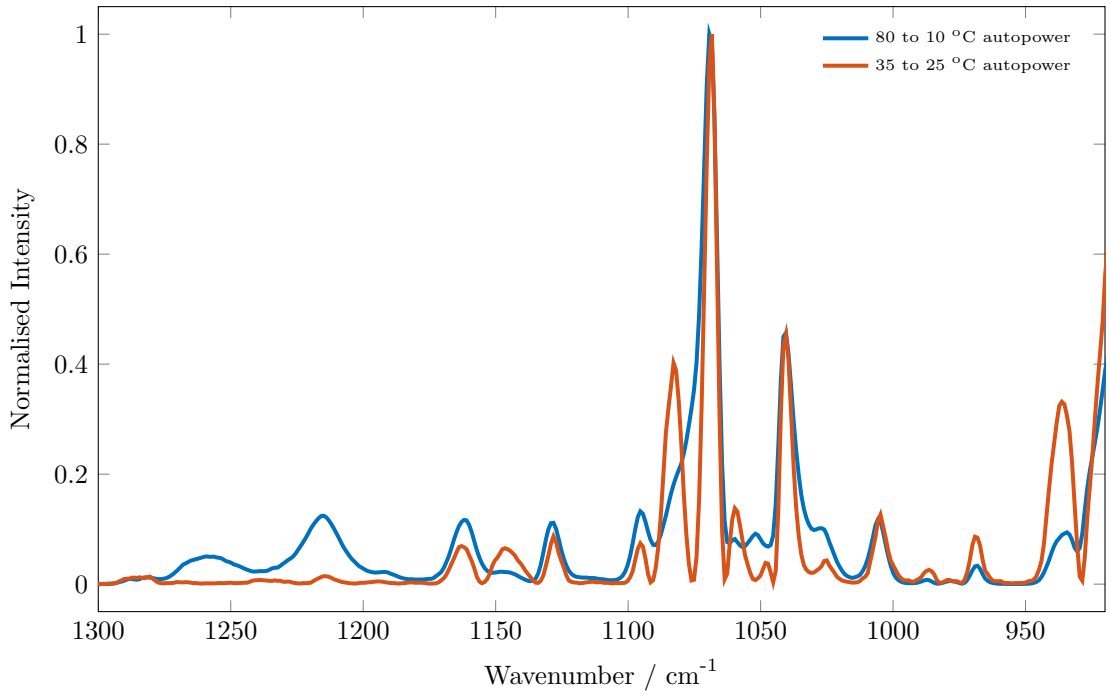

Figure 3.30: autocorrelation Spectrum comparison for κ-carrageenan, from 80 to 10 °C (orange) and from 35 to 25 °C (blue) normalised

The comparative increase of spectral intensity variation for backbone vibrations compared to sulfate based modes suggests that during the mid point of the gelation transition, reordering of the polymer backbone is seen to be more prevalent that the sulfate based interaction responsible for the conformational change. Figure 3.31 shows the autocorrelation spectrum extracted from

the 40 °C sub-dataset, *i.e.* 45 to 35 °C. There is a large increase of intensity of the sulfate bands at 1200 to 1270 cm^{-1}, as well as 1010 to 1050 cm^{-1}, ν(S=O). During the 2DCOS analysis, out of phase changes for the sulfate and C-O / C-OH modes were observed. Breaking the dataset into subsections using the MW2D methodology has allowed observation of the changes of spectral intensities as the sample is cooled. As κ-carrageenan is cooled, the most intense spectral variation occurs at *ca.* 30 °C, with the autocorrelation spectra showing enhanced skeletal modes. Preceding this change by 10 °C, the autocorrelation spectrum shows enhancement of sulfate based vibrations, suggesting that the conformational change of the biopolymer backbone occurs after interaction with sulfate bands.

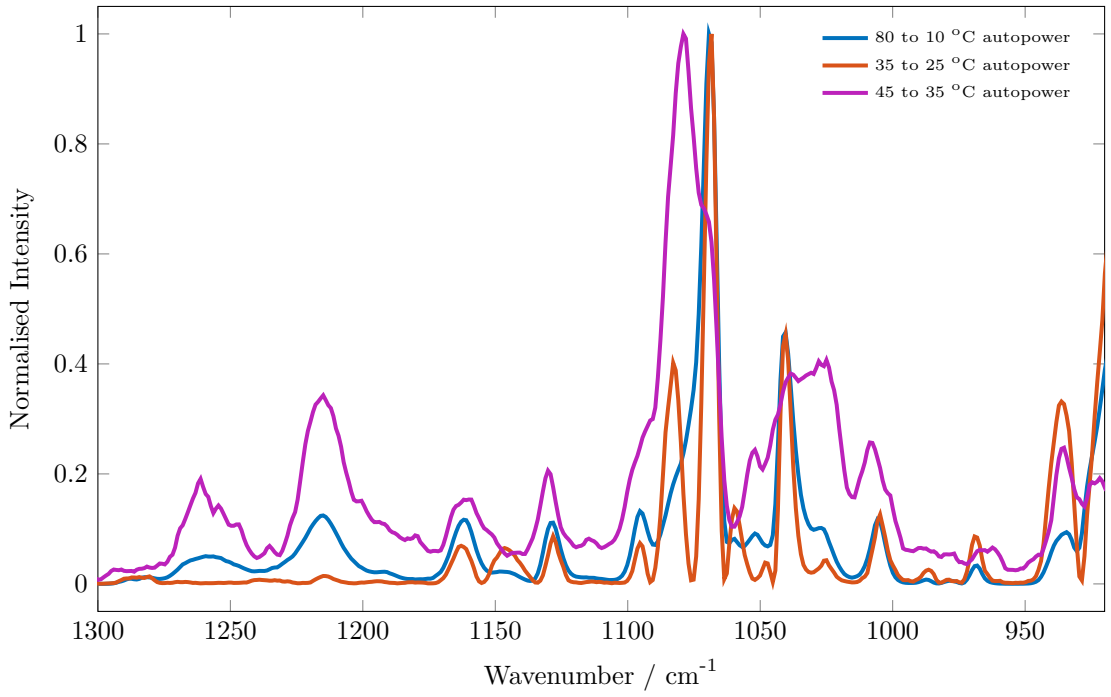

Figure 3.31: autocorrelation Spectra comparison of κ-carrageenan, from 80 to 10 °C (blue), from 35 to 25 °C (orange), and from 45 to 35 °C (purple), normalised

To aid in the visualisation of these temperature dependant changes in the susceptibility of spectral intensity variations, one can employ many methods to pre- and post-treat the data of MW2D spectra. For Figure 3.29 the spectral intensity variations around 30 °C were so intense

that other information had to be manually extracted, *i.e.* Figures 3.30 and 3.31. To reduce the overwhelming intensity of the bands at 30 °C, Figure 3.32 displays the same MW2D data of κ-carrageenan, however each data point has been divided by the square root of its value. This reduces the intensity of large features, however overuse can be impractical, as in effect, the method exaggerates features of less importance.

Within Figure 3.32, sulfate features, 1200 to 1270 cm^{-1}, can now be more easily visualised just before the main spectral changes; *ca.* 42 °C. This is also demonstrated within Figure 3.31, by selecting autocorrelation spectra from within a specific temperature range. The 45 to 35 °C autocorrelation spectrum of Figure 3.31 shows increased intensity of two sulfate based bands between 1200 and 1270 cm^{-1}, in comparison to the backbone modes at 1050 to 1100 cm^{-1}. There is also a broad band at 1025 cm^{-1} that has increased in relative intensity. There are both S=O and C-O modes in this region, due to the increase of intensity of the sulfate bands between 1200 and 1270 cm^{-1} however, this is more likely a sulfate based vibration that is showing susceptibility to the gelation.

The observed progression of vibrational bands as the sample undergoes cooling; sulfate bands, then C-O / backbone bands, follows the literature shown gelation transition of carrageenan gels. Coils of the biopolymers form helical structures before aggregating together laterally and forming rods, which are responsible for the formation of the gel. The formation of helical structures is heavily dependant on cation valency and concentration.[63,80,130] This transition has been shown to involve the sulfate groups due to the change in gel strength with regards to the number (and position) of sulfate groups per repeating unit, and cation valency and concentration.[65,92,101] This staggered structural change suggests conformational change of the backbone following polymer strands forming helices.

Both carrageenan helices and superhelical aggregates (rods) have been previously imaged by atomic force microscopy,[77 79] with the rod formations appearing linear. The lateral aggregation

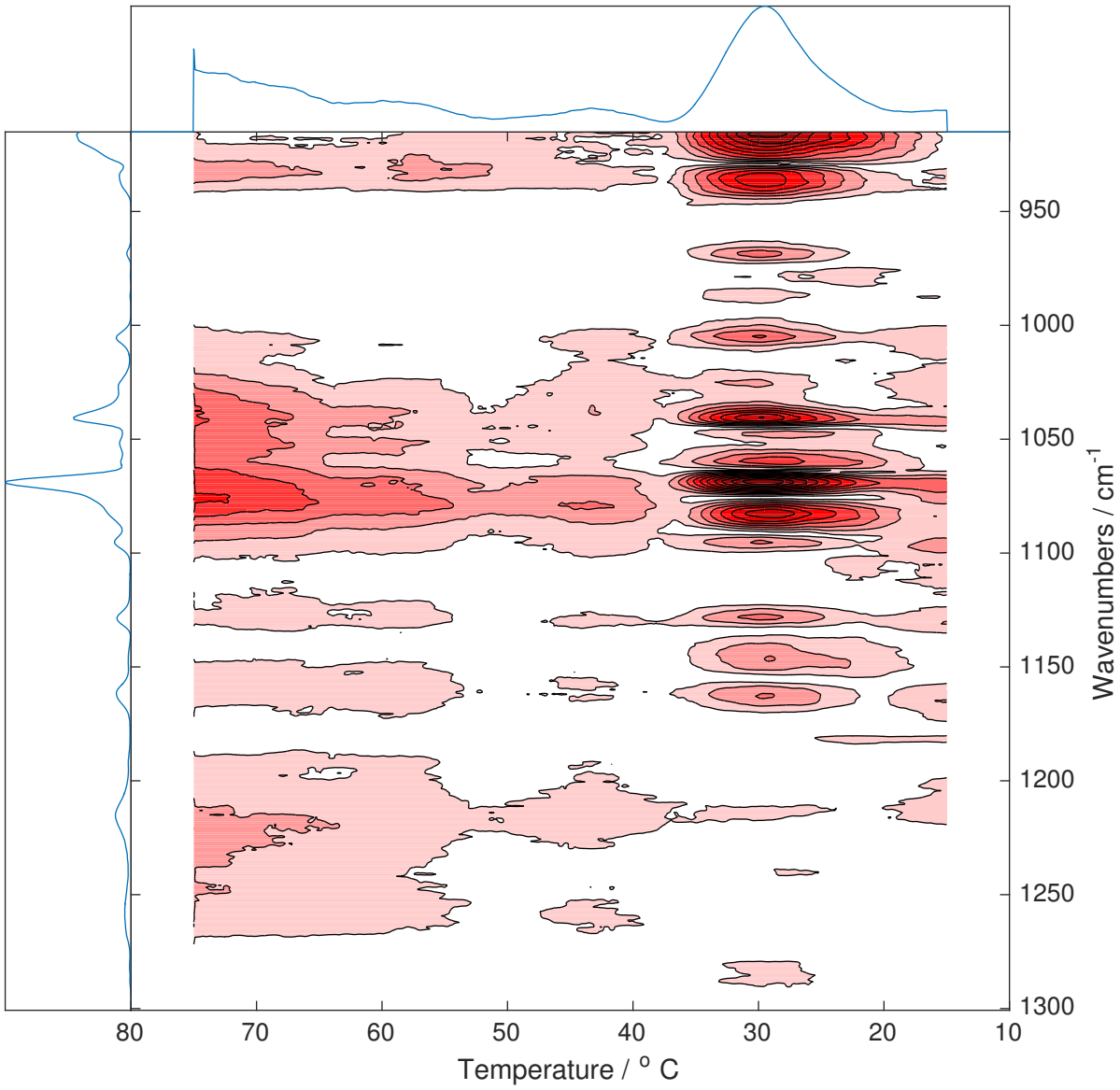

Figure 3.32: MW2D correlation map of κ-carrageenan, from 80 to 10 °C, window-size: 10 °C, normalised to $\sqrt{(data)}$, colourmap: blue-white-red; negative-0-positive

of the helices to form the rods restricts the conformational degrees of freedom within the sample. Spectroscopically, the reduced degrees of freedom will result in a narrowing of vibrational features due to the backbone structure; seen in the orange trace of Figure 3.31.

3.2.5.2 *ι*-carrageenan

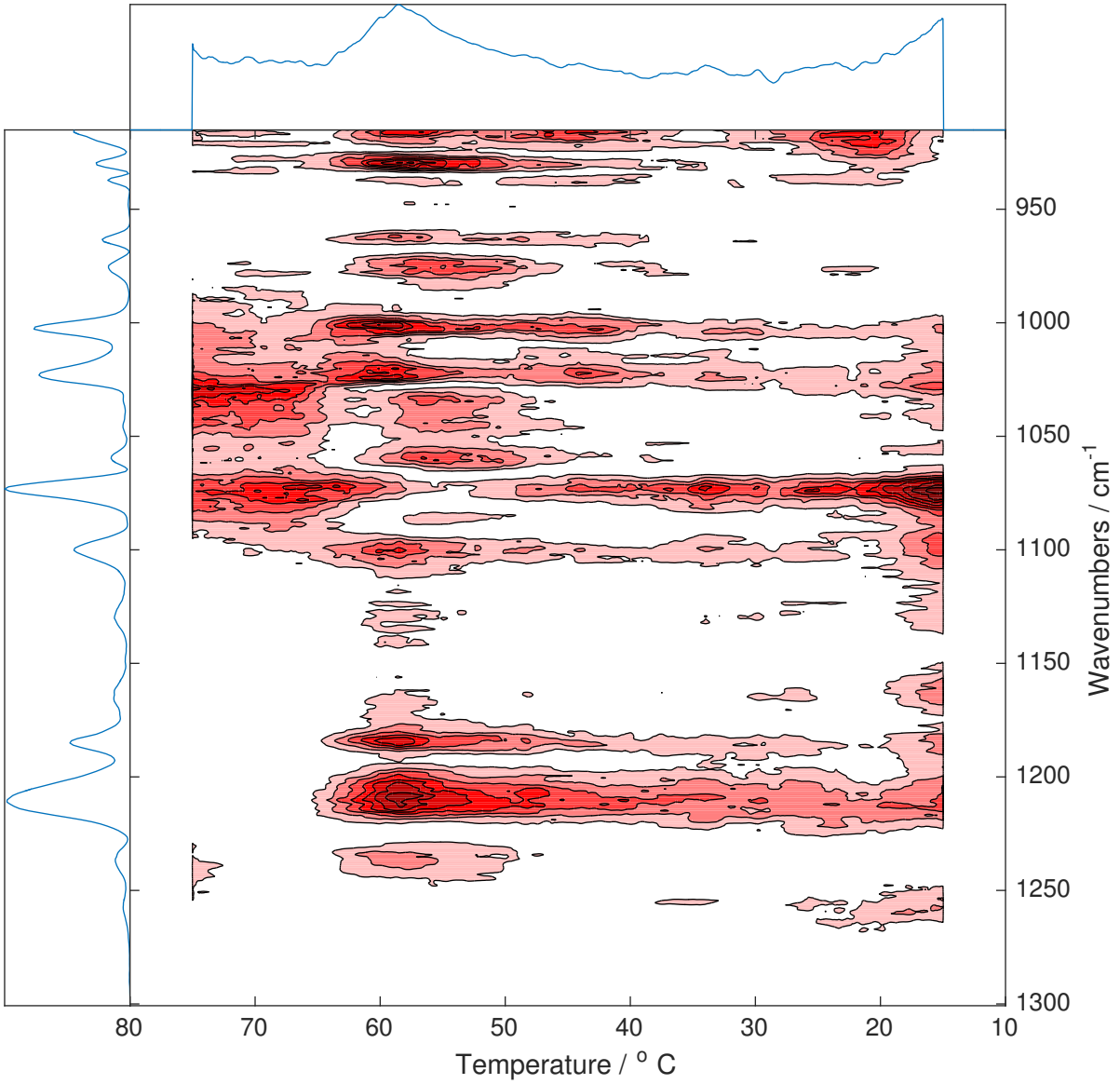

Figure 3.33: MW2D correlation map of *ι*-carrageenan, from 80 to 10 °C, window-size: 10 °C, colourmap: blue-white-red; negative-0-positive

Figure 3.33 shows the moving window 2D correlation utilising the autocorrelation spectrum for ι-carrageenan from 80 to 10 °C. As with the κ-carrageenan sample, spectral features can be seen to change within distinct temperature ranges, most notably the changes around 58 °C. This temperature was also seen within PCA and MCR studies (see Figure 3.15), indicating the gelation transition. In an attempt to observe the preceding formation of helical structures that perturb the sulfate vibration modes, as seen for κ-carrageenan, Figure 3.34 shows the autocorrelation spectra for the entire temperature range (80 - 10 °C) and for 80 - 70 °C. There are indeed increased intensities for (most-likely) sulfate based vibrations; 1200 - 1270 cm^{-1} and 1030 cm^{-1}, however these are much less prevalent that the autocorrelation spectra of temperatures above the gelation transition for κ-carrageenan. It is to be expected than κ- and ι-carrageenan show similar structural changes occurring during gelation due to the similarity of their gelation transition.[89]

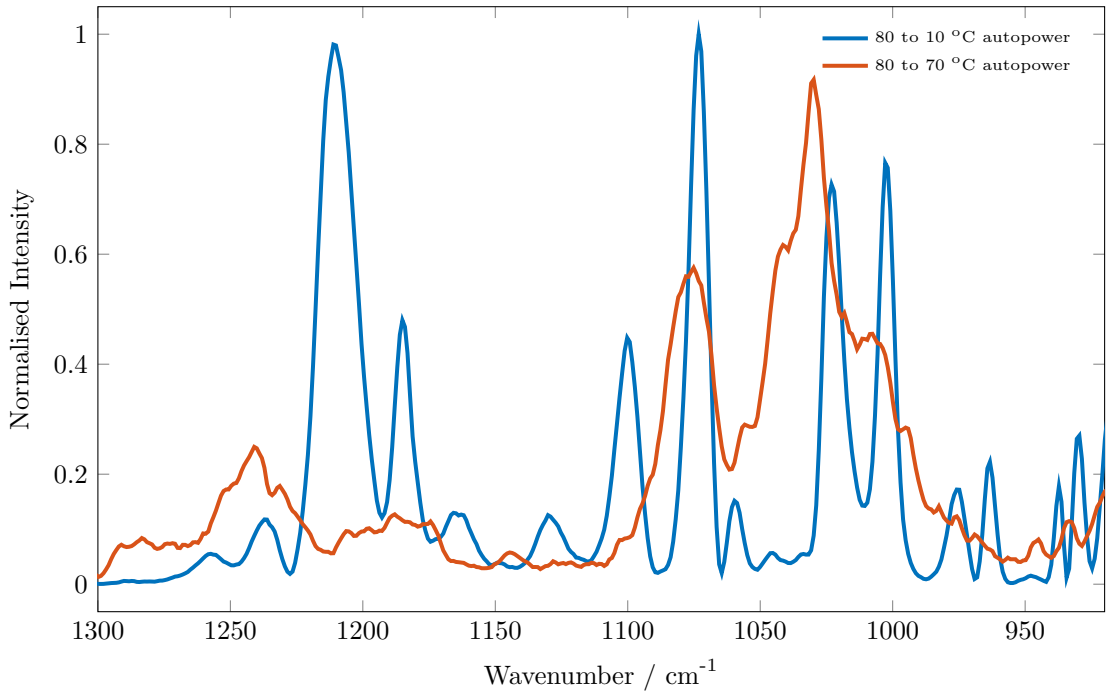

Figure 3.34: autocorrelation Spectra comparison of ι-carrageenan, from 80 to 10 °C (blue), from 80 to 70 °C (orange), normalised

Both κ- and ι-carrageenan gelation studies showed evidence of multiple structural changes occurring during gelation; the formation of helical structures before lateral aggregation. λ-carrageenan does not gel (except in rare cases of trivalent cations[32]), although a thickening of the solution at lower temperatures has been reported and this was also seen during the experiments.[24]

3.2.5.3 λ-carrageenan

Figure 3.35 shows the MW2D correlation map for λ-carrageenan as the sample is cooled from 80 to 10 °C. In immediate contrast to both the κ- and ι-carrageenan MW2D maps (Figures 3.29 and 3.33 respectively) there appears to be little change of intensity between different wavenumbers as a function of temperature. Figure 3.36 shows selected autocorrelation spectra from the entire temperature range; 80 to 10 °C, higher temperature and lower temperature autocorrelation spectra; 80 to 70 °C, and 20 to 10 °C, respectively. There are slight changes between the broadness of bands and distinct signal-to-noise level differences, however unlike the autocorrelation spectra comparisons of κ- and ι-carrageenan the relative intensities of bands do not change. This indicates that at different temperatures there are no differences spectral differences in susceptibility to temperature change.

Figure 3.21 compares the autocorrelation spectrum (80 to 10 °C) with the mean spectrum of λ-carrageenan during the temperature range and as also highlighted during the raw spectra of λ-carrageenan (Figure 3.7), the spectra only appears to increase intensity linearly across all wavenumbers as the sample was cooled. All spectral analysis of the λ-carrageenan system suggested that there are no structural changes occurring as a function of temperature, spectroscopically at least. The difference in noise levels between the high and low temperature autocorrelation spectra of Figure 3.36 suggest that the change in absorbance is not linear over the temperature range however. MCR and PCA also hinted at this by showing score plots that changed non-linearly over temperature. Infrared spectroscopy cannot necessarily identify a change in viscosity, although some band narrowing may be observable in certain systems due to

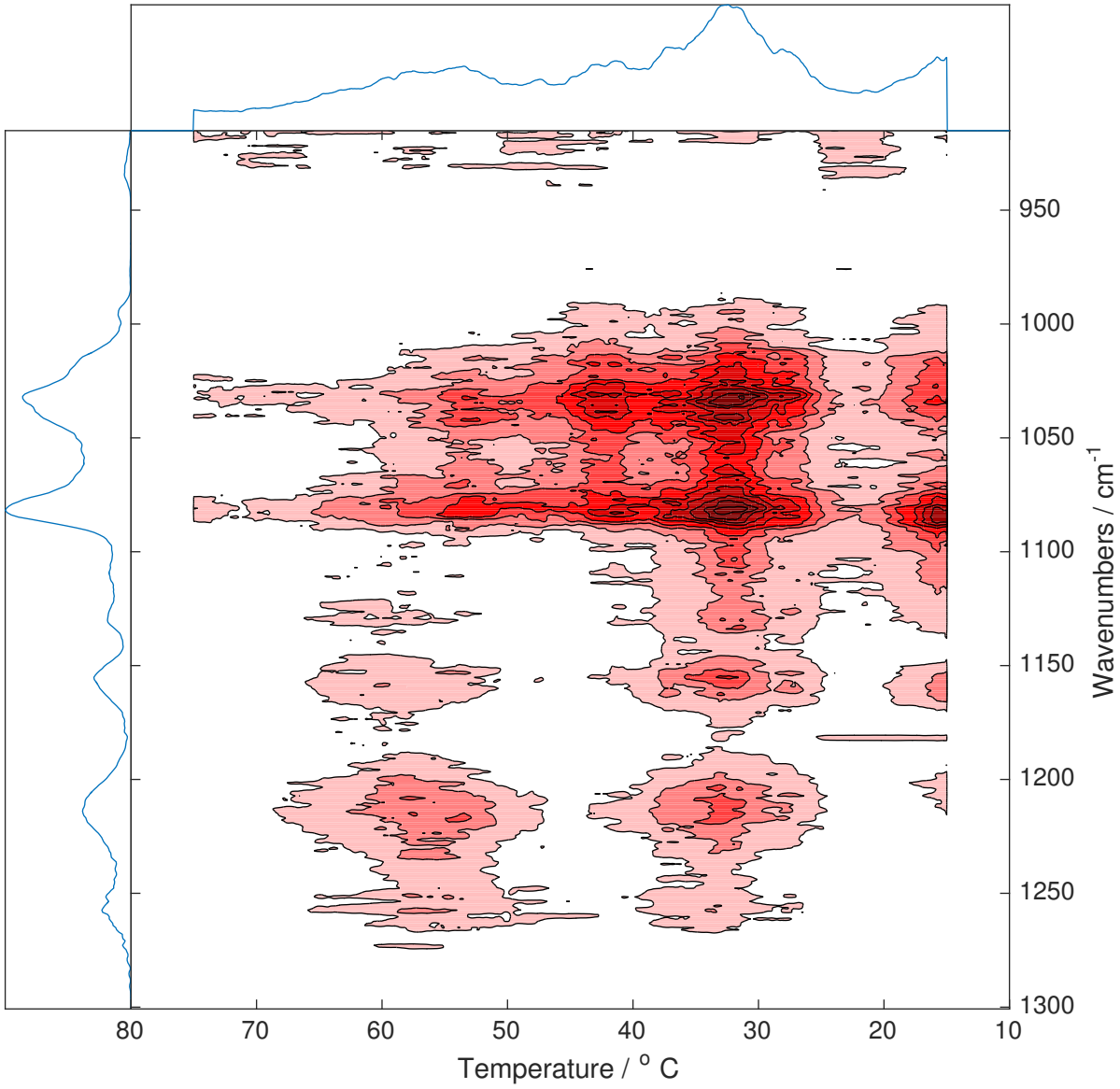

Figure 3.35: MW2D correlation map of λ-carrageenan, from 80 to 10 °C, window-size: 10 °C, colourmap: blue-white-red; negative-0-positive

a restriction in molecular movement as the viscosity is increased. This is especially more difficult considering the system under investigation is a complex biopolymer with physical characteristics occurring at specific temperatures (such as gelling). As the change observed is very similar to the original absorbance spectra it is perhaps most easily explained by an increase in the quantity of molecules sampled; whether that be a change in the penetration depth due to a change in sample refractive index, or an increase in sample density as it is cooled.

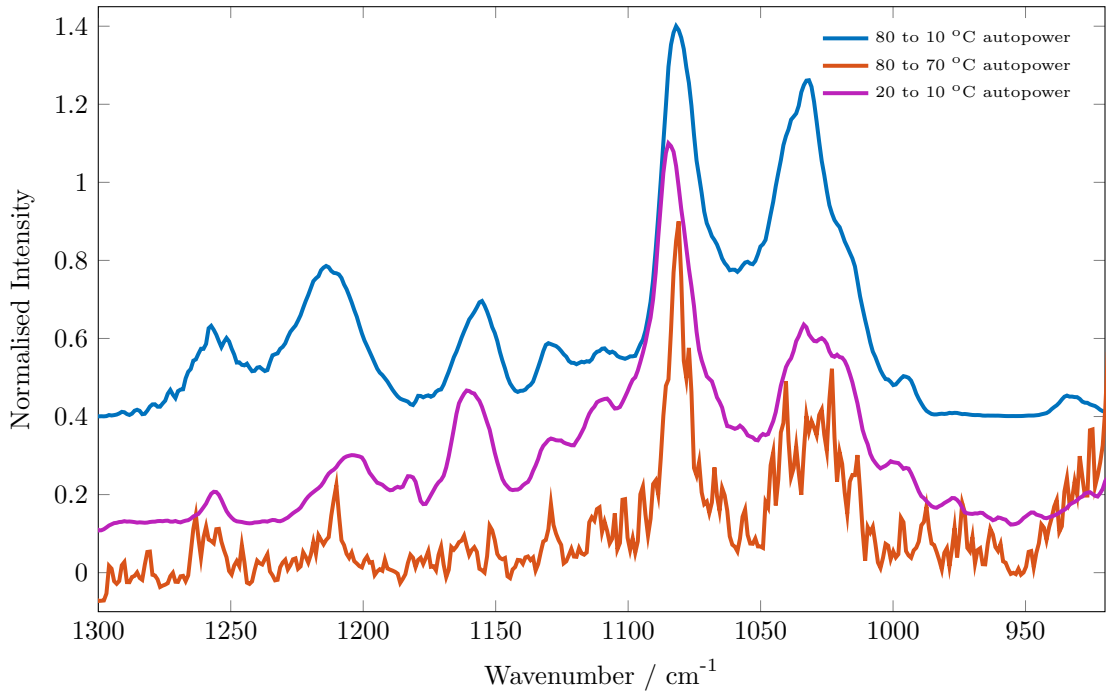

Figure 3.36: autocorrelation Spectra comparison of λ-carrageenan, from 80 to 10 °C (blue), from 80 to 70 °C (orange), and from 20 to 10 °C (purple) normalised and offset for clarity

Moving Window 2D Correlation Spectroscopy allows initial investigation into these features, however it's interpretation can be difficult due to their complex nature and often comparing autocorrelation spectra from perturbation zones of interest is needed.

3.2.6 Perturbation Correlation Moving Window Two-Dimensional Correlation Spectroscopy

Perturbation correlation moving window two-dimensional correlation spectroscopy (PCMW2D) is explained in section 1.3.5, it allows monitoring of complex spectral variation along the perturbation axis. As previously explained this technique is similar to performing a differentiation along the perturbation axis (1^{st} and 2^{nd} order differential for synchronous and asynchronous respectively). By comparing the synchronous and asynchronous maps we can understand how each of the bands is changing as a function of temperature. The synchronous PCMW2D shows if a spectral band is increasing or decreasing with respect to the perturbation and the asynchronous can tell us the rate of this change (i.e. convex / concave increment, using the terminology of Morita *et al.*[23]).

3.2.6.1 κ-carrageenan

Figures 3.37 and 3.38 show the synchronous and asynchronous PCMW2D maps for κ-carrageenan from 80 to 10 °C, with a window size of 10 °C. There is clearly an event occurring around 30 °C, a similar temperature to previously identified by PCA, MCR and MW2D. At around 30 °C, there are multiple regions of the spectra that appear to increase, decrease and stay steady; observable as positive (red), negative (blue) and 0 (white) areas of the synchronous PCMW2D plot, respectively. This helps to highlight the real advantage of PCMW2D over that of MW2D; Moving Window 2D Correlation Spectroscopy shows areas that are susceptible to change, whereas PCMW2D singles out individuals bands that change in a particular direction.

Although the PCMW2D spectral map is clear in indicating spectral regions that change and their direction, Figure 3.39 shows a temperature slice from the synchronous PCMW2D plot of κ-carrageenan at 30 °C, plotted alongside the mean spectrum of the raw κ-carrageenan data, to aid in understanding. The temperature slice is effectively a subset of data from $t = 25$ to

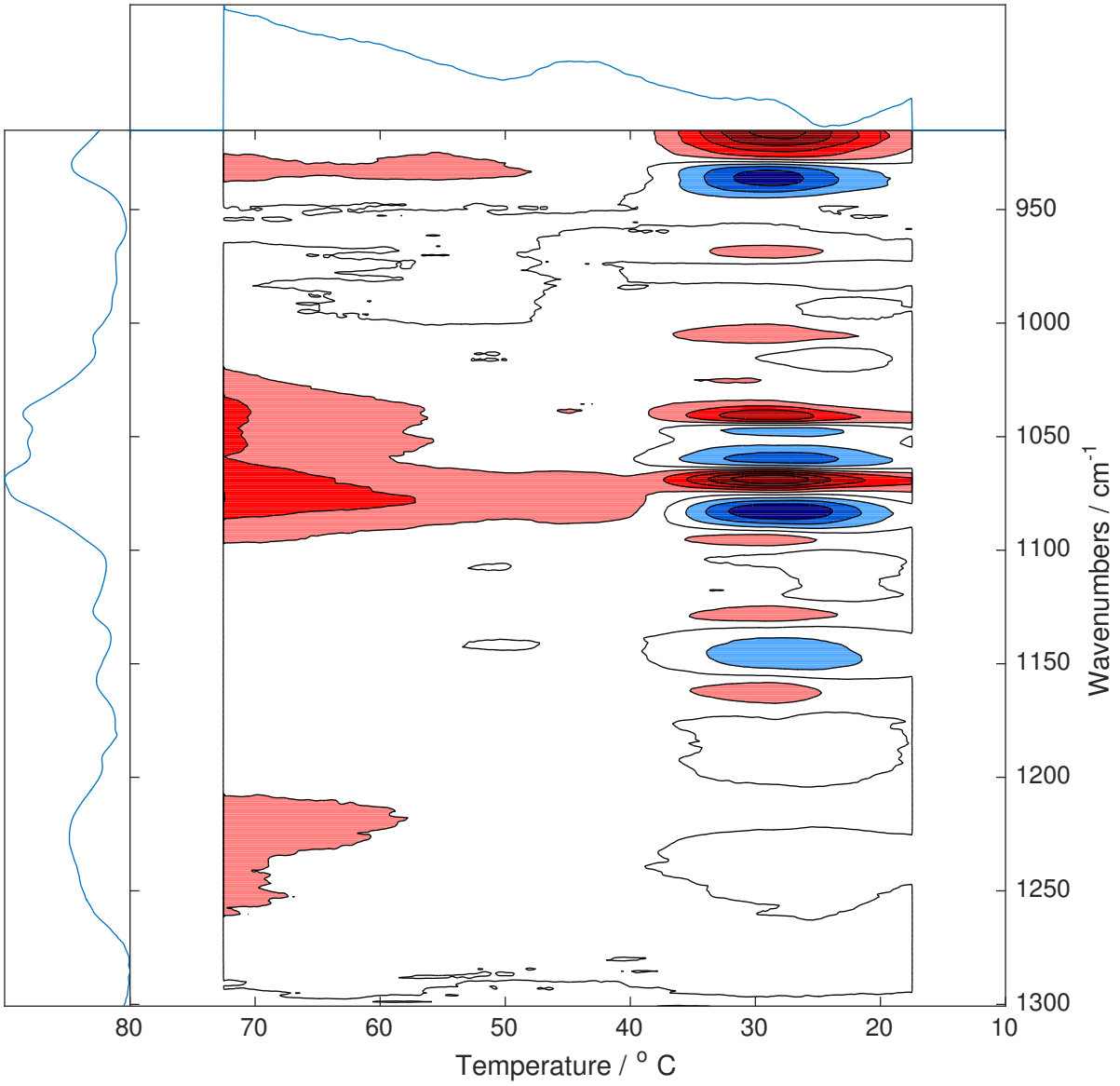

Figure 3.37: PCMW2D synchronous correlation map of κ-carrageenan, from 80 to 10 °C, window-size: 12.5 °C, colourmap: blue-white-red; negative-0-positive

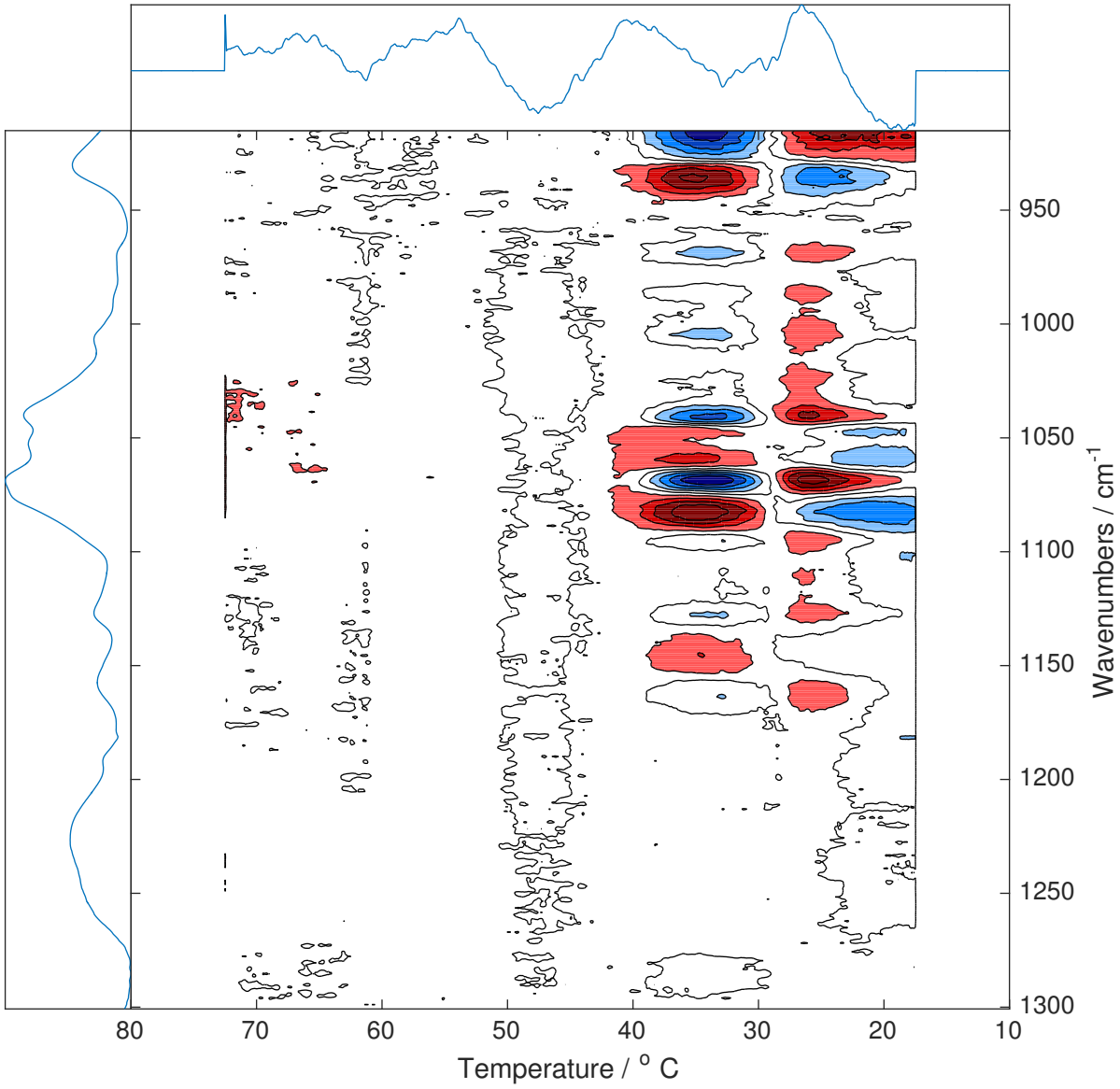

Figure 3.38: PCMW2D asynchronous correlation map of κ-carrageenan, from 80 to 10 °C, window-size: 12.5 °C, colourmap: blue-white-red; negative-0-positive

$t = 35$ °C that has been differentiated along the temperature direction. It is important when stating that PCMW2D spectra bear similarity to differential spectra that one appreciates the direction of the differentiation. A commonly used technique within infrared spectroscopy is to produce a differential spectrum, that has been calculated along the spectral variable.[131] This allows separation of overlapping bands somewhat and is particularly used during multivariate analysis of analytical systems. For Figure 3.39 the 30 °C PCMW2D slice shows the intensity and direction of change of spectral features as the sample is cooled from 35 to 25 °C, and provides a more classical spectral view of the changes we see in the PCMW2D plots. The slice analysis also allows direct comparison of band position with the original spectra, unlike conventional differential analysis along the spectral variable where the maximum of the original band now lies on the x-axis with positive and negative peaks indicating the gradient to lower and higher wavenumber.

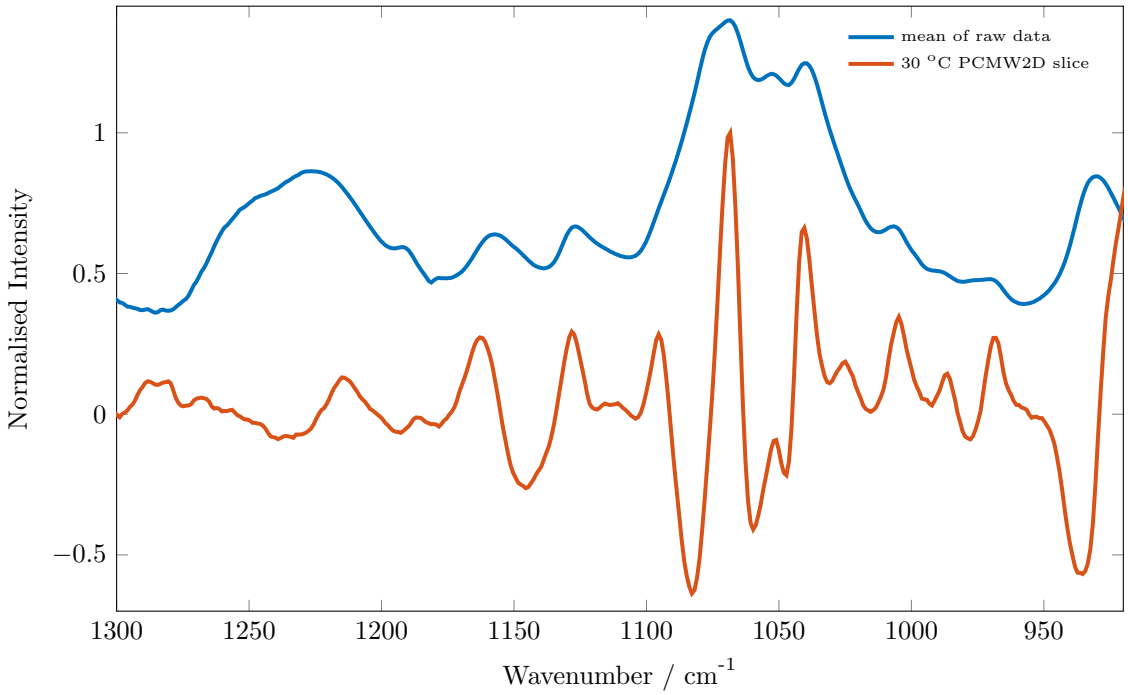

Figure 3.39: PCMW2D temperature slice comparison of κ-carrageenan, mean of raw spectra from 80 to 10 °C (blue) and 30 °C PCMW2D syn slice (orange), normalised and offset for clarity

The most prominent feature of the slice, at 1069 cm^{-1}, associated with C-O or C-OH modes was also featured heavily within the 2DCOS analysis and autocorrelation spectra (see Figure 3.19). During the midpoint of transition (at 30 °C) this feature is seen to increase significantly, suggesting a conformational change. Interestingly the band to slightly higher wavenumber; 1083 cm^{-1}, decreases over this temperature range, and another just next to this at 1096 cm^{-1} is seen to increase slightly. Previously when evaluating spectral feature within this region, there was a main band at *ca.* 1070 cm^{-1}, with a shoulder at 1090 cm^{-1}. With reference to previous literature (table 1.1) the main band was assigned to C-O / C-OH modes and the 1090 cm^{-1} shoulder to a S-O symmetric stretch. The features of Figure 3.39 between 1070 and 1100 cm^{-1}suggest two bands increasing during this temperature range, and one decreasing. It is also worth noting that the negative band at 1083 cm^{-1} is below 0, indicating that it is not just a joining of two spectral features that increase, but a definite decrease of a spectral feature. This information alone is not enough to make assignments as to whether there is a reduction of intensity of an S-O vibration, or a decrease of a particular C-O / C-OH mode. There are two bands seen to decrease at 1060 and 1047 cm^{-1}, it is unlikely that the 1060 cm^{-1} feature is a sulfate based mode, however the 1047 cm^{-1} could be. The conformational change occurring, along with the complexity of a biopolymeric system could infer that sulfate modes decrease as C-O increase, however it could be the case that particular C-O / C-OH vibrations within κ-carrageenan are perturbed as the confirmation changes.

As seen within the MW2D analysis, the midpoint of spectral changes showed no significant contribution from the sulfate modes between 1200 and 1250 cm^{-1}. Although there are some features that are associated with sulfate modes; 1215 and 1012 cm^{-1} are the most prominent, the midpoint of this transition is dominated by C-O and glycosidic bonds, especially when the bands present in Figure 3.39 are compared with the intensity of sulfate and C-O modes in the raw spectra.

Figure 3.40 shows the mean of the raw data along with PCMW2D slices at 30 and 40 °C.

The purple trace (40 °C) shows two higher wavenumber sulfate bands; 1215 and 1260 cm^{-1} that are seen to increase before the midpoint of the transition. Although many C-O and glycosidic modes are still apparent, their relative intensity to the sulfate based vibrations is significantly less within the 40 °C slice. There is also a significant increase of intensty of the 1012 cm^{-1} relative to the 30 °C slice. As with the MW2D analysis, these data suggest the disruption of sulfate vibration occurs before the midpoint of the transition, with these bands showing little contribution at the midpoint of the transition.

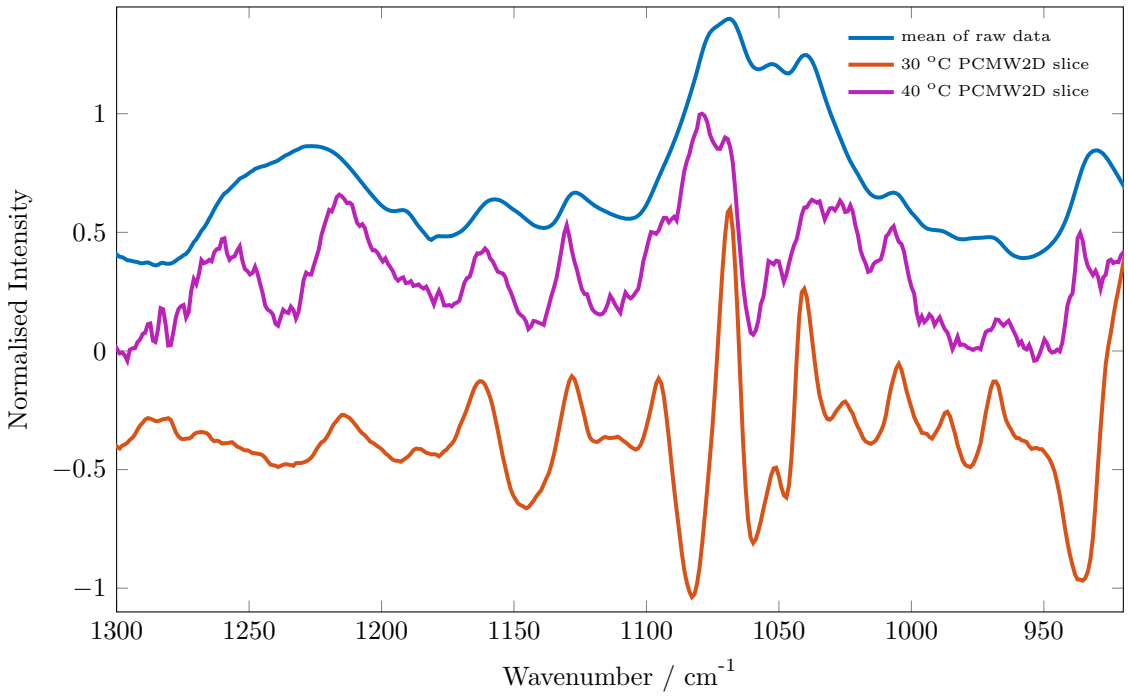

Figure 3.40: PCMW2D temperature slice comparison of κ-carrageenan, mean of raw spectra from 80 to 10 °C (blue), 30 °C PCMW2D syn slice (orange), and 40 °C PCMW2D syn slice (purple) normalised and offset for clarity

3.2.6.2 ι-carrageenan

Figures 3.41 and 3.42 show the synchronous and asynchronous PCMW2D maps for ι-carrageenan. As with κ-carrageenan, PCMW2D highlights the midpoint of the transition that matches the temperature from other analyses, *ca.* 55 °C for the ι-carrageenan sample. In contrast to the

κ-carrageenan PCMW2D, sulfate bands at *ca.* 1200 cm^{-1} appear more prominent during the transition midpoint, all features of the synchronous and asynchronous plots also extend across a wider temperature range within the ι-carrageenan sample. κ-carrageenan is known to be a stronger more brittle gel than ι-carrageenan,[132] spectroscopically however there is little evidence of more intense spectral changes through the gelation transition (see Figures 3.5 and 3.6), which could account for a sharper transition point for κ- vs. ι-carrageenan. The midpoint of κ-carrageenan's transition is *ca.* 30 °C, while ι-carrageenan's is 55 °C. Before being passed into the PCMW2D algorithm therefore, the κ-carrageenan sample undergoes a longer cooling period while in the solution state. When comparing the two, κ-carrageenan PCMW2D maps will show a wider temperature range of little change, giving the appearance of the scaled maps to be a sharper transition.

Following gelation, within the synchronous map, most spectral features appear to 'tail off', without an abrupt end point. This was also seen with the MCR analysis of ι-carrageenan (Figure 3.15. Although there is a distinct event that begins just above 60 °C, spectral changes continue to occur as the temperature is reduced. The asynchronous maps, Figure 3.42 shows the most intense spectral changes occurring just above 60 °C, C-O and C-OH modes (1000 to 1100 cm^{-1}) decreasing (convex decrement, i.e. with increasing rate), and higher wavenumber sulfate based modes (*ca.* 1200 cm^{-1}) increasing (concave increment, i.e. increasing rate) during the gelation transition. Interestingly two sulfate bands at 1210 and 1184 cm^{-1} increase, while the 1235 cm^{-1} sulfate band decreases. This is hinted at within the raw spectra (Figure 3.6) with the transition showing a "band shift" to lower wavenumber, i.e. the decay of the higher wavenumber components and the growth of a lower wavenumber component. This was not seen within the κ-carrageenan sample. ι-carrageenan has one more sulfate group per repeating unit and there is no reason to presume the the second set of sulfate groups undergo the same interactions as the first, especially considering their different position within the repeating unit.

The number and position of sulfate groups along the chain has been show to have a large

influence over the gel's physical properties, including the gelation transition, especially with regards to the cation concentration and valency.[63,80,133,134] Separation of bands within the sulfate group, particularly their distinct change in interaction has not previously been studied in this manor. However, the growth and decay of separate components of the sulfate vibrations, within ι-carrageenan and not κ-carrageenan suggests that the additional sulfate moiety plays a slightly different role within the gelation transition. These two features (decay at 1235 cm^{-1}, and growths at 1210 and 1184 cm^{-1}) start their changes a the same temperature, from the synchronous PCMW2D map, and have similar growth/decay rates as suggested by the similar intensity of the asynchronous correlation map. Although they might play slightly different roles in regard to the gelation process, their similar rates suggest a concerted effort. Previous studies have attributed ι-carrageenan's lesser gel strength to the increased negative charge along the chain that the extra sulfate group imparts, in comparison to κ-carrageenan.[135] The additional sulfate restricts extensive aggregation of double helices.

Figure 3.43 shows the mean of the raw data, and 75 and 55 °C PCMW2D slices for ι-carrageenan, in an attempt to separate C-O / C-OH vibrational modes from the sulfate based modes that MW2D suggested precede the backbone conformational changes. ι-carrageenan did not show as clear evidence for this as κ-carrageenan did however. The temperature slice at the midpoint of the transition (55 °C, purple trace) defiantly shows a cluster of sulfate based modes around 1200 cm^{-1}, with the higher wavenumber sulfate bands taking no prevalence to the backbone associated vibrations within the 75 °C (orange trace).

Unfortunately the current experimental system in use cannot take the sample temperatures much above 80 °C. ι-carrageenan is know to also follow the coil-helix-rod gel formation and it is to be expected that the sulfate groups play a (spectroscopically) larger role within the initial stages of this transition, however ι-carrageenan did not show this as clearly as the κ-carrageenan system. Perhaps a wider temperatures range would allow finer study of the interactions taking place as the solution state cools before gelation occurs.

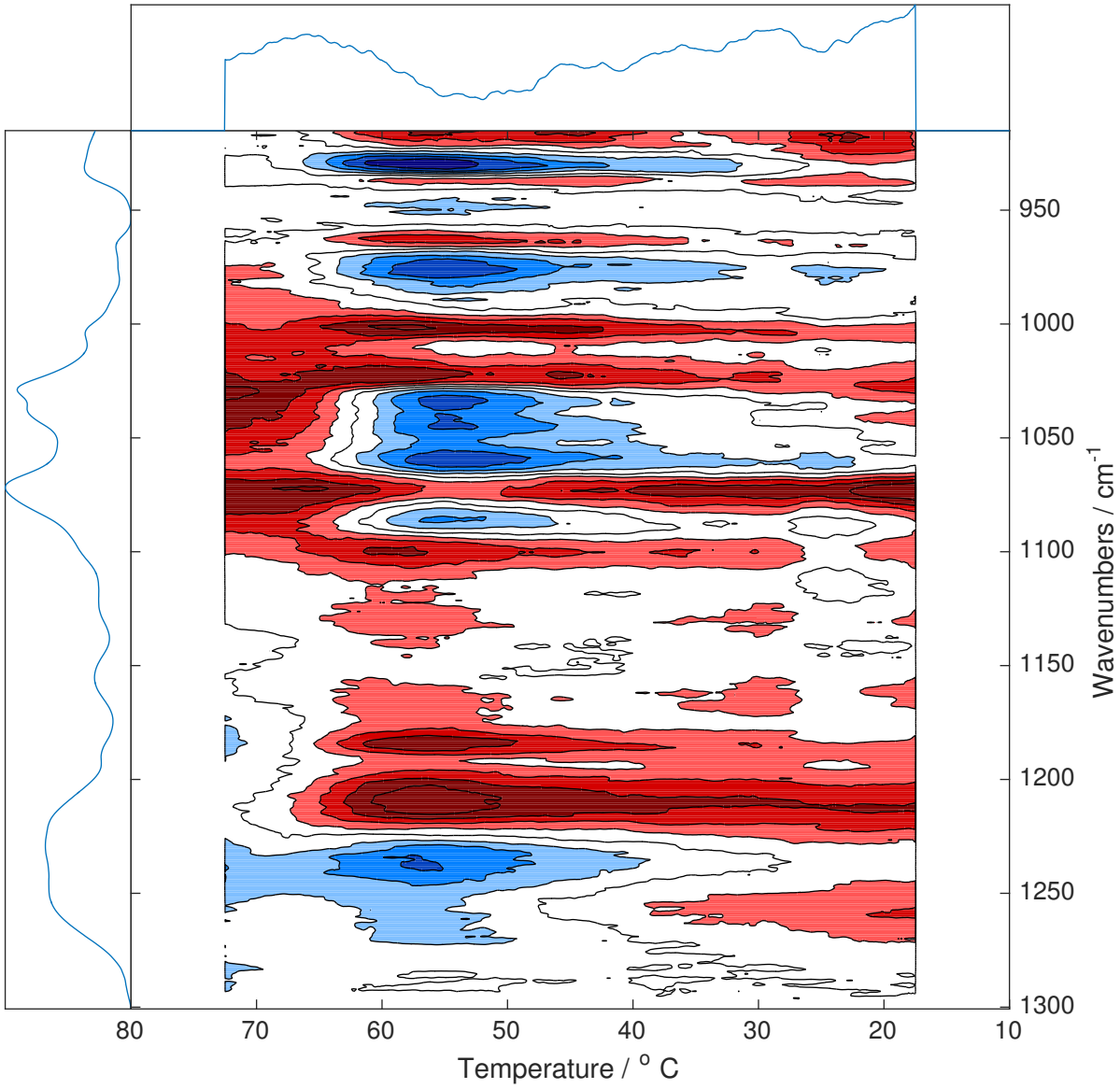

Figure 3.41: PCMW2D synchronous correlation map of ι-carrageenan, from 80 to 10 °C, window-size: 12.5 °C, colourmap: blue-white-red; negative-0-positive

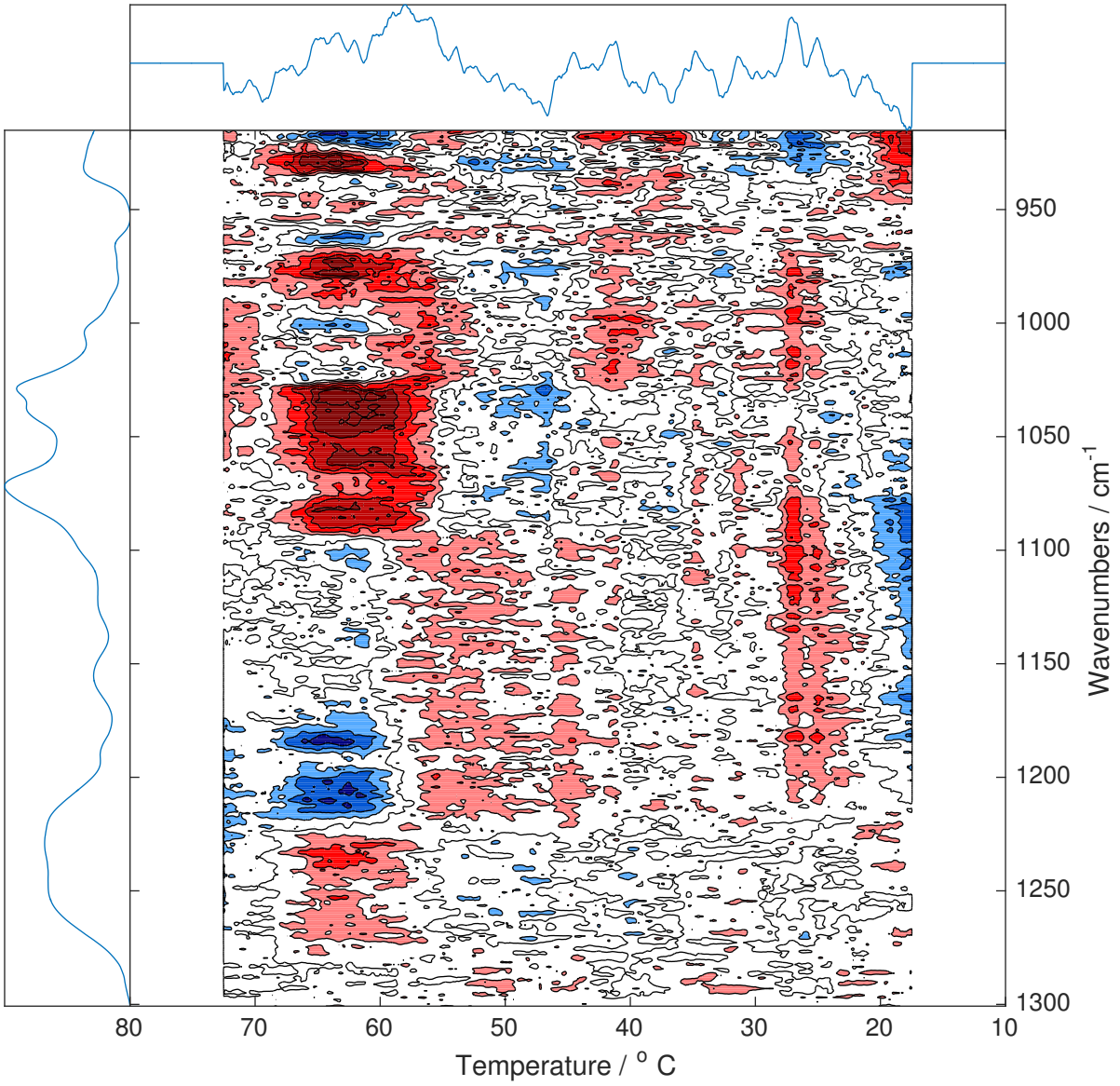

Figure 3.42: PCMW2D asynchronous correlation map of ι-carrageenan, from 80 to 10 °C, window-size: 12.5 °C, colourmap: blue-white-red; negative-0-positive

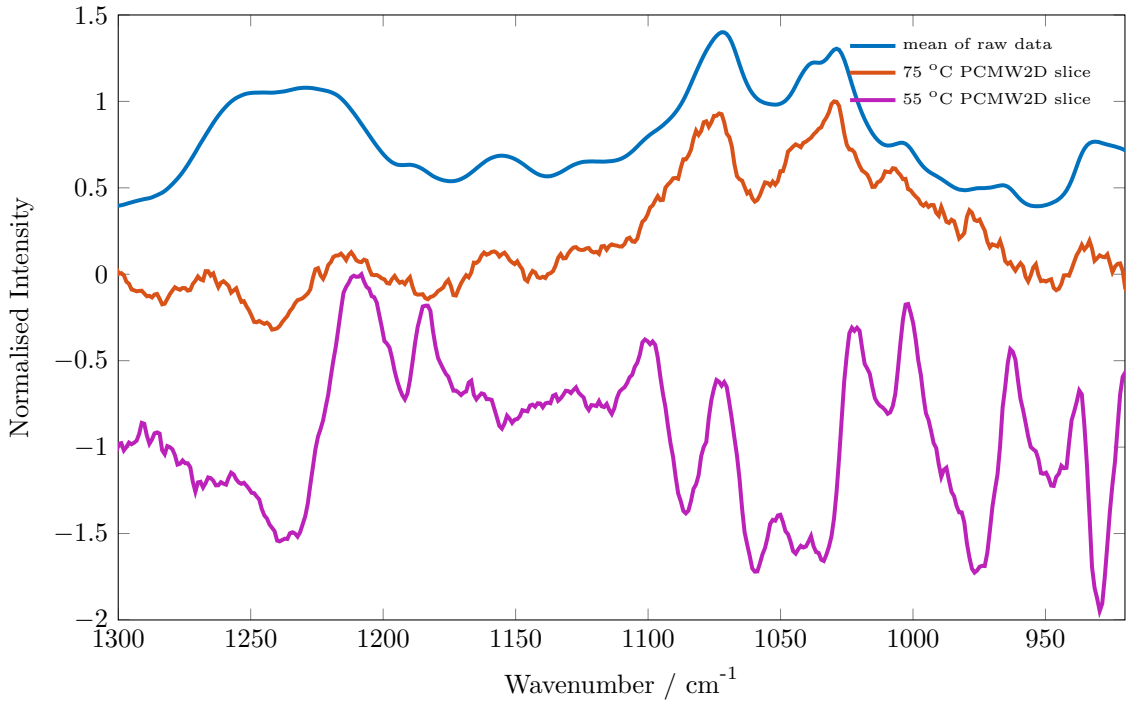

Figure 3.43: PCMW2D temperature slice comparison of ι-carrageenan, mean of raw spectra from 80 to 10 °C (blue), 70 °C PCMW2D syn slice (orange), and 55 °C PCMW2D syn slice (purple) normalised and offset for clarity

3.2.6.3 λ-carrageenan

Figures 3.44 and 3.45 show the PCMW2D correlation maps for λ-carrageenan, between 80 and 10 °C. The synchronous spectra show events at *ca.* 58 and 32 °C, with the spectral pattern matching that of the original raw spectra (mean raw spectrum plotted on left of plots). As with previous analysis of the λ-carrageenan system, the change in spectral intensities is proportional to the original absorbance spectrum, *i.e.* no bands change their relative intensity to one and another. This suggests purely physical changes occurring within the sample, possibly a change in sampling depth or sample density.

It is important to note here, as with other 2D plots presented, is that the plots are not scaled between each other, only within each plot. For example if the maximum intensity of one plot is twice that of the other, comparison of the colourmaps between each plots would not yield a difference in absolute intensity. Although this allows efficient investigation of one particular plot, by allowing the user to see subtle changes within the map with the restricted number of contour levels/colours, this does mean that every plot will have areas of low and high intensity, even if their absolute intensity is meaningless when comparing one plot to another.

Although there appear to be spectral features that change at particular temperatures within the PCMW2D plots, these are not consistent with evidence provided by the other techniques used previously. One may be able to propose that there is a real change at 30 °C, which, although the sample does not gel like κ- and ι-carrageenan, there still might be distinct spectral changes at a particular temperature, associated with molecular rearrangement. λ-carrageenan's extra sulfate group is postulated to prohibit gel formation by excluding cross-linking in the final aggregation stage of the gelation process.[35] The thickening properties of λ-carrageenan have not been extensively studied, however interactions between the linear chains has been shown to be the primary mechanism by which this occurs.[136] This is to say that there may be temperature dependant chemical interactions occurring, however the lack of relative intensity changes within

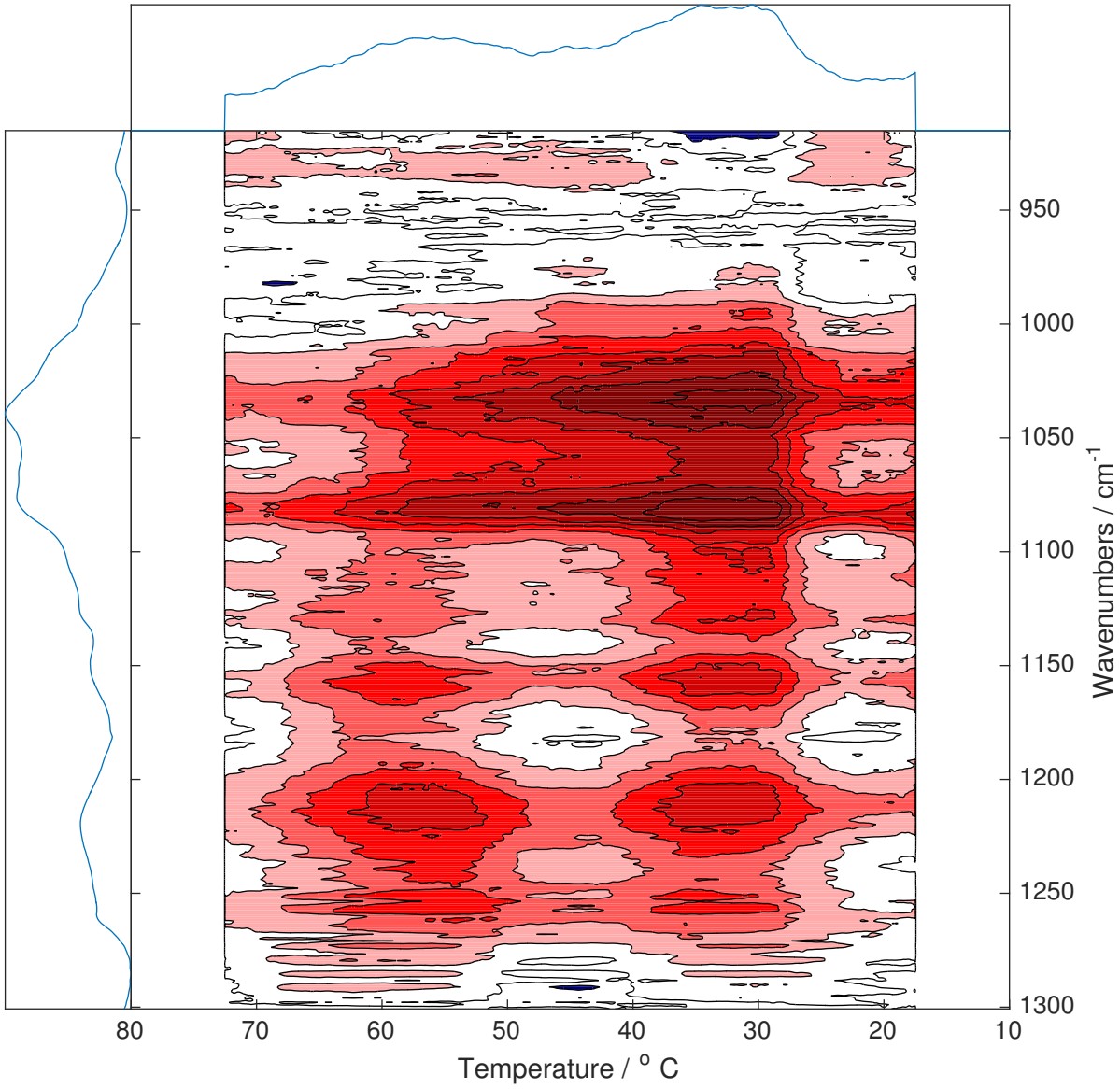

Figure 3.44: PCMW2D synchronous correlation map of λ-carrageenan, from 80 to 10 °C, window-size: 12.5 °C, colourmap: blue-white-red; negative-0-positive

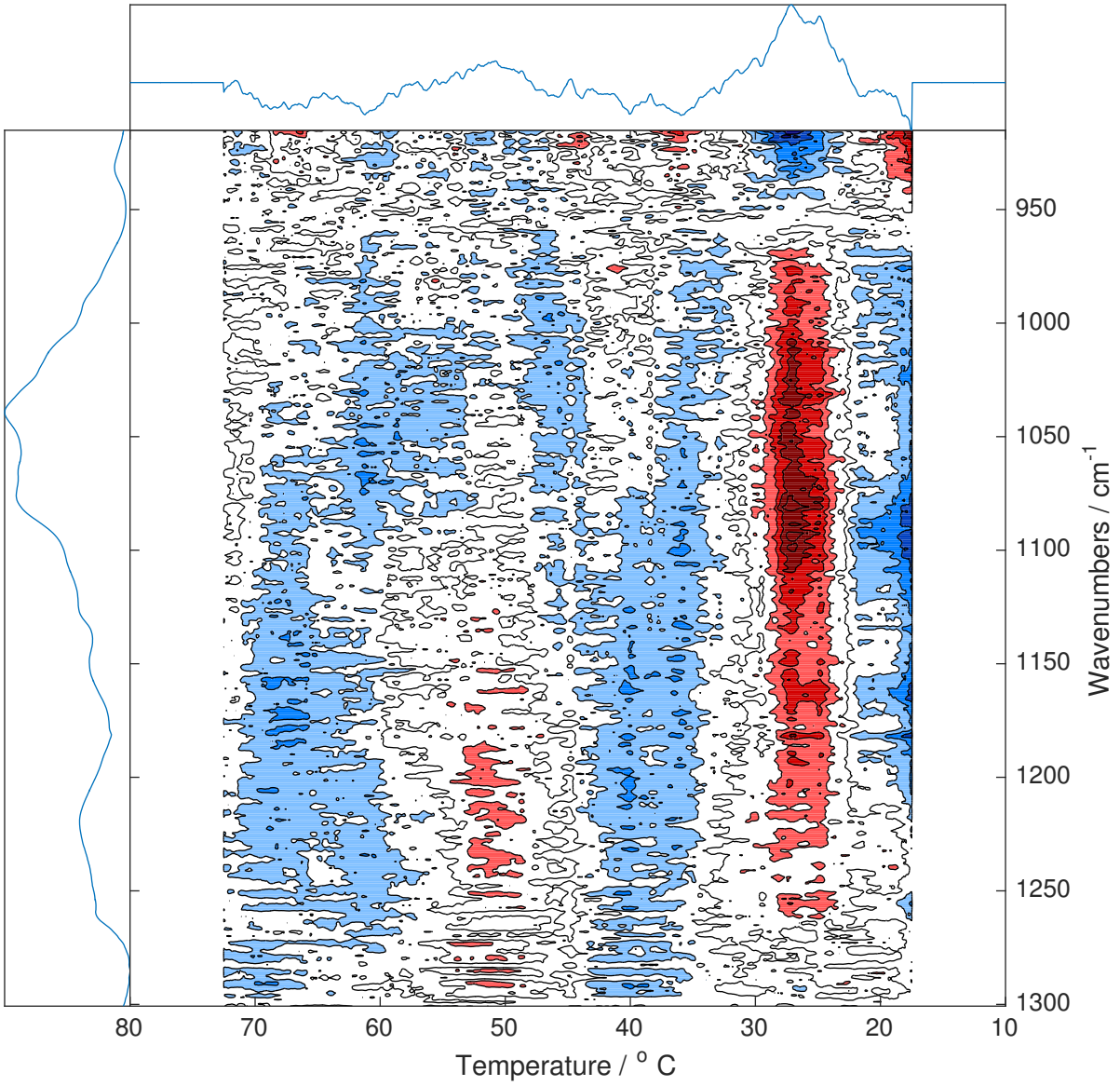

Figure 3.45: PCMW2D asynchronous correlation map of λ-carrageenan, from 80 to 10 °C, window-size: 12.5 °C, colourmap: blue-white-red; negative-0-positive

the spectra suggest that this is not observed here.

3.3 Conclusions

This Chapter used a modified low-temperature ATR accessory coupled with infrared spectroscopy to monitor the temperature dependant nature of three carrageenans as they were cooled from 80 to 10 °C. During this temperature range κ- and ι-carrageenan form gels and a variety of multivariate and two-dimensional techniques were used to study this transition. Data indicates that infrared spectroscopy is a powerful technique to monitor these changes with the ability to observe structural variation within the carrageenans occurring within a degree Celsius.

Studying the fingerprint region of infrared spectra of biopolymers is a complex task due to the complexity of vibrational modes found within. Multivariate and correlational techniques can aid in their interpretation. Both PCA and MCR results indicate specific temperatures which are similar to the gelation transition of the κ- and ι-carrageenan. Previous studies have suggested that monitoring the sol-gel transition by FTIR spectroscopy allows insight into the coil-helix transition, rather than the subsequent aggregation responsible for the network formation.[51] The fingerprint region of the IR spectra for carrageenans shows multiple bands associated with biopolymer backbone and sulfate group species. These modes are most susceptible when the biopolymer chain undergoes a large conformational change. The transition of polymer strands from a random coil to double helical confirmation is indeed a conformational perturbation, much larger than the expected conformational change when then helices aggregate together (whether this be at the superhelical or helical level, for κ- and ι-carrageenan respectively).

For κ-carrageenan, PCA suggests a conformational change starting between 35 - 30 °C, with the spectral perturbations decaying to a steady state at *ca.* 20 °C. MCR also echoes this temperature dependant nature; starting at 35 - 30 °C and becoming almost steady at 20 °C. The two moving window based two-dimensional correlation analyses; MW2D and PCMW2D also highlight this temperature range (35 - 20 °C) as the region with the most significant spectral variation. 2DCOS analysis of the κ-carrageenan system suggested that there might be some

small changes between 1070 and 1090 cm^{-1} that change out of phase with one and another, however the overlapping nature of the band position and multiple C-O / C-OH modes within this region does not allow any conclusions to be drawn.

MW2D allows for autocorrelation spectra between specific temperature ranges to be extracted. This is a very powerful feature as it allows investigation into spectral regions that are susceptible to change at different temperatures. Figure 3.31 showed autocorrelation spectra from different temperature regions; 80 - 10 °C (the overall range), 35 - 25 °C (range where majority of spectral variation occurs), and 45 - 35 °C (range preceding the sol-gel transition), for κ-carrageenan. The autocorrelation spectra from during the gelation transition (35 - 25 °C) showed a relative enhancement of backbone vibrations, compared to the overall autocorrelation spectra. Interestingly however the autocorrelation spectra from the temperature range preceding this (45 - 35 °C) shows a large enhancement of sulfate based vibrations: 1200 - 1270 and 1025 cm^{-1}. PCMW2D temperature slices of the same regions also echoed this apparent ordering of features; sulfate modes perturbed before the main sol-gel transition where backbone vibrations take precedent.

Carrageenan is a poly-electrolyte, the chain is negatively charged due to the sulfate groups. Cation stabilisation of these groups must occur prior to helix formation and subsequent aggregation. In fact, this is the very reason that λ-carrageenan does not form gels under normal condition; the inclusion of 3 sulfate groups per repeating unit precludes cross-linking (due to its position and charge) and does not allow gel formation.[32] Observation of sulfate vibrational modes undergoing a perturbation before the backbone based vibrations is not unexpected, however this has not been reported before.

ι-carrageenan also showed temperature dependance, however the spectral changes began at a higher temperature, *ca.* 65 - 60 °C, indicated from both multivariate analyses. The change, unlike those seen for κ-carrageenan however, did not appear to become steady state

within *ca.* 15 °C. PCA and MCR both showed a decreasing rate of change as the temperature continued to be lowered, although not as quickly as κ-carrageenan. This initial change was also highlighted within the moving window correlation techniques, starting at *ca.* 60 °C and continuing down through the entire temperature range. This evidence could suggest that the sol-gel transition for κ-carrageenan has a smaller temperature window than that of ι-carrageenan, and that ι-carrageenan's structure continues to change and 'settle' over a wider temperature range. Autocorrelation spectra for the temperature range before the main spectral variation (i.e. before the sol-gel transition), at 80 - 70 °C for ι-carrageenan also showed an increase in sulfate based bands compared to backbone bands. PCMW2D temperature slices however did not echo this ordering, although sulfate based vibrations are apparent within the temperature slices, their relative ratios to backbone bands did not change. The difference between the sulfate-backbone ordering within the sol-gel transition for κ-carrageenan compared to ι-carrageenan could be an insight into the superhelical / helical aggregation differences of the slightly different gelation mechanisms. However the wider temperature range observed for the transition for ι-carrageenan could be depressing temperature changes compared to κ-carrageenan; *i.e.* PCMW2D highlights rate of change of spectral components during perturbation as the rate of change for ι-carrageenan is much slower than that of κ-carrageenan's spectral variations. 2DCOS did highlight this ordering however, Figure 3.26 shows a sulfate band (1250 cm^{-1}) changing predominantly before almost every other spectral feature.

Figure 3.46 shows a comparison of autopower spectra for κ- and ι-carrageenan at the mid-point of their gelation transition (identified by MW2D, in this case, from the maxima of Figures 3.37 and 3.41, respectively). There is a clear difference in the susceptibility of sulfate based vibrations (1250 to 1175 cm^{-1}) during the period of most intense change between the carrageenans. At the midpoint of transition, the autopower spectra for ι-carrageenan shows features that suggest changes in the sulfate groups dominate the (spectrally observed) changes during gelation. In contrast κ-carrageenan shows no sulfate perturbations over the 10 °C change centered around

it's maximum spectral gelation midpoint. Instead, C-O and C-OH bands are seen to change. The observed difference in separate chemical vibrations changing over the course of the gelation transition could be spectral evidence for the (slightly) different gelation mechanisms between κ-carrageenan and ι-carrageenan. κ-carrageenan has been shown to undergo superhelical aggregation (see Figure 3.4) and Section 3.1), whereas ι-carrageenan gels at the helical level. This could be evidence for the orientation of the carrageenan chains while in their helical conformation. The lateral aggregation of helices (for κ-carrageenan) shows perturbations of C-O and C-OH vibrations, suggesting that these are protruding outwards from the helix, whereas the formation of a helix (during ι-carrageenan gelation) involves the sulfate groups much more than the hydroxyl groups.

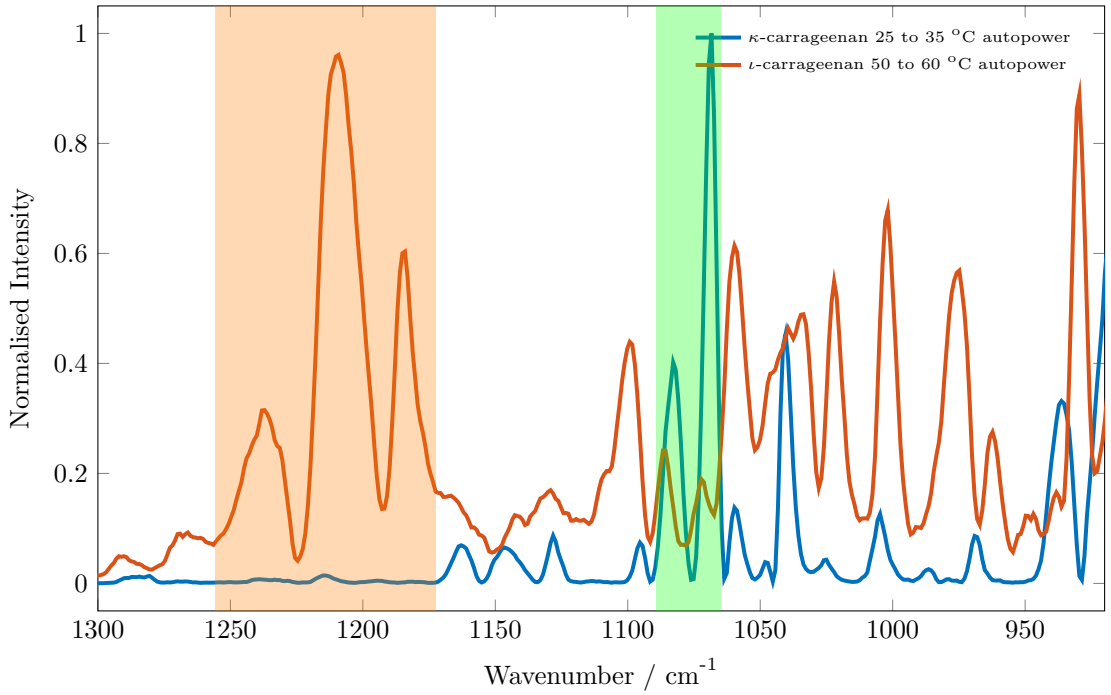

Figure 3.46: MW2D autopower slices for κ-carrageenan, from 25 to 35 °C (blue trace), and ι-carrageenan, from 50 to 60 °C (orange trace), showing difference in sulfate bands during the midpoint of the gelation transition. Orange overlay shows the $\nu(SO_2)$ antisymmetric stretch region and green overlay shows C-O and C-OH vibrational region

Although no gelation is observed for λ-carrageenan spectral features are seen to change over

the temperature range and a viscosity increase occurs. PCA and MCR both produced the most reliable models when only one component was selected (with PCA the 2nd loading showing only noise). This component matched the original spectra near-perfectly (Figure 3.18), indicating that the spectral features do not change relative to one and another. This is in stark contrast to κ- and ι-carrageenan, where various sulfate and backbone vibrations were seen to be perturbed significantly compared to ring vibrations of the biopolymer (*i.e.* the parts of the repeating unit that do not change confirmation during the transition). The moving window correlation techniques do suggest a change at about 30 °C for λ-carrageenan, however this observation is not clear enough to suggest a conformational change. Rheological studies have shown a steady increase in viscosity for λ-carrageenan over this temperature range.[32] As the spectral changes cannot be definitively attributed to a conformational change / reordering, other possibilities to explain the increase in absorbance can arise. An overall increase of absorbance (when using ATR-FTIR) can sometimes be attributed to a change in sample density. An increase in density as the λ-carrageenan sample is cooled will bring more molecules within the the sampling area of the evanescent wave of the diamond ATR crystal. A viscosity increase also suggests increased molecular interaction and could change the refractive index of the sample as a function of temperature,[137] changing the effective sampling depth. The lack of gelation for λ-carrageenan, compared to κ- and ι-carrageenan, does not rule out a conformational change for λ-carrageenan.

Chapter 4

Low Temperature Studies of Carrageenans

4.1 Introduction

This Chapter focuses on the use of FTIR spectroscopy to probe the nature of ι-carrageenan solutions as they undergo freezing. A variety of carrageenans are used for food products at low temperatures and ι-carrageenan is studied because of its potential interest for use within frozen food products. Due to the complexity of the infrared fingerprint spectral region, of biopolymeric systems, a collection of multivariate and correlative techniques to help understand this system.

Hydrocolloid stabilisers have been used in industry for a long period to provide a uniformity of product, resistance to melting and the desired smoothness. They are also used to reduce the fat content of ice-creams.[138,139] A possible major role of these additives is to hinder the growth of ice crystals as temperature fluctuates during storage. The size of the crystals within ice cream have a large effect on the taste and texture of the ice cream,[140] with the larger crystals producing a courser and grainier composite. Although any system will contain a distribution of

ice crystal sizes, it is generally accepted that a mean size greater than *ca.* 50 μm imparts a grainy texture to the ice cream and small crystals, less than 20 μm, produce the desired smoothness and creaminess.[140–142] The use of a stabiliser to minimise the growth of ice crystals is therefore a key aspect in the production of an ideal ice cream.

Various stabilisers have been directly observed to limit the rate of ice crystal growth during recrystallisation.[33,143–150] Although there has been extensive research in this area, the precise method of action is still an ongoing debate. At low (0.5% to 2% w/w) concentrations, these stabilisers have been shown to have a minimal impact on the initial size distributions of the ice crystals,[143,146,150] and do not significantly affect the glass transition temperature.[138,149,151] This led to the conclusion that the stabilisers do not have the crystal growth inhibition effects due to a general increase in viscosity of the solutions prior to freezing, nor significantly alter the phase transition properties.

Initially, the hinderance of ice recrystallisation upon temperature fluctuation was attributed to a large increase in viscosity of the unfrozen phase surrounding the ice crystals.[149,151,152] When frozen, ice crystals would form, forcing a large freeze concentration of the stabiliser containing solution to surround the crystals. It was theorised that this polymer network minimised the mobility of water molecules thus retarding their diffusion to the surface of the crystal, hence slowing the crystal growth. This type of recrystallisation is referred to as migratory, or Ostwald ripening which occurs due of the formation of larger crystals at the expense of smaller ones as they are more thermodynamically favourable.[153] This interpretation had continued for a long period of time but there was always doubt, as different stabilisers are not equally efficient at retarding crystal growth, allowing for variation in concentration or viscosity.[151] Another possibility for the variance in crystal sizes is that crystal growth can also occur through accretion, where two or more adjacent ice crystals join together forming a single, larger crystal.[154]

More recently, polysaccharide stabilisers have been found to show a structure formation upon

freeze concentration of the unfrozen phase.[155] The structure formation can interfere with the diffusion of water molecules to the surface of the ice crystal above and beyond that of a simple viscosity increase. The study, by Bolliger *et al.*, was conducted using Guar Gum, a polysaccharide of very similar construction to carrageenan.[155] This hypothesis allows for the mechanism of action to be limited to either a modification of the diffusion rates,[143,156] or by adsorption to the ice surface.[150] Importantly this hypothesis also suggests that there is a change in polysaccharide behaviour as a result of freeze concentration, suggesting this is due to hyper-entanglement of the polymer strands.

Inhibiting ice crystal growth by adsorption to the ice surface is a mode of action normally associated with ice binding proteins (IBPs), including other subsets known as antifreeze proteins (AFPs) and ice structuring proteins (ISPs). IBPs were originally found to be present in a variety of freeze avoiding organisms, such as Teleostei fishes found at high latitudes, contributing to their resistance of freezing.[157–159] More recently, plants that express freeze tolerant activities whereby surviving in sub-freezing temperatures by limiting the size of ice crystals have also been investigated.[160]

Figure 4.1 shows the inhibition of crystal growth by an IBP extracted from cold acclimated winter wheat grass extract.[161] As it can be seen, in both the sucrose (A) and ice cream (B) solutions the addition of 0.25% IBP has a large decrease on the rate of ripening of the ice crystals. Regand *et al.* also verified, by sensory evaluation, a remarkably smoother texture in the ice creams formulations containing the the IBP.[161]

κ-carrageenan is currently added to ice-cream as a secondary stabilising agent, at levels lower than 0.05 % to control phase separation due to the incompatibility of hydrocolloids with milk proteins.[162] Both κ- and ι-carrageenan show cross-linking with casein micelles,[163] and this has been reported to decrease the recrystallisation rate in model κ-carrageenan/sucrose systems in non-fat milk solids.[164]

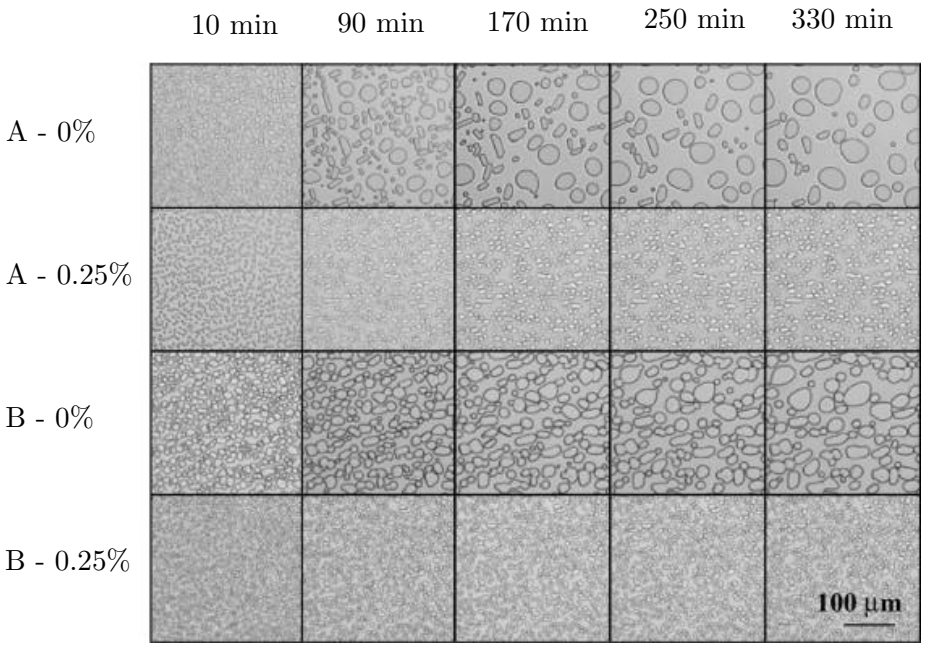

Figure 4.1: Bright field images accuired every 80 minutes (starting from 10 minutes) at -5 °C, from sucrose (A) and ice cream solutions (B) containing either 0 or 0.25% IBP from cold acclimated winter wheat grass extract. Reproduced from Regand *et al.*[161]

A recent study by Gaukel *et al.* showed that κ-carrageenan significantly reduced recrystallisation within sucrose-solutions and concluded (as previously thought) that the viscosity of the solution cannot explain this effect.[165] As the only other current theory, based on that of AFPs and IBPs, suggests interaction with the ice crystals, Gaukel concluded that it is highly likely that κ-carrageenan interacts with the ice crystal surface.

Antifreeze proteins have been shown to inhibit recrystallisation by binding to different planes of the ice crystals, where different AFPs show preference to different ice crystal planes.[166] Their limited availability, and very high price and precluded widespread use within industrial applications however. The exact mechanism of recrystallisation, connected to the surface binding process is still not understood in detail.[167]

During this Chapter the structure of ι-carrageenan within a frozen system is investigated by infrared spectroscopy and multivariate analysis. The binding of carrageenan to an ice crystal should invoke structural changes of the biopolymer that infrared spectroscopy has the potential to monitor.

4.2 FTIR Results

FTIR spectroscopy was used to analyse the low temperature nature of 2% ι-carrageenan solutions as they undergo freezing. The hot samples were stirred at 80 °C for 30 minutes and were then were placed into a hot ATR chamber, as described in Chapter 2. The samples were cooled at a rate of *ca.* 0.3C per hour.

The freezing point depression of water due to the carrageenan is slight, *ca.* 0.5 °C, however we observed all the samples undergo supercooling to *ca.* -9 °C before they froze. Although during spectral collection the samples are isolated the onset of freezing can be seen from changes in the IR spectra. As solid ice is formed, the O-H stretch at 3100-3600 cm^{-1} shows a sharpening and increase of intensity of the lower wavenumber portion of the band, *ca.* 3150 cm^{-1}, and a reduction of absorbance (with respect to liquid water) at the higher wavenumber part of the band, (*ca.* 3400 cm^{-1}).[168,169] There is also a substantial decrease in absorbance of the H-O-H bending mode at 1655 cm^{-1} as water passes through the liquid to solid transition.[168] To confirm supercooling the samples were monitored visually whilst being cooled (by removal of the ATR top chamber). We observed rapid freezing at *ca.* -9 °C, however agitation by a cotton bud could initialise crystallisation at -1 °C.

Figure 4.2 shows a 2% ι-carrageenan sample just before and just after freezing (*ca.* -9 °C), the spectra that are displayed have been processed against a diamond background of the correct temperature. The infrared fingerprint region of the spectra, where carrageenan bands are just visible (1000 - 1250 cm^{-1}) suffers large baseline distortions as a results of the produced phase change of water. Subtraction of water or ice spectra at the corresponding temperature produced smooth baselines (Section 2.2), which allowed investigation in changes in the infrared of carrageenan to be more easily visualised.

The temperature that the water to ice phase transition occurred varied slightly from experiment to experiment, with no obvious pattern presenting. It is expected that the crystallisation

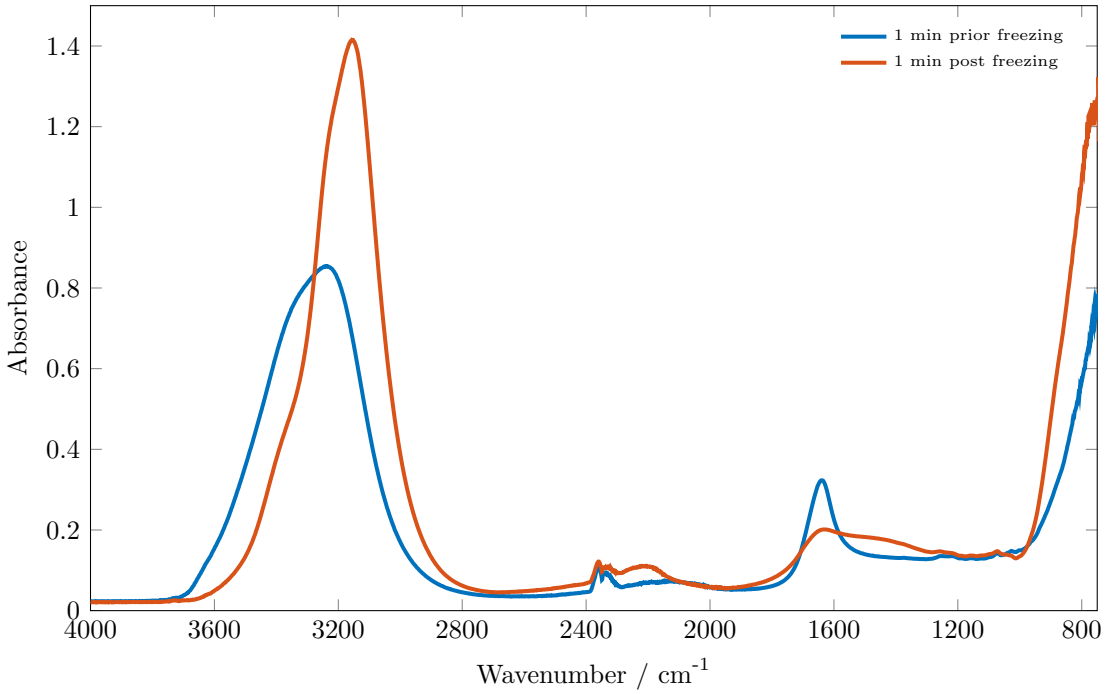

Figure 4.2: FTIR ATR spectra from pre- and post-freezing of 2 % ι-carrageenan, processed against diamond backgrounds of the correct temperature

following supercooling of the samples was initialised by the available nucleation points between each experiment, and variations in nucleation points leads to the differences mentioned above. An average freezing temperature of -9 °C was observed however extreme temperatures up to -7.5 °C and down to -12 °C were observed occasionally. The following discussions within this section comment on the post freezing perturbations of the system and it is important to note that the same post freezing effects were observed irrespective of the freezing temperature. This is assuming that freeze-concentration of the sample was not present; Section 2.1 demonstrates how the current system minimises the samples tendency to freeze-concentrate.

As the temperature was decreased, during the cooling phase (80 to -10 °C) the O-H stretch region of the infrared spectra changed as expected; the peak maxima shifting to lower wavenumbers due to the growth of a (lower wavenumber) component of the O-H stretch (*ca.* 3150 cm^{-1}). This change continued gradually down to the freezing event where a large step in absorbance

is observed, in accordance with what is expected.[170] The spectral changes occurring within the gelation of ι-carrageenan solutions is covered in Section 3.2.

To take a closer look at the fingerprint region of the spectra containing the carrageenan bands, it can be processed in one of two ways; to subtract a water (processed against diamond of correct temperature) spectrum away from a carrageenan sample (processed against diamond), or to process the carrageenan sample directly against the water single beam. In essence these two methods are the same, however the former introduces another variation into the processing chain; selecting the correct diamond temperature for each of the sample and solvent spectra. The other main difference between the two methods is that, when processing directly against water, no additional correction for the possible differences in water absorbances can be accounted for. For example, water may provide better ATR contact than the carrageenan solution due to the lower viscosity, producing a more absorbing sample and large residual water absorbance when processed directly against water. There is also the fact that the sample is no longer 100 % water, but 98 %, which could influence the baseline distortion as well as the intensity of absorbance of the O-H modes. The change of the sample's refractive index will also influence the absorption due to change in the effective depth of penetration of the evanescent wave (Figure 1.1). Section 2.2 explains this in detail, however unless stated otherwise, spectra within this section (Low Temperature Studies) will use the subtraction route, except difference spectra, which will be processed against a spectrum from within the spectral dataset under investigation, allowing only the changes in absorption to be viewed.

Figure 4.3 shows the pre- and post-freezing spectra, within the fingerprint region, of ι-carrageenan. Both spectra are very similar, indicating little change of the carrageenan's structure as the sample is frozen. The noise level within this plot is higher than a lot of the spectra to be shown within this chapter due to a reduction in the number of averages taken; increasing the time resolution, this is explained in Section 2. The spectra displayed here have been averaged for *ca.* 10 seconds at a 2 wavenumber resolution. It can be seen that there is very little change within

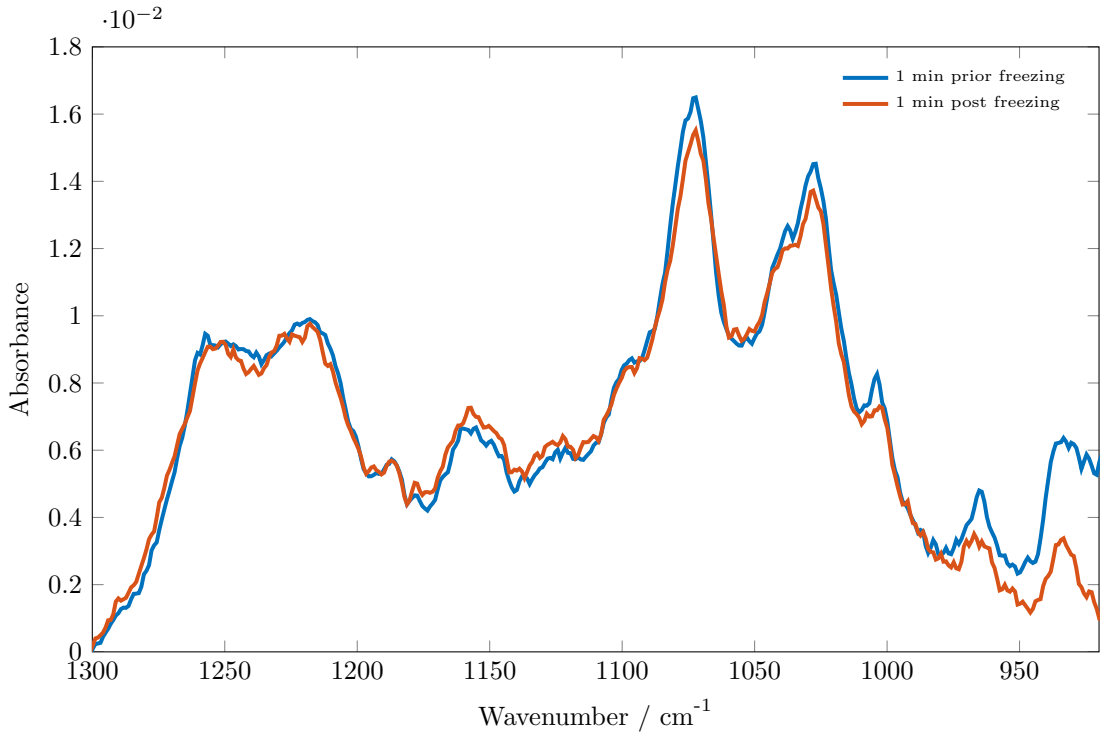

Figure 4.3: Spectra from pre- and post-freezing of ι-carrageenan, water spectra of correct temperature subtracted. Both spectra are at a temperature of *ca.* -10 °C.

the carrageenan region between the pre- and post-freezing spectra. The deviation towards the lower wavenumber end of the spectrum is due to the significant change in baseline between water and ice FTIR spectra.

After the sample has frozen the Juablo chiller keeps the sample compartment at a steady temperature. Spectra are continually collected for several hours. Figure 4.4 shows changes occurring within the carrageenan region over a period of 3 hours. There is a large band growth occurring as a function of time, when then sample is held at a steady temperature. This is surprising, as one would expect a frozen (*i.e.* solid) system to be steady state over these short time scales. These changes represent a change in the vibrational nature of the carrageenan bonds (as water has no vibrational modes in this region). This change could be related to an interaction with the ice surface, similar to those interactions seen by ice-binding-proteins (antifreeze proteins).[26,171]

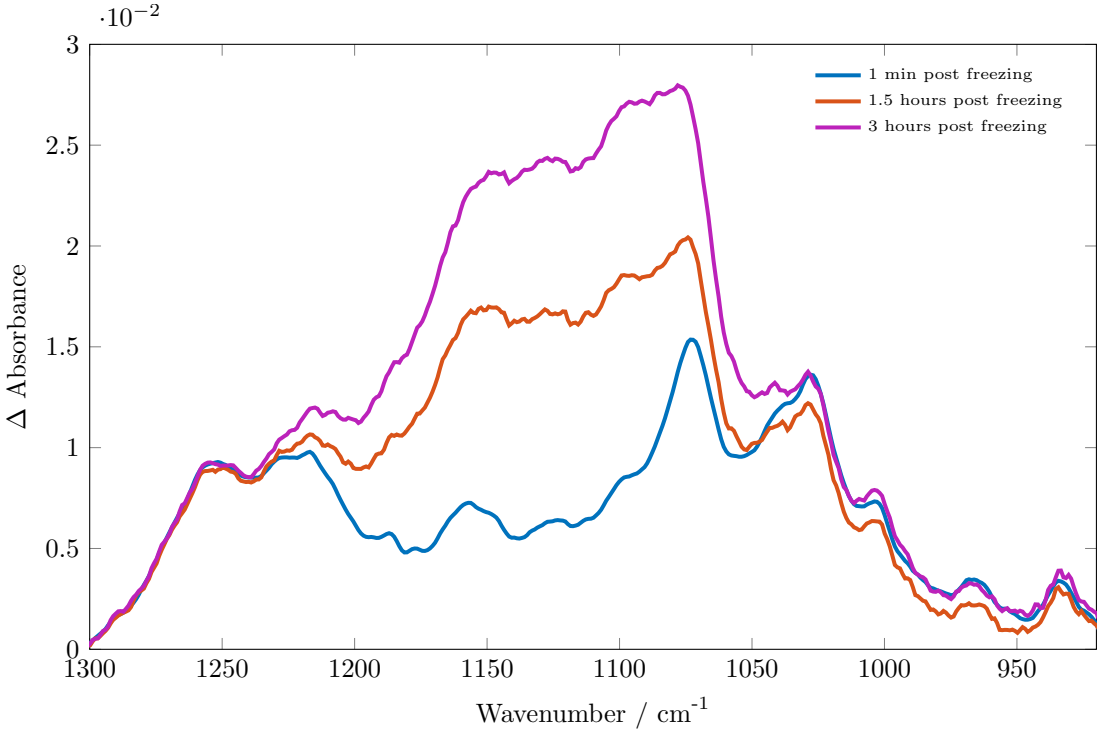

Figure 4.4: Spectra showing growth in ι-carrageenan region as a function of time following freezing of the sample, 1st order polynomial baseline applied

As we are only interested in analysing what has changed post-freezing relative to the sample's state prior to freezing, the majority of this chapter will be based around the analysis of difference spectra. Traditionally within FTIR spectroscopy this is done by subtracting one spectrum from another, however FTIR always produces a difference spectrum - spectra are calculated through taking a ratio of the sample single beams against a background power spectrum, *i.e.* one is observing the difference spectrum of before *vs* after a sample is placed within the beam path. Here we are collecting single beam (*i.e.* IR light throughput) spectra and calculating the ratio from a different time point within the same dataset. Figure 4.5 shows difference spectra, of the entire mid-IR spectral range, for ι-carrageenan as it is held at a constant temperature following freezing. The background for these spectra is a carrageenan single beam collected just after the sample has frozen.

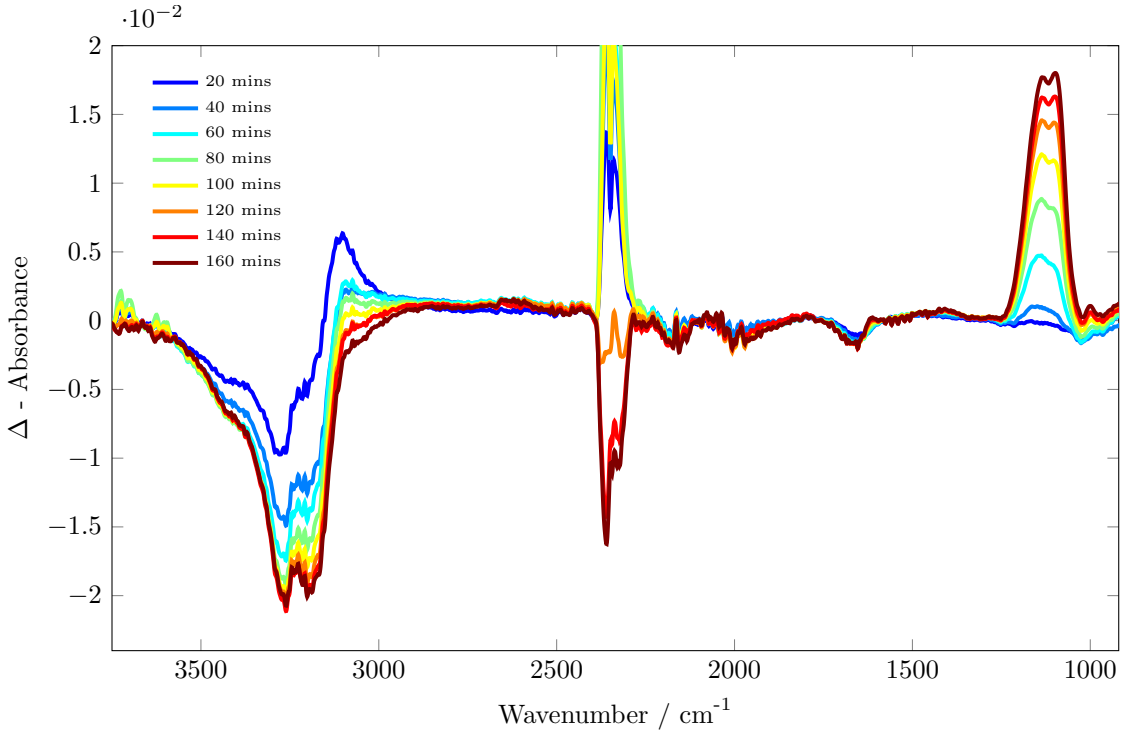

Figure 4.5: Difference spectra showing change in ATR FTIR as a function of time following freezing of 2% ι-carrageenan, 1st order polynomial baseline applied

Starting at the higher wavenumber portion of the spectrum (Figure 4.5), multiple changes

within the O-H stretch region can be observed. Over the period of 3 hours (blue → green → red trace colours) bleaching of a band with two maxima occur; 3265 and 3190 cm^{-1}, however its rate slows rapidly over the time period observed. A growth to lower energy (3110 cm^{-1}) is seen within the first 20 minutes, however there is no contribution observed in the later spectra. The spectral features of the O-H stretch here are much more defined than absorbance spectra seen within Chapter 3. The difference spectra allows us to investigate what is changing as a function of time while the system remains at a constant temperature. When investigating ice/water systems, the lower wavenumber section of the O-H stretch is normally associated with ice vibrations, and the higher wavenumber portion of the band to water based modes, this is due to the shift to a lower wavenumber as water freezes. This is investigated later within the chapter, however from this simple understanding it appears that we see slightly more ice based vibrations over the first 30 minutes post-freezing, and a gradual decrease in the water O-H stretch modes as the experiment proceeds. This approach is greatly oversimplified however, as the O-H stretch region is comprised of multiple modes and observing some of them changing may be due to a change in interaction with the ice crystal. The H-O-H bend mode at *ca.* 1650 cm^{-1} is also seen to have its higher wavenumber portion of the band significantly decrease while a small increase in absorbance is seen from the lower wavenumber part.

Large absorbance changes for CO_2 can be seen between 2400 and 2280 cm^{-1}, these are due to a current issue with the carbon dioxide scrubbers of our purge gas system (small CO_2 overtones can be seen at 3700 cm^{-1} as well). They vary periodically, in synchronisation with the purge cycles.

Substantial noise around the 2000 cm^{-1} mark can also be observed, this is due to the large diamond absorbance of the ATR crystal. Not only is there more noise within the middle section of the spectrum (1800 - 2700 cm^{-1}), a bleaching of two bands at 2000 and 2170 cm^{-1} can be seen; these are diamond's most intense absorptions. The water to ice transition changes the refractive index matching of the sample with the diamond, this leads to a change in the amount

of interaction the evanescent wave has with the diamond, showing a change in the absorption intensity. Throughout the entire mid-IR region the spectra are also quite noisy, the changes in absorptions are relatively small and, for most of the spectrum, we are in effect examining the spectrometer's 100 % line.

Finally, within the fingerprint region of Figure 4.5 lies a large change in absorbance following freezing, centered at roughly 1120 cm^{-1}. As there are no water-based vibrations within this region, the growth following freezing of the sample is presumed to be due to carrageenan. Figure 4.6 focuses on the fingerprint region of the spectra, showing the difference spectra post-freezing. The most apparent feature of this band is its broadness, which is not usually seen within the fingerprint region. It has a full-width-half-maximum (FWHM) of *ca.* 110 cm^{-1}, however there are clearly at least two bands which comprise the overall growth. The two bands can be visually located at 1137 and 1098 cm^{-1}. For both the water and carrageenan absorbencies, their change following freezing implies a change in the vibrational nature of the molecules. This could be due to a multitude of reasons, however it is clear that, once the system is frozen, following this specific cooling regime and system setup, it is not steady state and additional interactions within the system persist.

It has been shown that freezing of water / sugar solutions undergo perturbations post-freezing, these changes will undoubtably be vibrationally active as the water / ice ratio changes to reach the most thermodynamically stable state.[167] As the sample has been cooled past its freezing point (supercooled), the rate of crystallisation is much faster, producing smaller ice-crystals. For many years, the ice-cream industry has been exploiting the relationship between cooling rate and crystal size distributions to produce frozen food products with smaller crystal sizes.[140] Although complex, the changes of the O-H stretch and bend regions of the spectra are therefore not unexpected. However the changes seen within the fingerprint region suggest a change in confirmation or interactions of the biopolymers.

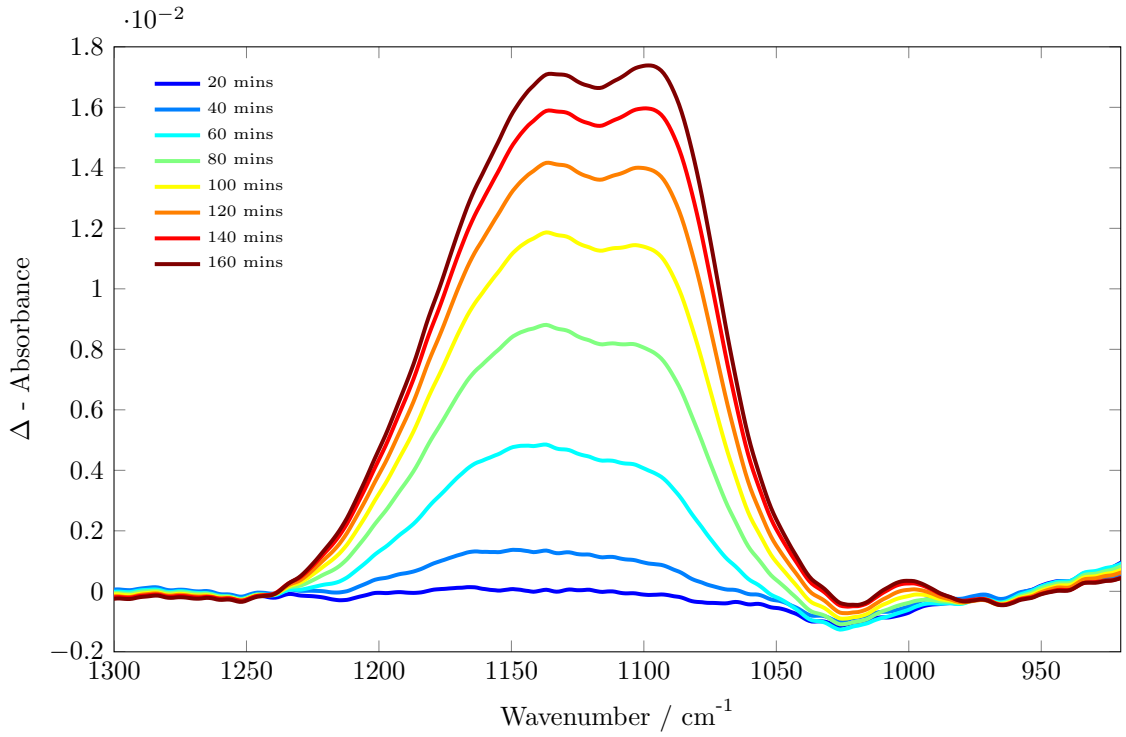

Figure 4.6: Difference spectra showing ι-carrageenan region as a function of time following freezing of the sample, 1st order polynomial baseline applied

Within Figure 4.6 it appears that the higher wavenumber band, *ca.* 1137 cm^{-1}, grows in faster than the lower wavenumber band. The spectrum at 60 minutes post freezing (cyan trace) shows the higher wavenumber portion more intense than the lower wavenumber part of the growth, at 160 minute mark however the lower wavenumber (1098 cm^{-1}) band appears more intense. To investigate this Figure 4.7 shows the change in Δ-absorbance values for the two peak maxima, 1137 and 1098 cm^{-1}, as a function of time post-freezing. Both bands grow in over time, in a sigmoidal nature, with the maximum rate occurring between 40 and 60 minutes. The growth is delayed between the bands however, with the 1137 cm^{-1} band increasing intensity prior to the lower wavenumber band, until about 120 minutes, where the 1098 cm^{-1} band catches up with the absorbance of the higher wavenumber band. Although fairly obvious that the change in absorbance within the fingerprint region of the spectra is due to more than one band, evidence provided by Figure 4.7, where two components of the growth change at slightly different rates, suggests that there is more than one underlying process. The difference in rates of change for the 1137 and 1098 cm^{-1} bands is not very large however, the difference could be attributed to non-optimal baselining routines. Further clarification on the multicomponent nature of this growth is needed. A smaller band to lower energy than the main body is also seen to increase in absorbance post-freezing. Although much less intense (and therefore noisy) the feature at 1004 cm^{-1}appears to be real.

As previously mentioned, the O-H stretch region of the spectra also shows changes in absorbance following freezing of the ι-carrageenan sample. A large bleaching with two minima at 3265 and 3190 cm^{-1} is seen, as well as a growth to lower wavenumber at 3110 cm^{-1} that is quenched after 20 minutes. Figure 4.8 shows the change in Δ-absorbance of these three bands as a function of time following freezing. The two higher wavenumber bands (blue and orange trace, 3265 and 3190 cm^{-1}) decrease in absorbance near identically, with an exponential decline in their rate of change. The lower wavenumber band (purple trace, 3110 cm^{-1}) is seen to increase in intensity for the first 5 minutes before decaying to a plateau. All 3 bands change

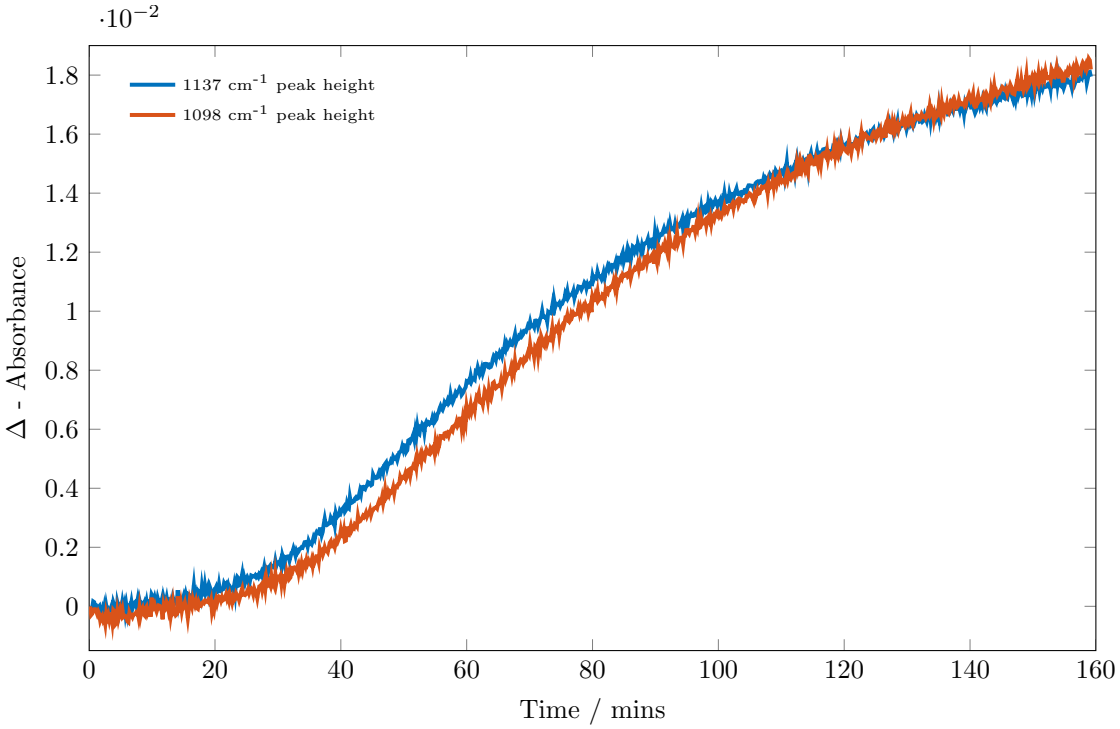

Figure 4.7: Height of difference spectra, for 1137 and 1098 cm^{-1} bands of ι-carrageenan post-freezing as a function of time, 1st order polynomial baseline applied

very little after 30 minutes, with barely no distinguishable change occurring post 100 minutes. This is unlike spectral changes seen in the fingerprint region (most likely) due to carrageenan where at $t = 30$ minutes post freezing the rate of change was still increasing. The difference in IR responses with respect to time, between the water and carrageenan regions implies that the spectral changes are due to more than one underlying process. For example, if the ice-crystal sizes were increasing for a short period of time following freezing and the carrageenan network was being pushed out of the way then the rate of change of the carrageenan and water based vibrations would be similar. As this is not the case it suggests that, although possibly linked, the perturbations of the water/ice and carrageenan are due to different processes. These conclusions give weight to the suggestion that ι-carrageenan may be interacting with the ice crystals and play more than just a spectator role during the freezing (and recrystallisation) process.

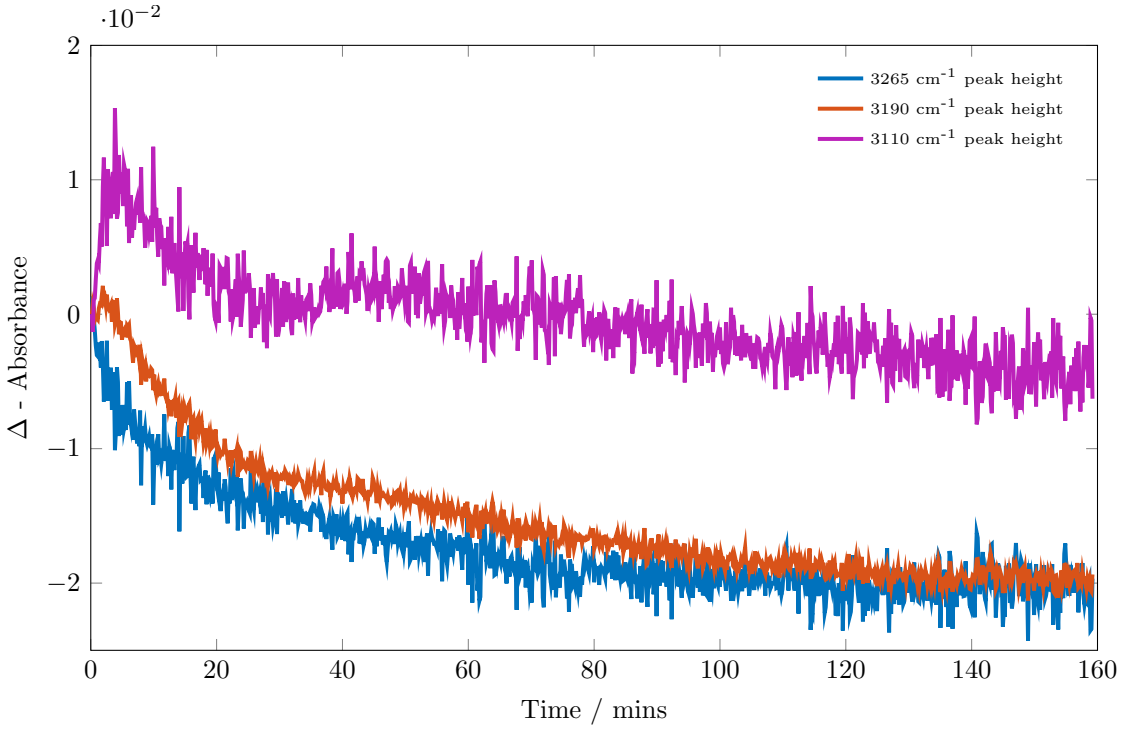

Figure 4.8: Height of difference spectra, for 3265, 3190 and 3110 cm^{-1} bands of OH stretch within the ι-carrageenan system post-freezing as a function of time, 1st order polynomial baseline applied

4.2.1 Principal Component Analysis

Principal component analysis is a useful tool for deconvoluting overlapping bands that have different origins. The loadings produced from PCA are mathematically orthogonal, meaning that as the system undergoes perturbation (time post-freezing in this case) the loading vectors will represent spectral features that change independently of each other. Although the orthogonality of a PCA model is mathematically stringent, the lack of true orthogonal components within a system being studied (or just the complex nature of the system) can often lead to confusion of the model, and analysis must be done carefully. The PCA analysis of an example system was performed in Section 1.2.3.

4.2.1.1 Entire MIR Spectral Region

As we are interested in the time dependant post-freezing nature of the ι-carrageenan system, the difference spectra, as shown in Figure 4.5, are passed into the PCA algorithm. The O-H stretch and fingerprint region of the spectra are of the most interest, therefore the other regions have been removed prior to analysis. As mentioned in the previous section these regions contain significant CO_2 contamination and excess noise from the low throughput over the diamond absorbencies. Removal of these infrared regions not only allows for a simpler interpretation, but reduces the uncorrelated variation that might confuse the PCA algorithm. For example the CO_2 bands increase and decrease regularly due to the 20 minute purge cycle of our compressor system. The analysis would "lock-on" to this regular variation and dilute the information that we are attempting to extract; the water and carrageenan. The wavenumber regions used for analysis are 3570-2700 cm^{-1} (O-H stretch) and 1400-960 cm^{-1} (fingerprint). Inspection of Figure 4.5 in relation to these regions shows that the vast majority of clutter was removed prior to analysis.

Figure 4.9 shows the root-mean-square error of calibration (RMSEC) and the root-mean-square error of cross-validation (RMSECV) per principal component number of the ι-carrageenan

system post-freezing. Utilising these curves allows us to select the number of principal components to be investigated. The blue trace (RMSEC) shows that no addition reduction in RMS error is achieved by using more than 3 PCs. The cross validation was done in a venetian blind fashion using 90 % of the data. The RMSECV (orange trace) shows plateauing at both 3 and 6 principal components, indicating that the majority of the information within the post-freezing system can be explained within the first three principal components, however there is slightly more information that is worth exploring within PCs 4 to 6.

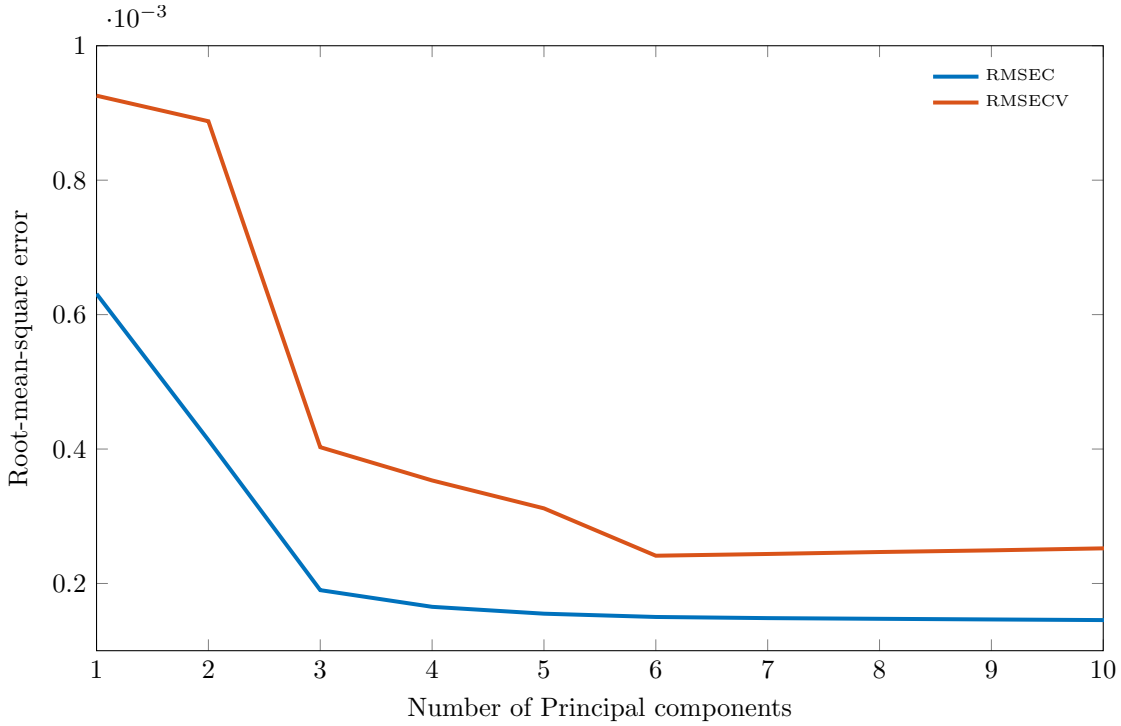

Figure 4.9: RMSEC and RMSECV for PCA analysis per number of principal components for PCA of ι-carrageenan difference spectra post-freezing, held at -10 °C, monitored by ATR-FTIR spectroscopy, RMSECV calculated using a venetian blind 10 % data exclusion

Principal components 1 to 3 capture 98.74 % of the variance within the data, and inclusion of up to 6 components captures 99.21 % of the data. For clarity, these two sets; PCs 1-3 and PCs 4-6, have been split into two separate figues; Figures 4.10 and 4.11 respectively. The top plot in each of these figures shows the principal components (loadings) and the bottom plot

shows the associated scores for each principal component as a function of time post-freezing.

By analysing the O-H stretch region of the first 3 principal components (Figure 4.10, top plot), several bands can be observed. Although loadings 1-3 show different maxima for the change in the water's O-H stretch as a function of time post-freezing, it is clear that PCA has not extracted the pure fundamental vibrations as the loadings are comprised of more than one Gaussian/Lorentzian band, *i.e.* shoulders are observed. The implication of this observation is that the changes in the nature of the H_2O's vibration post-freezing are not due to a perturbation a single vibrational mode. Although water accounts for 98 % of the system's composition, the presence of the carrageenan means that a lot of the water molecules are acting as if they were not in bulk solution. This is easily demonstrated by the fact that carrageenans form gels; transforming the bulk solution properties of water into an entirely new material. On the micro scale, carrageenan contains multiple different functional groups (per repeating unit) that interact with water, and the solvation of these biopolymers undoubtably results in a large variety of perturbations to the O-H stretch of water. The gelation of carrageenan, as discussed within Section 3.1 shows macroscopic changes of the biopolymer's interaction with water, such as aggregation and formation of helices. These features will also have an effect on the solvating water molecules as well.

Principal components 1-3 show three main maxima and minima within the O-H stretch region of the loading; 3265, 3174 and 3120 cm^{-1} of loadings 2, 1 and 3 respectively. As previously seen with the absorbance spectra of pre- and post-freezing systems (Figure 4.2), when water freezes to ice, a lower wavenumber feature, centered at *ca.* 3150 cm^{-1} grows in, dominating the O-H stretch region. For the maxima / minima features of loadings 1 to 3, this corresponds the 3174 and 3120 cm^{-1} features of loadings 1 and 3 appear either side of this, suggesting these principal components are observing changes in the ice structure. The maxima of component 2 (orange trace) is centered at 3265 cm^{-1}, however a minima at lower wavenumber is also observed. This component somewhat resembles a difference spectrum that one would expect as ice transitions

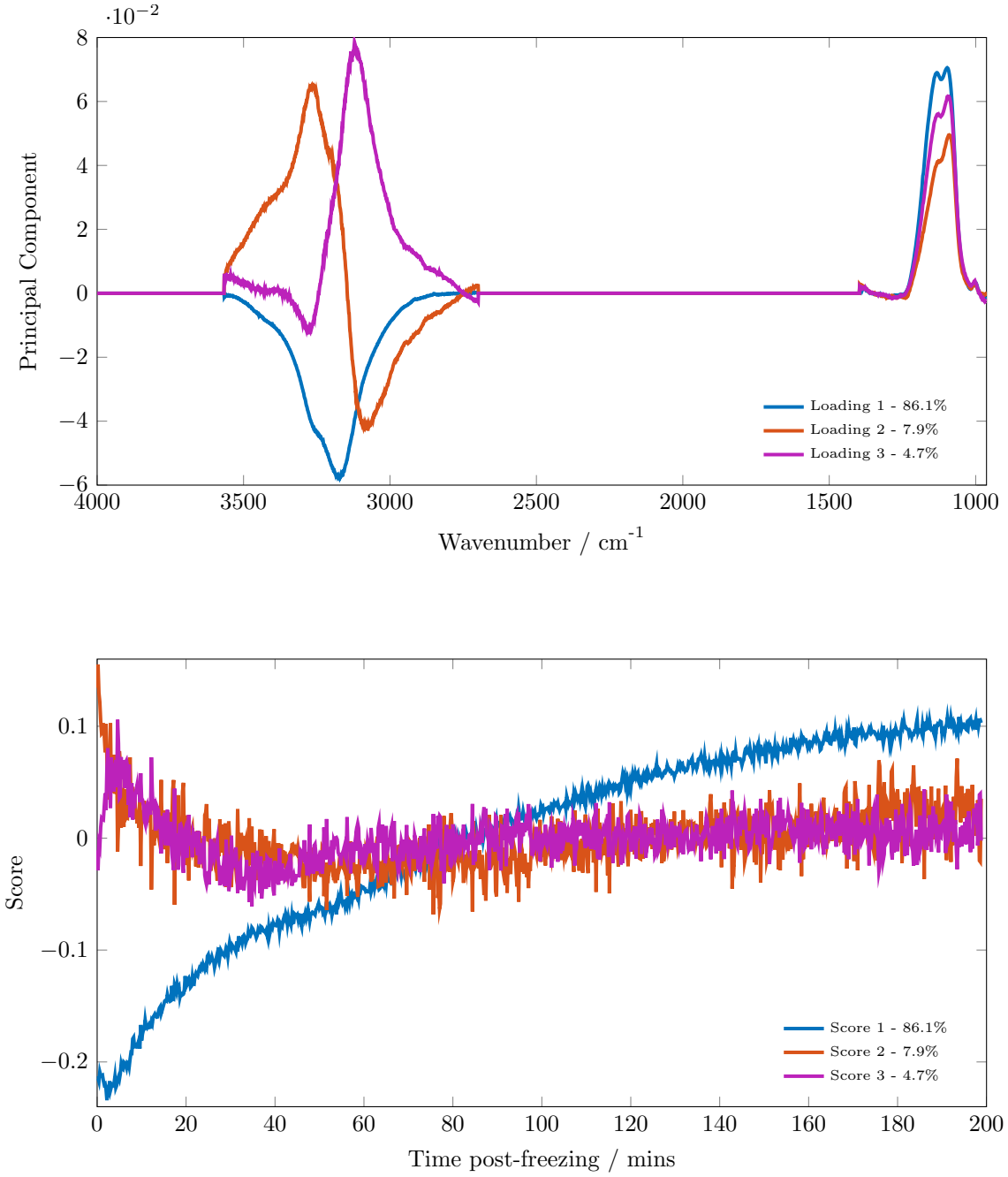

Figure 4.10: PCA Loadings and Scores (top and bottom), for PCs 1-3 of ι-carrageenan post-freezing, held at -10 °C as monitored by ATR-FTIR. Input spectra as Figure 4.5; difference spectra post-freezing, O-H stretch and fingerprint region only. Preprocessing: 1st order polynomial baseline and mean-centering

to water; *i.e.* a lower wavenumber bleach and a higher wavenumber growth within the O-H stretch band. Examination of the scores of loading 2 (bottom plot, Figure 4.10, orange trace) shows an exponential-like decay over the first 40 minutes post-freezing, and little change after this. The scores plot demonstrates how the respective loadings vary with the perturbation. The decrease of score for loading 2 effectively shows a decrease of the lower wavenumber portion of the O-H stretch and an increase of the higher wavenumber section, suggesting that over the first 40 minutes, water continues to freeze to ice.

At the point of freezing the ι-carrageenan system is supercooled to about *ca.* -10 °C. Freezing happens comparatively quicker compared to a non-supercooled system. A portion of the water molecules is solvating the biopolymer and post-freezing as the system attempts to reach its most thermodynamically stable state loading two could be observing the removal of solvating water molecules into the surrounding ice structures. Conclusions drawn here must be very tentative however, especially as the PCA model is not based solely on the O-H stretch region, but includes the fingerprint region as well.

Within the fingerprint region of Figure 4.10, all three loadings show a two band growth, centred at 1137 and 1098 cm^{-1}. This feature was previously highlighted in Figure 4.6. Loading 1 shows the two bands to be in equal ratio, however loadings 2 and 3 show the lower wavenumber component to be more intense. As these two loadings show a difference in intensity of the two bands comprising the growth within the carrageenan region, it is to be expected that there is a difference in the rate of growth between the two bands. Within principal component analysis however, there theoretically shouldn't be two loadings showing (near) identical features. Components 2 and 3 (orange and purple), within the fingerprint region show very similar traces, and within the O-H stretch region their traces appear inverted. The maxima of loading 2 matches the minima of loading 3, and the minima of loading 2 matches the maxima of loading 3. Although the shape of each individual loadings are not identical to one another the similarities suggest confusion of the PCA model. The O-H stretch region and fingerprint region are separated and

models calculated for each later in this section.

The scores plot of Figure 4.10 shows an event occurring before 5 minutes, as scores for loadings 1 and 3 (blue and purple) appear to sharply change direction at about the 5 minute mark. Due to the mathematical confusion within the model however, it wouldn't be prudent to assign spectral origins for this change as it occurs over a relatively small percentage of the total variation. Scores 2 and 3 show little change after 40 minutes after freezing and although there is disruption of the rate of change of score 1 at *ca.* 40 minutes, the contribution from the first loading continues to change over the duration of the experiment at a decreasing rate.

Figure 4.11 shows principal components 4-6 of the PCA model for the entire spectral range. Although it has already been suggested that this particular model suffers from mathematical confusion it can bee seen within the scores plot (bottom) that events are observed at *ca.* 5 and 40 minutes. The O-H stretch region of the loading plot (top) shows multiple structured components within the three loadings, however loadings 4-6 only capture 0.47 % of the data's total variance. The fingerprint region of the loadings shows a difference like spectrum, with positive and negative components to the growth observed, within all three loadings. This implies that within the two band growth in the fingerprint region the two bands grow at a different rate. To investigate this further the data was split into two sections; the O-H stretch region and the fingerprint region. PCA analyses of these splits was pursued independently.

4.2.1.2 Fingerprint Region

For the fingerprint region, data from 960 to 1300 cm^{-1} of the ι-carrageenan system, post-freezing was baselined with a linear 1st order polynomial prior to PCA analysis. Examination of the RMSECV plot showed no further decrease in cross validated RMS error when 3 or more components were used to model the system. The first two components captured 99.94 % of the variance and inspection of latter loadings showed little but noise. Figure 4.12 shows the first

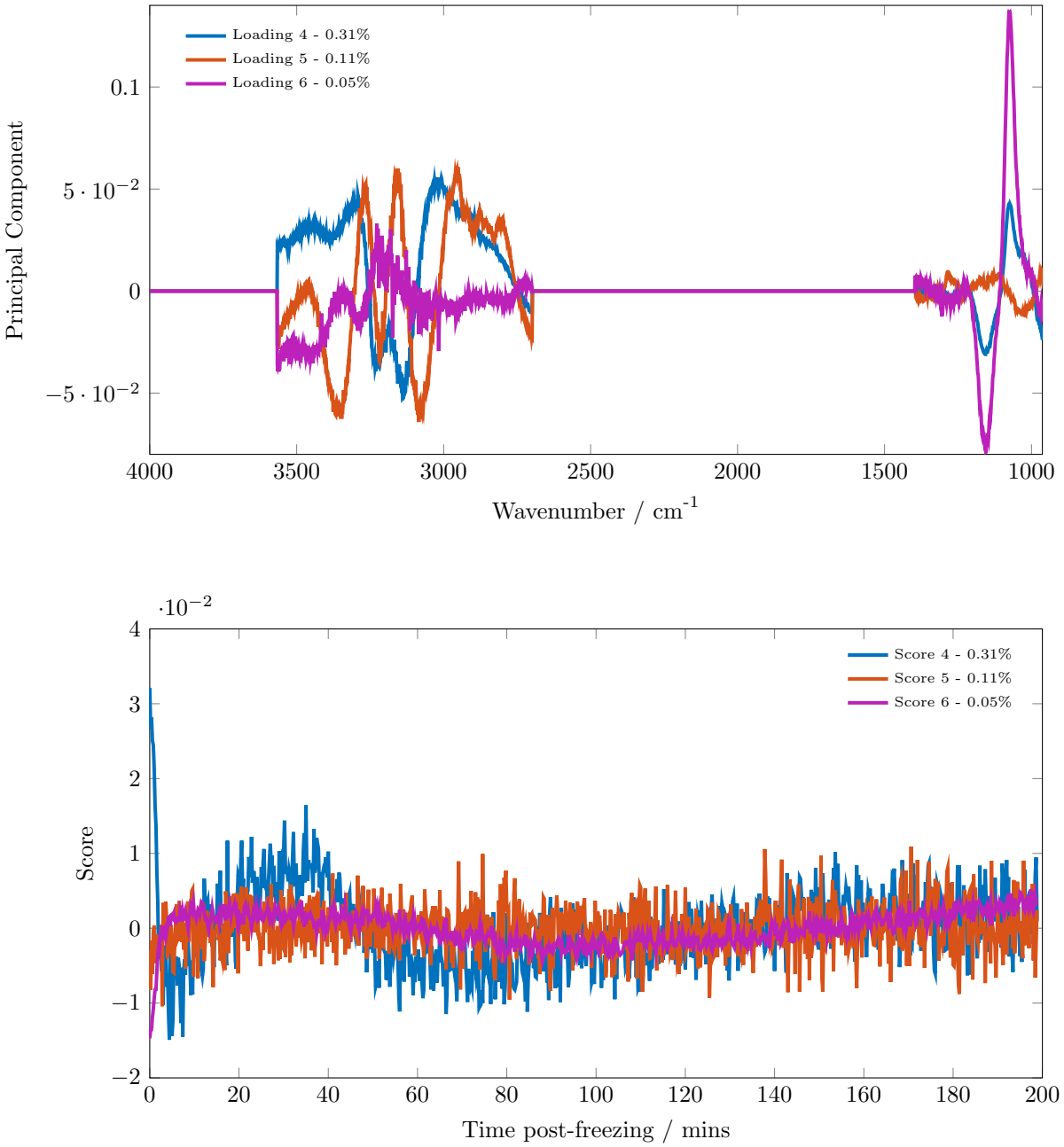

Figure 4.11: PCA Loadings and Scores (top and bottom) of ι-carrageenan post-freezing, for PCs 4-6 held at -10 °C as monitored by ATR-FTIR. Input spectra as Figure 4.5; difference spectra post-freezing, O-H stretch and fingerprint region only. Preprocessing: 1st order polynomial baseline and mean-centering

two loadings (top plot) and scores (bottom plot) for the PCA model. The first loading (blue trace, top plot) is near identical to the growth found in the original data (see Figure 4.6. Over the first 40 minutes post-freezing, this loading is not seen to change significantly. Interestingly, this corresponds to the 40 minute event that was observed within the PCA model of the entire spectral region. After 40 minutes, the loading increases in intensity, with a gradually decreasing rate for the remainder of the experiment. Relating this back to the original data, the analysis implies that the band shows little growth over the first 40 minutes, then increases its absorbance rapidly. Although a plateau was not observed within the timeframe of the experiment, the exponential-like decrease in growth rate suggests the curve (blue trace, bottom plot) is rapidly approaching an asymptote.

The second loading of Figure 4.12 (orange trace) only contains 0.3 % of the data's variance. Both positive and negative contributions are seen to this loading. The negative portion of loading 2 appears at the same wavenumber as the higher wavenumber peak of loading 1, while the positive component is very close in energy to the lower wavenumber peak of loading 1. The score of loading 2 (orange trace, bottom plot) shows a decrease in intensity from *ca.* 40 to 80 minutes, then gradually recovers over the remainder of the perturbation until it's score is the same as the start. The shape of loading 2 implies that as one band increases, the other decreases. However, to understand the loadings variation in relation to the spectra, both loadings must be considered simultaneously. Loading 1 increases over time, demonstrating a 2 band growth, during this growth loading 2 decreases over the first 80 minutes, then increases. The negative higher wavenumber and positive lower wavenumber components of loading 2 are therefore an inverted representation of what is occurring (because the score is decreasing) over the first 80 minutes. As a function of time (over the first 80 minutes) the higher wavenumber component of the band is seen to increase, and the lower wavenumber portion decreases. The outcome of the interplay between loadings is that during the growth of this two-band feature, the higher wavenumber portion is seen to increase more than the lower wavenumber band. From 80 minutes

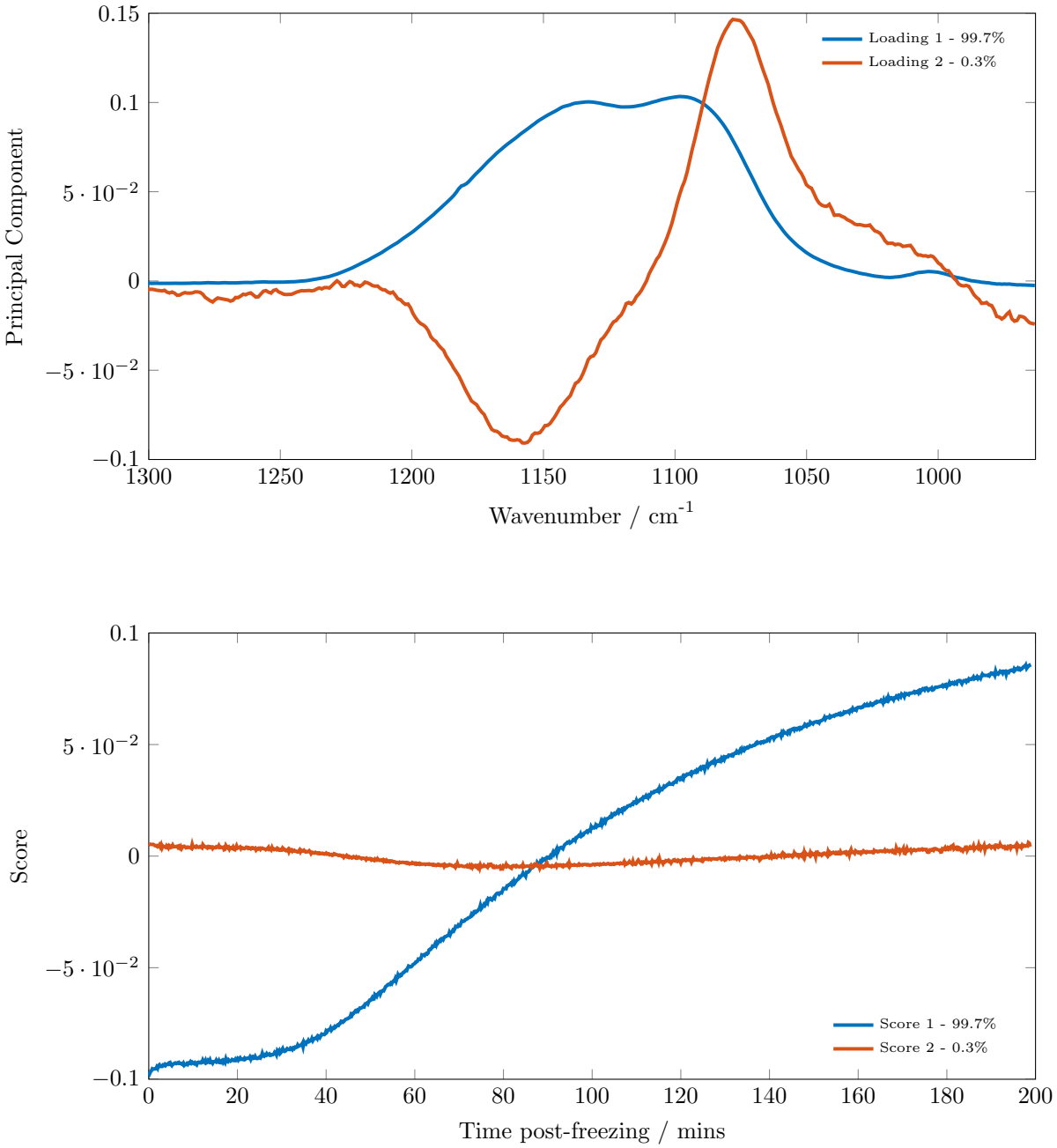

Figure 4.12: PCA Loadings and Scores (top and bottom) of ι-carrageenan post-freezing, held at -10 °C as monitored by ATR-FTIR, from 1300 to 960 cm^{-1}. Input spectra as Figure 4.5; difference spectra post-freezing, preprocessing: 1st order polynomial baseline and mean-centering

onwards the opposite is true, the lower wavenumber band increases at a faster rate than the higher wavenumber band.

As loading 2 contains both positive and negative components, indicating that the two bands within the overall growth change in different directions, it can be concluded that the two bands that comprise the overall growth are not intrinsically linked to one another. Their rate of growth is not identical, suggesting more than one underlying process. Unfortunately, as PCA extracts mathematically orthogonal components and not individual bands, the absolute difference in growth rates cannot be determined. Principal component analysis is a hugely useful exploratory technique, and the information found within this section infers properties of the iterative band fitting procedures used within Section 4.2.4.

The location of these two bands is directly within other absorbencies for carrageenan, this is nicely displayed within the original data of Figure 4.4. Even with the overall band being deconvoluted, *via* PCA, into two separate bands, they are still relatively wide for fundamental vibrations within this region of the spectrum.

4.2.1.3 O-H Stretch Region

For the O-H stretch region of the spectrum, data from 3570 to 2700 cm^{-1} was utilised for the difference spectra post-freezing of the ι-carrageenan system. To the lower wavenumber side of the O-H stretch, all the Δ-absorbances are captured, however the tailing higher wavenumber side is cut slightly short. This is due to the CO_2 overtone at *ca.* 3570 cm^{-1}. As previously mentioned, the systematic, time dependant variation of the CO_2 absorbance due to the purge-gas cycling would cause the PCA algorithm to lock-onto this variation, diluting and confusing the O-H stretching information.

Figure 4.13 shows the loadings (top plot) and scores (bottom plot) for the PCA analysis of the O-H stretch region of the spectrum post-freezing. The RMSECV plots suggested 3 principal

components and although inspection of latter PCs appeared to show some information, the loadings were very noisy and there was large confusion and inversion of multiple features at similar wavenumbers. The scores of latter PCs also appeared to show no overall trend across the data, indicating a randomness to their variation. Three principal components captured 98.21 % of the variance within the model.

The scores of all three components show an event at *ca.* 5 minutes. The time dependant score of loading 3 (purple trace, bottom plot) shows little change after the first 5 minutes, although with closer inspection a decrease is seen at *ca.* 40 minutes. Score 2, although very noisy, shows a very similar response, a large initial change from $t = 0$ to $t = 5$, leading to a gradual change at *ca.* 40 minutes before becoming constant. The score of loading 1 is also subject to change between $t = 0$ and $t = 5$ and undergoes a small change of rate at 40 minutes, however over the course of the experiment, continues to change with an exponential-like decrease of its intensity. The first loading accounts for 85.8 % of the data's variance, and in general, is seen to decrease at a decaying rate during the experiment. It is possible that the changes in rate of score 1 at $t = 5$ and $t = 40$ are due to PCA model confusion, rather than a distinct event, that affects all orthogonal components in the same way.

Loading 1 (blue trace, top plot of Figure 4.13) identifies the main component that is lost as a function of time post-freezing. This was seen clearly within the original data (Figure 4.5) A maxima is apparent at 3175 cm^{-1} with a shoulder centered at *ca.* 3265 cm^{-1}. These positions are the same as the three main maxima of the loading from the PCA model of the entire spectral range, Figure 4.10. The minimum of loading 2 (orange trace) is also centered at 3265 cm^{-1} with its maximum at 3100 cm^{-1}. As mentioned before, repeated features such as these can sometimes suggest confusion of the model. Principal component 3 shows a doubly peaked feature with centres at 3235 and 3145 cm^{-1}.

In comparison to the time dependant changes seen within the fingerprint region, both the O-H

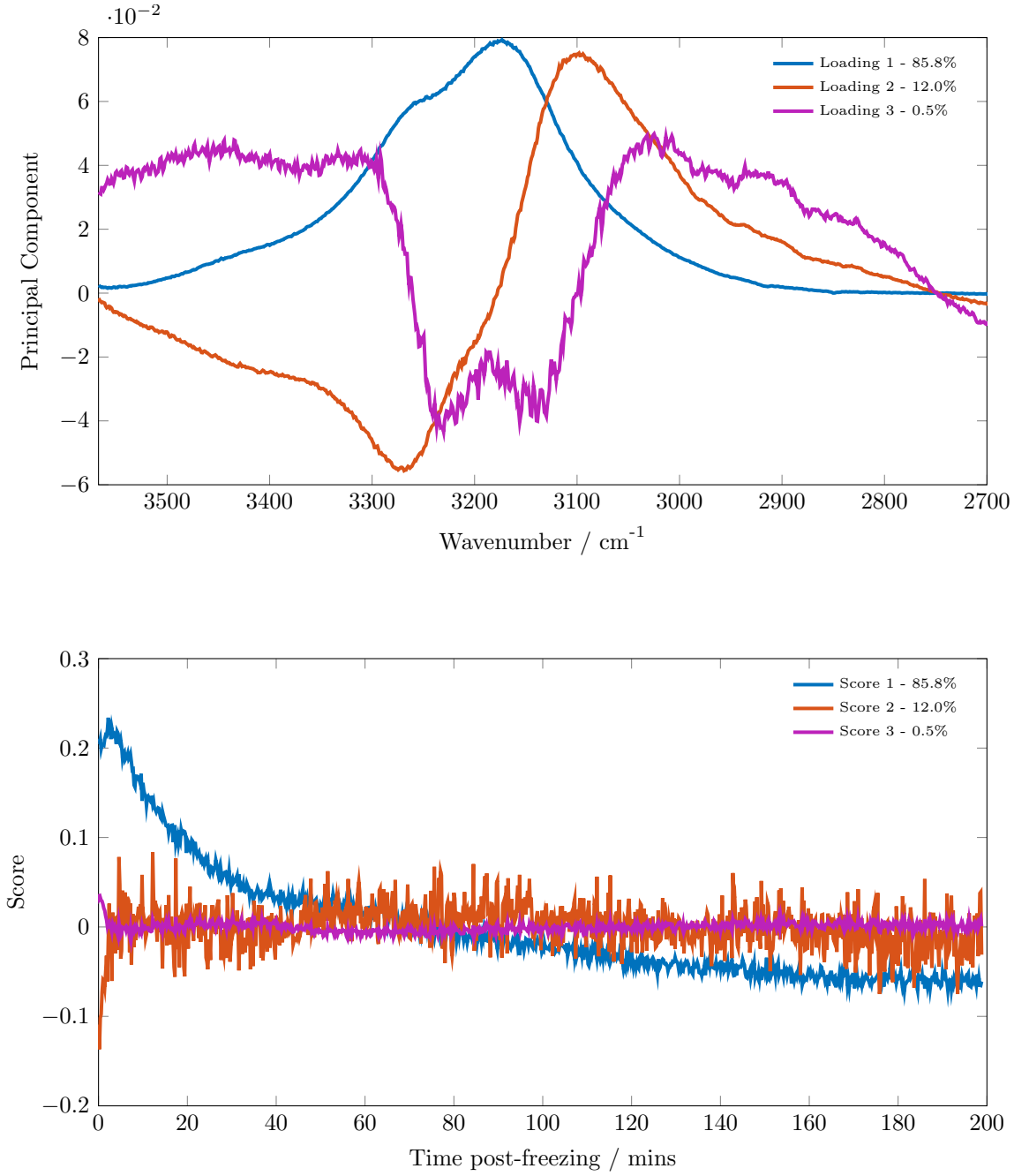

Figure 4.13: PCA Loadings and Scores (top and bottom) of ι-carrageenan post-freezing, held at -10 °C as monitored by ATR-FTIR, from 3570 to 2700 cm^{-1}. Input spectra as Figure 4.5; difference spectra post-freezing, preprocessing: 1st order polynomial baseline and mean-centering

stretch and carrageenan absorbencies show a synchronised change at *ca.* 40 minutes, however only the O-H stretch region displays a large spectral perturbation between $t = 0$ and $t = 5$. This suggests that the response at $t = 40$ could be due to one or both of the solvent or solute, however as only the O-H stretch region observes changes at before $t = 5$, this perturbation is water based. Infrared spectroscopy is not all-encompassing however, the lack of spectral change within a region does not guarantee there is no molecular change, although the $t = 0$ to $t = 5$ timeframe does appear to be water-centric.

When the O-H stretch and fingerprint region data were concatenated together (Figures 4.10 and 4.11 at the beginning of this section) the PCA modelling procedure attempted to find loadings that changed independent of each other. The results found when the modelling was done on the individual regions, the analysis helped to highlight why the original approach was not as successful. Although the perturbations observed within the O-H and carrageenan regions appear to be synchronised; an event at *ca.* 40 minutes and a gradual rate-decay over the course of the experiment, changes occurring before 5 minutes were only observed within the O-H stretch region. Parts of the spectral variation were linked together however others were independent. This lack of orthogonality of the data (*i.e.* sometimes orthogonal and sometimes synchronised) resulted in confusing PCA results that were difficult to interpret.

Although multivariate curve resolution (MCR) is a powerful tool for the extraction of chemical information from complex systems using a PCA based approach, it cannot be used effectively here. The primary reason for the use of MCR over that of PCA, in relation to IR spectroscopy is its ability to model pure-component spectra, rather than mathematical variation. This is because the MCR components (equivalent to PCA loadings) have more spectral relevance due to the non-negativity constraints imposed within the algorithm. As we are examining difference spectra, with both positive and negative parts, the resulting MCR components would have little relevance as they cannot model the negative portion of the Δ-absorbance.

The application of MCR algorithms to the carrageenan portion of the spectrum can be achieved, as no negative bands are observed. However the analysis solely revealed what was already learnt from the PCA deconvolution: the higher wavenumber portion of the band changes at an increased rate compared to the lower wavenumber band. It is also worth mentioning that MCR analysis of the O-H stretch region was carried out through increasing the baseline offset of the data, so that no portions were negative. In practice this works efficiently as circumventing the non-negativity constraints of the algorithm, in an attempt to extract data, however no additional information, compared to the PCA modelling, was found.

4.2.2 Two-Dimensional Correlation Spectroscopy

Two-dimensional correlation spectroscopy (2DCOS) is a useful tool for exploring data, often aiding in visual interpretation by spreading data over an addition dimension through the use of a complex correlation function. The methodology and interpretation of 2DCOS is described in Section 1.3.1. The real component of the correlation highlights regions of the spectra which are susceptible to change. The complex part of the correlation (referred to as the asynchronous/imaginary spectrum) identifies spectral regions changing out of phase, *i.e.* at a different rate to one and another, this is particularly useful at separating overlapping bands from different sources.

Principal component analysis revealed several components within the post-freezing difference spectra that appeared to change at different rates. In this section, 2D correlation analysis will be used in an attempt to understand the spectral correlations and differences of the post-freezing system. Although PCA analysis of the entire spectral region (minus CO_2 and diamond contributions) suggested orthogonal components that contained both O-H stretch region and fingerprint region bands, there was significant confusion (repeated instances of near identical features) that suggested some of this correlation is not unique and the relationship between the O-H region and fingerprint region might not be strong. 2D correlation analysis allows us to probe the correlation between these different spectral features and analyse if the O-H region and fingerprint region features are changing in the same manner.

4.2.2.1 Entire MIR spectral Region

The difference spectra from the post-freezing 2 % ι-carrageenan system, as shown in Figure 4.5 has been utilised, without the CO_2 absorbances. Data from 3570 to 2700 cm^{-1} and 1300 to 960 cm^{-1} was augmented and passed through the 2DCOS algorithm (see Section 5.6).

Figure 4.14 shows the autopower spectrum, overlaid with the mean spectrum of the ι-carrageenan system post freezing. The correlation utilised data from $t = 0$ to $t = 200$ minutes. An au-

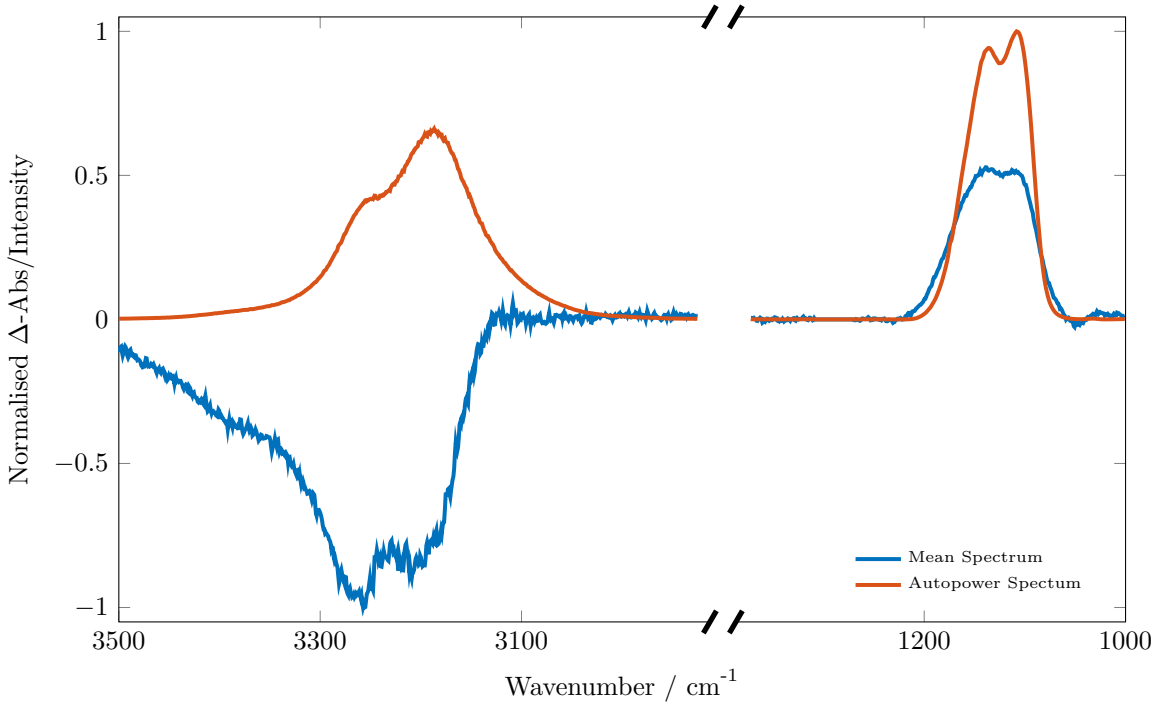

Figure 4.14: Autopower and mean spectra from FTIR data of ι-carrageenan, post-freezing; $t = 0$ to $t = 200$, held at -10 °C, spectral window: 3570 to 2700 cm^{-1} and 1300 to 960 cm^{-1}

topower spectrum is extracted from the diagonal axis of the synchronous correlation ($\nu_1 = \nu_2$). This mathematically correspond to the autocorrelation function of spectral intensity variations during the perturbation. At a particular ν the magnitude of the autopeak represents the extent of the variation during the perturbation.

The fingerprint region of Figure 4.14 shows a slight sharpening of the band for the autopower spectrum, compared to the mean spectrum. For systems undergoing a perturbation, autopower spectra can often provide a resolution enhancement.[123] Interestingly the lower wavenumber peak within this band growth is slightly more intense, suggesting that it undergoes a larger change than the higher wavenumber band.

Figures 4.15 and 4.16 show the synchronous and (modified Noda's rule) asynchronous two-dimensional correlation spectra. The synchronous spectrum shows simultaneous changes of spectral intensity variations between $t = 0$ and $t = 200$ of the 2 % ι-carrageenan system post freezing. Positive regions indicate that the spectral intensity variations occurring at (ν_1, ν_2) are in the same direction, while negative peaks show spectral feature changing in opposite directions. Within Figure 4.15, the negative cross peaks (blue), centred at (3200 cm^{-1}, 1050 cm^{-1}) and (1050 cm^{-1}, 3200 cm^{-1})indicate that the the spectral intensity variation within the O-H and fingerprint regions, although their change in simultaneous, it is in the opposite direction. This confirms observations of the raw data, a post-freezing decay within the O-H stretch region and a growth within the fingerprint region.

The asynchronous spectrum, displayed in Figure 4.16, allows investigation of the spectral dataset through separation of spectral intensity variations that occur out of phase with one another. Figure 1.10 within Section 1.3.3 explained the use of modified Noda's rules. These rules, that have been applied to all asynchronous spectra within this Section, allow simplification of their interpretation. A positive peak (red) indicates ν_1 changing before ν_2, and a negative (blue) peak shows that spectral intensity variates at ν_1 occur after ν_2.

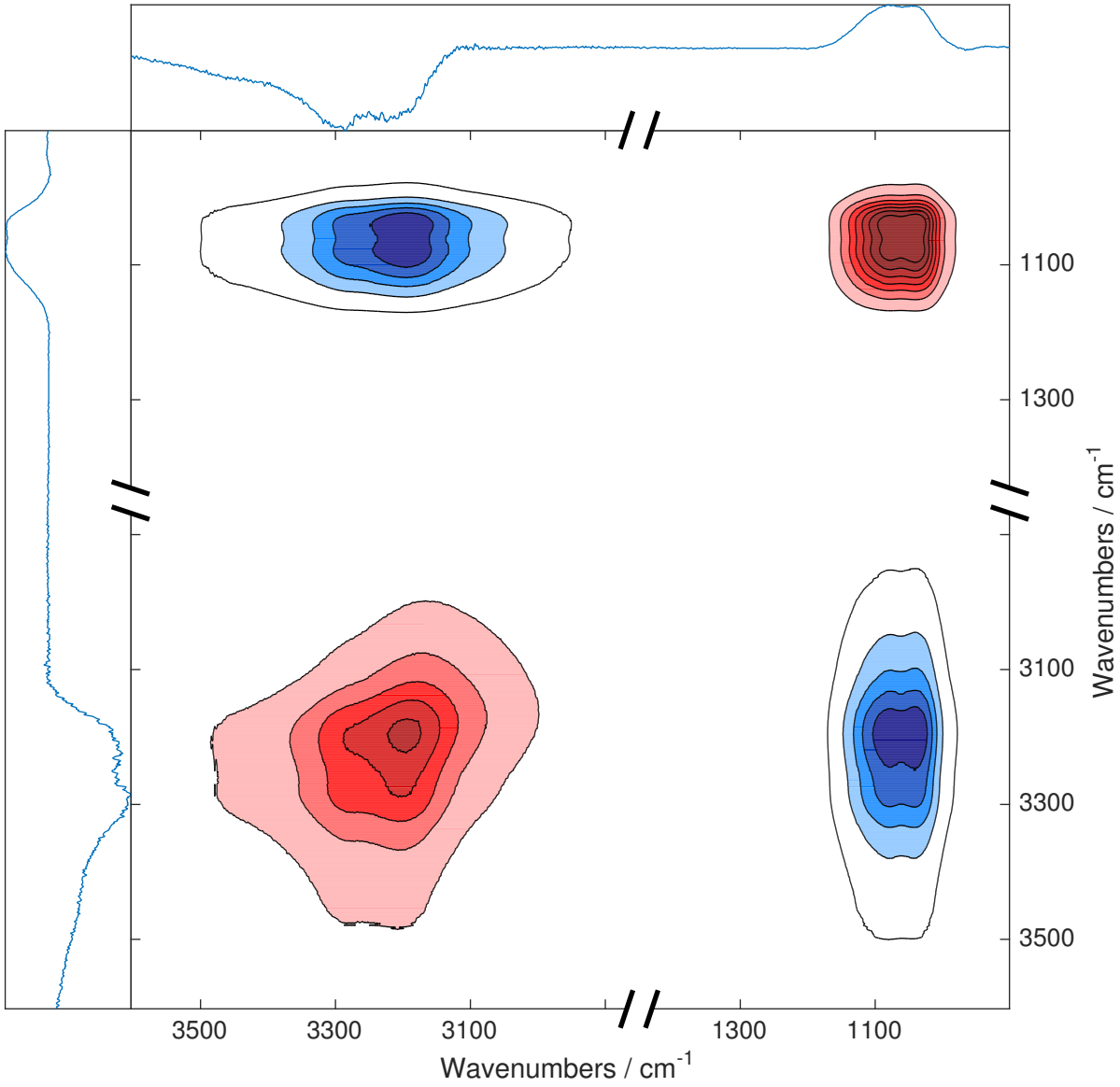

Figure 4.15: 2DCOS synchronous correlation map of ι-carrageenan, post-freezing; $t = 0$ to $t = 200$, colourmap: blue-white-red; negative-0-positive

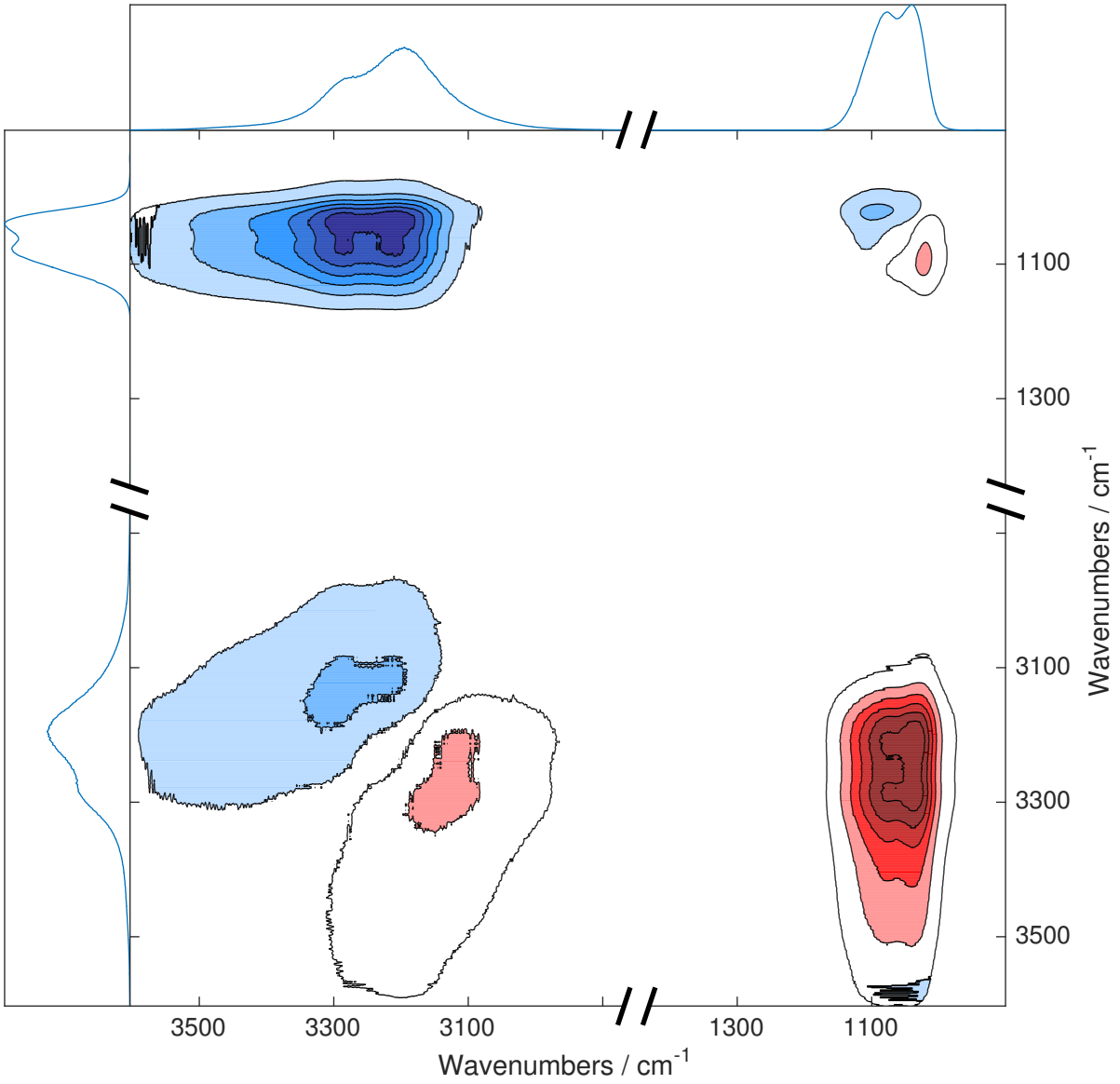

Figure 4.16: 2DCOS asynchronous (Modified Noda's rules) correlation map of ι-carrageenan, post-freezing; $t = 0$ to $t = 200$, colourmap: blue-white-red; negative-0-positive

The cross peaks of Figure 4.16, located at (3200 cm^{-1}, 1050 cm^{-1}) and (1050 cm^{-1}, 3200 cm^{-1}) shows the carrageenan band (1050 cm^{-1}) changing before (and at a different rate) to the O-H stretch band (*ca.* 3250 cm^{-1}). This is in somewhat contrast to the results produced by PCA, where the growth of the band in the fingerprint appeared to lag behind the decay of the water band. It is important to remember during interpretation of Figures 4.15 and 4.16 that the time window used for the analysis was $t = 0$ to $t = 200$ post-freezing, *i.e.* the entire experiment. The asynchronous spectrum from 2DCOS analysis will identify spectral intensity variations that occur out of phase and indicate the order of change, however the variation is observed for the entire time window. Although there might be small intensity variations occurring within the water region before the carrageenan region, the majority of the variation within the dataset occurs at 1050 cm^{-1} before 3250 cm^{-1}.

Cross peaks are also observed within each band of Figure 4.16. The southwest quadrant of the plot shows the intra-asynchronous-correlation of the O-H stretch region, and within the northeast quadrant the carrageenan band can be observed. Both of these features shows asynchronous peaks, implying multiple components within each band that change at a different rate as the system is held at -10 °C post freezing. The contour lines, and richness of colour indicate the intensity of the correlation. The intra-peak asynchronous correlations are less intense than the inter-peak correlation; *i.e.* $\Psi_{mod}(OH, carrageenan) > \Psi_{mod}(OH, OH) \wedge \Psi_{mod}(carrageenan, carrageenan)$. This indicates that although there are out of phase changes within each band, the differences in rate between the carrageenan and water regions is much more significant, over the 200 minutes post freezing.

4.2.2.2 O-H Stretch Region

The following figures of the 2DCOS section have split the data into two separate regions prior to analysis; 3570 to 2700 cm^{-1} and 1300 to 960 cm^{-1}. This will allow a more in depth look at the intra-band changes, as the differences in rate between the O-H stretch and fingerprint regions

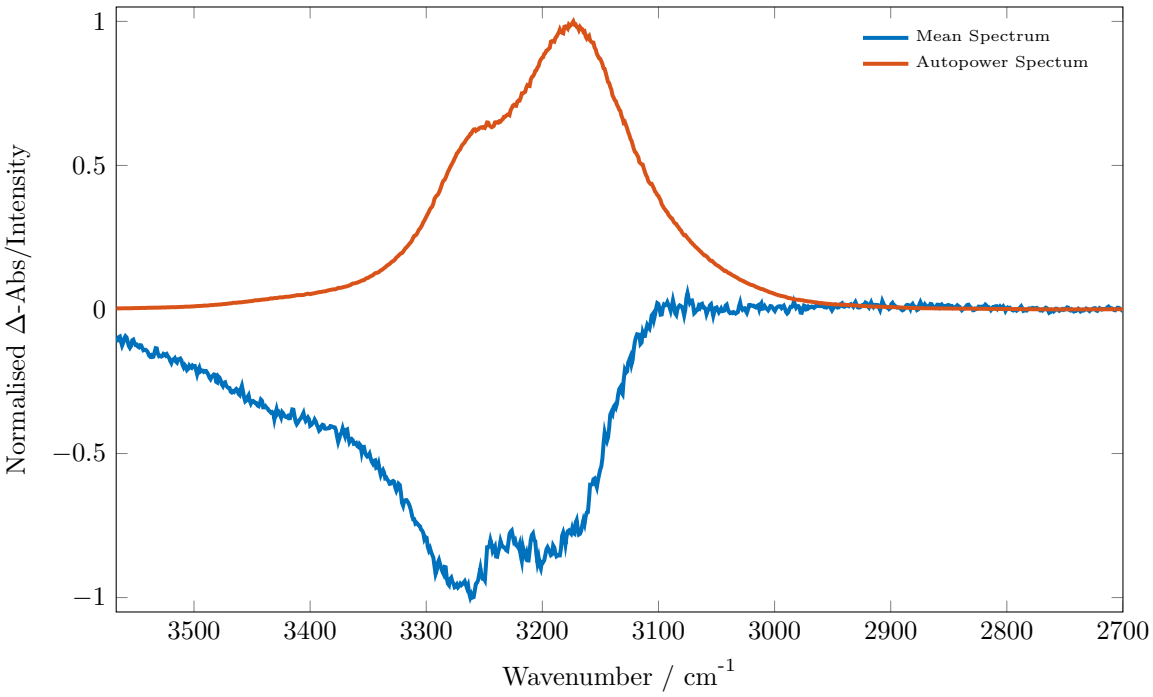

Figure 4.17: Autopower and mean spectra from FTIR data of ι-carrageenan, post-freezing; $t = 0$ to $t = 200$, held at -10 °C, spectral window: 3570 to 2700 cm^{-1} and 1300 to 960 cm^{-1}

dominates the correlation. Figure 4.17 shows the autopower and mean spectra for the O-H stretch region (3570 to 2700 cm^{-1}) post freezing for $t = 0$ to $t = 200$. The autopower spectrum shows a peak centered at 3175 cm^{-1} with a shoulder to higher wavenumber at 3260 cm^{-1}. These two components of the autopower spectrum match the two peaks of the mean spectrum, however their intensities are inverted. The mean spectrum shows the higher wavenumber band to be slightly more intense, however the autopower spectrum shows that the lower wavenumber band (3175 cm^{-1}) is more susceptible to change over the course of the experiment. The lower wavenumber trailing edge of the mean spectrum approaches zeros in a sharper fashion than the autopower spectrum which has a more of a trailing edge. Referring back to the original data (Figure 4.4), it can be seen that within the first 20 minutes there is a growth at 3310 cm^{-1}. As the overall change within the O-H region is a bleach, the mean spectrum is distorted slightly by the 3110 cm^{-1} growth.

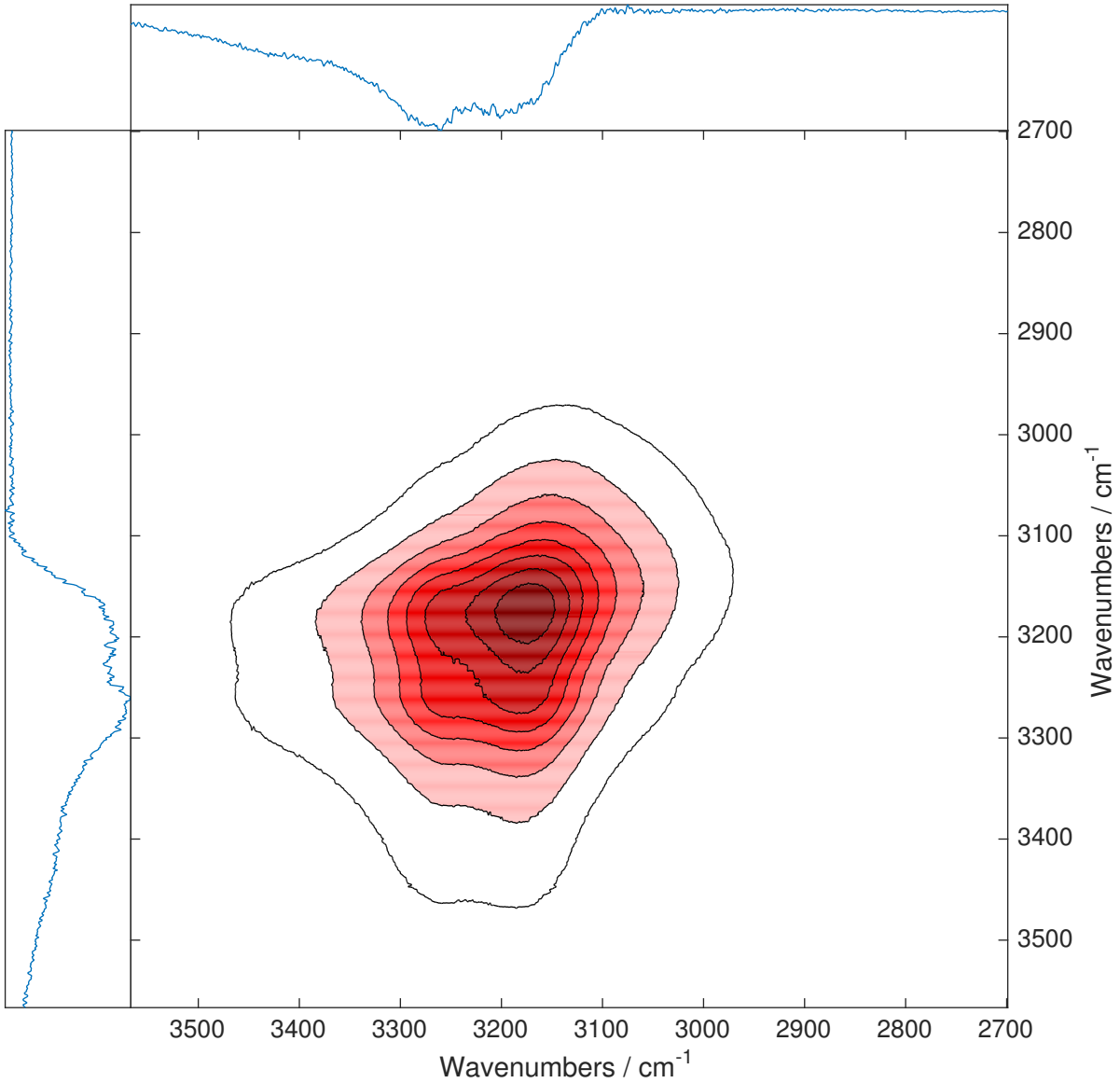

Figure 4.18: 2DCOS synchronous correlation map of ι-carrageenan, post-freezing; $t = 0$ to $t = 200$, held at -10 °C, spectral window: 3570 to 2700 cm^{-1}, colourmap: blue-white-red; negative-0-positive

The two-dimensional synchronous correlation spectrum for the O-H region is shown in Figure 4.18. No negative (blue) datapoints are observed, indicating that all wavenumbers change in the same direction (if they are observed to change at all). At first impression, this is in contradiction to the raw data (and PCA analysis), where a band at 3110 cm^{-1} is seen to grow, while the majority of the O-H stretch region decays in absorbance. However, it is important to remember that the 2DCOS analysis displayed here if for $t = 0$ to $t = 200$ after freezing of the ι-carrageenan system. Although data show a growth at 3110 cm^{-1} within the raw data, this only lasted for *ca.* 20 minutes, with the remaining time (180 minutes) of the experiment, this spectral region decreased in absorbance. PCA analysis indicated this event only occurred up to 5 minutes post-freezing, the vast majority of the time the feature at 3110 cm^{-1} was decreasing in intensity, along with the rest of the O-H region. Therefore 2DCOS analysis correctly extracted that the direction of change from $t = 0$ to $t = 200$ is all in the same direction. To highlight the time dependant nature of this system, the synchronous 2DCOS map of the O-H stretch region has been recalculated within a smaller spectral window - $t = 0$ to $t = 10$ minutes.

Figure 4.19 shows the synchronous correlation of the frozen system for the first 10 minutes post-freezing. Both positive (red) and negative (blue) areas are present, indicating that some spectral features change in different directions to one another. The southeast quadrant shows a negative band, where ν_1 changes in a different direction to ν_2. A spectral feature centred at 3110 cm^{-1} changes in the opposite direction to features from 3500 to 3200 cm^{-1}. For the first 20 minutes after freezing, growth of the 3110 cm^{-1} feature is observed, however this is not observed for the majority of the experiment. Although it is possible that the molecular vibration responsible for the 3110 cm^{-1} change in absorbance continues for the remainder of the experiment, and is obscured by the Δ-absorbance of another vibrational mode, the time-averaged results is the overall reduction in absorbance at 3110 cm^{-1}. The confusion within the 2D spectra is a result of a non-linear spectral response over the observed time period and this highlights that although 2DCOS is a hugely powerful technique, care must be taken when interpreting the

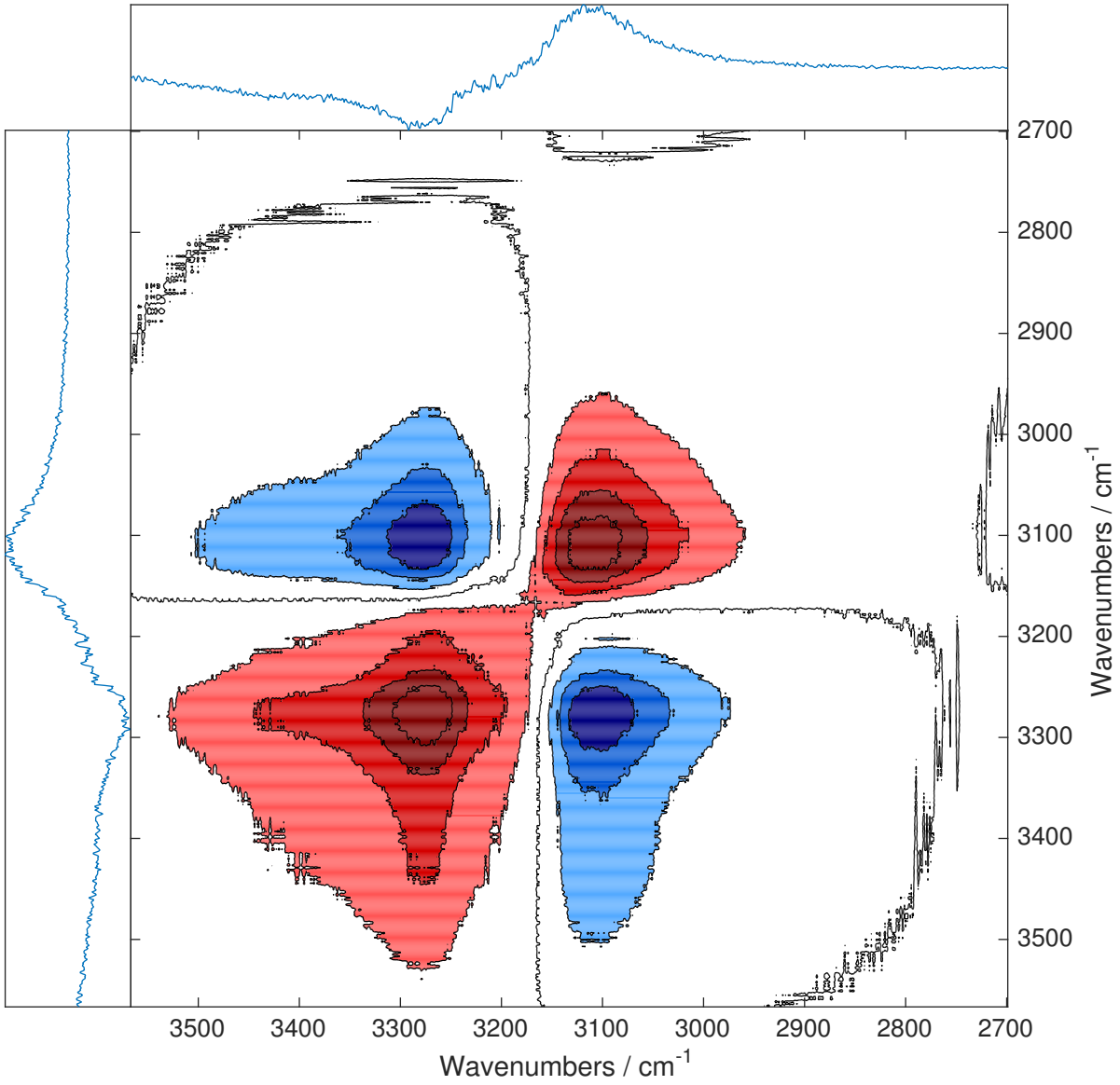

Figure 4.19: 2DCOS synchronous correlation map of ι-carrageenan, post-freezing; $t = 0$ to $t = 10$, held at -10 °C, spectral window: 3570 to 2700 cm^{-1}, colourmap: blue-white-red; negative-0-positive

results of real (non-linear) spectral systems.

Figure 4.20 shows the (modified Noda's rules) asynchronous correlation spectrum of the O-H region, for the entire post-freezing experiment, $t = 0$ to $t = 200$. Positive and negative cross peaks shows component changes within the O-H stretch occurring at different rates. In general, the spectrum shows the lower wavenumber components of the band changing before the higher wavenumber components. Although the synchronous (for $t = 0$ to $t = 200$) spectrum did not identify the opposite direction of the 3110 cm^{-1} band compared to the rest of the spectrum, the asynchronous spectrum suggests an out of phase change for this component. As seen within the raw data and PCA analysis as well, this feature shows large intensity variations in the first 20 minutes. Little change is observed after at 3110 cm^{-1}, however other components change at a decaying rate as the experiment proceeds.

4.2.2.3 Fingerprint Region

Figure 4.21 shows the autopower spectrum, within the fingerprint region, for ι-carrageenan held at -10 °C post freezing, from 0 to 200 minutes. Two maxima for the autopower spectrum are observed at 1133 and 1098 cm^{-1}. As noted within the autopower spectrum of the entire mid-IR spectral region, although the higher wavenumber band has a larger Δ-absorbance value, the lower wavenumber band shows more susceptibility to change over the course of the experiment, *i.e.* the lower wavenumber peak is more intense within the autopower spectrum. Within the raw data a smaller peak to lower energy than the main band, at *ca.* 1000 cm^{-1}, is also seen to change slightly during the experiment and can be observed in the mean Δ-abs trace (blue) of Figure 4.21 as well. Although the autopower spectrum appears to show no response in this region, re-adjustment of the scaling shows a very clear peak at 1004 cm^{-1}.

The synchronous spectrum is shown in Figure 4.22, In accordance with the raw data, the entire doubly peaked band changes in the same direction. The plotting variable that controls

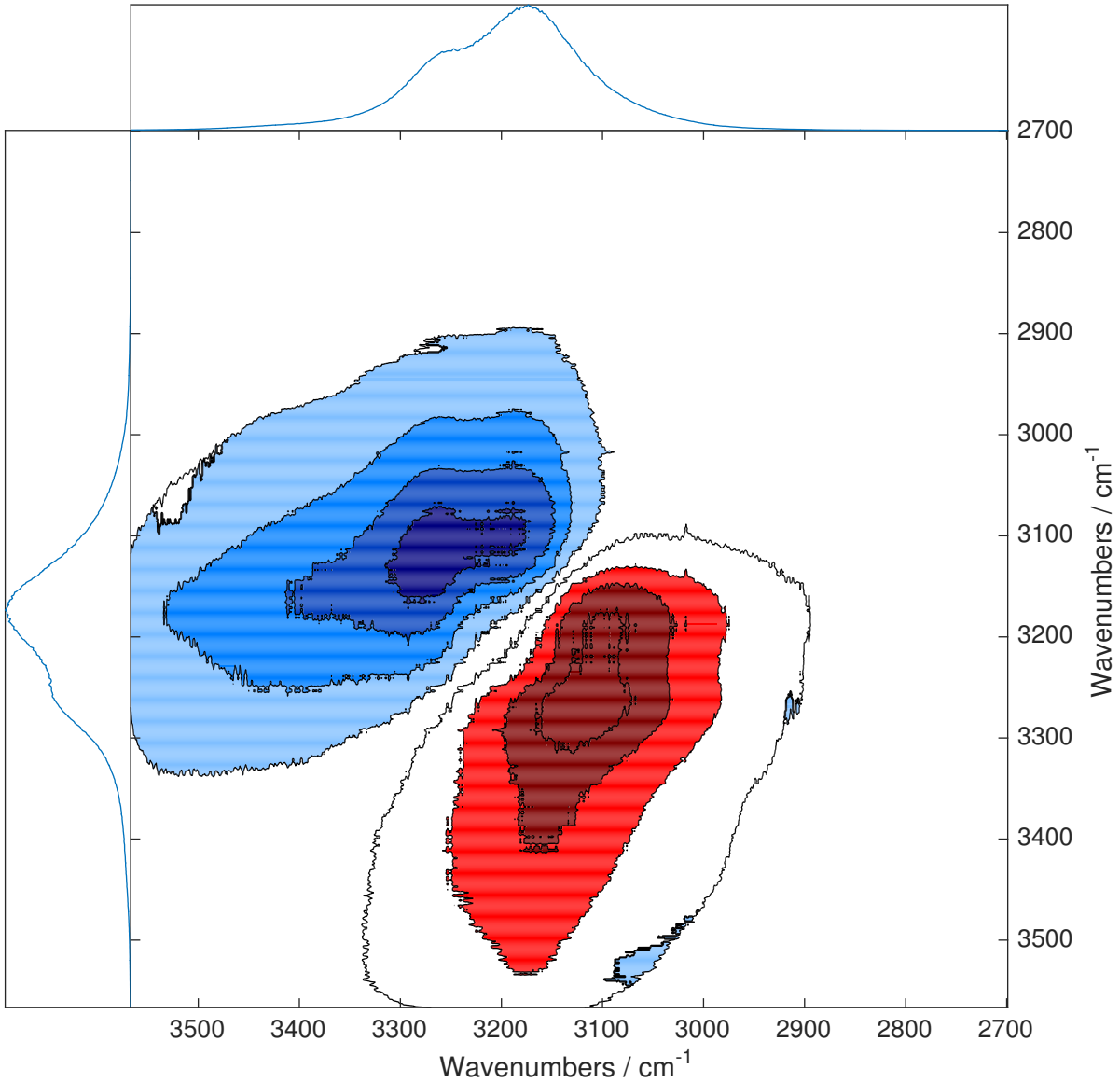

Figure 4.20: 2DCOS asynchronous (Modified Noda's rules) correlation map of ι-carrageenan, post-freezing; $t = 0$ to $t = 200$, held at -10 °C, spectral window: 3570 to 2700 cm^{-1}, colourmap: blue-white-red; negative-0-positive

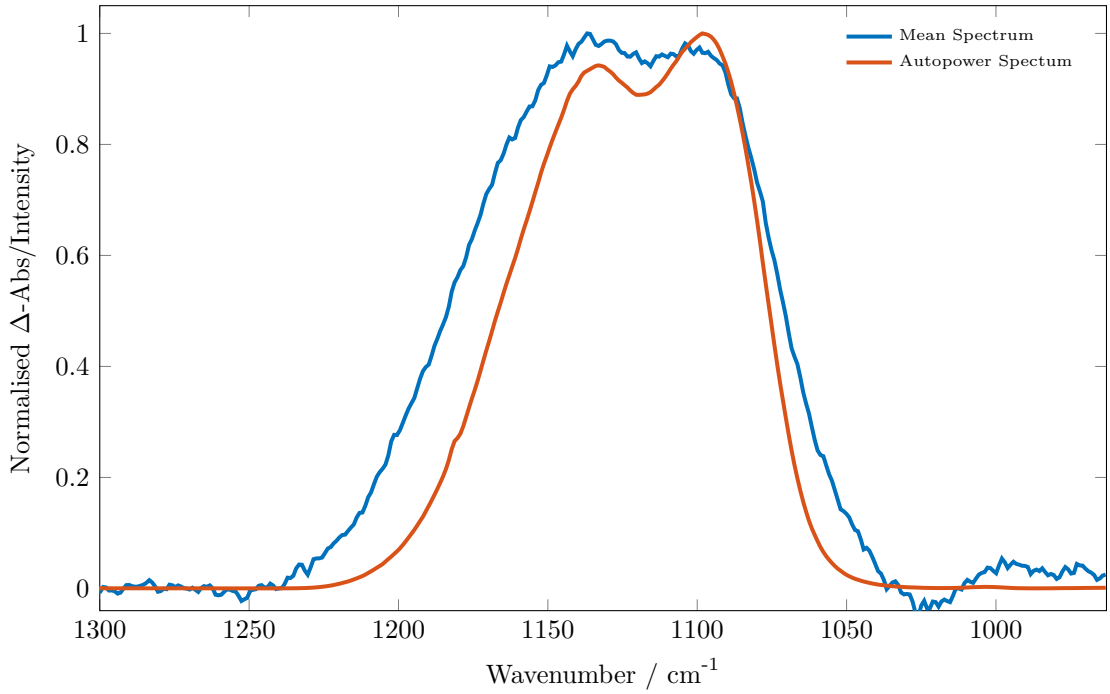

Figure 4.21: Autopower and mean spectra from FTIR data of ι-carrageenan, post-freezing; $t = 0$ to $t = 200$, held at -10 °C, spectral window: 1300 to 960 cm^{-1}

the number of contour levels to draw has also been increased within this figure compared to others. The increase allows the observation of the simultaneous (and same direction) change of the two main peaks (1133 and 1098 cm^{-1}), with the smaller band to lower energy (1004 cm^{-1}). See the variable "contour_level" within Section 5.10 for more information.

The asynchronous spectra (modified Noda's rules) for the post-freezing two-dimensional correlation of the fingerprint region is shown in Figure 4.23. The positive (red) area shows the lower wavenumber band changing before and at a different rate, to the higher wavenumber band. The 1080 cm^{-1} band can been seen to change before and out of phase to the feature between 1200 and 1100 cm^{-1}. The plot also helps to identify the band profiles of the underlying components. The red area, centered at (1080 cm^{-1}, 1150 cm^{-1}) is elongated in the vertical axis. This suggests that the ν_1 (1080 cm^{-1}) component, has a smaller spectral width that the ν_2 (*ca.* 1150 cm^{-1}) component.

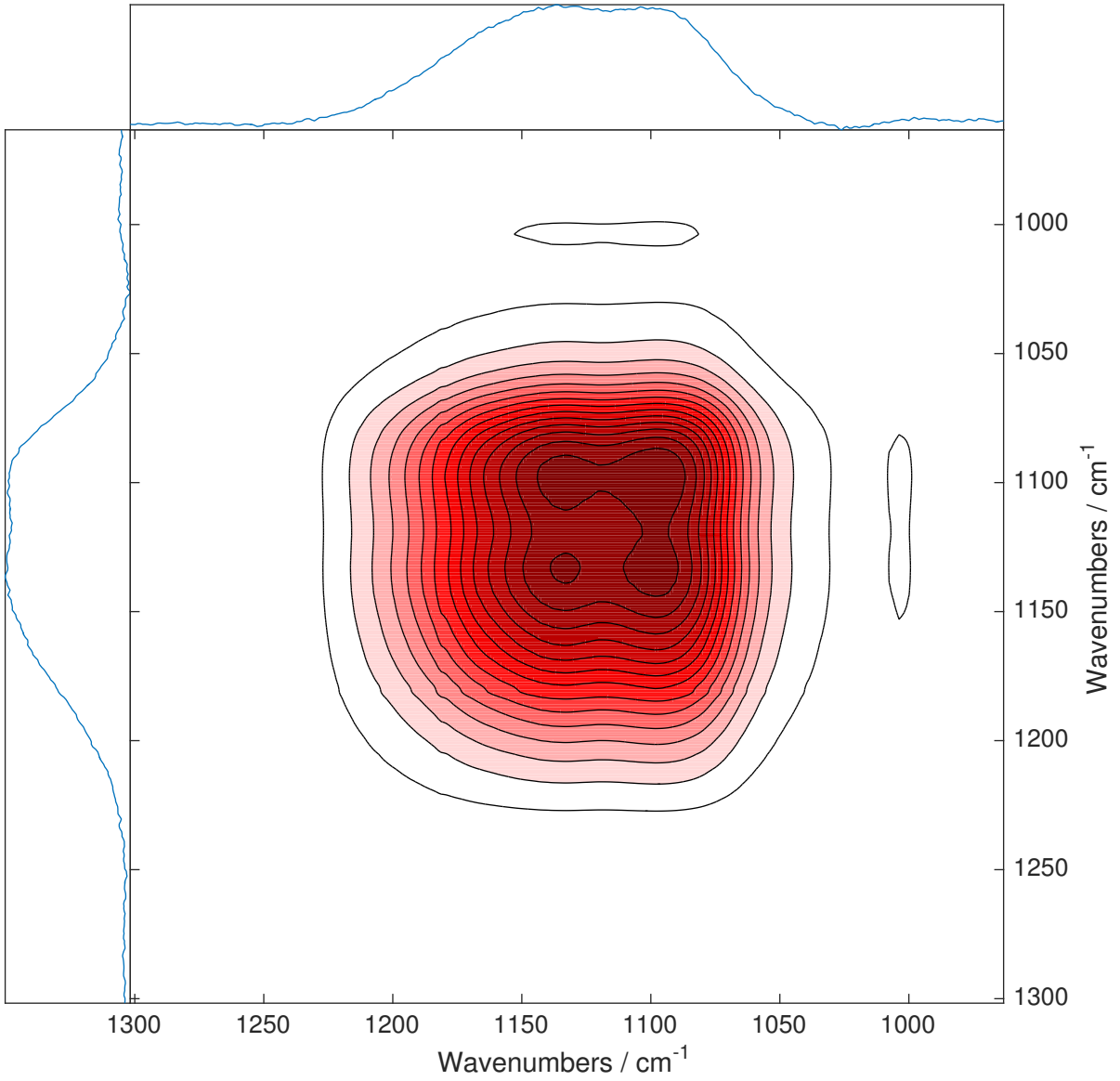

Figure 4.22: 2DCOS synchronous correlation map of ι-carrageenan, post-freezing; $t = 0$ to $t = 10$, held at -10 °C, spectral window: 1300 to 960 cm^{-1}, colourmap: blue-white-red; negative-0-positive

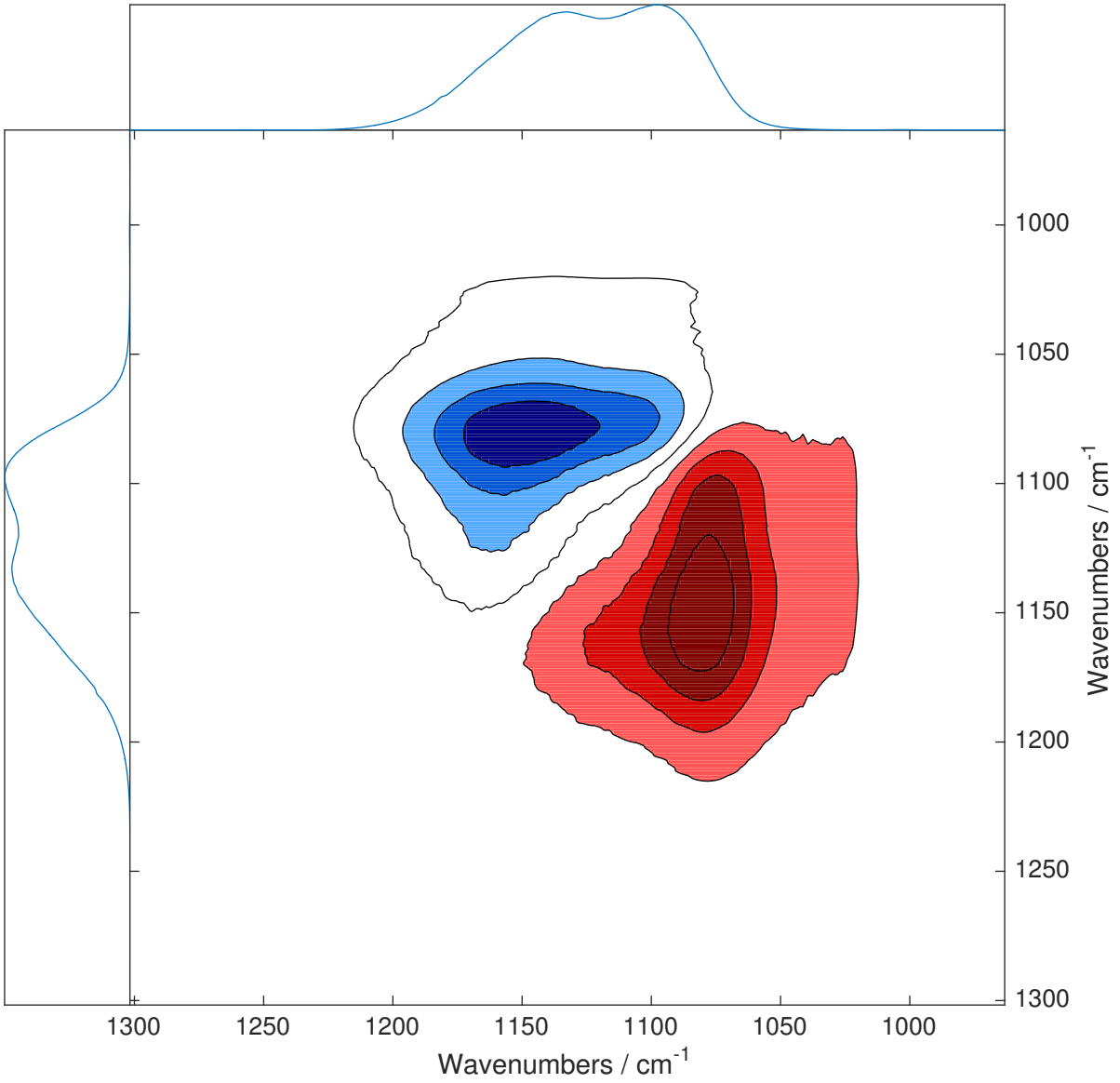

Figure 4.23: 2DCOS asynchronous (Modified Noda's rules) correlation map of ι-carrageenan, post-freezing; $t = 0$ to $t = 200$, held at -10 °C, spectral window: 1300 to 960 cm^{-1}, colourmap: blue-white-red; negative-0-positive

Two-dimensional correlation analysis can aid in the deconvolution of overlapping bands that change at different rates to one another, and provide spectral resolution enhancement through the use of autopower spectra. As was particularly prevalent during analysis of the O-H stretch region, the study of a real (non-perfect) system that has complicated spectral responses must be interpreted with care the using 2DCOS. Changing the range of the perturbation used (in this case the time range) passed into the 2DCOS algorithm can significantly affect the results gained. Several "moving-window" analyses can be utilised in an attempt to understand this time dependant behaviour, and these are discussed in the following sections.

Once a fuller understanding of the system is present, it would be useful to completely reconstruct the data from component vibrational bands. This approach allows an in depth look at the system, separating every overlapping peak. An iterative curve fitting routine is implemented within Section 4.2.4 that utilises much of the information regarding band shapes, positions, widths and synchronicity gained within the 2DCOS section.

4.2.3 Moving Window Two-Dimensional Correlation Analysis

Moving window two-dimensional correlation analysis (MW2D, section 1.3.4) allows the study of systems, in a perturbation dependant nature. The spectral dataset is split into subsets and the autopower spectrum from the resulting 2DCOS analysis is extracted. For $t = x$ minutes, subsets of $t = x - 10$ to $t = x + 10$ minutes form the window from which autopower spectra are calculated. The time dependant nature of the autopower spectrum is observed, showing the time post-freezing where spectral bands are most susceptible to change.

The output of these spectra is displayed in the same manner as the 2DCOS spectra, a contour map with a blue-white-red colour scheme and reference panels to the top and left. Along the y-axis the wavenumbers are displayed, with autopower spectrum of the entire time region in the left panel. The x-axis shows the time post-freezing, with the top panel showing the sum of the autocorrelation function along the wavenumber axis. Simply put, at each time, t along the x-axis, the autopower spectrum has been calculated for the sub-dataset of $t - 10$ to $t + 10$ minutes, and displayed in a contour format.

The two-dimensional correlation analysis (previous section) calculated the synchronous and asynchronous correlation spectra for the entire post-freezing experiment. Figure 4.18 showed the synchronous correlation spectrum from $t = 0$ to $t = 200$ for the 2 % ι-carrageenan system post-freezing of the O-H stretch region. During inspection of the raw data and PCA analysis a post-freezing growth at 3110 cm^{-1} was observed to occur, in contrast to an overall bleach seen within the O-H region. This growth at 3110 cm^{-1} was not represented in Figure 4.18, when the 2DCOS included the entire experimental time range, however Figure 4.19 showing the first 10 minutes of the experiment did show the 3110 cm^{-1} growth changing in a different direction to the overall bleach. The differences between these two figures indicated that changing the time window of the autocorrelation function allowed insight into different processes occurring during the post-freezing ι-carrageenan system.

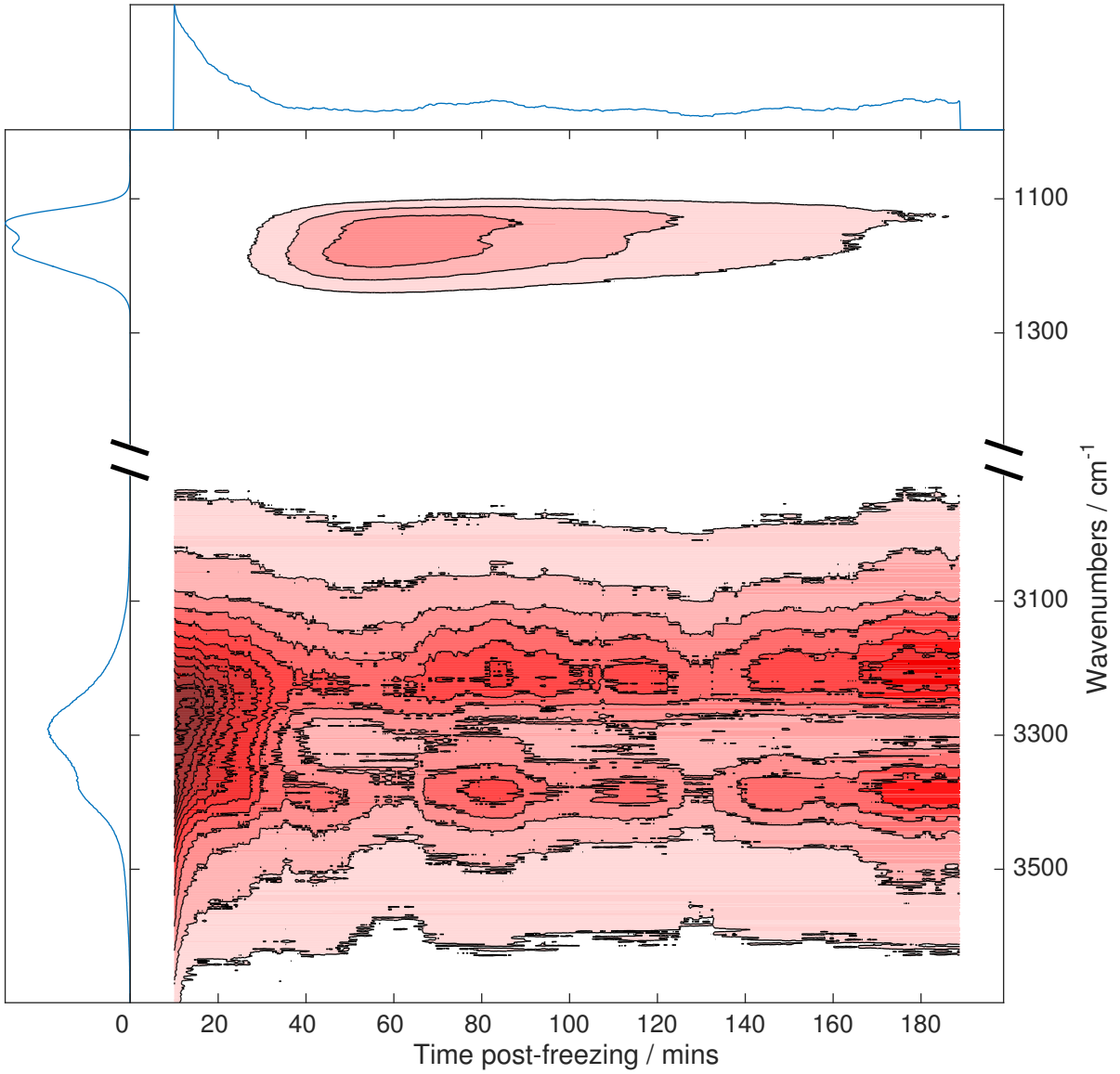

Figure 4.24: MW2D autopower correlation map of ι-carrageenan, from $t = 0$ to $t = 200$ minutes post freezing, window-size: 20 minutes, normalised to $\sqrt{(data)}$, colourmap: blue-white-red; negative-0-positive

Figure 4.24 shows the (square-root normalised) MW2D autopower spectrum for the post-freezing perturbations of ι-carrageenan, from $t = 0$ to $t = 200$ minutes with a window size of 20 minutes. The data has been scaled by its reciprocal square-root for display purposes, without this additional scaling the band present in the fingerprint region is dominated by the O-H stretch changes, this is because over the course of the experiment, it is less susceptible to change. The figure indicates immediate change within the O-H region, however the fingerprint region doesn't initially display any variation until *ca.* 30 minutes, with a maximum susceptibility to change at *ca.* 60 minutes. This was observed in previous analyses, however it is clear that the changes present within the system do not occur uniformly across the spectrum, with the changes due to ι-carrageenan appearing delayed by up to an hour after perturbation to the O-H stretch vibrations.

At $t = 10$ a large band, resembling that of the left panel (*i.e.* the autopower from $t = 0$ to $t = 200$), centered at 3175 cm^{-1} with a shoulder to higher wavenumber at 3265 cm^{-1} is present, indicating substantial change within this region of the spectrum, no autocorrelation intensity is seen within the fingerprint region however. This O-H feature decays by *ca.* 30 minutes, giving rise to two separate bands, centered at 3090 and 3265 cm^{-1}. This suggests the perturbation of the 3265 cm^{-1} shoulder is persistent across the entire time range, while the maxima observed from $t = 10$ to $t = 30$ minutes is not. Interestingly this transition within the O-H region appears correlated, in time, to the susceptibility to change of the growth within the carrageenan region. To examine these features more closely, the autopower spectra from various time ranges (post-freezing) can be calculated. These are displayed within Figure 4.25.

Figure 4.25 shows 3 different autopower spectra that have been normalised and offset. The blue trace shows the autopower of the entire time range, from 0 to 200 minutes, the orange trace shows the first 40 minutes post-freezing and the purple trace shows $t = 60$ to $t = 100$ minutes. These three autopower spectra reflect the observations seen within the MW2D autopower spectrum of Figure 4.24. Over the entire post-freezing experiment, two main spectral features

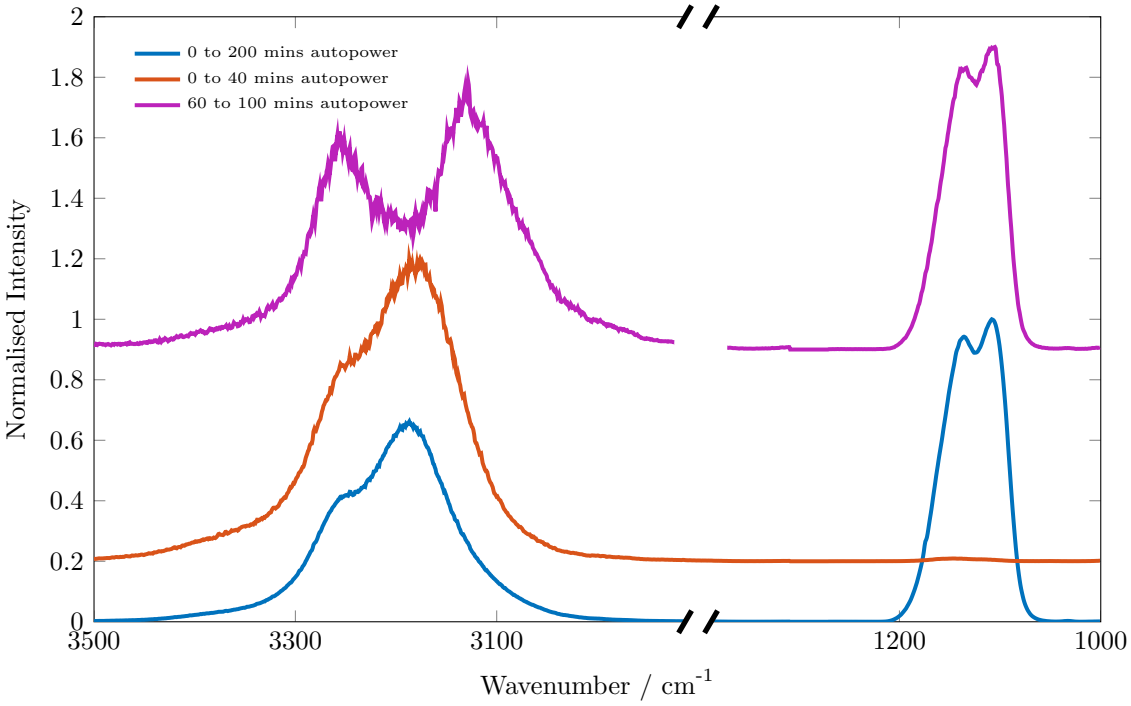

Figure 4.25: Autopower Spectra calculated post-freezing of ι-carrageenan, as monitored by FTIR, from $t = 0$ to $t = 200$ minutes post freezing (blue trace), from $t = 0$ to $t = 40$ minutes post freezing (orange trace), and from $t = 60$ to $t = 100$ minutes post freezing (purple trace), normalised and offset for clarity

are susceptible to change; within the O-H region a band at 3175 cm^{-1} with a shoulder at 3265 cm^{-1}, and within the carrageenan region a band with two maxima of almost equal intensity at 1095 and 1135 cm^{-1}. During the first 40 minutes post freezing (orange trace) the O-H region is seen to change in the same way, however the carrageenan region shows no autopower intensity, confirming the lack of spectral variation within the first 40 minutes of the 1095-1135 cm^{-1} band. At later time, when Figure 4.24 indicated that the carrageenan region peaked in autopower intensity and the O-H region shifted maxima, the purple trace ($t = 60$ to $t = 100$) shows this. The higher wavenumber shoulder within the O-H region (seen in the blue trace) persists, however no maximum is observed at 3175 cm^{-1}. Instead, a lower energy maximum at 3090 cm^{-1} is present.

The feature at 3090 cm^{-1} of the $t = 60$ to $t = 100$ minutes (purple trace) of Figure 4.25 could be the same band observed during PCA analysis that was present at 3110 cm^{-1}. Although there is quite a large discrepancy between these two maxima the analysis methods (2DCOS and PCA) do not decompose data in the same manner and it is possible for orthogonal intensity various (PCA) and mean-centered susceptibility to change (autopower spectrum) to be spectrally offset from one another, perhaps not by 20 wavenumbers however. The 3110 cm^{-1} band only presented during the first 10 minutes post freezing, while the 3090 cm^{-1} band highlighted by the autopower spectrum appeared later.

Viewing the autopower spectra at different perturbation delays is a powerful technique to analyse the perturbation dependant susceptibility of spectral variation, however selection of different window sizes can have a dramatic effect on the results. Figure 4.24 showed a change of nature around 40 minutes of the system, with the carrageenan region increasing in intensity and the O-H stretch Δ-absorbance moving from a 3175 cm^{-1} maximum (with shoulder) to two separate peaks located at 3090 and 3265 cm^{-1}. This MW2D spectrum utilised a window size of 10 minutes. The dataset was also investigated with various other window sizes, ranging from 1 minute to 30 minutes. Lowering the window size effectively increases the time resolution, however in doing so, there are less spectra available for analysis, increasing the noise of the

autopower spectra. The inverse is true for larger perturbation windows, although autopower noise is decreasing, one is now inspecting the susceptibility of Δ-absorbance change over a longer time period, perhaps missing spectral variations which occur on a short time scale.

Figure 4.26 demonstrates the effect of a varying window size. Four autopower spectra are shown, centered around the $t = 20$ minutes autocorrelation, with window sizes of 5, 10, 20 and 40 minutes (blue, orange, purple and green traces, respectively). No carrageenan autocorrelation intensities are observed for $t < 40$. Although O-H Δ-abs autocorrelations are present, the window size appears to affect their nature greatly. It is immediately obvious that as the window size is increased (going from bottom to top of the traces) the noise is reduced. For the smaller window sizes two distinct peaks are observed. As the window size is increased the autocorrelation spectrum starts to resemble the 3165 cm^{-1} shouldered band seen previously within the MW2D that occurs during the first 40 minutes. As the window size is increased the autocorrelation function is sampling more of the data, including variation from a wider time window. The choice of window size during MW2D analysis of the dynamic spectra can greatly affect the results, seen here as a large wavenumber shift.

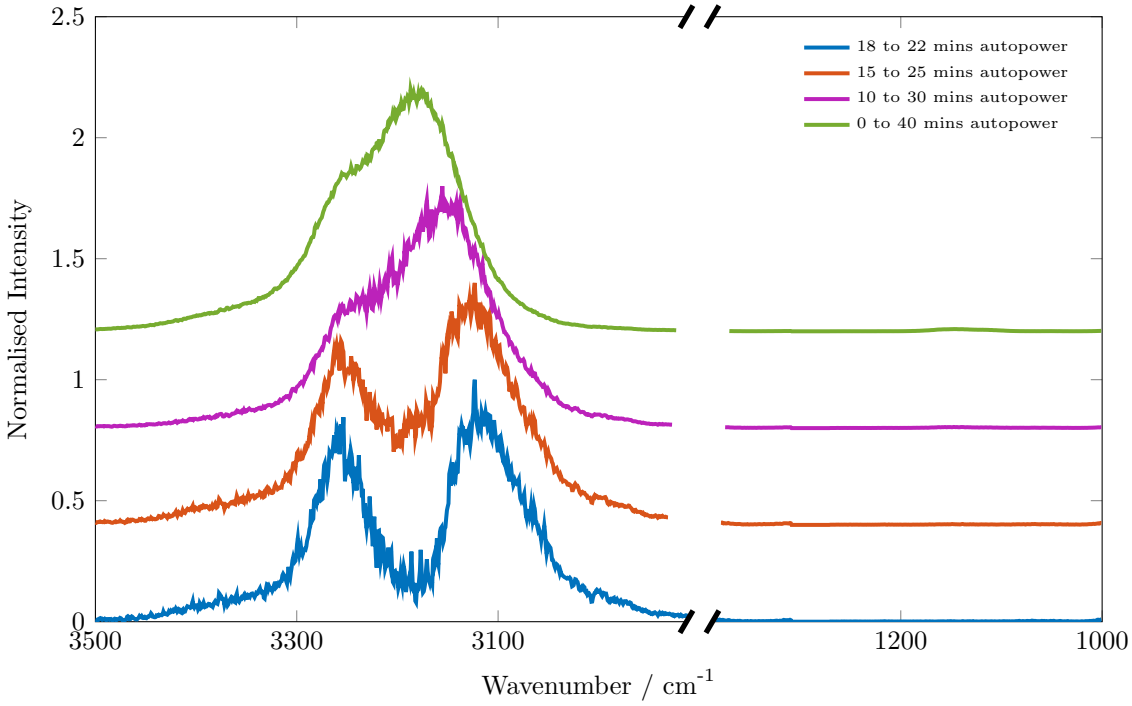

Figure 4.26: Autopower spectra calculated post-freezing of icar, as monitored by FTIR. Showing different spectral windows widths centered abound the 20 minute mark, from t = 18 to 22 minutes (blue trace), from t = 15 to 25 minutes (orange trace), from t = 10 to 30 minutes (purple trace), and from t = 0 to 40 minutes (green grace) post freezing, normalised and offset for clarity.

4.2.4 Band Fitting

This sections takes a more absolute approach to modelling the post-freezing nature of the ι-carrageenan system. By uniquely fitting each pure vibrational component of the Δ-absorbance post-freezing experiment, a robust solution to the time-dependant nature of these bands can be examined. Previous sections within this chapter have highlighted specific bands which change at different rates to one another, however the exact kinetic variation of these changes has not been alluded to. Both PCA analysis and 2DCOS/MW2D highlighted spectral changes occurring pre-10 minutes post-freezing and between 40-60 minutes, after about an hour, the changes appear to decay exponentially in their rate, reaching a stable state at about 3 hours.

4.2.4.1 Setup of Band Fitting Environment

The MATLAB environment has many inbuilt functions, an iterative curve fitting algorithm is used to model the bands. The algorithm used is essentially a least-squares iterative approach, minimising the residuals (un-modelled data) between the original data and specific combination of parameters, in this case, a mathematical description of multiple vibrational bands. Discrete vibrational transitions from one state to another are of a fixed energy gap, however the population of these states (at equilibrium) is controlled by a Boltzmann distribution. For solid materials, where the relaxation lifetime (vibrationally excited state returns to ground) is much shorter than the coherence lifetime (excited molecules vibrate out of synchronisation), infrared bands can be practically modelled using a Boltzmann distribution. The resulting distribution is referred to as a bell curve, or Gaussian profile. In gases, where vibrational incoherence sets in rapidly (due to rotations and collisions randomising the synchronicity of the excited vibrations) the resulting line shape is a Lorentzian profile. Liquids exist between these limits, with extremely rapid motion is prevented by molecular interaction, however the molecules are not locked in place.[172]

To effectively model infrared peaks that are not purely Gaussian or Lorentzian a Voigt function can be used. This is a convolution (combined in the Fourier transform integral) of a Gaussian and Lorentzian profile. Unfortunately a Voigt profile is a non-analytical function and does not have well defined parameters, essential for implementing an iterative code-based approach that is easily interpretable. Using a mixed function of the relative sums of a Gaussian and Lorentzian profile provides a good approximation to their convolution, and allows simpler practical implementation.

Equation 4.1 shows the pseudo-Voigt (mixed Gaussian and Lorentzian) profile, $f(x)$, used to model the vibrational bands within the post-freezing ι-carrageenan system. m is a variable parameter for the fraction of Gaussian character of the profile ($0 \leq m \leq 1$, *i.e.* $m : (1 - m)$ = Gaussian : Lorentzian). Unlike a true Voigt profile, where maxima and widths of the Gaussian and Lorentzian components are independent $f(x)$ locks these together. It was found that allowing fitting parameters to vary independently produced overfitting of the curve, often in a divergent manner. The amplitude (a), peak maxima (c) and full-width-half-maxima (FWHM, w) for the Gaussian and Lorentzian components are matched.

$$f(x) = a\left[me^{-4ln2(\frac{x-c}{w})^2} + \frac{1-m}{1+4(\frac{x-c}{w})^2}\right] \tag{4.1}$$

Figure 4.27 shows the comparison of the pseudo-Voigt function defined in Equation 4.1 with $m = 0.5$, *i.e.* a 50:50 Gaussian:Lorentzian mix, with pure Gaussian and Lorentzian profiles. The m parameter effectively controls the tailing of the edge of the profile, an increase in m results in a more Gauss-like distribution. 2 % ι-carrageenan solutions form a gel at temperatures below *ca.* 45 °C. The restriction in mobility of the molecules, compared to a more fluid substance will undoubtedly result in a more Gaussian band profile. This section deals with the post-freezing changes observed, when the system is held at *ca.* -10 °C. Although the system is not completely solid, as seen by time dependant infrared spectral changes, the mobility of the molecules has

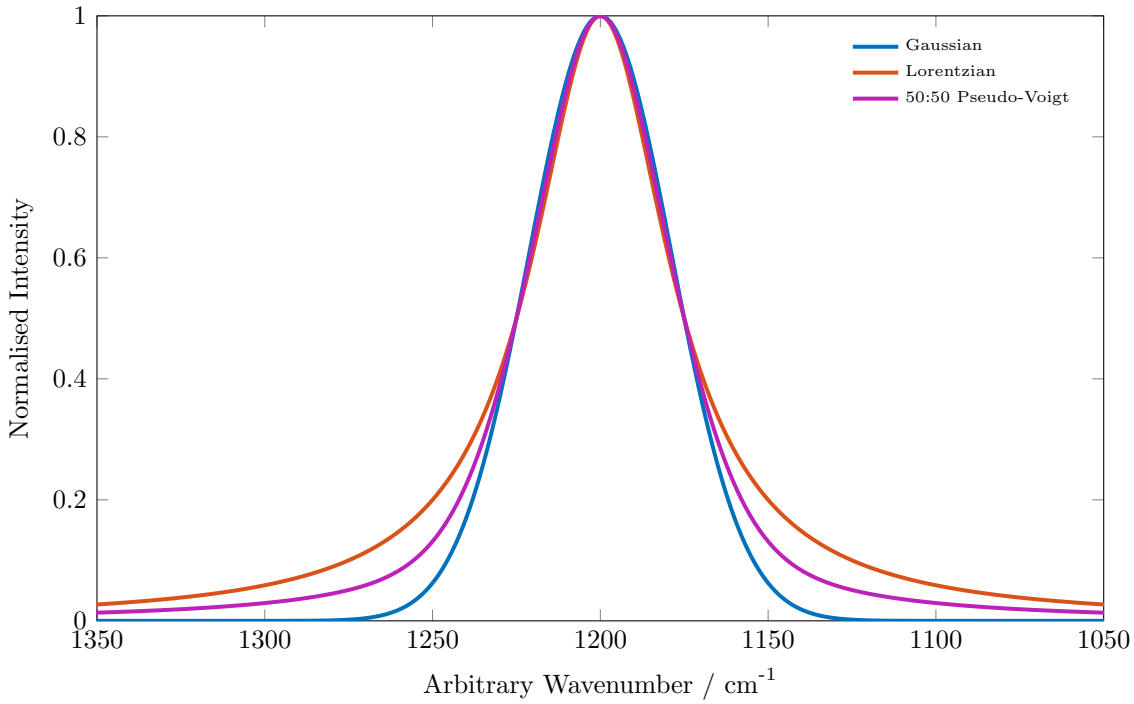

Figure 4.27: Simulated Gaussian (blue), Lorentzian (orange) and pseudo-Voigt (50:50, G:L) spectra, with a peak position of 1200 cm^{-1}, FWHM of 50 $cm^{-1}$and an amplitude of 1

been severely restricted. It was found through multiple permutations and iterative least-squares loops that the post-freezing bands could be modelled in s superior fashion with a pseudo-Voigt function, rather than pure Gaussian profiles.

4.2.4.2 Fingerprint Region

The post-freezing infrared spectra showed spectral changes occurring within two regions; the O-H stretch region and the fingerprint (or carrageenan) region. This section will deal with the carrageenan region first, as it is somewhat simpler to model due to fewer number of bands and the (relative) lack of overlap between these features. Inspection of the Δ-abs data for the post-freezing ι-carrageenan system monitored by ATR-FTIR within the carrageenan region revealed a growth occurring as a function of time (see Figure 4.6 in Section 4.2). This growth had two maxima, located at 1137 and 1098 cm^{-1}, with a smaller peak to slightly lower wavenumber, *ca.* 1000 cm^{-1}. Principal component analysis and two-dimensional techniques revealed the band with dual maxima had components which changed at different rates. Although visual inspection of the raw data is sufficient to indicate that this feature is comprised of two vibrational bands, 2D and PCA techniques did not suggest more than two components. The post-freezing system, within the fingerprint region was successfully modelled with 3 components. Three instances of Equation 4.1 are simultaneously fitted to each discrete spectrum collected post-freezing, a total of *ca.* 1000 spectra.

$$
\begin{aligned}
carrageenan \quad f(x) =& a_1\left[m_1 e^{-4ln2(\frac{x-c_1}{w_1})^2} + \frac{1-m_1}{1+4(\frac{x-c_1}{w_1})^2}\right] \\
&+a_2\left[m_2 e^{-4ln2(\frac{x-c_2}{w_2})^2} + \frac{1-m_2}{1+4(\frac{x-c_2}{w_2})^2}\right] \\
&+a_3\left[m_3 e^{-4ln2(\frac{x-c_3}{w_3})^2} + \frac{1-m_3}{1+4(\frac{x-c_3}{w_3})^2}\right]
\end{aligned}
\tag{4.2}
$$

Equation 4.2 shows the 3 pseudo-Voigt function solution to the Δ-absorbance post-freezing

	a_1	a_2	a_3	c_1	c_2	c_3	m_1	m_2	m_3	w_1	w_2	w_3
Lower limit	0	0	0	990	1084	1136	0.8	0.8	0.8	2	22	49
Start point	0.01	0.01	0.01	1000	1088	1140	0.9	0.9	0.9	10	26	53
Upper limit	0.2	0.2	0.2	1010	1092	1144	1	1	1	15	30	57

Table 4.1: Pseudo-Voigt parameters for the 3 component fit of the fingerprint region of the infrared spectra for ι-carrageenan post-freezing

changes within the carrageenan region. Table 4.1 shows the start point and upper and lower limits that the non-linear least-squares algorithm fits the pseudo-Voigt function to. The Gaussian character parameter, m was allowed to vary from 0.8 to 1. Inspection of the fit parameters for each spectrum post-freezing showed that the limits, for the final solution were not reached. The starting points for the algorithm were identified through inspection of the raw data, principal component analysis and two-dimensional analyses.

Following successful fitting of the post-freezing changes within the fingerprint region the spectra were reconstructed from the fit parameters. Figure 4.28 shows the raw spectra and the reconstructed spectra (top and bottom plots, respectively). It can be seen that the reconstructed spectra very closely match the original spectra. Figure 4.29 displays the residuals from the fitting procedure. Each reconstructed spectrum at a fixed time post-freezing has been subtracted from the corresponding real data to show features that are not accounted for by the band fitting routine. There is very little baseline deviation within the residual spectra, indicating that no major components of the real system have not been modelled by the 3 pseudo-Voigt profiles. At *ca.* 1000 cm^{-1} some deviation is see; this somewhat resembles a difference spectrum of a shifting band. During the fitting routines, the component centered at 1000 cm^{-1} was given significant freedom ($\pm$10 cm^{-1}); a spectral shift of this feature would have been successfully modelled by the algorithm and therefore this feature is more likely due to baselining errors. It is also possible that a small negative band exists at *ca.* 1250 cm^{-1}, however these absorbance changes for the un-modelled data are on the order of 10^{-4}. Although possibly real, such small absorbance changes are difficult to prove and attempting to fit such feature will quickly result

in overfitting of the post-freezing growth.

Figure 4.30 shows two plots; the top plot gives a schematic representation of the component bands that have been fit to the raw data and the bottom plot shows how fitted bands vary as a function of time post-freezing. The top plot gives an example (in this case $t = 200$ minutes post-freezing) of the fit; this same procedure, using the parameters given in Table 4.1, was applied for every spectrum collected post-freezing enabling the bottom plot to be calculated. The bottom plot shows that for the first 40 minutes post-freezing there's little change within the carrageenan region. $t = 40$ to $t = 80$ shows the largest gradient with the rate gradually decaying from $t = 100$ minutes post-freezing onwards.

The lowest wavenumber band, 998 cm^{-1}, shows a very noisy trace as it is of the smallest overall intensity. The baseline around this region is also subject to slight changes causing the band's area to vary from one spectrum to the next quite significantly, relative to itself. The changes observed for this band however do very much appear to mimic the changes seen within the other bands, albeit at a slightly delayed rate. This kinetic trace has also been smoothed by a Savitzky-Golay filter for display purposes and the trace is too noisy for any meaningful conclusions to be drawn.

Although the 1087 and 1140 cm^{-1} bands vary in a very similar way, it can be seen that the lower wavenumber band becomes separated (in normalised integration area) from the 1140 cm^{-1} band at *ca.* $t = 20$. The growth of the less intense, 1087 cm^{-1} component is delayed with respect to the higher wavenumber, 1140 cm^{-1} component. The difference in rates between these two bands suggests that they are not inextricably linked, *i.e.* although the two vibrational modes responsible for the post-freezing spectral perturbations change in a similar manner they do not behave identically. This effect is most likely due to two different processes instead of one, although it is possible that a single underlying process produces slightly offset rates to different vibrational modes through slightly different interaction methods. The observation

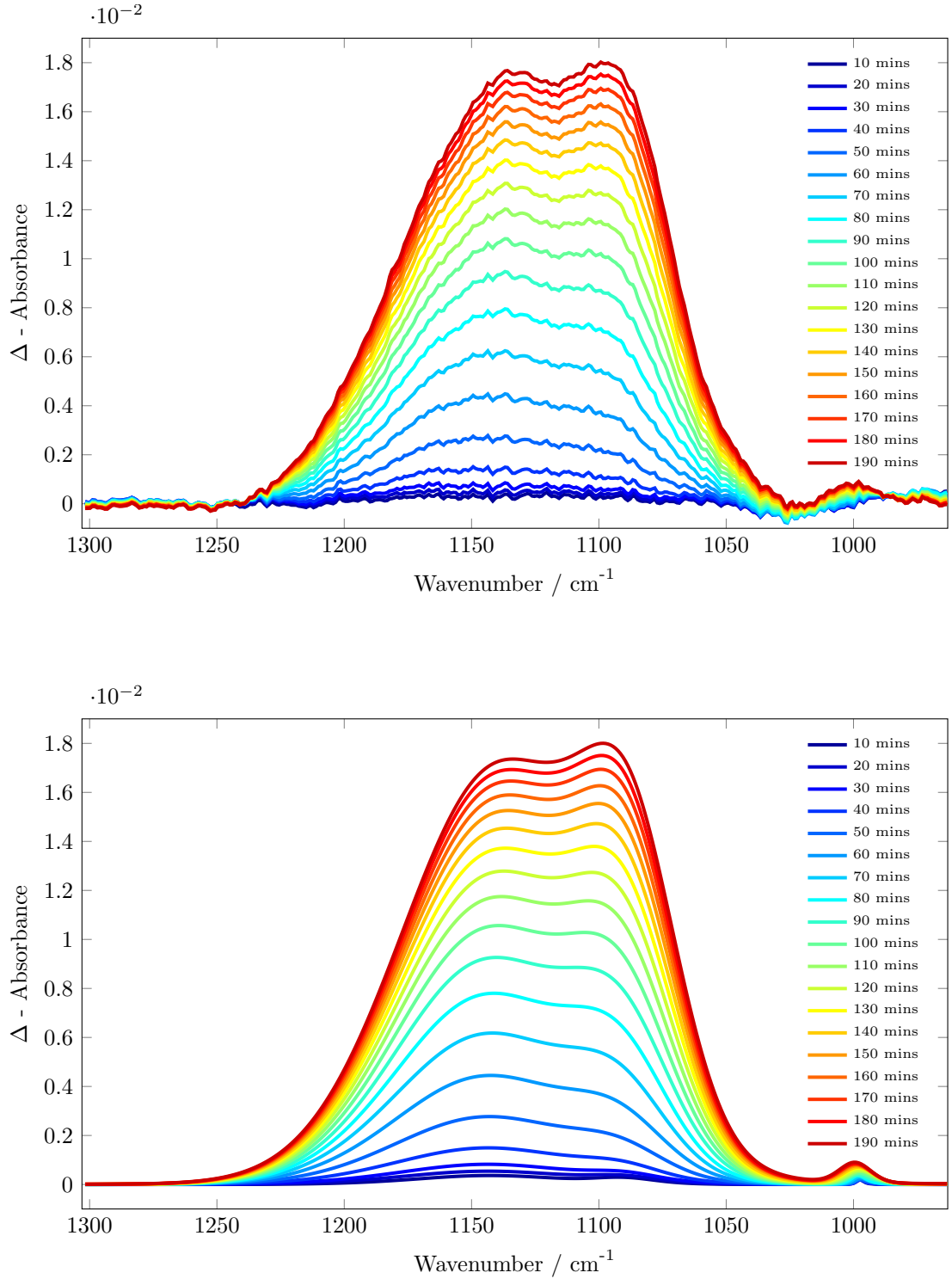

Figure 4.28: Raw (top) and reconstructed (bottom) spectra of the post-freezing changes, occurring in the fingerprint region, of ι-carrageenan, as monitored by FTIR-ATR spectroscopy. Reconstructed spectra consist of 3 bands located at 998, 1088 and 1140 cm^{-1}

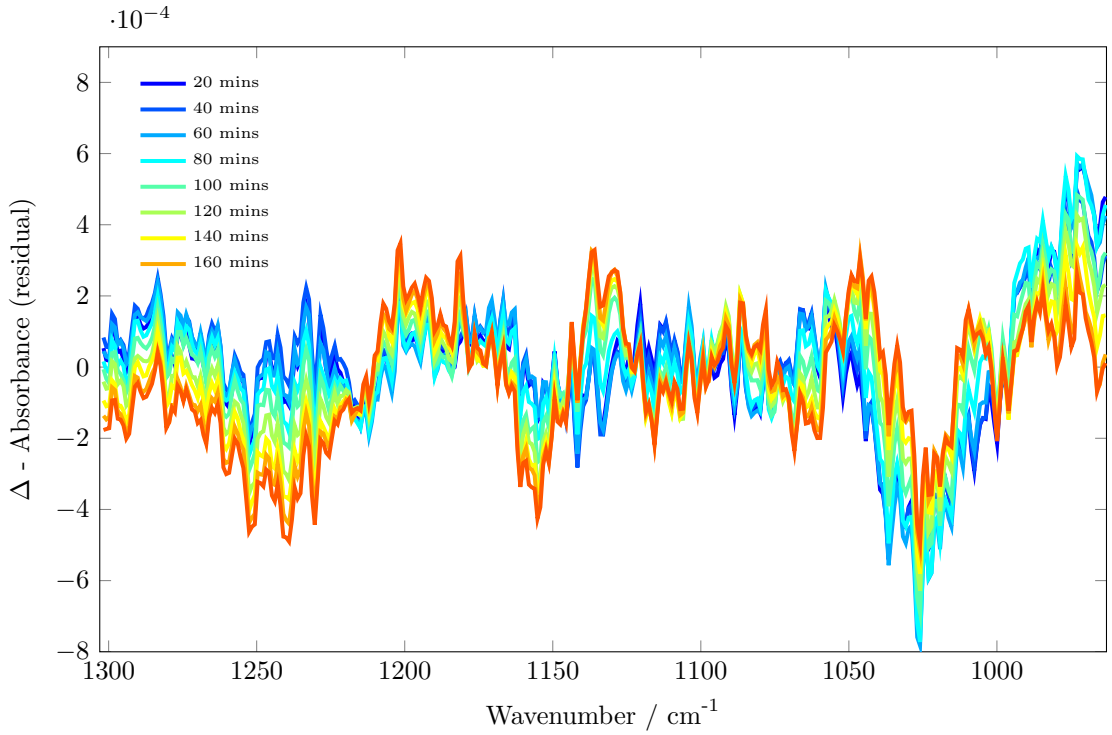

Figure 4.29: Residual spectra from the band fitting procedure of ι-carrageenan post-freezing for the fingerprint region. Calculated by subtracting the raw spectra from the reconstructed spectra, as shown in Figure 4.28

of the increase of normalised integration are for the higher wavenumber band before that of the lower wavenumber band matches the asynchronous spectrum from 2DCOS analysis earlier in this Chapter (Section 4.2.2, specifically Figure 4.23). Even following deconvolution of the changes within the carrageenan region post freezing, into presumed component vibrations, still shows large FWHM for these bands. It is therefore presumed that there is large environmental variations contributing to the line broadening of these features.

4.2.4.3 O-H Stretch Region

Fitting of the O-H stretch region of the spectrum proved to be more complicated due to multiply overlapping positive and negative regions of the Δ-absorbance spectra. Inspection of the raw data, and principal component analysis revealed the majority of the O-H region to bleach post-freezing, however a band at *ca.* 3110 cm^{-1} was seen to grow in over the first 20 minutes. Although this positive growth was successfully fitted using mixed positive and negative pseudo-Voigt functions, subsequent analysis of the residual of the fitting routine revealed a multicomponent nature to the 3110 cm^{-1} growth. When fitting routines such as these are implemented, with positive and negative bands with very close maxima, the algorithms used can easily overfit the spectrum.

The procedure attempts to minimise the residual error by finding a solution that closely matches the raw spectrum; overlapping positive and negative features nearly always result in the production of very large features that bear no spectral significance. For this reason, the amount that the peak maximum (on the wavenumber axis) is allowed to "wander" was significantly restrained. The O-H region of the spectra was fit in an identical manner to the fitting method described above in Equation 4.1, however 7 distinct instances of the pseudo-Voigt function are invoked. Table 4.2 shows the start points and limits used for the 7 components pseudo-Voigt fit algorithm.

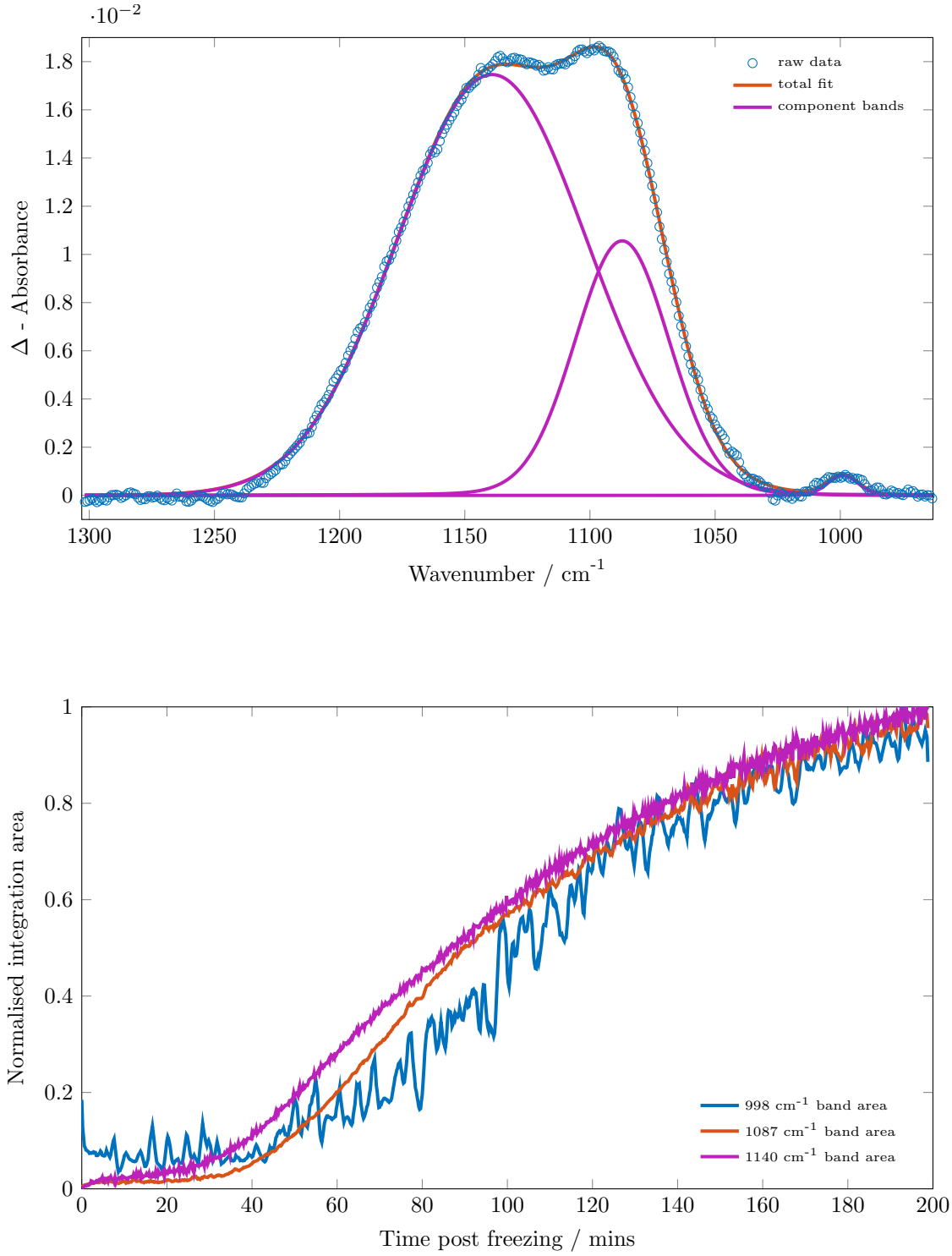

Figure 4.30: Top: raw data and simulated component bands showing fit of the ι-carrageenan system at $t = 200$ minutes post-freezing. Bottom: normalised integration areas of the 998, 1087 and 1140 cm^{-1} bands as a function of time post-freezing

	a_1	a_2	a_3	a_4	a_5	a_6	a_7	c_1	c_2	c_3
Lower limit	0	0	0	-0.01	-0.1	-0.1	-0.1	3000	3080	3105
Start point	0.002	0.002	0.002	-0.005	-0.05	-0.05	-0.05	3015	3095	3120
Upper limit	0.1	0.1	0.1	0	0	0	0	3030	3110	3135
	c_4	c_5	c_6	c_7	m_1	m_2	m_3	m_4	m_5	m_6
Lower limit	3070	3165	3260	3370	0.8	0.8	0.8	0.8	0.8	0.8
Start point	3090	3180	3270	3390	0.9	0.9	0.9	0.9	0.9	0.9
Upper limit	3110	3195	3280	3410	1	1	1	1	1	1
	m_7	w_1	w_2	w_3	w_4	w_5	w_6	w_7		
Lower limit	0.8	20	20	20	110	20	30	80		
Start point	0.9	50	50	50	120	80	120	190		
Upper limit	1	100	100	100	150	100	150	230		

Table 4.2: Pseudo-Voigt parameters for the 7 component fit of the negative bands within the O-H stretch region of the infrared spectra for ι-carrageenan post-freezing, first 3 variable for each parameter are positive bands, subsequent 4 variables fit negative bands

The parameters displayed in Table 4.2 were fit to the O-H stretch region, between 2700 and 3570 cm^{-1}, this region includes all variation occurring within the O-H stretch region, however does not include the CO_2 overtone. The raw spectra passed to the algorithm and the resulting reconstructed spectra are calculated. The reconstructed spectra show very good similarity, however, unlike the fit for the carrageenan region, they are not shown here as the similarity can be observed through the residual spectra. The residuals (raw spectra minus the reconstructed spectra) are shown in Figure 4.31. The residuals are on the order of 10^{-4}, two orders of magnitude below the Δ-absorbance within the O-H stretch region post-freezing. There is substantial noise within the residuals, especially *ca.* 3200 cm^{-1}, most likely due to the higher IR absorption of the O-H stretch (and therefore less throughput). Although the baseline is not perfectly flat, there appears to be no growth or decay of any band-like features as a function of time post freezing (displayed as different colour traces), this leads to the conclusion that the 7 pseudo-Voigt profile were fit very well. Inspection of various GOF variables (goodness of fit), detailing the exact deviation from the raw spectra also confirmed the excellent model produced with 7 components.

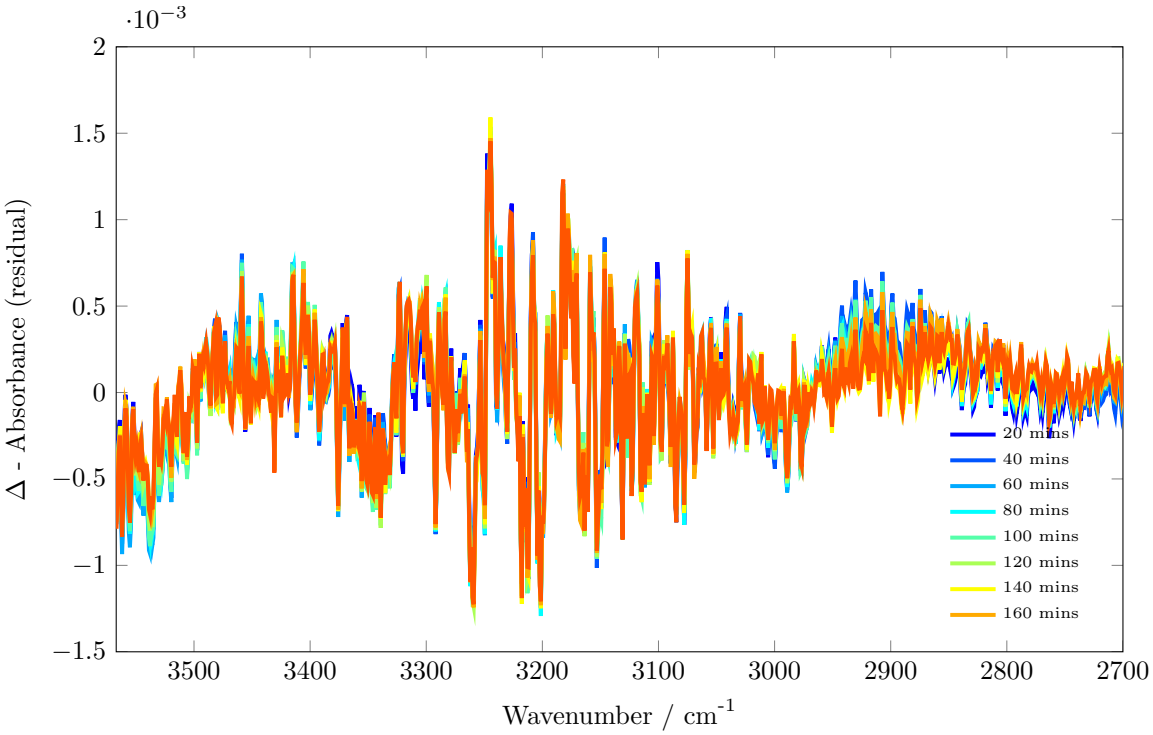

Figure 4.31: Residual spectra from the band fitting procedure of ι-carrageenan post-freezing for the O-H stretch region. Calculated by subtracting the raw spectra from the 7 pseudo-Voigt profile reconstructed spectra

Figure 4.32 displays two examples of the fit from spectra at $t = 200$ (top plot) and $t = 10$ (bottom plot) minutes post freezing, giving a visual representation of how the components co-add together to simulate the spectra at two different phases of the the changes seen within the O-H stretch region. The residuals from Figure 4.31 demonstrate that the spectra are well fitted by the component profiles, however it is possible to observe some potential overfitting when examining the the co-added profiles at particular delays post-freezing. The bottom plot of Figure 4.32 shows large negative and positive components that overlap to lower wavenumber. Generally this is a sign of overfitting however information present within the subsequent figure (Figure 4.33) shows the effectiveness of the fitting.

Figure 4.33 shows how the pseudo-Voigt profiles fit to the data change integration area with respect to time post-freezing. The top plot shows the normalised integration areas of the 7 components and the bottom plot shows the mean integration areas for the positive and negative bands separately. The collective positive and negative bands within the top plot each show distinct patterns post-freezing, hence their averaging in the bottom plot. Every spectrum in the post-freezing is fit separately to the function within the given parameters. This means that although the subsequent raw spectrum to be fit is very similar to the previous one, nothing informs the algorithm of this. There is substantial noise within the time-dependant integration area plots, however the similarity of linked components demonstrates the robustness of the fitting procedure.

It can be seen within the bottom plot of Figure 4.33 that the positive and negative bands change in a different manner post freezing. Post-freezing the positive bands, centered at 3017, 3090 and 3130 cm^{-1} rapidly increase in intensity for the first 5 minutes, then decay to a near-zero value after about 20 minutes. The negative bands (orange trace) show a rapid bleach for the first 5 minutes, then continues to decrease integration area, at a slower rate, until about 80 minutes post-freezing. For both of these traces, it is very obvious that their behaviour is (at least) bi-exponential. This suggests separate processes occurring within the O-H region, post

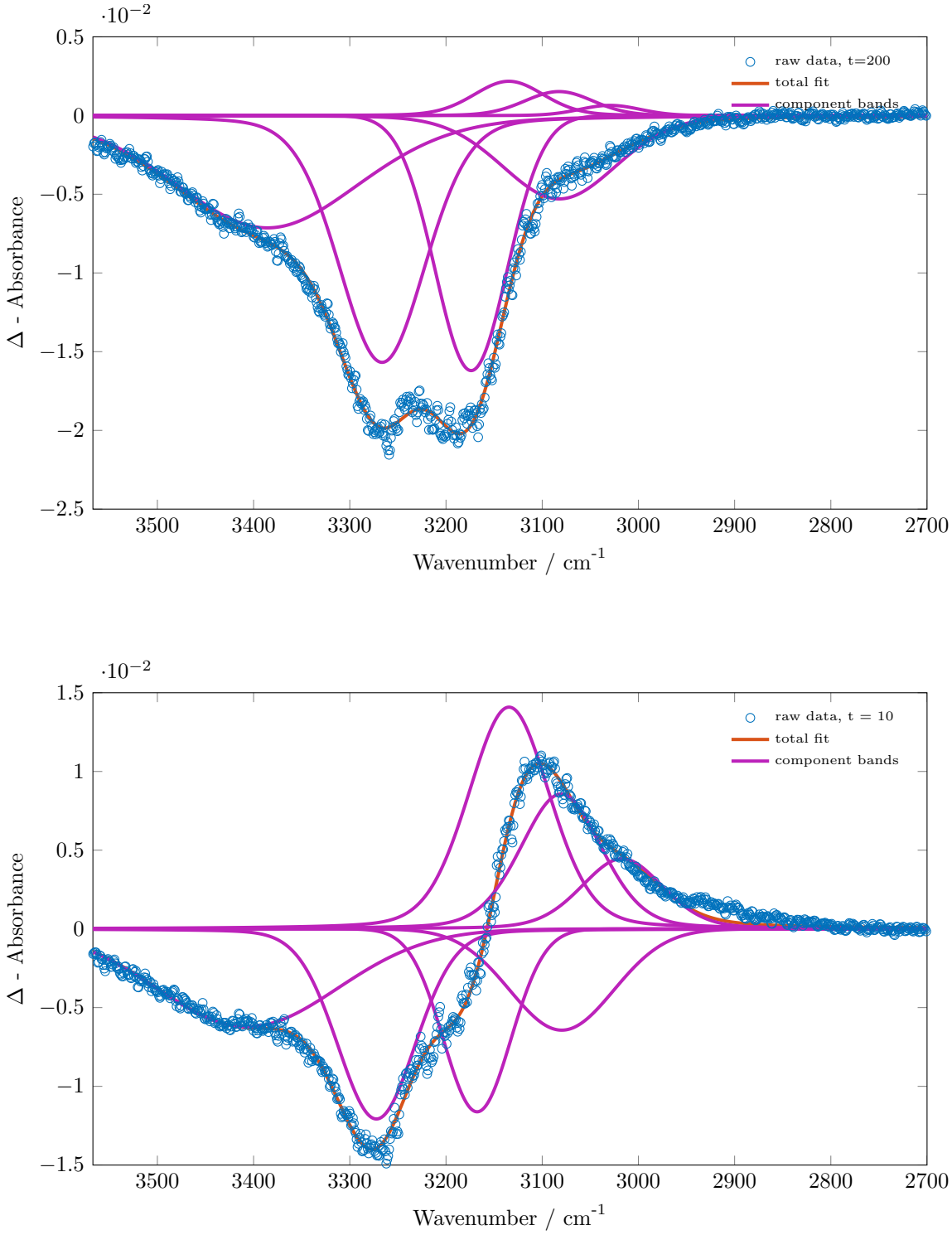

Figure 4.32: Top: raw data and simulated component bands showing fit of the ι-carrageenan system at $t = 200$ minutes post-freezing. Bottom: raw data and simulated component bands showing fit of the ι-carrageenan system at $t = 10$ minutes post-freezing

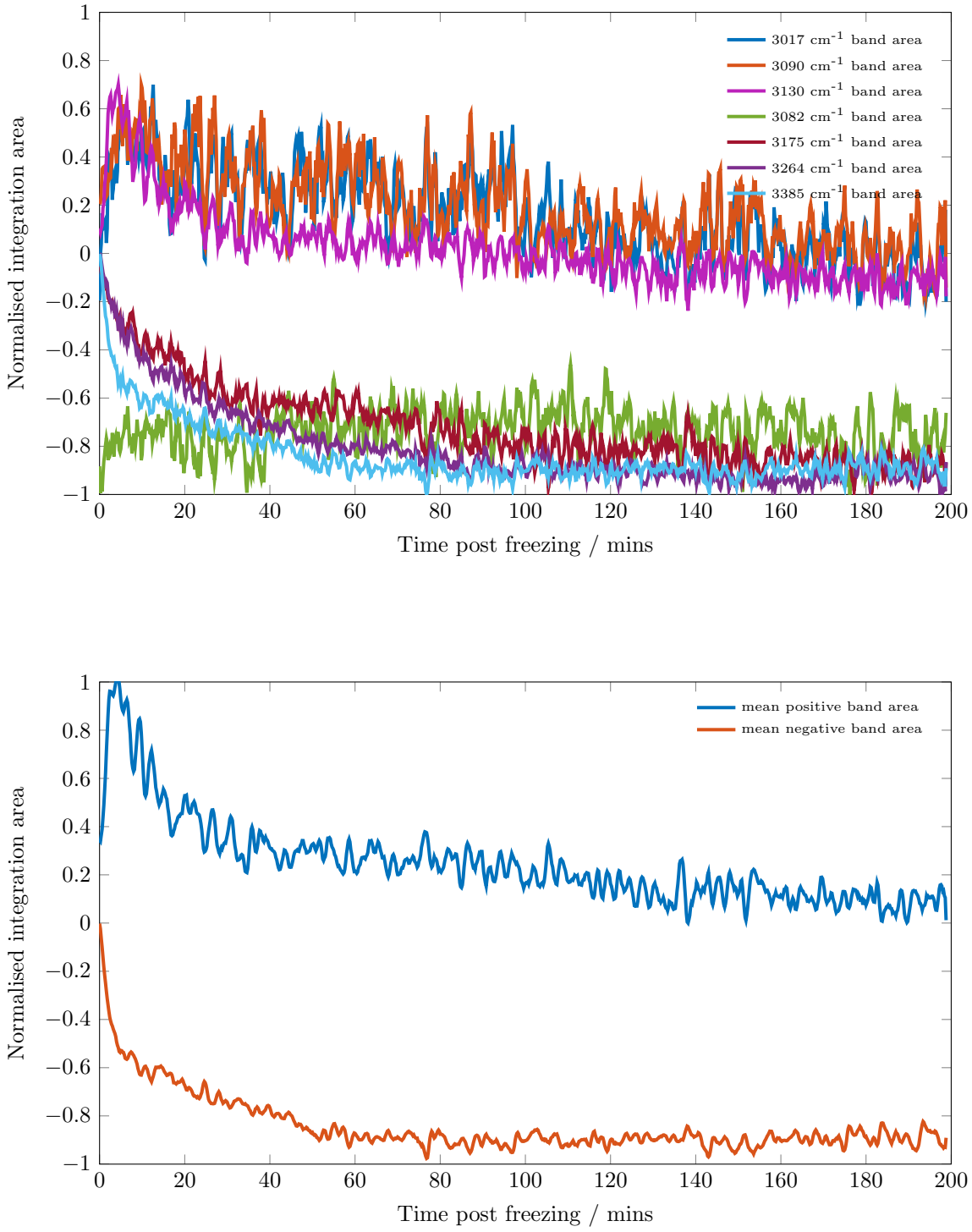

Figure 4.33: Top: normalised integration areas of all component pseudo-Voigt profiles as a function of time post-freezing. Bottom: mean integration areas of the positive (blue) and negative (orange) pseudo-Voigt profiles as a function of time post-freezing.

freezing.

4.3 Conclusions

This chapter attempts to understand the changes occurring within a 2 % ι-carrageenan solution (gel) as the sample is frozen. ATR infrared spectroscopy has identified changes that occur post-freezing. These changes are observed within the O-H stretch region and the fingerprint region (where only carrageenan has absorbances) suggesting that the conformation of both the water and carrageenan changes as a function of time, when it is held at a constant temperature, after freezing. Experiments of the post-freezing nature of κ- and λ-carrageenan did not show any spectral changes post-freezing within the carrageenan / fingerprint region. Some small, and irregular changes within the O-H stretch region for these systems were seen and these should be investigated further. Perturbations (although irregular) within the water region of the infrared and not the fingerprint region suggest possible changes in the structure of water, but not the carrageenans, for κ- and λ-carrageenan. The pure water system was also investigated post-freezing, and this showed no spectral changes, suggesting a steady state was achieved. As ι-carrageenan was the only carrageenan to present structural changes and the other systems did not, it can be presumed that the changes observed are due solely to the interactions of ι-carrageenan with water or ice.

All of the techniques used within this chapter point to several facts; post-freezing both the O-H region and fingerprint region show spectral changes, the changes occurring between these regions are not entirely in synchronisation, and changes occurring within each region show components which appear to change out of phase with each other. The observation of spectral changes after the gel has frozen suggest that the system is not in a steady state, and there are processes occurring which alter the conformation of both the biopolymer and the structure / distribution of the water molecules. Within this section, the O-H stretch region will firstly be discussed, then the fingerprint region, before they are reconciled together.

4.3.1 O-H Stretch Region

The underlying vibrational bands of the O-H stretch absorption of water or ice are composed of contributions from H_2O molecules in different hydrogen bonding environments. There is still lots of discussion to the exact assignment of the underlying bands and the prediction of the macroscopic configuration of water is very complicated.[173] Generally, lower wavenumber components are attributed to water molecules with stronger hydrogen bonds and higher wavenumber components have a weaker hydrogen bonding environment.[174,175] Liquid water has been shown to correspond to a linear combination of just two contributing components.[176] Although there is evidence for continuous variation of contributing factors.[177] The two-component model is also confounded when applied to the system under study here due to the presence of ice, whether it be amorphous or crystalline. The observed changes post freezing, highlighted within the Section 4.2.4, do appear to shows two distinct components seen within the band fitting as the positive and negative collection of bands. Based upon the simplified separation of high and low wavenumber regions of the O-H stretch corresponding to weaker and stronger hydrogen bonding environments respectively, conclusions about the changes of water molecules post freezing can be drawn.

Although there is large overlap between the collection of positive and negative bands (shown in Figure 4.32) it is clear that the post-freezing growth largely occupies the lower energy side of the O-H stretch region, while the bleaching components dominate the higher wavenumber side of the O-H band, immediately after freezing. This suggests that there is an increased presence of more strongly hydrogen bonded H_2O molecules which coincides with a decrease in the the number of weakly hydrogen bonded molecules. This effect is what is observed, on a much larger scale however, when water freezes to ice. The difference spectra were calculated by taking a ratio of another spectrum within the same dataset. The background for these spectra is an ice spectrum, suggesting that for the first 5 minutes post freezing, liquid water

molecules are still being frozen. As the sample is supercooled prior to freezing the propagation of crystallisation occurs very rapidly, producing small ice crystals. Many of the water molecules that are hydrating the biopolymer could remain unfrozen. An assumption can be made that in a liquid system, the carrageenan chains will have more water molecules within their solvation space, however as the water is frozen and the temperature reduced, more liquid water molecules will be removed from their solvating role into ice crystals in an attempt for the system to reach its most thermodynamically stable state. The increased rate of crystallisation due to supercooling could have perturbed the thermodynamic equilibrium between the carrageenan and water. Although there is a very small change in the fingerprint region between $t = 0$ and $t = 5$, the majority of the changes within the carrageenan conformation occur at later times.

Following this initial change for $t < 5$ the lower wavenumber bands decay rapidly over 30 minutes while the higher wavenumber bands continue their bleach suggesting no further increase in more strongly hydrogen bonded water molecules after 5 minutes. There is however a continuous removal of the higher wavenumber components for a further hour, at a decaying rate, until an equilibrium is met. The changes observed could be due to many features, although it is important to note that no post-freezing changes were observed within pure water systems, suggesting that these perturbations of the water's environment post-freezing are a direct result of the carrageenan.

All of the techniques used indicate a large change in the first 5 minutes post freezing. When a supercooled liquid is frozen, its internal temperature increases to roughly its original freezing point, this is due to the latent heat of crystallisation. Inspection of the PT100 temperature sensor's data, and additional thermocouple data (inserted directly into the sample) showed this to be the case. However, due to the large thermal mass of the cooling system and it's high thermal conductivity, the excess heat was quickly removed. Initially the changes within the first 5 minutes were though to be due to this, however removal of heat from within the sample, returning it to the temperature pre-freezing (*ca.* -10 °C) occurred within about 10 seconds.

This effect could lead to the melting of smaller crystals, increasing the mobile fraction of water, allowing for an increased rate of Ostwald ripening. However it is unclear if this effect would be sustained for *ca.* 5 minutes, as suggested by the infrared spectra. As previously mentioned these post-freezing changes within the O-H region were not observed with pure water. Therefore the 0 to 5 minutes changes post-freezing, although most likely originating from the water are present due to the inclusion of ι-carrageenan.

4.3.2 Fingerprint Region

The fingerprint region displayed within this chapter (1300 - 950 cm^{-1}) does not contain any H_2O absorbances, all of the spectral features are due to ι-carrageenan. The changes observed post freezing are shown as difference spectra in Figure 4.6. Two broad bands grow in, as a function of time, post freezing and the separation of these bands can be seen clearly within the band fitting section (Section 4.2.4, specifically Figure 4.30). These two bands are located at 1087 and 1140 cm^{-1}, with a smaller band at 998 cm^{-1}. The smaller band appears to change in the same way as the other two bands, however due to it's size, it is difficult to be sure. PCA and 2DCOS analyses both indicated that the two spectral components of the growth changed at different rates. Both of the major bands observed in the post freezing growth of the fingerprint region are very wide. This suggests that there is considerable variations in the environments of the molecular vibrations responsible for these growths, that give rise to line broadening.

The band fitting routines found that, although the 1087 and 1140 cm^{-1} bands both grew in a similar sigmoidal fashion, the higher wavenumber band appeared to change before the lower wavenumber band. Figure 4.35 shows the ATR-FTIR spectrum of a 2 % ι-carrageenangel at 20 °C. The positions of the band growth post freezing have been overlaid. The Figure above, Figure 4.34, shows structure of the repeating unit of ι-carrageenan. The location of the bands with respect to the original FTIR spectrum allows suggestions to be made as to their vibrational origin. This approach is by no means rigorous, however as these changes post-freezing for

ι-carrageenan have not been seen before suggestions are made.

The higher wavenumber component of the growth post freezing within the fingerprint region (at 1140 cm^{-1}) overlaps with vibrations due to glycosidic linkages of the carrageenan chain. The small growth at 998 cm^{-1} also overlaps with glycosidic bonds. The 1087 cm^{-1} component, that is delayed in its change post freezing with respect to the 1140 cm^{-1} component, lies between S-O symmetric stretch and C-O / C-OH vibrational modes. The link between spectral position and the part of the ι-carrageenan structure is highlighted using green and orange overlays.

The higher wavenumber component is seen to change before the lower wavenumber component, suggesting that a perturbation of glycosidic linkages occurs prior to a change in S-O and C-OH vibrations. S-O and C-OH modes are associated with parts of the carrageenan chain that protrude from the main chain backbone and are therefore interacting with their environment. A change in the nature of the vibration of glycosidic linkages suggests that the chain backbone has changed conformation. Assuming these tentative assignments to the origin of the growths within the fingerprint region are correct, this suggests that the overall conformation of the biopolymer is changed prior to the protruding groups of the biopolymer interacting with their surroundings. *i.e.* the biopolymer is moved and then the biopolymer interacts with something, rather than the interaction of the biopolymer is responsible for the movement. Although the latter is not ruled out over the course of the time post freezing, perturbation of the backbone vibrations prior to protruding groups does suggest that this is the initial driving factor.

The O-H region will undoubtably contain contributions from the O-H stretches of alcohol groups from the carrageenan spectra. However there is no sign in the difference spectra post freezing that these are observed. The main reason for this is the lack of synchronicity between the OH and fingerprint stretch region, and the signal from the bulk water is much greater than the signal from the carrageenan based O-H stretches. Absorbances between 1100 and 1010 cm^{-1} are due to combinations of C-O, C-OH and S-O vibrational modes. As there are no perturbations

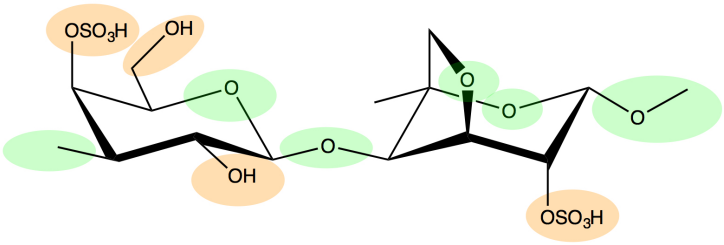

Figure 4.34: ι-carrageenan structure overlaid with green and orange ellipses showing the location of possible vibrational modes responsible for the post-freezing changes, corresponding to the growths shown in the plot below, centered at 1087 cm^{-1} (orange), and 1140 and 998 cm^{-1} (green)

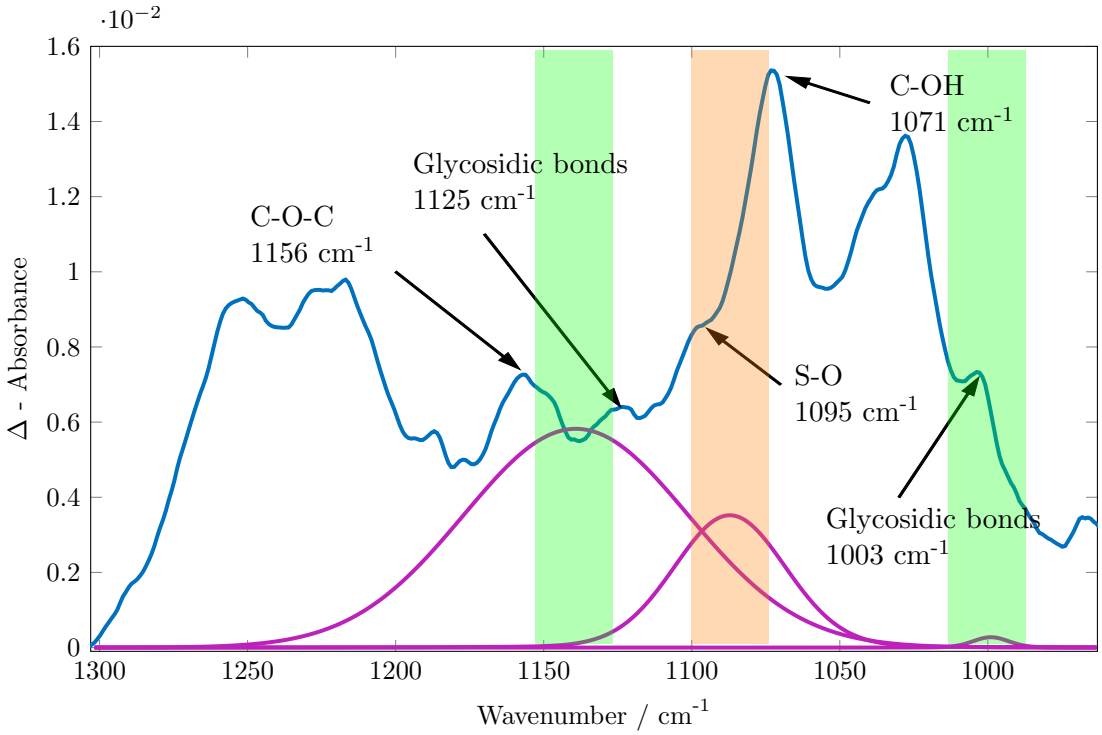

Figure 4.35: FTIR of carrageenan (blue trace) overlaid with fit components of band growth post-freezing (purple traces), green and orange bars show centre of growths in comparison to FTIR spectrum, notable bands also annotated

within the O-H region that change at the same rate as growths within the carrageenan region, this suggests that the lower wavenumber growth, at 1087 cm^{-1} is more likely due to an S-O mode.

In the gelled state, the bulk water exists in pockets within solvated carrageenan chains. Freeze concentration of the carrageenan was observed within early system development (Section 2.1) and involves the physical movement of the biopolymer chains as they are pushed out of the way during crystallisation of the water molecules. The rapid freezing of water due to the supercooled sample suggests minimal movement of the carrageenan chains during the freezing event, the lack of spectral changes within the carrageenan between pre- and post-freezing spectra also support this.

The rapid crystallisation will form small ice crystals and, over time, these crystals could grow and shrink due to Ostwald ripening. The effects of certain ice crystal structures within pockets of the carrageenan changing size is an inevitable change in the conformation of the carrageenan chains that surround these pockets. The 'pushing' of the biopolymer by the ice crystals, followed by interaction of the protruding groups with their new environment could be responsible for the changes seen within the spectra. However, conclusions at this stage are premature, it is also possible that ι-carrageenan is acting in a similar way to ice-binding proteins and interactive with the ice crystal surface in a particular manner.

Another factor that should be brought to light that might add weight to the suggestion of ι-carrageenan interacting with the ice surface is the temporal correlation between changes in the O-H stretch region and fingerprint region. The growth within the fingerprint region starts at roughly 40 minutes post freezing and the majority of changes seen within the O-H stretch region subside by *ca.* 40 minutes, indicating a sequential order.

Although a mechanism and explanation for the processes occurring post freezing have not been concretely proposed, the changes occurring within the carrageenan and O-H stretch regions

suggest an interaction between ι-carrageenan and water / ice that is not observed with other carrageenans.

4.4 Future Work

During this chapter changes occurring within the post-freezing 2 % ι-carrageenan system have been highlighted and described. It is clear that there are underlying processes that change the conformational nature of the biopolymer and water molecules, however more study is needed to understand causes of the spectral perturbations observed.

Use of imaging techniques in combination with infrared spectroscopy will allow investigation of the changes of ice crystal size and distribution as a function of time post freezing. The use of ATR has been invaluable to this project, there are several commercial systems that allow ATR imaging using FPAs (Mid IR imaging using a focal-plane array). The use of a visible camera focused onto the ATR surface from below in tandem with FTIR spectra collect has been developed by Pike Technologies and would allow, observation of the ice crystal size during spectral acquisition.

Although the post-freezing changes are only seen with one specific form of carrageenan, suggesting their validity, there is also a possibility that there are due to the interface with the diamond ATR crystal. Development of a system that utilised a Raman probe in tandem with the ATR was undertook for a period of time. Unfortunately however, the use of certain plastics (and their binders) that fluoresced within the ATR chamber, successful collection of Raman spectra was not achieved.

Enabling the current system to handle much longer experimental times, would allow monitoring of these post freezing changes to be accomplished over days, instead of hours. The changes post-freezing appeared to approach an asymptote, with their rate of change slowing to near 0,

however the 'endpoint' of the spectral perturbations was not fully met within the time limits of the experiments.

Changing the concentration of ι-carrageenan is also a worthwhile experiment to complete. The increase or decrease of ι-carrageenan within the frozen environment should, at the very least, exaggerate or lessen the post-freeing changes. The same effects would most-likely be observed with different cations and ionic concentrations. Producing a measurable change in the physical properties of the gel and attempting to observe the spectral change post-freezing could help eludicate the exact mechanisms of these changes.

A recent review by Perakis *et al.* suggested isotope doping to significantly simplify the O-H stretch band of water within the Mid IR. Instead of studying the O-H stretch in 100 % H_2O, one can study the stretch in 5 % HOD in D_2O.[73] This allows decoupling of the vibrational modes, resulting in almost pure Gaussian ice and water O-H stretch profiles. κ-carrageenan has been shown to have a higher elastic modulus in D_2O compared to H_2O,[173] however study of these systems *via* FTIR will undoubtably be useful in a fuller understanding.

Chapter 5

Raman Studies of Carrageenan

This Chapter utilises a confocal Raman spectrometer in an attempt to study the behaviour of carrageenan gels when frozen. With reference to carrageenan studies, Raman spectroscopy has mostly been used as a tool for characterisation.[44–46,178]

Confocal Raman spectroscopy was carried out at Unilever's research facility in Colworth, Bedford. The spectrometer used is a WiTec confocal Raman Alpha300, with a spot size of a few microns. A 532nm laser with a Olympus 20x/0.35 long working distance objective was used to collect Raman spectra, with an exposure time of 10 seconds and 6 co-additions. The sample was placed onto a glass microscope slide and covered with a quartz cover slip (0.17 mm thick). The sample assemble was then placed into a temperature gradient Linkam stage, allowing cooling and heating of two sides of the sample.

The primary purpose of this investigation is to attempt to observe changes in the structure of ι-carrageenan when in ice compared to water. The gradient stage allows an ice-front to be created (above and below 0 °C on either side of the stage), successive spectra can be collected from within the same experiment across the ice-front. Similar to changes observed for ice-binding proteins, where their secondary structures change when bound to an ice face,

the spacial resolution of confocal Raman spectroscopy could provide insight into changes of the carrageenans' structure close to a ice surface.[171] Raman microscopy has been previously used to quantify the microstructures of κ-carrageenan and gellan containing complex composite materials microstructures.[58,179,180]

ι-carrageenan is of the most interest within this Chapter. The 805 cm^{-1} peak, associated with a sulfate ester vibration, located in the 2-position of the anhydro-D-galactose residue, has been used to identify ι-carrageenan when in mixtures of other carrageenans as it is characteristic to only the ι-form.[44,60]

Figure 5.1 shows Raman spectra of the sample assembly; glass microscope slide, a water sample, and a quartz cover slip. The spectrum of the quartz cover slip (orange trace) also shows some scattering from water. The traces have been arbitrarily offset for clarity, however they have not been scaled. Some of the experiments carried out utilised a quartz microscope slide, instead of glass.

The thickness of the sample layer that is sandwiched between the slide and cover slip varied from 30 to 50 μm, depending on sample preparation. Carrageenan samples were placed, in a gel form, onto the slide and then a thin film was created by gently squeezing the cover slip down. The cover slip was then sealed with nail varnish to prevent evaporation and secure the cover slip from movement. A Linkam low temperature gradient stage was used to control the temperature of the sample. This was placed on top of an XYZ stage to control sample focus and position.

During initial FTIR investigations of carrageenan gels, using the un-modified Specac low temperature ATR equipment, freeze concentration of the carrageenan occurred. This is discussed in Section 2.1.2 and is due to the rapid freezing of water from the outside of the ATR chamber (where the liquid N_2 is located), pushing the carrageenan towards diamond ATR crystal. When monitored by FTIR spectroscopy there was a several fold absorbance increase of bands associated with carrageenan, suggesting a concentration increase of 2 - 5 times upon

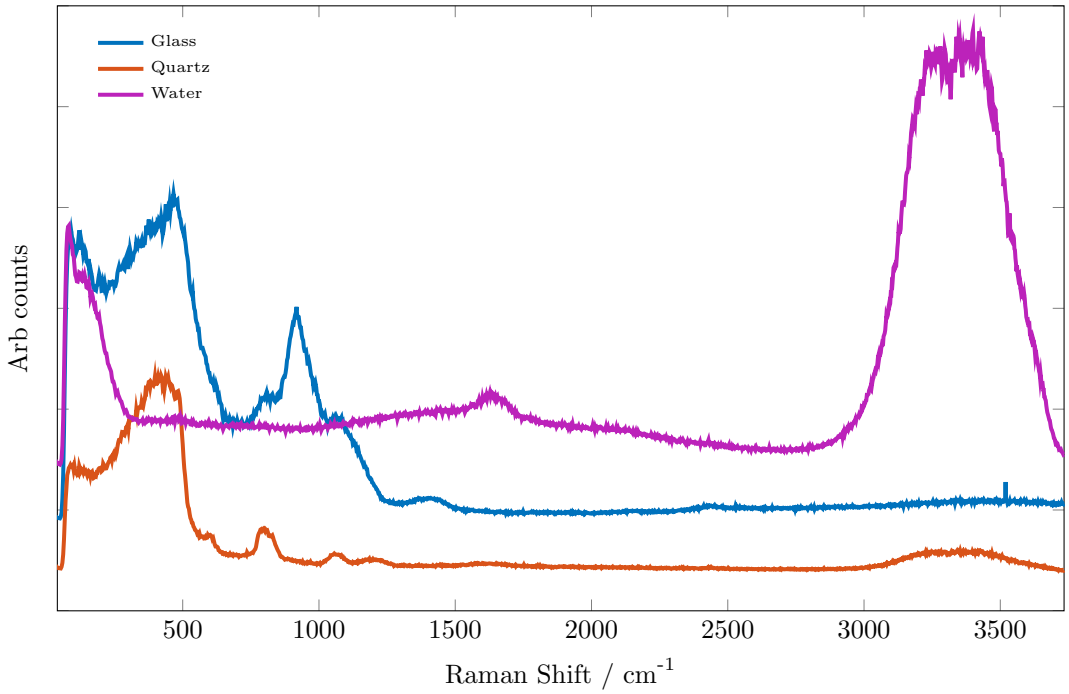

Figure 5.1: Raman spectra of the different components within the sample assembly (z-direction scan)

freeze concentration. Movement of the carrageenan chains due to the ice crystal growth has previously been observed, and this is studied later within this section. Initially to minimise this migration of the carrageenan network for these Raman experiments, flash freezing of the entire sample was conducted using the Linkam stage.

The Linkam temperature controlled gradient stage, has two metal blocks with a 2 mm gap between them, which the microscope slide is seated against. These blocks are capable of individual temperature control using a liquid N_2 pump and heating elements. A gelled 2 % ι-carrageenan sample is placed onto a microscope slide, covered with a cover slip and sealed with nail varnish. Both blocks are rapidly cooled to -40 °C, causing supercooling of the gel, followed by rapid crystallisation. The rapid crystallisation and lack of direction of freezing does not allow any large movements of the carrageenan chains.

5.1 Formation of a Stable Ice-Front

Within this section, a stable ice front within the 2 % ι-carrageenan sample is formed and probed with confocal Raman microscopy. Following flash freezing of the sample, the Linkam stage was then slowly warmed to *ca.* -10 °C and allowed to settle for a period of time.

A temperature gradient was setup across the sample such that the midpoint of the sample was at *ca.* 0 °C. The left and right cooling blocks of the Linkam stage were set to -9 °C and +4 °C, respectively. This allowed the right side of the sample to reach temperatures above the freezing point of the gel, while the left side remained frozen. Once the system had equilibrated, formation of a stable ice-front can be observed. The ice-front was formed in the middle of the gap between the two heating / cooling blocks of the Linkam stage, allowing bright field and Raman microscopy. During slow heating of one side of the sample, the ice front can be seen to recede (to the left hand side of the microscope's visible image) in real time, until an equilibrium point is reached. This took between 10 and 30 minutes for the ice-front to become stable.

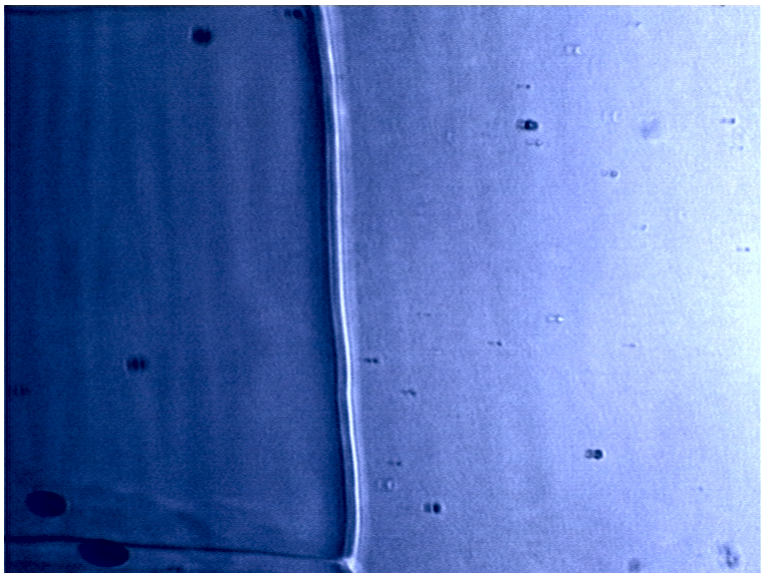

Figure 5.2: Bright field visible image of a stable ice front within a 2 % ι-carrageenan sample, on a Linkam low temperature gradient stage, left held at -9 °C and right held at +4 °C, contrast enhanced for clarity

Figure 5.2 shows the bright field image obtained from the microscope's visible camera, with a stable ice front. As the sample is *ca.* 50 μm deep, with respect to the line of sight of the camera, the ice-front can often appear slightly out of focus as it is not perfectly vertical. The linkam stage is sealed, with a flow of cold N_2 gas passed across the surface to reduce condensation build up. Although sealed, as the cooling elements are in contact with the base of sample, the ice front formed can often protrude, in the horizontal direction, slightly more at the base of the sample. All Raman measurements of the sample are conducted within the middle of the sample to reduce the quartz and/or glass scattering. Once a stable ice front had formed, Raman spectra were collected across the front.

Figure 5.3 shows frozen and unfrozen 2 % ι-carrageenan, collected about 5 μm either side of the ice front. The O-H stretch scattering can be seen to increase in intensity on the lower wavenumber side of the band, *ca.* 3150 cm^{-1}, with a slight reduction of the higher wavenumber side. This same effect was observed for the FTIR of frozen *vs* unfrozen carrageenan gels (Figure 4.2). Within the gelled 2 % ι-carrageenan sample (orange trace), features to the lower wavenumber side of the O-H stretch band can be observed (*ca.* 2850 - 3050 cm^{-1}). These are C-H stretches of the carrageenan chains and can be observed with Raman spectroscopy due to an intensity inversion between the O-H and C-H vibrations between Raman and infrared spectroscopies. This is because of the difference of selection rules between IR and Raman, with less polar more neutral bonds appearing weaker in the IR but stronger within the Raman due to changes of their polarisability during a vibration. Characteristic carrageenan vibrations can bee seen within the fingerprint region of the Raman spectra as well.

Figure 5.3 also appears to show more carrageenan scattering from the gelled sample than the frozen sample. Figure 5.4 shows the same frozen and gelled sample data within the fingerprint region. Carrageenan scattering at 815 (C-O-S), 855 (C-O-S) and 1060 (C-O) cm^{-1} appears more intense within the gelled sample compared to the frozen sample.[44] As previously mentioned, the 805 cm^{-1} peak, associated with a particular sulfate ester vibration has been used to identify

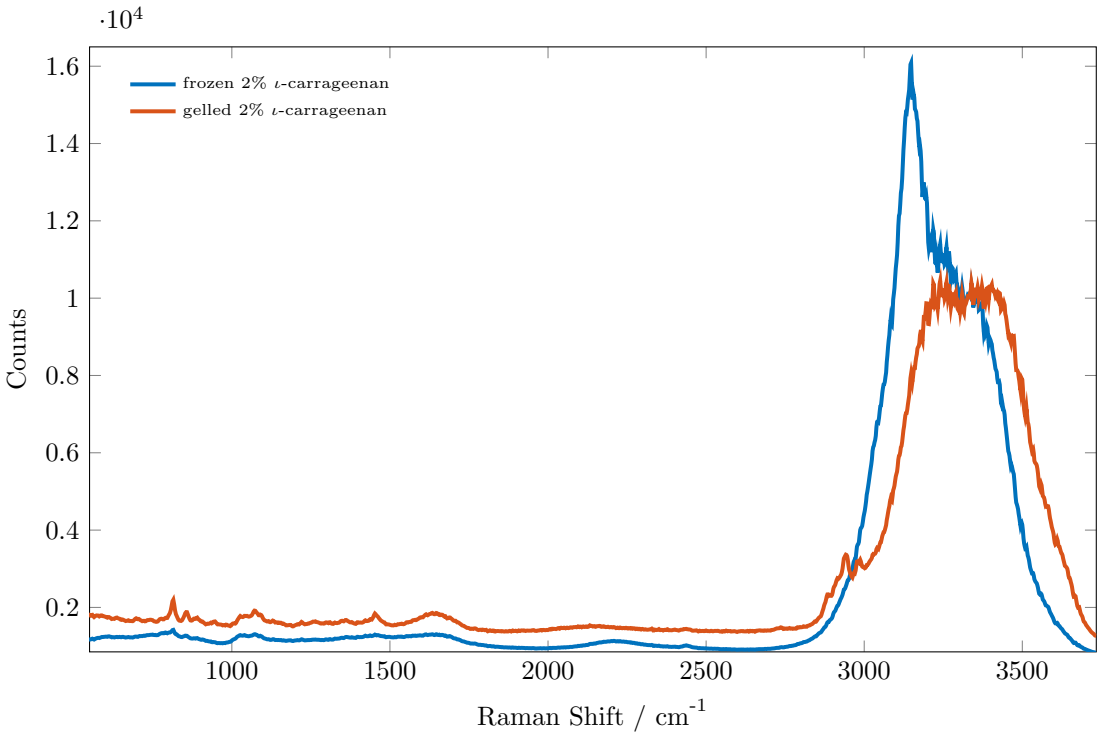

Figure 5.3: Raman spectra of frozen and gelled 2 % ι-carrageenan samples, corresponding to the left and right regions of Figure 5.2 respectively

ι-carrageenan as it is specific to that form. Comparing the spectra collected with literature, it appears that the 815 cm^{-1} peak seen in Figure 5.4 is in fact supposed to appear at 805 cm^{-1}. ι-carrageenan does not the contain the particular bond to show a 815 cm^{-1} peak, however, λ-carrageenan does. Although it is a possibility that λ-carrageenan was incorrectly used instead of ι-carrageenan, multiple samples preparation by multiple users of ι-carrageenan gave the same 815 cm^{-1} peak. The exact reason for this is still not understood and it is suggested that repeat experiments with ι- and λ-carrageenan are undertaken and compared against previous literature results to ascertain the origin of this incorrect band placement.

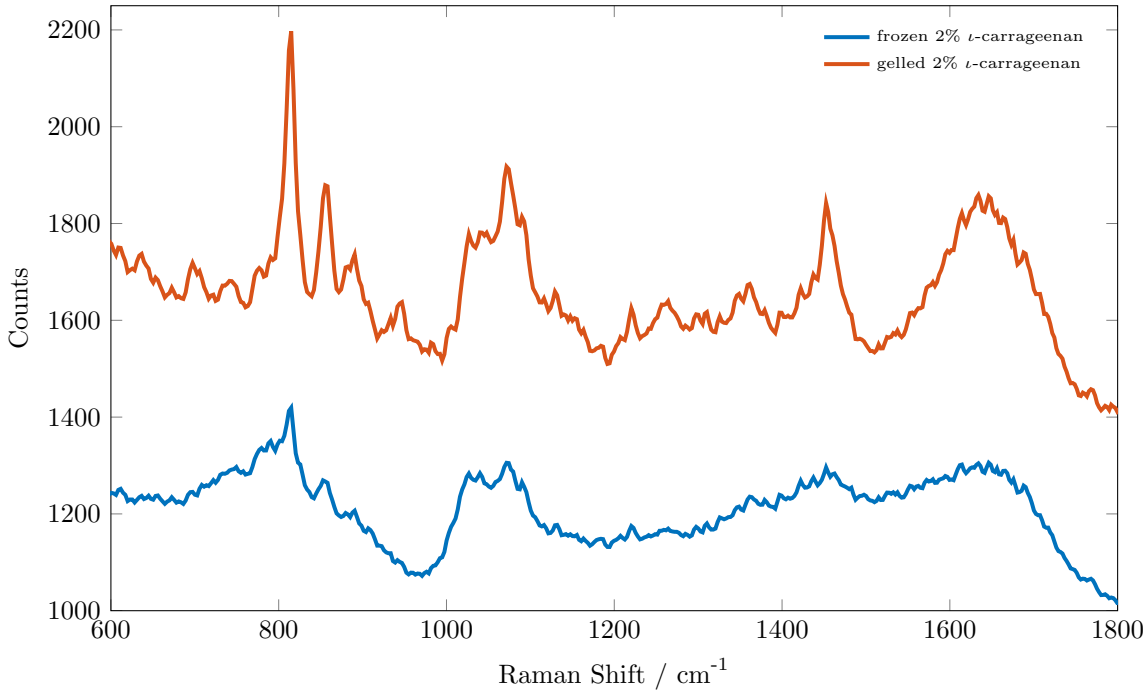

Figure 5.4: Raman spectra of the fingerprint region of frozen and gelled 2 % ι-carrageenan samples, corresponding to the left and right regions of Figure 5.2 respectively

Within Figure 5.4 there is also a large baseline change between the gelled and frozen samples, suggesting more laser light is scattered from the gelled sample, most likely due to the less ordered structure of water compared to ice. One could explain the reduction in carrageenan scattering through localisation of the carrageenan network following freezing, *i.e.* the chains are pushed out of the way by ice crystals.

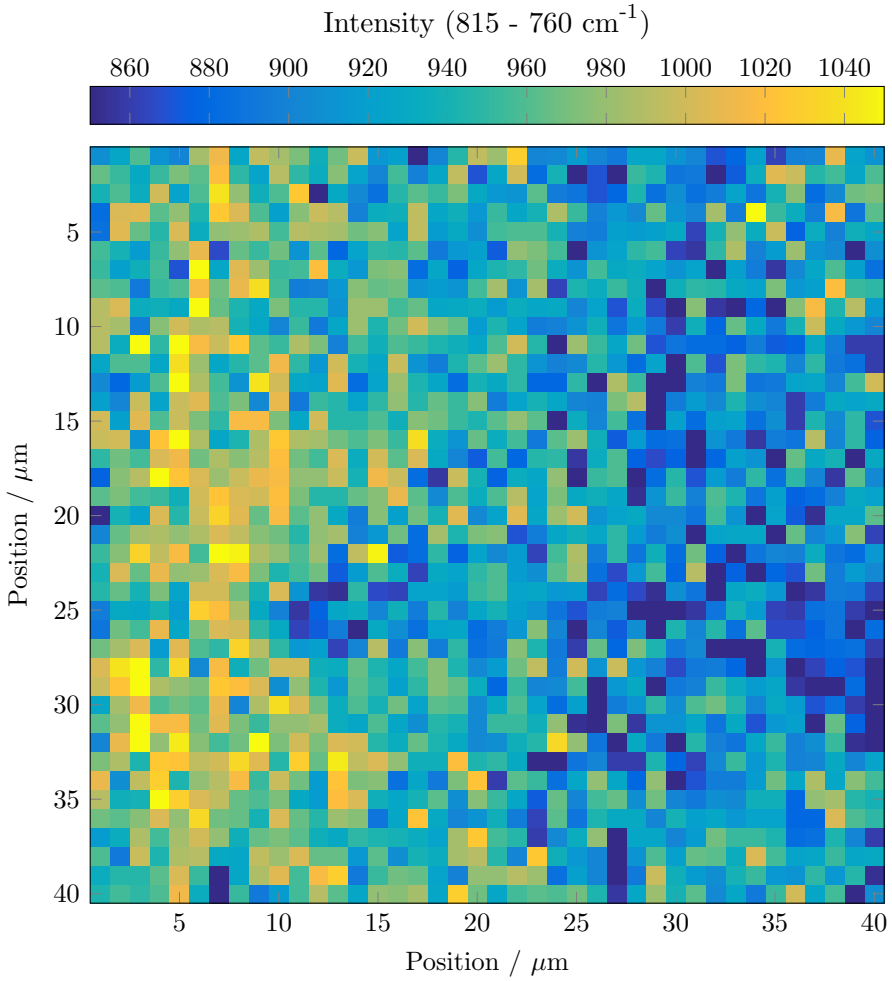

Figure 5.5: Raman map, 40∗40 μm area, 1 μm step size, of a 2 % ι-carrageenan at room temperature, showing intensity of 815 - 760 cm^{-1} as blue to yellow (low to high)

To check the distribution of carrageenan within a gelled sample a Raman map was collected at room temperature of 2 % ι-carrageenan. A 40∗40 μm square area, from within the center of the gelled sample was collected with a step size of 1 μm. Although there will always be some variation in the scattering intensities of a map collected in this way, due to random noise, the map displayed in Figure 5.5 does appear to show structure. If the carrageenan network was truly homogeneous, the intensity of a Raman peak would vary with random noise and there would be no pattern within an intensity map. Figure 5.5 shows areas of the gel which have more or less Raman scattering, from the 815 cm^{-1} peak (subtracted from a baseline position at 760 cm^{-1}). This suggests that the concentration of ι-carrageenan is not constant across the area mapped. However, this does still not explain the differences between the frozen and gelled sample. As the sample is cooled from below, it is possible that freeze concentration pushed the carrageenan towards the top of the sample. Unfortunately experiments to prove the localisation of carrageenan within the frozen gel were not undertaken.

5.2 Scanning Across the Ice-Front

Following formation of a stable ice-front, Raman experiments were conducted where the stage was moved such that spectra were collected in a line across the ice front. The basis behind this section was to determine if any changes within the structure of carrageenan can be seen as the network approaches an ice crystal surface. Ice binding proteins have been shown to change their conformation, binding to specific ice surfaces and are used in several industries to retard ice crystal growth.[171]

A Raman line map across the ice-front formed within an ι-carrageenan sample was collected. A spectrum was collected in micron steps from -20 to +20 μm, left to right, with the 0 μm step indicating the approximate ice-front location, perpendicular to the ice-front. Referring back to Figure 5.2, this is a horizontal line scan across this image.

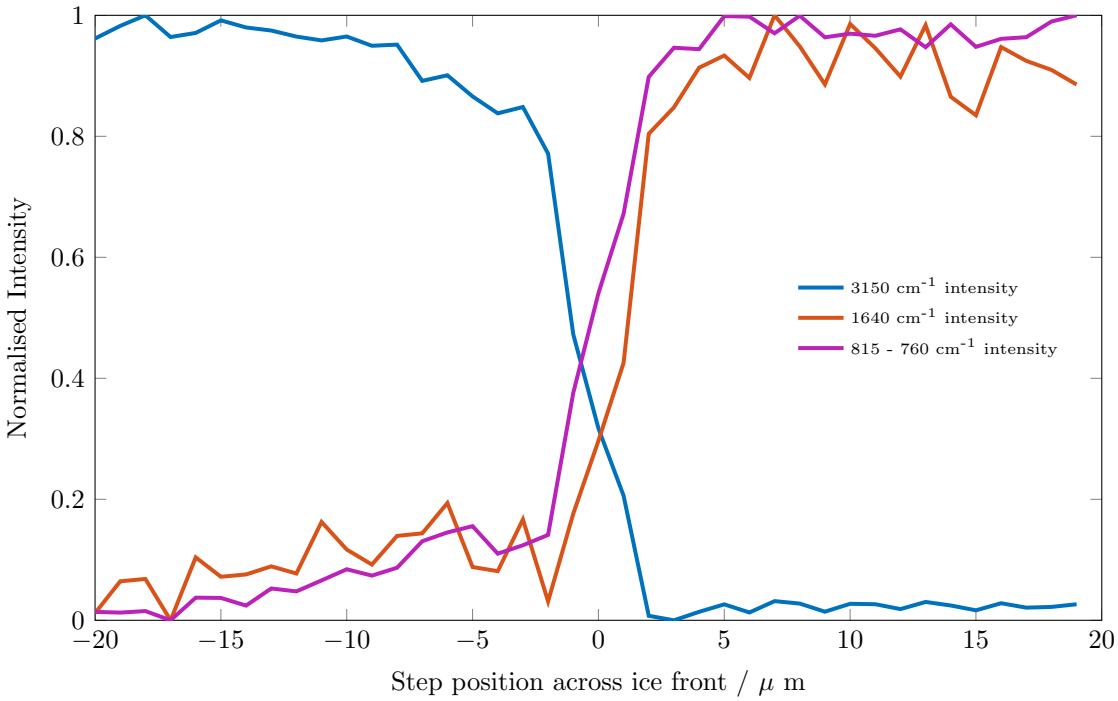

Figure 5.6: Normalised Raman intensity of the O-H stretch (blue), H-O-H bend (orange), and ι-carrageenan's 815 - 760 cm^{-1}intensities across the ice-front of a 2 % ι-carrageenan sample, spectrum collected every micron from -20 to +20 μm, left to right, frozen to gelled, centered at the ice-front as per Figure 5.2

Figure 5.6 shows the normalised Raman intensity of water's O-H stretch, H-O-H bend vibration and ι-carrageenan's 815 - 760 cm^{-1}, as a function of the step position during the line map. The 3150 cm^{-1} peak (blue trace) decreases in intensity as the map steps from ice to water, and the 1640 cm^{-1} peak (orange trace) increases in intensity. The more fixed structure of ice reduces the intensity of the H-O-H bend vibration. It can be seen from Figure 5.6 that the gelled to frozen transition is completed within 3 microns. The intensity of the normalised 3150 cm^{-1} trace is monitoring ice-like characteristics of the H_2O molecules, while the normalised intensity of the 1640 cm^{-1} trace monitored liquid water-like characteristics of the H_2O molecules within the ι-carrageenan system. Comparing the ice side (left and negative step positions) with the water side (right and positive step positions) of Figure 5.6 allows some conclusions to be drawn. Once the change from ice to water is complete (*ca.* step position +2 μm) there is no further changes in ice or water contributions on the water side of the ice-front. However, on the ice-side, there is a decrease in the 3150 cm^{-1} intensity and an increase in the 1640 cm^{-1} intensity as the ice-front is approached. This suggests that once past the ice front, on the water side, there is no ice, however there is a larger water contribution within the ice as the ice-front is approached. This difference between the ice side and the water side of the ice-front are replicated within the ι-carrageenan intensities shown in the purple trace.

Within the previous section, Figure 5.4 indicated that less Raman scattering for ι-carrageenan is observed within the frozen sample compared to the gelled sample. This is seen within the the line map as well, the observed Raman scatter from ι-carrageenan (815 - 760 cm^{-1} intensities, purple trace of Figure 5.6), shows more carrageenan scattering from the water side compared to the ice side of the sample. Also, on the ice side of the sample, as the ice-front is approached, the carrageenan scattering increases in the same manor as the water contribution increases, suggesting that carrageenan scattering is observed to a much greater extent in water-based environments, not ice.

Figure 5.7 shows three Raman spectra of the gelled side of the ice-front, 1, 2 and 10 μm

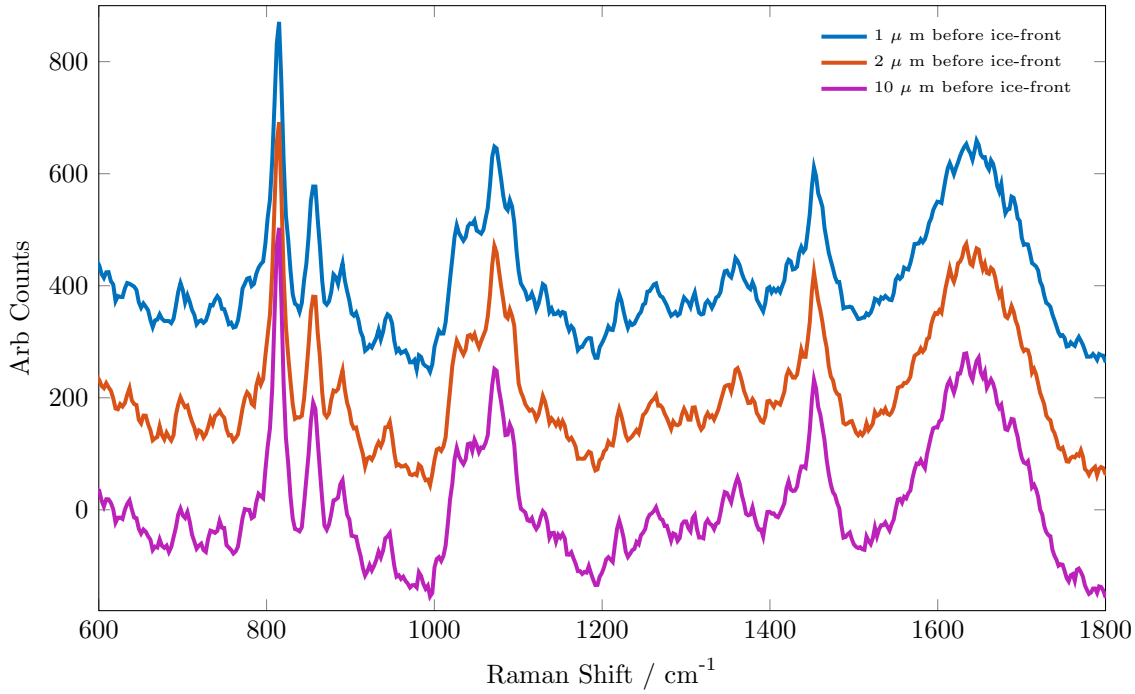

Figure 5.7: Raman spectra showing fingerprint region of a gelled 2 % ι-carrageenan sample at different distances to a stable ice-front, offset for clarity

before the front. All the spectra appear identical and there are no large changes that indicate a change in the carrageenans structure as the ice-front is approached. A Multivariate approach was taken in an attempt to observe any changes as the ice-front is approached. Neither Principal Component Analysis or Multivariate Resolution indicated structural changes between bulk gelled ι-carrageenan and ι-carrageenan that was close to the ice-front.

The autocorrelation spectrum can reveal wavenumbers that are subject to change during the approach and this is shown, along with the mean gelled spectrum in Figure 5.8. The two largest features of the autocorrelation spectrum, at 1100 and 900 cm^{-1}, are cosmic rays that have caused spikes within one of the spectra as they hit the CCD. The other features of the autocorrelation spectrum belong to the C-O-S intensity at 815 cm^{-1} and the C-O vibration at 1050 cm^{-1}. As the autocorrelation spectrum resembles a (much lower intensity) baselined version of the mean spectrum of ι-carrageenan, the autocorrelation function is most likely locking onto small changes

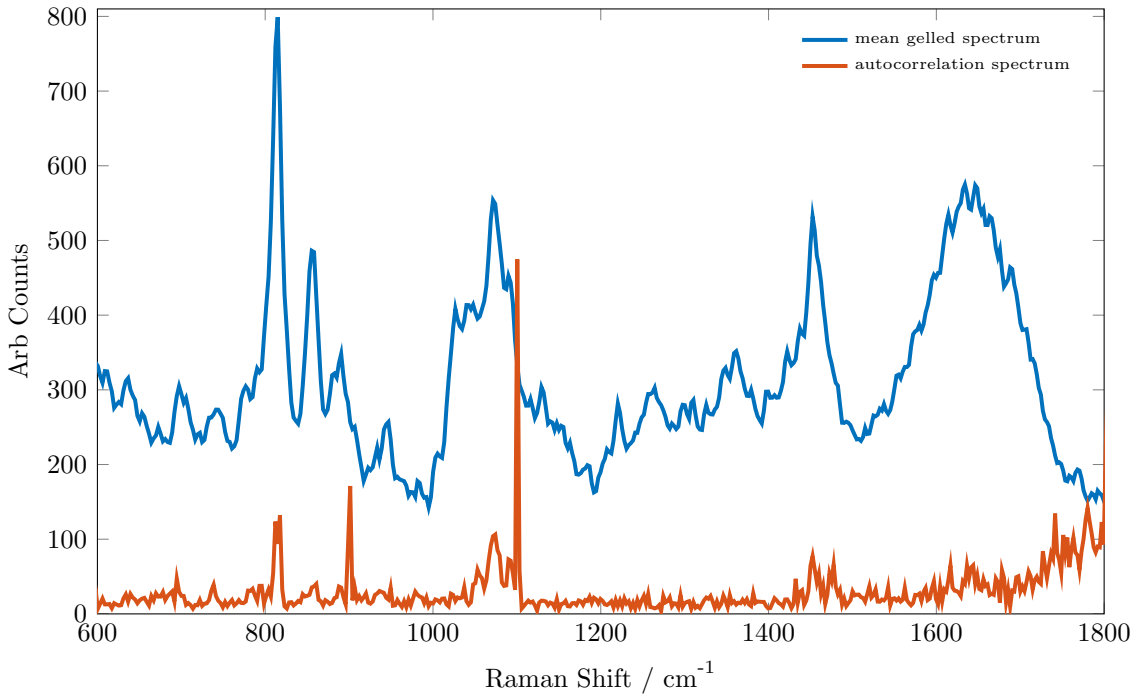

Figure 5.8: Mean Raman spectrum and autopower spectrum, of a gelled 2 % ι-carrageenan sample for distances 0-20 μm of the approach to a stable ice front

in the concentration of ι-carrageenan. This could either be due to random variation in Raman scattering / sampling method, or the natural heterogeneous nature of the gelled sample as shown in Figure 5.5

Moving window two-dimensional correlation spectroscopy (MW2D) and perturbation correlation moving window two-dimensional correlation spectroscopy(PCMW2D) were also used to analyse the data of the approach of the ice-front, from both the frozen and gelled sides. however these techniques provided no additional information over those gained in Figure 5.6. No changes to the carrageenan structure was observed as a function of distance from the ice-front. The gelled side showed a concise step, of both the H_2O and carrageenan base vibrational scattering, from water to ice and a decrease in carrageenan concentration respectively. From the frozen side, the change was more gradual, with an increased water content before the major change, and an increase in carrageenan scattering near the frozen side of the ice-front. These techniques

again confirmed the increased scattering due to carrageenan within the unfrozen component and indication of an increase of water content also points to a increased carrageenan concentration.

5.3 Moving the Ice-front

Early experiments with the low temperature ATR systems showed the ability of the crystallisation of water to physically move the carrageenan chains. This was observed as an increase of absorbance of carrageenan bands as water was frozen at the extremities of the sample chamber, pushing the carrageenan network towards the centre, where the ATR crystal is located. This was discussed in Section 2.1.2 and due to the variable temperature gradient stage in use with Raman spectroscopy this can be investigated further.

Following formation of a stable ice-front within the sample, where one side is held at a temperature above 0 °C and the other below, small changes in drive temperatures of either side of the gradient will result in the movement of the ice-front as it approaches a new equilibrium position. In the previous section, a stable ice-front was formed and then the Raman laser was scanned across it using a motorised stage. Instead of sampling across the front by moving the sample, the work within this section will keep the Linkam stage fixed and collect Raman spectra across the ice front by causing the ice-front to move by changing the temperature gradient.

Changing the temperature gradient of a stable ice-front will result in one of two options; regression of the ice-front, or progression of the ice-front. With respect to the previous section, and the original geometry of the ice-front, this means the ice-front either recedes left (into the frozen sample) or progresses right (into the gelled sample).

The regression and progression runs were runs were collected in sequence. The sample was flash frozen to -40 °C, then a stable ice-front was formed with the left and right temperature controllers set to -9 and 4 °C, respectively. The right temperature controller was set to change

the temperature from 4 →4.5 °C, producing a receding ice-front that moved to the left. The visible camera of the Raman microscope was used to located the ice-front. Spectral acquisition was set on a loop, to continuously record spectra and upon initiation of the acquisition the XYZ stage was used to align the sampling spot to 20 μm to the left of the ice-front (*i.e.* within the frozen sample). The ice-front moved very slowly, *ca.* 1 μm every 4 minutes, and spectra were collected continuously for 4 hours. Within this time, the ice-front receded across the Raman laser. After completion of the recession run, the progression run was then collected. The right temperature controller was set to change from 4.5 →4 °C, causing the ice front to re-grow (progress), moving right. The visible camera was monitored and when the ice-front came within 20 μm of the center spot, spectral acquisition began for the progression run.

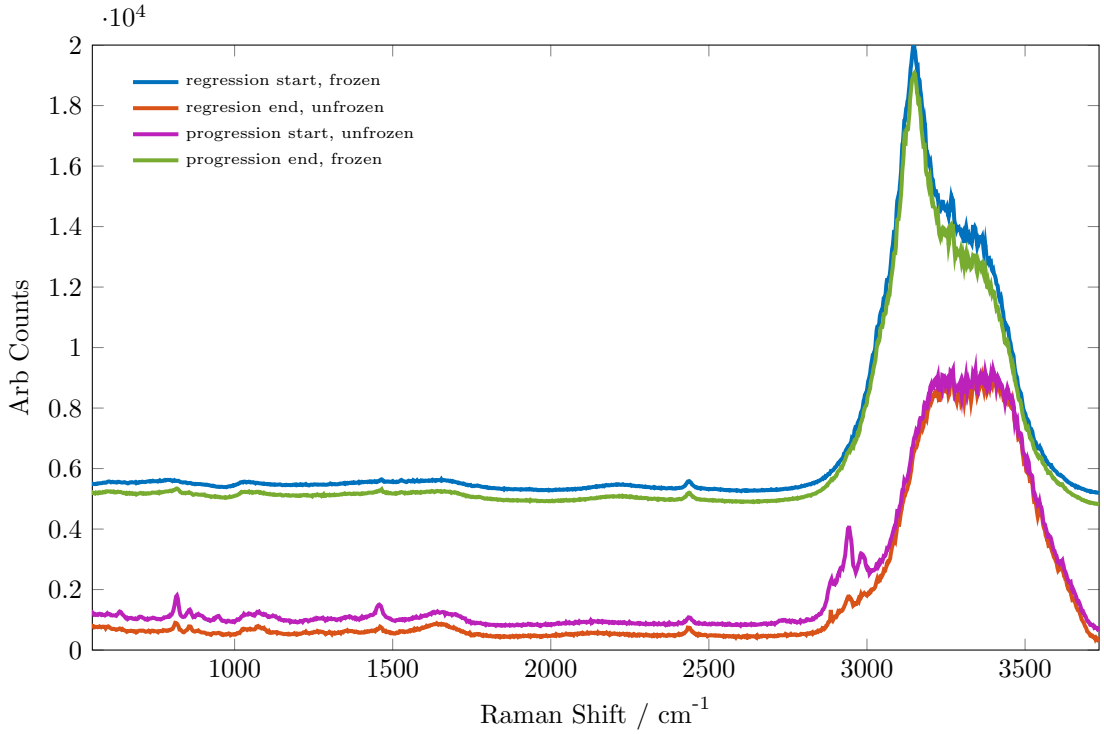

Figure 5.9: Raman spectra from the start and end of the regression and progression runs, showing the frozen sample (for 'start regression' and 'end progression') and gelled sample (for 'end regression' and 'start progression')

Figure 5.9 shows Raman spectra obtained at the start and end of both the regression and

procession runs. It is clear that both the start of the recession run and end of the progression run, a frozen sample is being probed. These two spectra (blue and green traces) appear almost identical (they have been offset slightly for clarity). It is immediately obvious within the gelled samples (orange and purple for 'end regression' and 'start progression', respectively) that there appears to be a difference in carrageenan concentration between the two runs. This is due to a freeze concentration effect. As the ice-front progresses slowly, the carrageenan is 'pushed' out of the way by the slow formation of ice-crystals. The exclusion of carrageenan from the ice-crystals causes a concentration build up in the liquid phase, *i.e.* the unfrozen gel. This effect is a similar process to that observed with the freeze concentration of the ATR system (Section 2.1.2), however at a slowed rate, due to a temperature difference.

Figure 5.10 shows how the ice and carrageenan content changes as a function of time for the recession and progression runs. The top panel shows the intensity of Raman scattering at 3150 cm^{-1} for the regression (blue) and progression runs (orange). The bottom panel shows the intensity of 815 - 760 cm^{-1} as a function of time for the recession (blue) and progression (orange) runs. As previously mentioned the intensity of the 3150 cm^{-1} feature effectively shows the ice-content of the sample and 815 - 760 cm^{-1} is a baselined C-O-S carrageenan band.

The top panel of Figure 5.10 shows that after *ca.* 80 minutes, for both the recession and progression runs, the sample's ice-like characteristics are seen to change. The intensity of the 3150 cm^{-1} feature for the recession run (blue trace) decreases rapidly, with the change taking 5 minutes in total. This is the observation of the ice melting (due to the ice-front recessing and moving left) as a fucntion of time caused by the temperature differential described above. At $t < 80$ and $t > 80$ the height of the 3150 cm^{-1} is constant, indicating a clear and quick transition from ice to water. The progression run (orange trace) shows a similar transition, except inverted and much slower. The intensity of the progression run increases gradually after $t = 90$ in a sigmoidal manor and does not show completion until *ca.* $t = 180$ minutes. This indicates that unlike the recession run the phase transition (water to ice) takes roughly 90

minutes for the progression run.

The differences between the recession and progression runs (blue and orange, top panel, Figure 5.10) suggest that the melting transition (ice to water) is much quicker than the freezing transition (water to ice). Unfortunately due to available time on the equipment and repeated temperature controller failures a baseline experiment of a pure water system was not undertook. This means that this effects cannot be definitively assigned to influences that carrageenan has imparted to the system. These set of experiments most defiantly should form part of future work with ι-carrageenan gels as this may be spectroscopic evidence for the influence of ι-carrageenan on the freezing rate or thermal hysteresis of the system.

The bottom panel of Figure 5.10 shows how the Raman scattering at 815 cm^{-1} (baselined against 760 cm^{-1}) changes for the recession (orange trace) and progression (blue trace) runs. The recession run shows a higher carrageenan concentration within the gelled system compared to the frozen system; $t < 80$ shows near 0 scattering from carrageenan, *ca.* $t = 80$ shows a large increase in carrageenan signal, and $t > 80$ shows a constant carrageenan signal from the gelled sample for the remainder of the ice front movement. The progression run (orange trace) shows a steady signal for $t < 80$, a 90 minute sigmoidal-like decrease and then a constant signal for $t > 180$ to the end of the experiment. The carrageenan scattering for both the recession and progression runs appears to follow a similar trend as the intensity of the 3150 cm^{-1} O-H stretch shown in the top panel. The main difference is that an increase in 3150 cm^{-1} intensity is linked to a decrease in 815 cm^{-1} intensity (*i.e.* they are inverted), indicating that carrageenan scattering is more present within gelled, non-frozen, parts of the sample.

Figure 5.10 also shows a much higher carrageenan concentration for the progression run that the recession run, in accordance with what was observed in figure 5.9. Not only is the carrageenan concentration for the gelled side of the progression run higher than that of the gelled regression run, the frozen part progression run also shows a more carrageenan scattering

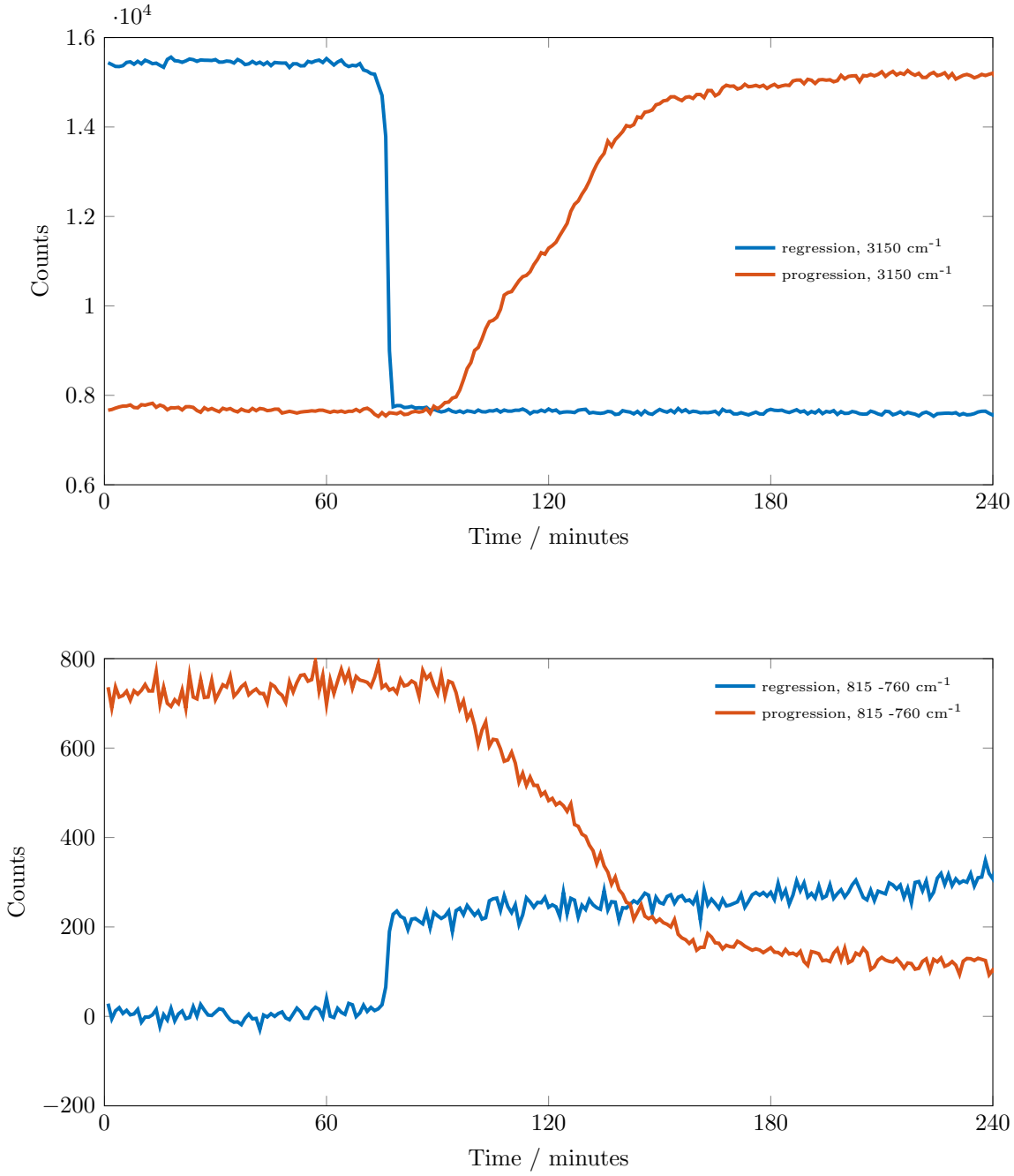

Figure 5.10: Intensity of Raman spectra during the recession and progression runs for; top panel: 3150 cm^{-1} intensity, showing ice-like characteristics, and bottom panel: 815 - 760 cm^{-1} intensity, showing carrageenan concentration

than the start of the regression run. As the carrageenan chains are excluded are from frozen sample, due to the slow progression of ice crystals forming, when progression run freezes, more carrageenan is included within frozen structure. This analysis also helps suggest the cause for the increased length of the unfrozen → frozen transition of the progression run, compared to the frozen → unfrozen transition of the regression run. When the progression run is undergoing it's freezing transition (at the point of Raman collection) there is a higher carrageenan concentration within the unfrozen sample. The higher "impurity" of carrageenan the may be responsible for the longer transition. An increased concentration of biopolymer means that more of the water molecules will be placed into a solvating role, instead of within a bulk water role, slowing the crystallisation process.

Figure 5.11 shows the O-H stretch of water and the C-H vibrations of carrageenan (normalised to the O-H stretch maxima) for the end of the recession run (blue), start of the progression run (orange) and a gelled 2 % ι-carrageenan sample (purple) at room temperature.

Figure 5.11 shows that the concentration of carrageenan at the end of the recession run is about the same as that of a 2 % gelled ι-carrageenan sample. Whereas the ι-carrageenan concentration of the start of the progression run (orange) is much higher. This is attributed to the freeze concentration of carrageenan as the slow formation of ice crystals excludes the biopolymer chains from the frozen sample, causing an increased concentration within the remaining unfrozen sample.

The difference in line shape of the O-H stretch vibration of Figure 5.11 between the gelled 2 % ι-carrageenan sample (purple), and the regression (blue) and progression (orange) runs is due to a difference of sample temperature. The purple trace is of a gelled carrageenan sample at room temperature, whereas the temperatures of the other two are between *ca.* 0 - 4 °C. As the temperature of water based systems is increased the ratio between the higher wavenumber components and lower wavenumber components of the O-H stretch is increased. Generally, lower

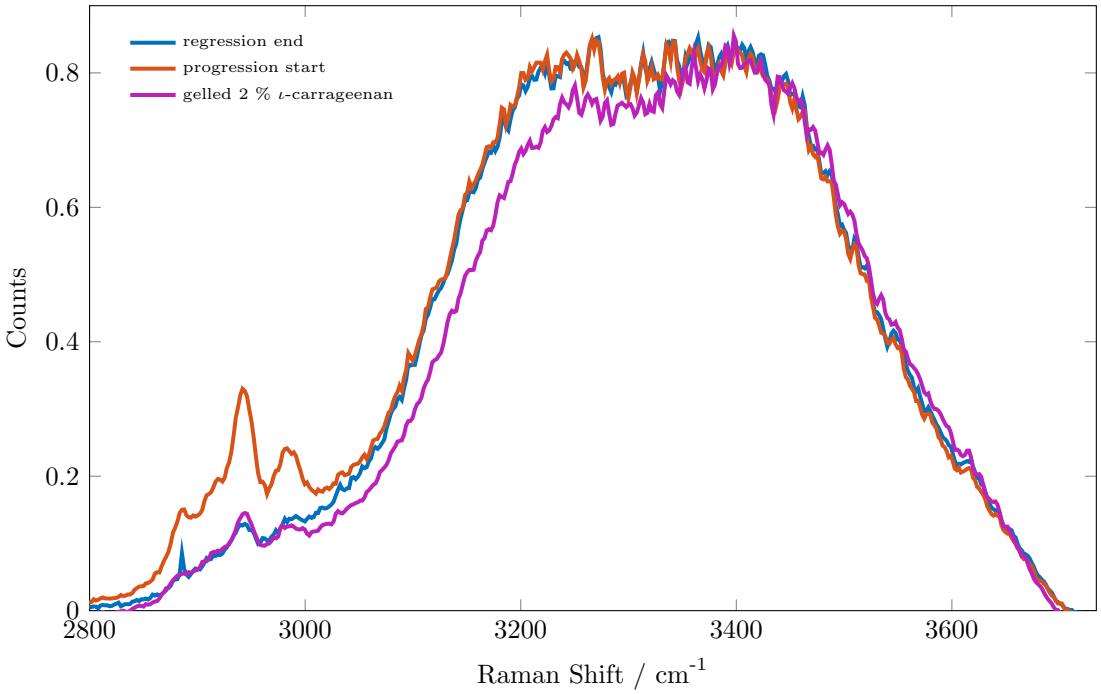

Figure 5.11: Raman spectra showing the O-H stretch region of the end of the recession run (blue trace), the start of the procession run (orange trace) and a gelled 2 % ι-carrageenan sample at room temperature. Differences in carrageenan concentration can be seen *via* the C-H vibrations at *ca.* 2850 - 3050 cm^{-1}

wavenumber components are attributed to water molecules with stronger hydrogen bonds and higher wavenumber components have a weaker hydrogen bonding environment.[174,175]

5.4 Conclusions

The Raman scattering from carrageenan vibrations is greater within gelled, unfrozen, samples that within frozen samples. This suggests an increased concentration of carrageenan within the unfrozen side of the sample, compared to the frozen side. Movement of carrageenan due to freezing (freeze concentration) was previously observed within the FTIR-ATR studies of the carrageenan system (Section 2.1.2), however flash freezing of the sample to -40 °C was performed for the Raman experiments in an attempt to stop this happening. Experiments conducted on movement of the ice front confirmed the presence of carrageenan within the frozen samples once thawed.

Raman mapping of a stable ice-front formed within a 2 % ι-carrageenan gel showed a clear transition between the frozen and unfrozen sides of the samples. The transition appeared to spread over *ca.* 4 μm. The right (unfrozen) side of the sample showed a quick and sharp transition to ice, as monitored by the intensities at 3150 (O-H stretch) and 1640 (H-O-H bend) cm^{-1}. Whereas the left (frozen) side of the ice-front showed a slower transition, with an increase of intensity at 3150 $cm^{-1}$for *ca.* 10 μm prior the main transition. This implies that within the unfrozen side of the sample there is no ice-like Raman scattering, but the frozen side of the sample shows an increase in water-like Raman scattering as the front is approached.

The carrageenan content was seen to vary across the ice front as well. There is more scattering due to carrageenan from the unfrozen side compared to the frozen side of the sample. As the ice-front is approached from the frozen side, an increase in water-like scattering is observed, this is accompanied by an increase in Raman scattering from carrageenan (seen within Figure 5.6). This could be due to localisation of the carrageenan chains between the ice crystals as they are

formed, however further study is needed.

Following creation and Raman mapping of a stable ice-front, experiments were performed where a temperature differential was setup, causing the ice-front to move. Within these experiments, the XYZ stage (and therefore Raman sampling position) was kept fixed, and the ice front was moved left and right. The recession and progression runs showed similar data, with a transition from frozen to unfrozen, and unfrozen to frozen samples, respectively. The changes within the O-H stretch scattering were mimicked by the changes within scattering due to carrageenan and broadly followed the observed changes within the stable ice front section; more carrageenan based scattering from unfrozen samples compared to frozen samples.

At the end of the progression run, a substantial increase in carrageenan concentration was seen, presumed to be due to freeze concentration effects. The increased scattering from carrageenan was present within the unfrozen and frozen samples. The increase in concentration may be a major cause in the difference of transition rates between the regression and progression runs (seen within Figure 5.10).

The rate of recession and progression of the ice-front at the point of Raman collection may not be identical. This is because during the recession run, the spectral acquisition was near the start of the ice-front movement, whereas the procession run collected data near the end of the ice-front movement,*i.e.* near where a stable front would be formed at the end of the experiment. Although this may have compounded effects seen within Figure 5.10 the close start times of the changes seen within the sample indicate that the rate of change is similar, as spectral acquisition was started 20 μm from the ice-front.

A possible solution to this difference in rate would be to examine the moving ice front at the midpoint of its transition. During the experiments, the recessing ice-front was monitored at the beginning of its transition, where the largest temperature difference existed and therefore most likely where the highest rates occurred. The end of the progression run is near where a

stable ice-front would be formed (at 4 °C), there exists the smallest temperature difference and probably the slowest rate of ice growth. To determine the midpoint of the transition, one can form stable ice fronts at two different temperature differential (left: -9 °C, right: 4 °C and left: -9 °C, right 4.5 °C, for example) and find the midpoint of the two fronts. This should allow a closer match of recession and progression rates.

Unfortunately due to equipment availability and malfunction, multiple repeats of the recession and progressions runs could not be completed. Multiple regression runs were successfully undertook that showed identical information, however progression runs were not. Following the results of the regression and progression experiments, it was clear that baseline repeat experiments with a pure water sample need to be done. It would be worthwhile within future experiments to vary to concentration of carrageenan within the sample. This would increase the SNR of the sample and also, if these effects are due to carrageenan, exaggerate the effects seen within this chapter.

It would also be beneficial to run these experiments on another imaging apparatus such as an imaging FTIR (FPA, focal plane array based) system to confirm the results with another experimental approach. The Spero system manufactured by Daylight Solutions would allow near real-time spectral collection within fingerprint region (showing water HOH bend and carrageenan traces) across an ice front. The Spero system features a 480∗480 pixel microbolometer with a pixel resolution of *ca.* 1 μm allowing for the entire front to be imaged simultaneously.

Appendix - MATLAB Code

This section contains the various Matlab scripts that have been written and implemented within this thesis. These scripts and functions work 'as is', and allow analysis of data with methods used in this thesis. Please contact calum.welsh@gmail.com should assistance be required. A variety of MATLAB versions were used during this thesis, with the latest version being 2015b, on OSX. The operating systems makes little difference apart from files linked to paths which utilise forward slashes rather than backslashes as per Windows. MATLAB versions from 2007 onwards should function seamlessly. Various MATLAB toolboxes are also required: Curve Fitting Toolbox, Optimization Toolbox and Signal Processing Toolbox. PLSToolbox and MiaToolbox from Eigenvector Inc have also been used extensively, versions 8 (build 18015) and 3 (build 19904), respectively.

5.5 Principal Component Analysis and Multivariate Curve Resolution Sample Data

```
function [ AB ] = sample_data_pca(  )
%Generation of sample data for PCA example in Introduction
%(c) Calum Welsh, University of Nottingham - calum.welsh@gmail.com

% Setup 2 different psueod-components: A & B
% Gaussian profiles, 500 vars
A1 = 1.0 * exp(-0.5*(([1:500]-100)/20).^2);
A2 = 0.6 * exp(-0.5*(([1:500]-150)/30).^2);
A3 = 0.8 * exp(-0.5*(([1:500]-300)/10).^2);
A = A1 + A2 + A3;

B1 = 0.7 * exp(-0.5*(([1:500]-200)/25).^2);
B2 = 0.2 * exp(-0.5*(([1:500]-320)/40).^2);
B3 = 0.3 * exp(-0.5*(([1:500]-350)/15).^2);
B = B1 + B2 +B3;

% Setup how they change over 1000 datapoints, normalised to 1
a = 1:-0.001:0.001;
b = 0.001:0.001:1;

% Compose entire dataset, add Gaussian noise, with SNR 20
AB = awgn((a'*A + b'*B),22);
```

5.6 Two-Dimensional Correlation Spectroscopy

```
function [ syn,asyn ] = cor2d( varargin )
%Generalised 2D correlation using Hilbert-Noda Matrix
%[syn,asyn] = cor2d(data,plot);
%Data input as (sample,spectra)
%Plot is optional, put 1 for plot, leave empty for none
%Algorthim is implementaion of Isoa Noda's 2DCOS - "Two Dimensional
%Correlation Spectroscopy" John Wiley and Sons, 2004, Isao Noda and
%Yukihiro Ozaki
%(c) Calum Welsh, University of Nottingham - calum.welsh@gmail.com

% Deal with input variables: {1} is data
data = varargin{1};

% Create dynamic spectra (y-tilda) from Noda
[m,¬] = size(data);
data_mean = mean(data,1);
dynam = data - repmat(data_mean,m,1);

% Generation of the Hilbert Noda Matrix for 90deg phase shift
N = zeros(m);
for j = 1:m
    for k = 1:m
        if j==k
            N(j,k) = 0;
        else
            N(j,k) = 1/(k-j);
        end
    end
end

% Output Synchronous and Asyncrhonous
syn = (1/(m-1)) * (dynam' * dynam);
% N * dynam gives the orthoganol spectra
asyn = (1/(m-1)) * dynam' * N * dynam;

% Plot funciton for quick viewing of the 2D output
if length(varargin) == 2

    figure('units','normalized','outerposition',[0.05 0.05 0.9 0.9]);

    subplot (2,2,1);
    contour (syn,50);
    title('Synchronous')

    subplot (2,2,2);
    mesh (syn);
    title('Synchronous')

    subplot (2,2,3);
    contour (asyn, 50);
    title('Asynchronous')
```

```
52
53      subplot (2,2,4);
54      mesh (asyn);
55      title('Asynchronous')
56
57  else
58  end
59
60  end
```

5.7 Two-Dimensional Correlation Spectroscopy Sample Data

```
function [ ABCD ] = sample_data_2dcos(  )
%Generation of sample data for 2DCOS example
%Data is adaptation of sample data from Isoa Noda's 2DCOS - "Two Dimensional
%Correlation Spectroscopy" John Wiley and Sons, 2004, Isao Noda and
%Yukihiro Ozaki
%(c) Calum Welsh, University of Nottingham - calum.welsh@gmail.com

A = exp(-0.5*(([1:50]-10)/2).^2);
B = exp(-0.5*(([1:50]-20)/2).^2);
C = exp(-0.5*(([1:50]-30)/2).^2);
D = exp(-0.5*(([1:50]-40)/2).^2);

AC_couple = zeros(50,50);
BD_couple = zeros(50,50);

for i = 1:50
    AC_couple(i,:) = (A * i) + (C * (51-i));
end

for i = 10:40
    BD_couple(i,:) = (B * 1.15 * i) + (D * 1.15 * i);
end

ABCD = AC_couple + BD_couple;
```

5.8 Moving-Window Two-Dimensional Correlation Spectroscopy

```
function [ output ] = cor2d_mw( varargin )
%Moving Window 2D correlation using Hilbert-Noda Matrix
%[syn,asyn] = cor2d(data,syn/asyn,width,slice,plot);
%Data input as (sample,spectra)
%syn/asyn - type 1 for syn or 0 asyn for analysis
%Slice is optional, diagonal of syn is
%Plot is optional, put 1 for plot, leave empty for none
%Algorthim is implementaion of Isoa Noda's 2DCOS - "Two Dimensional
%Correlation Spectroscopy" John Wiley and Sons, 2004, Isao Noda and
%Yukihiro Ozaki
%(c) Calum Welsh, University of Nottingham - calum.welsh@gmail.com

% Deal with input variables
data = varargin{1};
syn_asyn = varargin{2};
m = round(varargin{3}/2);
slice = varargin{4};

if nargin < 5, plot = 0; else plot = varargin{5}; end
if nargin < 4, disp('not enough inputs'); return; end

[size_len, size_wid] = size(data);
mw_data = [];

% Main loop cycling through all the windows
for i = (m+1):(size_len - m)
    % index for window
    l_lim = i - m;
    u_lim = i + m;
    data_matrix = data(l_lim:u_lim,:);
    data_matrix_mean = repmat(mean(data_matrix,1),(2*m+1),1);
    dynam = data_matrix - data_matrix_mean;

    switch syn_asyn
        case 0
            mw_loop = (1/(m-1)) * (dynam' * dynam);
        case 1
            if slice == 0
                disp('You are trying to compute the autocorrelation of the ...
                    asynchronous!');
                return;
            end
            % Hilbert-Noda transformation matrix
            N = zeros(2*m+1);
            for j = 1:2*m+1
                for k = 1:2*m+1
                    if j==k
                        N(j,k) = 0;
                    else
                        N(j,k) = 1/(k-j);
                    end
```

```
51                 end
52             end
53
54             mw_loop = (1/(m-1)) * dynam' * N * dynam;
55     end
56
57
58     if slice == 0
59         mw_data = [mw_data diag(mw_loop)];
60     else
61         mw_data = [mw_data mw_loop(slice,:)];
62     end
63
64 end
65
66 % Fill the remaining with zeros, 1:m and end-m:end
67 fill_data = zeros(size_wid,m);
68 output = [fill_data mw_data fill_data];
69
70 % Plot funciton for quick viewing of the 2D output
71 if plot == 1
72
73     figure('units','normalized','outerposition',[0.05 0.05 0.9 0.9]);
74
75     subplot (1,2,1);
76     contour (output,50);
77
78     subplot (1,2,2);
79     mesh (output);
80
81 else
82 end
83
84 end
```

5.9 Perturbation-Correlation Moving-Window Two-Dimensional Correlation Spectroscopy

```
function [ syn, asyn ] = pcmw2d( varargin )
%Perturbation-Correaltion Moving-window Two-Dimensional Correlation Spectroscopy
%[syn,asyn] = pcmw2d(data,width,plot);
%Data input as (sample,spectra), width as scalar
%Plot is optional, put 1 for plot, leave empty for none
%Algorithm is based on Morita and Ozaki's - Appl Spec, 60,4,2006
%(c) Calum Welsh, University of Nottingham - calum.welsh@gmail.com
% Code developed with David Tiemessen

% Deal with input variables: {1} is data, {2} is width,if {3} exists then plot
data = varargin{1}'; % data transpose as this is how Morita uses
m = round(varargin{2}/2);
if length(varargin) == 3
    plot = 1;
else
    plot = 0;
end

[size_len, size_wid] = size(data); % determine number of perturbations

% Initialise arrays
mw_data_syn = [];
mw_data_asyn = [];
pert = [0:(size_wid - 1)];

% Hilbert-Noda transformation matrix
N = zeros(2*m+1);
for j = 1:2*m+1
    for k = 1:2*m+1
        if j==k
            N(j,k) = 0;
        else
            N(j,k) = 1/(k-j);
        end
    end
end

% Main loop cycling through all the windows
for i = (m+1):(size_wid - m)
    % index for window
    l_lim = i - m;
    u_lim = i + m;
    data_matrix = data(:,l_lim:u_lim); % data in window
    data_matrix_mean = repmat(mean(data_matrix,2),1,(2*m+1)); % mean of data ...
        in window

    % calculation of p-bar j from equation 16
    p_bar = 1 / (2*m+1) * sum(pert(1,l_lim:u_lim));

```

```
49      % calculation of p-tilda J from equation 17
50      p_bar_dif = pert(1,l_lim:u_lim) - repmat(p_bar,1,(2*m+1));
51
52      % calculating the dynamic spectrum (y-tilda) equation 11
53      data_matrix_r = data_matrix - data_matrix_mean;
54
55      %calculation of the Syn part of pcmw2d for 1 window, from equation 18
56      pcSyn = (1 / (2*m)) * sum( data_matrix_r .* repmat(p_bar_dif,size_len,1),2);
57
58       %calculation of the Asyn part of pcmw2d for 1 window, from equation 19
59      pcAsyn = (1 / (2*m)) * sum( data_matrix_r .* repmat(sum(N .* ...
            repmat(p_bar_dif,(2*m+1),1),2)',size_len,1),2);
60
61      % filling syn and asyn pcmw2d arrays
62      mw_data_syn = [mw_data_syn pcSyn];
63
64      mw_data_asyn = [mw_data_asyn pcAsyn];
65
66  end
67
68
69  % filling remaining columns with zeros
70  fill_data = zeros(size_len,m);
71
72  mw_data_syn_r = [fill_data mw_data_syn fill_data]';
73
74  mw_data_asyn_r = [fill_data mw_data_asyn fill_data]';
75
76  % outputing data
77  syn = mw_data_syn_r;
78  asyn = mw_data_asyn_r;
79
80  % Plot funciton for quick viewing of the 2D output
81  if plot == 1
82
83      figure('units','normalized','outerposition',[0.05 0.05 0.9 0.9]);
84
85      subplot (2,2,1);
86      contour (syn,50);
87      title('Synchronous')
88
89      subplot (2,2,2);
90      mesh (syn);
91      title('Synchronous')
92
93      subplot (2,2,3);
94      contour (asyn, 50);
95      title('Asynchronous')
96
97      subplot (2,2,4);
98      mesh (asyn);
99      title('Asynchronous')
100
101 else
102 end
```

```
103
104 end
```

5.10 Plot2D function for displaying 2DCOS, MW2D and PCMW2D within thesis

```
function plot2d_latex(syn_or_asyn,data_mean,xaxes,contour_level,axes_labels)
% 2D plotting fucntion for 2DCOS, MW2D and PCMW2D for thesis presentation

% Check if syn&asyn are square for 2DCOS or rectangle for MW

if size(syn_or_asyn,1)==size(syn_or_asyn,2)
    % Square
    if nargin < 2
        data_mean{1} = mean(syn_or_asyn,2);
        data_mean{2} = mean(syn_or_asyn,1);
    end
    if nargin <3
        xaxes{1} = repmat([1:size(syn_or_asyn,1)],2,1);
        xaxes{2} = repmat([1:size(syn_or_asyn,1)],2,1);
    end
    if nargin <4
        contour_level = 11;
    end
    if nargin <5
        axes_labels{1} = '';
        axes_labels{2} = '';
    end
else
    % Rectangle
    if nargin < 3
        xaxes{1} = [1:size(syn_or_asyn,1)];
        xaxes{2} = [1:size(syn_or_asyn,2)];
    end
    if nargin < 2
        data_mean{1} = mean(syn_or_asyn,2);
        data_mean{2} = mean(syn_or_asyn,1);
    end
    if nargin <4
        contour_level = 11;
    end
    if nargin <5
        axes_labels{1} = '';
        axes_labels{2} = '';
    end
end


fig = figure('Units','pixels','Position',[100 100 800 800 ]);

% Left
sub_left = subplot('position',[0.1 0.1 0.1 0.7]);box on;
plot(sub_left,xaxes{1},data_mean{1}); view(-90,90); axis tight;
set(gca,'xdir','reverse');
set(gca,'XTickLabel','','YTickLabel','','xtick',[],'ytick',[]);
```

```
ax(1) = gca;

% Center
sub_center = subplot('position',[0.2 0.1 0.7 0.7]);box on;
contourf(sub_center,xaxes{2},xaxes{1},syn_or_asyn,contour_level);
colormap(bluewhitered_thesis(contour_level));
set(gca,'yaxislocation','right')
set(gca,'xdir','reverse');
set(gca,'ydir','reverse');
xlabel(axes_labels{1}); ylabel(axes_labels{2});
ax(2) = gca;

% Top
sub_top = subplot('position',[0.2 0.8 0.7 0.1]);box on;
plot(sub_top,xaxes{2},data_mean{2}); axis tight;
set(gca,'xdir','reverse');
set(gca,'XTickLabel','','YTickLabel','','xtick',[],'ytick',[]);
ax(3) = gca;

% Allow zooming in of main figure and top and side to match for playing
% around with the plots before plublished
hZoom = zoom(fig);
set(hZoom,'ActionPostCallback',{@halfZoom,ax});

function halfZoom(fig,evd,ax)

newLimx = get(ax(2),'XLim');
set(ax(3),'XLim',newLimx);
newLimy = get(ax(2),'YLim');
set(ax(1),'XLim',newLimy);
```

5.11 Colourmap for 2D plots

```
function newmap = bluewhitered_thesis(m)
%BLUEWHITERED_THESIS   Blue, white, and red color map
%   Altered from ...
    http://uk.mathworks.com/matlabcentral/fileexchange/4058-bluewhitered for ...
    0 to always be white, for thesis.
%   BLUEWHITERED(M) returns an M-by-3 matrix containing a blue to white
%   to red colormap, with white corresponding to the CAXIS value closest
%   to zero.  This colormap is most useful for images and surface plots
%   with positive and negative values.  BLUEWHITERED, by itself, is the
%   same length as the current colormap.
%
%   Examples:
%   ------------------------------
%   figure
%   imagesc(peaks(250));
%   colormap(bluewhitered(256)), colorbar
%
%   figure
%   imagesc(peaks(250), [0 8])
%   colormap(bluewhitered), colorbar
%
%   figure
%   imagesc(peaks(250), [-6 0])
%   colormap(bluewhitered), colorbar
%
%   figure
%   surf(peaks)
%   colormap(bluewhitered)
%   axis tight
%
%   See also HSV, HOT, COOL, BONE, COPPER, PINK, FLAG,
%   COLORMAP, RGBPLOT.


if nargin < 1
   m = size(get(gcf,'colormap'),1);
end


bottom = [0 0 0.5];
botmiddle = [0 0.5 1];
middle = [1 1 1];
topmiddle = [1 0 0];
top = [0.5 0 0];

% Find middle
lims = get(gca, 'CLim');

% Find ratio of negative to positive
if (lims(1) < 0) & (lims(2) > 0)
    % It has both negative and positive
```

```
50      % Find ratio of negative to positive
51      ratio = abs(lims(1)) / (abs(lims(1)) + lims(2));
52      neglen = round(m*ratio);
53      poslen = m - neglen;
54
55      % Just negative
56      new = [bottom; botmiddle; middle];
57      len = length(new);
58      oldsteps = linspace(0, 1, len);
59      newsteps = linspace(0, 1, neglen);
60      newmap1 = zeros(neglen, 3);
61
62      for i=1:3
63          % Interpolate over RGB spaces of colormap
64          newmap1(:,i) = min(max(interp1(oldsteps, new(:,i), newsteps)', 0), 1);
65      end
66
67      % Just positive
68      new = [middle; topmiddle; top];
69      len = length(new);
70      oldsteps = linspace(0, 1, len);
71      newsteps = linspace(0, 1, poslen);
72      newmap = zeros(poslen, 3);
73
74      for i=1:3
75          % Interpolate over RGB spaces of colormap
76          newmap(:,i) = min(max(interp1(oldsteps, new(:,i), newsteps)', 0), 1);
77      end
78
79      white_space = [1,1,1;1,1,1];
80      % And put 'em together
81      newmap = [newmap1(1:end-1,:); white_space; newmap(2:end,:)];
82
83  elseif lims(1) ≥ 0
84      % Just positive
85      new = [middle; topmiddle; top];
86      len = length(new);
87      oldsteps = linspace(0, 1, len);
88      newsteps = linspace(0, 1, m);
89      newmap = zeros(m, 3);
90
91      for i=1:3
92          % Interpolate over RGB spaces of colormap
93          newmap(:,i) = min(max(interp1(oldsteps, new(:,i), newsteps)', 0), 1);
94      end
95
96  else
97      % Just negative
98      new = [bottom; botmiddle; middle];
99      len = length(new);
100     oldsteps = linspace(0, 1, len);
101     newsteps = linspace(0, 1, m);
102     newmap = zeros(m, 3);
103
104     for i=1:3
```

```
105         % Interpolate over RGB spaces of colormap
106         newmap(:,i) = min(max(interp1(oldsteps, new(:,i), newsteps)', 0), 1);
107     end
108 
109 end
110 %
111 % m = 64;
112 % new = [bottom; botmiddle; middle; topmiddle; top];
113 % % x = 1:m;
114 %
115 % oldsteps = linspace(0, 1, 5);
116 % newsteps = linspace(0, 1, m);
117 % newmap = zeros(m, 3);
118 %
119 % for i=1:3
120 %     % Interpolate over RGB spaces of colormap
121 %     newmap(:,i) = min(max(interp1(oldsteps, new(:,i), newsteps)', 0), 1);
122 % end
123 %
124 % % set(gcf, 'colormap', newmap), colorbar
```

5.12 Import Julabo

```
function [ output ] = import_julabo( filename )
%IMPORT_JULABO Imports an Easy Temp txtfile into matlab

delimiter = '\t';

% Read columns of data as strings:
% For more information, see the TEXTSCAN documentation.
formatSpec = '%s%s%s%s%s%s%[^\n\r]';

% Open the text file.
fileID = fopen(filename,'r');

% Read columns of data according to format string.
% This call is based on the structure of the file used to generate this
% code. If an error occurs for a different file, try regenerating the code
% from the Import Tool.
dataArray = textscan(fileID, formatSpec, 'Delimiter', delimiter,  ...
    'ReturnOnError', false);

% Close the text file.
fclose(fileID);

% Convert the contents of columns containing numeric strings to numbers.
% Replace non-numeric strings with NaN.
raw = repmat({''},length(dataArray{1}),length(dataArray)-1);
for col=1:length(dataArray)-1
    raw(1:length(dataArray{col}),col) = dataArray{col};
end
numericData = NaN(size(dataArray{1},1),size(dataArray,2));

for col=[4,5,6]
    % Converts strings in the input cell array to numbers. Replaced non-numeric
    % strings with NaN.
    rawData = dataArray{col};
    for row=1:size(rawData, 1);
        % Create a regular expression to detect and remove non-numeric ...
           prefixes and
        % suffixes.
        regexstr = ...
            ['(?<prefix>.*?)(?<numbers>([-]*(\d+[\,]*)+[\.]{0,1}\d*[eEdD]'...
            '{0,1}[-+]*\d*[i]{0,1})|([-]*(\d+[\,]*)*[\.]{1,1}\d+[eEdD]{0,1}'...
            '[-+]*\d*[i]{0,1}))(?<suffix>.*)'];
        try
            result = regexp(rawData{row}, regexstr, 'names');
            numbers = result.numbers;

            % Detected commas in non-thousand locations.
            invalidThousandsSeparator = false;
            if any(numbers==',');
                thousandsRegExp = '^\d+?(\,\d{3})*\.{0,1}\d*$';
                if isempty(regexp(thousandsRegExp, ',', 'once'));
```

```
49                      numbers = NaN;
50                      invalidThousandsSeparator = true;
51                  end
52              end
53              % Convert numeric strings to numbers.
54              if ¬invalidThousandsSeparator;
55                  numbers = textscan(strrep(numbers, ',', ''), '%f');
56                  numericData(row, col) = numbers{1};
57                  raw{row, col} = numbers{1};
58              end
59          catch me
60          end
61      end
62  end
63
64  % Split data into numeric and cell columns.
65  rawNumericColumns = raw(:, [4,5,6]);
66  rawCellColumns = raw(:, [1,2,3]);
67
68  % Replace non-numeric cells with NaN
69  R = cellfun(@(x) ¬isnumeric(x) && ¬islogical(x),rawNumericColumns); % Find ...
        non-numeric cells
70  rawNumericColumns(R) = {NaN}; % Replace non-numeric cells
71
72  % Length to rip
73  first_nan = find(R(2:end,:),1,'first') - 2;
74
75  % Clear temporary variables
76  clearvars filename delimiter formatSpec fileID dataArray ans col numericData ...
        rawData row regexstr result numbers invalidThousandsSeparator ...
        thousandsRegExp me rawNumericColumns rawCellColumns R;
77
78  if (isempty(first_nan) == 1)
79      length_to_rip = size(raw,1);
80  else
81      length_to_rip = first_nan;
82  end
83
84  datenumber(1:length_to_rip - 1) = 0;
85  setpoint(1:length_to_rip - 1) = 0;
86  temp_int(1:length_to_rip - 1) = 0;
87  temp_ext(1:length_to_rip - 1) = 0;
88
89  for i = 2:length_to_rip
90      date = strsplit(raw{i,1},'/');
91      time_1 = strsplit(raw{i,2},' ');
92      time_2 = strsplit(time_1{1},':');
93      mm = str2double(date{1});
94      dd = str2double(date{2});
95      yyyy = str2double(date{3});
96      if strcmp(time_1{2},'AM') == 1
97          if str2double(time_2{1}) == 12
98              HH = 0;
99          else
100             HH = str2double(time_2{1});
```

```
101         end
102     else
103         if str2double(time_2{1}) == 12
104             HH = str2double(time_2{1});
105         else
106             HH = str2double(time_2{1}) + 12;
107         end
108     end
109     MM = str2double(time_2{2});
110     SS = str2double(time_2{3});
111     datenumber(i-1) = datenum([yyyy,mm,dd,HH,MM,SS]);
112     setpoint(i-1) = raw{i,4};
113     temp_int(i-1) = raw{i,5};
114     temp_ext(i-1) = raw{i,6};
115 end
116 output = [datenumber;setpoint;temp_int;temp_ext];
117 end
```

5.13 Dynamic Water Subtraction

```
1
2  input = carrageenan_spectra;
3  water = water_spectra;
4
5  % Initialise the output array
6  sub = zeros(size(input,1),size(input,2));
7  % For all of the carrageenan spectra
8  for j = 1:size(input,1)
9  %     Simple one point baselining
10     a = input(j,:) - input(j,1);
11
12 %     Initialise the looping variables
13     ys = zeros(size(water,1),1);
14     sums = zeros(size(water,1),1);
15
16 %     For all the water spectra, calculate the best subtraction
17     for i = 1:size(water,1)
18 %         Setup relative function to optimise
19         f = @(x)minsum(x,a,water(i,:));
20 %         Perform fminbnd optimistion / search
21         y = fminbnd(f,0,1.5);
22 %         Calculate the subracted spectrum
23         n = a - y*b;
24 %         Sum the O-H stretch region with an 8th power scaling
25         sums(i) = (sum(n(400:1000).^8));
26 %         trackthe best subtraction parameter for each water spectrum
27         ys(i) = y;
28     end
29
30 %     For each of the carrageenan spectra, find the water subtraction with
31 %     the smallest residicual (scaled to power of 8 to intensify)
32     [¬, idx] = min(sums);
33 %     Calcualte the subtracted spectrum
34     sub(j,:) = a - ys(idx) * water(idx,:);
35 end
36
37 % % % % %
38 % minsum function used for optimisation
39 % % % % %
40 function y = minsum(x,a,b)
41 % simlpy linear subtraction with x as the scaling variable.
42 n = a - x.*b;
43 % sum of the O-H stretch region, scaled to 8th power
44 y = (sum(n(400:1000).^8));
45 end
```

5.14 Band Fitting Example

```
% Initialise results cells
fitresult = cell( size(input,1), 1 );
gof = struct( 'sse', cell( 2, 1 ), ...
    'rsquare', [], 'dfe', [], 'adjrsquare', [], 'rmse', [] );
% Setup the fit-type by depinging the function to fit
% In this case, a 3 component pseudo-Voigt
ft = fittype( ['a1*((mix1*exp(-4*log(2)*((x-c1)/w1)^2))'...
    '+ ((1-mix1)/(1+4*((x-c1)/w1)^2 )))+ ...
        a2*((mix2*exp(-4*log(2)*((x-c2)/w2)^2))'...
    '+ ((1-mix2)/(1+4*((x-c2)/w2)^2 ))) + ...
        a3*((mix3*exp(-4*log(2)*((x-c3)/w3)^2))'...
    '+ ((1-mix3)/(1+4*((x-c3)/w3)^2 )))'], 'independent', 'x', 'dependent', ...
        'y' );

% Deping options for algorithm used
opts = fitoptions( 'Method', 'NonlinearLeastSquares' );
opts.Display = 'Off';
% Set the startpoints and boundaries for the fit
% For vaibles displayed in "fitttype", listed in alphanumerical order
opts.Lower = [0 0 0 990 1084 1136 .8 .8 .8 2 24 51];
opts.StartPoint = [0.01 0.01 0.01 1000 1088 1140 .9 .9 .9 10 26 53];
opts.Upper = [0.2 0.2 0.2 1010 1092 1144 1 1 1 15 50 90];

% Loop through all spectra that we wish to fit
for k = 1:size(input,1)
    [xData, yData] = prepareCurveData( input_wn, [input(k,:) );
    % Fit model to data.
    [fitresult{k}, gof(1)] = fit( xData, yData, ft, opts );
end

% Collect and re-assemble all data so we can obsreve the components
x = input_wn;
for p = 1:size(car,1)
    coeffs = num2cell(coeffvalues(fitresult{p}));
    [a1,a2,a3,c1,c2,c3,mix1,mix2,mix3,w1,w2,w3] = coeffs{:};
    for k = 1:length(x)
        overall_fit(k) = a1*((mix1*exp(-4*log(2)*((x(k)-c1)/w1)^2)) + ...
            ((1-mix1)/(1+4*((x(k)-c1)/w1)^2 )))+ ...
            a2*((mix2*exp(-4*log(2)*((x(k)-c2)/w2)^2)) + ...
            ((1-mix2)/(1+4*((x(k)-c2)/w2)^2 ))) + ...
            a3*((mix3*exp(-4*log(2)*((x(k)-c3)/w3)^2)) + ...
            ((1-mix3)/(1+4*((x(k)-c3)/w3)^2 )));
        m1(k) = a1*((mix1*exp(-4*log(2)*((x(k)-c1)/w1)^2)) + ...
            ((1-mix1)/(1+4*((x(k)-c1)/w1)^2 )));
        m2(k) = a2*((mix2*exp(-4*log(2)*((x(k)-c2)/w2)^2)) + ...
            ((1-mix2)/(1+4*((x(k)-c2)/w2)^2 )));
        m3(k) = a3*((mix3*exp(-4*log(2)*((x(k)-c3)/w3)^2)) + ...
            ((1-mix3)/(1+4*((x(k)-c3)/w3)^2 )));
    end
    overall_fit_trapz(p,:) = trapz(overall_fit);
    m1_trapz(p,:) = trapz(m1);
```

```
41      m2_trapz(p,:) = trapz(m2);
42      m3_trapz(p,:) = trapz(m3);
43      recon(p,:) = overall_fit;
44      residual(p,:) = bsxfun(@minus,input(p,:),recon(p,:));
45  end
```

Bibliography

[1] P. Hariharan, *Basics of Interferometry*, Academic Press, San Diego, 2006.

[2] J. Fahrenfort, *Spectrochim. Acta*, 1961, **17**, 698–709.

[3] N. J. Harrick, *Internal Reflection Spectroscopy*, John Wiley & Sons Inc, New York, 1967.

[4] L. A. Averett, P. R. Griffiths and K. Nishikida, *Anal. Chem.*, 2008, **80**, 3045–3049.

[5] A. R. Hind, S. K. Bhargava and A. McKinnon, *Adv. Colloid Interface Sci.*, 2001, **93**, 91–114.

[6] R. G. Brereton, *Chemometrics*, John Wiley & Sons, Chichester, 2003.

[7] *https://www.mathworks.com/matlabcentral/fileexchange/*.

[8] B. M. Wise, N. B. Gallagher, R. Bro and J. M. Shaver, *PLS toolbox 8.0.2*, Eigenvector Research Inc., 2016.

[9] A. de Juan, J. Jaumot and R. Tauler, *Anal. Methods*, 2014, **6**, 4964.

[10] I. Noda, *J. Mol. Struct.*, 2014, **1069**, 3–22.

[11] I. Noda, *Appl. Spectrosc*, 1993, **47**, 1329–1336.

[12] M. T. Zanni and R. M. Hochstrasser, *Curr. Opin. Struct. Biol.*, 2001, **11**, 516–522.

[13] K. Ohta and H. Ishida, *Appl. Spectrosc*, 1988, **42**, 952–957.

[14] J. W. Cooley and J. W. Tukey, *Math. Comput.*, 1965, **19**, 297.

[15] I. Noda, *Appl. Spectrosc*, 2000, **54**, 994–999.

[16] I. Noda, *Appl. Spectrosc*, 2000, **54**, 994–999.

[17] I. Noda and Y. Ozaki, *Two-Dimensional Correlation Spectroscopy*, John Wiley & Sons, Chichester, 2005.

[18] I. Noda, A. E. Dowrey, C. Marcott, G. M. Story and Y. Ozaki, *Appl. Spectrosc*, 2000, **54**, 236A–248A.

[19] N. Childress, *https://uk.mathworks.com/matlabcentral/fileexchange/4058-bluewhitered*.

[20] I. Noda, *J. Am. Chem. Soc.*, 1989, **111**, 8116–8118.

[21] M. Thomas and H. H. Richardson, *Vib. Spectrosc.*, 2000, **24**, 137–146.

[22] S. Morita, H. Shinzawa, R. Tsenkova, I. Noda and Y. Ozaki, *J. Mol. Struct.*, 2006, **799**, 111–120.

[23] S. Morita, H. Shinzawa, I. Noda and Y. Ozaki, *Appl. Spectrosc*, 2006, **60**, 398–406.

[24] V. D. Prajapati, P. M. Maheriya, G. K. Jani and H. K. Solanki, *Carbohydr. Polym.*, 2014, **105**, 97–112.

[25] D. Renard, G. Della Valle and Y. Popineau, *Plant Biopolymer Science*, Royal Society of Chemistry, Cambridge, 2002.

[26] H. J. Bixler and H. Porse, *J. Appl. Phycol.*, 2010, **23**, 321–335.

[27] H. J. Bixler, *Hydrobiologia*, 1996, **326-327**, 35–57.

[28] H. Knutsen, I. Usov, D. Myslabodski and B. Larsen, *Botanica Marina*, 1994, **37**, 163–169.

[29] N. S. Anderson, T. C. S. Dolan and D. A. Rees, *J. Chem. Soc., Perkin Trans. 1*, 1973, 2173–2176.

[30] W. Helbert, in *W. Helbert*, Royal Society of Chemistry, Cambridge, 2012, pp. 19–25.

[31] T. Thành, Y. Yuguchi, H. Yasunaga, R. Takano, H. Urakawa and K. Kajiwara, *Macromol. Chem. Phys.*, 2002, **203**, 15–23.

[32] C. A. Running, C. A. Running, R. Falshaw, R. Falshaw, S. Janaswamy and S. Janaswamy, *Carbohydr. Polym.*, 2012, **87**, 2735–2739.

[33] A. H. Clark, *Curr. Opin. Colloid Interface Sci.*, 1996.

[34] A. Tecante and M. d. C. Nez Santiago, *Solution Properties of κ-Carrageenan and Its Interaction with Other Polysaccharides in Aqueous Media*, InTech, Rijeka, 2012.

[35] V. L. Campo, D. F. Kawano, D. B. d. Silva Jr. and I. Carvalho, *Carbohydr. Polym.*, 2009, **77**, 167–180.

[36] J. Liu, X. Zhan, J. Wan, Y. Wang and C. Wang, *Carbohydr. Polym.*, 2015, **121**, 27–36.

[37] L. Li, R. Ni, Y. Shao and S. Mao, *Carbohydr. Polym.*, 2014, **103**, 1–11.

[38] I. Wijesekara, R. Pangestuti and S.-K. Kim, *Carbohydr. Polym.*, 2011, **84**, 14–21.

[39] C. B. Buck, C. D. Thompson, J. N. Roberts, M. Müller, D. R. Lowy and J. T. Schiller, *PLoS Pathog.*, 2006, **2**, e69.

[40] J. N. Roberts, C. B. Buck, C. D. Thompson, R. Kines, M. Bernardo, P. L. Choyke, D. R. Lowy and J. T. Schiller, *Nat. Med.*, 2007, **13**, 857–861.

[41] M. Kacurakova and R. H. Wilson, *Carbohydr. Polym.*, 2001, **44**, 291–303.

[42] M. Černá, A. S. Barros, A. Nunes, S. M. Rocha, I. Delgadillo, J. Čopková and M. A. Coimbra, *Carbohydr. Polym.*, 2003, **51**, 383–389.

[43] R. Climaco Pinto, V. Bosc, H. Noçairi, A. S. Barros and D. N. Rutledge, *Anal. Chim. Acta*, 2008, **629**, 47–55.

[44] L. Pereira, A. M. Amado, A. T. Critchley, F. van de Velde and P. J. A. Ribeiro-Claro, *Food Hydrocoll*, 2009, **23**, 1903–1909.

[45] L. Pereira, A. Sousa, H. Coelho and A. M. Amado, *Biomol Eng.*, 2003.

[46] E. Gómez-Ordóñez and P. Rupérez, *Food Hydrocoll*, 2011, **25**, 1514–1520.

[47] M. Sekkal, J.-P. Huvenne, P. Legrand, B. Sombret, J.-C. Mollet, A. Mouradi-Givernaud and M.-C. Verdus, *Mikrochim. Acta*, 1993, **112**, 1–10.

[48] C. Rochas, M. Lahaye and W. Yaphe, *Botanica Marina*, 1986, **29**, 335–340.

[49] P. S. Belton, R. H. Wilson and D. H. Chenery, *Int. J. Bio. Macromol.*, 1986.

[50] T. Chopin and E. Whalen, *Carbohydr. Res.*, 1993, **246**, 51–59.

[51] P. S. Belton, B. J. Goodfellow and R. H. Wilson, *Macromolecules*, 1989, **22**, 1636–1642.

[52] M. Sekkal, P. Legrand, J.-P. Huvenne and M.-C. Verdus, *J. Mol. Struct.*, 1993, **294**, 227–230.

[53] R. H. Wilson, B. J. Goodfellow and P. S. Belton, *Food Hydrocoll*, 1988, **2**, 169–178.

[54] B. Matsuhiro and B. Matsuhiro, *Hydrobiologia*, 1996, **326-327**, 481–489.

[55] J. Prado-Fernandez, J. A. Rodrguez-Vázquez, E. Tojo and J. M. Andrade, *Anal. Chim. Acta*, 2003, **480**, 23–37.

[56] M. A. Roberts and B. Quemener, *Trends Food Sci. Technol.*, 1999, **10**, 169–181.

[57] T. Malfait, H. Van Dael and F. Van Cauwelaert, *Int. J. Biol. Macromol.*, 1989, **11**, 259–264.

[58] P. D. A. Pudney, T. M. Hancewicz, D. G. Cunningham and M. C. Brown, *Vib. Spectrosc.*, 2004, **34**, 123–135.

[59] VIBRATIONAL SPECTROSCOPY (FTIR-ATR AND FT-RAMAN) - A Rapid and Useful Tool for Phycocolloid Analysis, 2009.

[60] L. Pereira, S. F. Gheda and P. J. A. Ribeiro-Claro, *Int. J. Carbohydr.*, 2013, **2013**, 1–7.

[61] O. Tari, S. Kara and O. Pekcan, *J. Appl. Polym. Sci.*, 2011, **121**, 2652–2661.

[62] A. J. Weaver, M. D. Kemple, J. W. Brauner, R. Mendelsohn and F. G. Prendergast, *Biochemistry*, 1992, **31**, 1301–1313.

[63] S. Kara, C. Tamerler, H. Bermek and O. Pekcan, *Int. J. Biol. Macromol.*, 2003, **31**, 177–185.

[64] Y. Nitta, B. S. Kim, K. Nishinari, M. Shirakawa, K. Yamatoya, T. Oomoto and I. Asai, *Biomacromolecules*, 2003, **4**, 1654–1660.

[65] F. van de Velde, A. S. Antipova, H. S. Rollema, T. V. Burova, N. V. Grinberg, L. Pereira, P. M. Gilsenan, R. H. Tromp, B. Rudolph and V. Y. Grinberg, *Carbohydr. Res.*, 2005, **340**, 1113–1129.

[66] H. Friebolin, *Basic One- and Two-Dimensional NMR Spectroscopy*, Wiley-VCH, Weinheim, 2005.

[67] A. J. Dingley and S. M. Pascal, *Biomolecular NMR Spectroscopy*, IOS Press, Amsterdam, 2011.

[68] A. G. Palmer, A. G. Palmer, J. Williams, J. Williams, A. McDermott and A. McDermott, *J. Phys. Chem.*, 1996, **100**, 13293–13310.

[69] T. Turquois, S. Acquistapace, F. A. Vera, F. A. Vera and D. H. Welti, *Carbohydr. Polym.*, 1996, **31**, 269–278.

[70] M. Lahaye, *J. Appl. Phycol.*, 2001, **13**, 173–184.

[71] M. Rinaudo, *Polym. Int.*, 2008, **57**, 397–430.

[72] F. van de Velde, *Trends Food Sci. Technol.*, 2002, **13**, 73–92.

[73] M. V. C. Cardoso and E. Sabadini, *Carbohydr. Res.*, 2010, **345**, 2368–2373.

[74] Q. Xu, S. Zou, W. Zhang and X. Zhang, *Macromol. Rapid Commun.*, 2001, **22**, 1163.

[75] T. Funami, M. Hiroe, S. Noda, I. Asai, S. Ikeda and K. Nishimari, *Food Hydrocoll*, 2007, **21**, 617–629.

[76] V. J. Morris, A. R. Mackie, P. J. Wilde, A. R. Kirby, E. C. N. Mills and A. P. Gunning, *Lebenson Wiss Technol*, 2001, **34**, 3–10.

[77] S. Ikeda, V. J. Morris and K. Nishinari, *Biomacromolecules*, 2001, **2**, 1331–1337.

[78] S. Liu and Y. Wang, *Adv. Food Nutr. Res.*, 2011, **62**, 201–240.

[79] A. R. Kirby, A. P. Gunning and V. J. Morris, *Biopolymers*, 1996, **38**, 355–366.

[80] V. M. F. Lai, P. A. L. Wong and C. Y. Lii, *J. Food Sci.*, 2000, **65**, 1332–1337.

[81] P. E. Marszalek, H. Li and J. M. Fernandez, *Nat. Biotechnol.*, 2001, **19**, 258–262.

[82] J. T. Pelton and L. R. McLean, *Anal. Biochem.*, 2000, **277**, 167–176.

[83] H. Fabian, C. Schultz, D. Naumann and O. Landt, *J. Mol. Biol.*, 1993, **232**, 967–981.

[84] J. J. Turner, F. W. Grevels, S. M. Howdle, J. Jacke, M. T. Haward and W. E. Klotzbuecher, *J. Am. Chem. Soc.*, 1991, **113**, 8347–8353.

[85] J. J. Turner, C. M. Gordon and S. M. Howdle, *J. Phys. Chem.*, 1995, **99**, 17532–17538.

[86] P. D. A. Pudney, *Private communication, 2012*.

[87] S. Janaswamy and R. Chandrasekaran, *Carbohydr. Res.*, 2001, **335**, 181–194.

[88] S. Banerjee and S. Bhattacharya, *Crit Rev Food Sci Nutr*, 2012, **52**, 334–346.

[89] C. Viebke, L. Piculell and S. Nilsson, *Macromolecules*, 1994, **27**, 4160–4166.

[90] L. Piculell, in *L. Piculell*, CRC Press, 2009, pp. 239–287.

[91] E. E. Braudo, I. R. Muratalieva, I. G. Plashchina, V. B. Tolstoguzov and I. S. Markovich, *Colloid Polym Sci*, 1991, **269**, 1148–1156.

[92] I. Heertje and D. F. Lewis, *Food Struct.*, 1993, **12**, 343–364.

[93] D. A. Rees, *Adv. Carbohydr. Chem. Biochem.*, 1969, **24**, 267–332.

[94] C. Rochas and M. Rinaudo, *Biopolymers*, 1984, **23**, 735–745.

[95] P. A. Williams, S. M. Clegg, M. J. Langdon, K. Nishinari and L. Piculell, *Macromolecules*, 1993, **26**, 5441–5446.

[96] S. Y. Xu, D. W. Stanley, H. D. Goff and V. J. Davidson, *J. Food. Sci.*, 1992.

[97] M. E. Zabik and P. J. Aldrich, *J. Food Sci.*, 1968, **33**, 371–377.

[98] P. MacArtain, P. MacArtain, J. C. Jacquier, J. C. Jacquier, K. A. Dawson and K. A. Dawson, *Carbohydr. Polym.*, 2003, **53**, 395–400.

[99] M. Takemasa and K. Nishinari, *Colloids Surf B Biointerfaces*, 2004, **38**, 231–240.

[100] V. Lai, V. Lai, P. A. L. Wong, P. A. L. Wong, C. Y. Lii and C. Y. Lii, *J. Food Sci.*, 2006, **65**, 1332–1337.

[101] W. Zhang, W. Zhang, L. Piculell, S. Nilsson, S. Nilsson, S. H. Knutsen and S. H. Knutsen, *Carbohydr. Polym.*, 1994, **23**, 105–110.

[102] J. Doyle, P. Giannouli, K. Philp and E. R. Morris, in *J. Doyle, P. Giannouli, K. Philp and E. R. Morris*, Royal Society of Chemistry, Cambridge, 2007, pp. 158–164.

[103] S. Y. Xu, D. W. Stanley, H. D. Goff, V. J. Davidson and M. Maguer, *J. Food Sci.*, 1992, **57**, 96–102.

[104] P. S. Belton, R. H. Wilson and D. H. Chenery, *Int. J. Bio. Macromol.*, 1986.

[105] M. Takemasa, A. Chiba and M. Date, *Macromolecules*, 2001, **34**, 7427–7434.

[106] C. Rochas and M. Rinaudo, *Carbohydr. Res.*, 1982, **105**, 227–236.

[107] C. Rochas and M. Rinaudo, *Biopolymers*, 1980, **19**, 1675–1687.

[108] F. van de Velde, N. D. Lourenco, H. M. Pinheiro and M. Bakker, *Adv. Synth. Catal.*, 2002, **344**, 815–835.

[109] K. Nishinari and R. Takahashi, *Curr. Opin. Colloid Interface Sci.*, 2003, **8**, 396–400.

[110] M. R. Mangione, D. Giacomazza, D. Bulone, V. Martorana and P. L. San Biagio, *Biophys. Chem.*, 2003, **104**, 95–105.

[111] Y. Yuguchi, Y. Yuguchi, H. Urakawa, H. Urakawa, K. Kajiwara and K. Kajiwara, *Food Hydrocoll*, 2003, **17**, 481–485.

[112] V. J. Morris and G. R. Chilvers, *Carbohydr. Polym.*, 1983, **3**, 129–141.

[113] C. Viebke, J. Borgstrom, I. Carlsson, L. Piculell and P. Williams, *Macromolecules*, 1998, **31**, 1833–1841.

[114] C. J. Lawson and D. A. Rees, *Nature*, 1970, **227**, 392–393.

[115] J. Prado-Fernandez, J. A. Rodrguez-Vázquez, E. Tojo and J. M. Andrade, *Anal. Chim. Acta*, 2003, **480**, 23–37.

[116] M. Şen and E. N. Erboz, *Food Res Int*, 2010, **43**, 1361–1364.

[117] V. J. Morris and G. R. Chilvers, *J. Sci. Food Agric.*, 1981, **32**, 1235–1241.

[118] D. R. Picout and S. B. Ross-Murphy, *Scientific World J.*, 2003, **3**, 105–121.

[119] P. S. Belton, V. J. Morris and S. F. Tanner, *Macromolecules*, 1986, **19**, 1618–1621.

[120] A. M. Stephen, *Food Polysaccharides and Their Applications*, CRC Press, 1995.

[121] H. J. Bixler, *British Food Journal*, 1994, **96**, 12–17.

[122] C. Ruckebusch and L. Blanchet, *Anal. Chim. Acta*, 2013, **765**, 28–36.

[123] L. Ma, V. Sikirzhytski, Z. Hong, I. K. Lednev and S. A. Asher, *Appl. Spectrosc*, 2013, **67**, 283–290.

[124] J. C. Harrington, E. A. Foegeding, D. M. Mulvihill and E. R. Morris, *Food Hydrocoll*, 2009, **23**, 468–489.

[125] M. T. Nickerson and A. T. Paulson, *Carbohydr. Polym.*, 2004, **58**, 15–24.

[126] M. T. Nickerson, A. T. Paulson and F. R. Hallett, *Carbohydr. Polym.*, 2004, **58**, 25–33.

[127] B. Denef, N. Mischenko, M. H. J. Koch and H. Reynaers, *Int. J. Biol. Macromol.*, 1996, **18**, 151–159.

[128] P. B. Tooke, *Trends Anal. Chem.*, 1988, **7**, 130–136.

[129] C. Viebke, J. Borgstrom and L. Piculell, *Carbohydr. Polym.*, 1995, **27**, 145–154.

[130] M. Sekkal and P. Legrand, *Spectrochem. Acta. A*, 1993, **49**, 209–221.

[131] J. A. Arancibia, P. C. Damiani, G. A. Ibañez and A. C. Olivieri, *J AOAC Int*, 2014, **97**, 39–49.

[132] Q. Wang, B. Rademacher, F. Sedlmeyer and U. Kulozik, *Innov. Food Sci. & Emerg. Technol.*, 2005, **6**, 465–472.

[133] *Gums and Stabilisers for the Food Industry 11*, ed. P. A. Williams and G. O. Phillips, Royal Society of Chemistry, Cambridge, 2007.

[134] V. J. Morris and P. S. Belton, *Prog Food Nutr Sci*, 1982, **6**, 55–66.

[135] D. Oakenfull and V. J. Morris, *Chem. Ind. (london)*, 1987, 201–202.

[136] N. S. Anderson, T. C. S. Dolan, C. J. Lawson, A. Penman and D. A. Rees, *Carbohydr. Res.*, 1968, **7**, 468–473.

[137] R. T. Lagemann, *J. Am. Chem. Soc.*, 1945.

[138] A. Regand and H. D. Goff, *J. Dairy Sci.*, 2002, **85**, 2722–2732.

[139] G. Narsimhan, H. G. Schwartzbereg and R. W. Hartel, *Physical Chemistry of Foods*, Elsevier, San Diego, 1992.

[140] K. L. K. Cook and R. W. Hartel, *Compr. Rev. Food Sci. Food Saf.*, 2010, **9**, 213–222.

[141] D. P. Donhowe, R. W. Hartel and R. L. Bradley, *J. Dairy Sci.*, 1991, **74**, 3334–3344.

[142] N. Buyong, N. Buyong, O. Fennema and O. Fennema, *J. Dairy Sci.*, 1988, **71**, 2630–2639.

[143] K. Caldwell, H. D. Goff and D. W. Stanley, *Food Struct.*, 1992, **11**, 11–23.

[144] D. P. Donhowe and R. W. Hartel, *Int. Dairy J.*, 1996, **6**, 1191–1208.

[145] D. P. Donhowe and R. W. Hartel, *Int. Dairy J.*, 1996, **6**, 1209–1221.

[146] A. A. Flores and H. D. Goff, *J. Dairy Sci.*, 1999, **82**, 1399–1407.

[147] A. A. Flores and H. D. Goff, *J. Dairy Sci.*, 1999, **82**, 1408–1415.

[148] H. D. Goff, *Int. Dairy J.*, 1997, **7**, 363–373.

[149] T. Hagiwara and R. W. Hartel, *J. Dairy Sci.*, 1996, **79**, 735–744.

[150] R. L. Sutton and J. Wilcox, *J. Food Sci.*, 1998, **63**, 9–11.

[151] E. R. Budiaman and O. Fennema, *J. Dairy Sci.*, 1987, **70**, 547–554.

[152] R. W. Hartel, *Trends Food Sci. Technol.*, 1996, **7**, 315–321.

[153] R. Boistelle and J. P. Astier, *J. Cryst. Growth*, 1988, **90**, 14–30.

[154] A. Kaminska-Dworznicka, M. Matusiak, K. Samborska, D. Witrowa-Rajchert, E. Gondek, E. Jakubczyk and A. Antczak, *J. Food Eng.*, 2015, **167**, 162–165.

[155] S. Bolliger, H. Wildmoser, H. D. Goff and B. W. Tharp, *Int. Dairy J.*, 2000, **10**, 791–797.

[156] H. D. Goff, K. Caldwell, D. W. Stanley and T. J. Maurice, *J. Dairy Sci.*, 1993, **76**, 1268–1277.

[157] G. L. Fletcher, C. L. Hew and P. L. Davies, *Annu. Rev. Physiol.*, 2001, **63**, 359–390.

[158] J. G. Duman, *Annu. Rev. Physiol.*, 2001, **63**, 327–357.

[159] Y. Yeh, Y. Yeh, R. E. Feeney and R. E. Feeney, *Chem. Rev.*, 1996, **96**, 601–618.

[160] M. Griffith and M. W. F. Yaish, *Trends Plant Sci.*, 2004, **9**, 399–405.

[161] A. Regand and H. D. Goff, *J. Dairy Sci.*, 2006, **89**, 49–57.

[162] C. Soukoulis, I. Chandrinos and C. Tzia, *Lebenson Wiss Technol*, 2008, **41**, 1816–1827.

[163] V. Langendorff, G. Cuvelier, C. Michon, B. Launay, A. Parker and C. G. de Kruif, *Food Hydrocoll*, 2000, **14**, 273–280.

[164] A. Regand and H. D. Goff, *Food Hydrocoll*, 2003, **17**, 95–102.

[165] V. Gaukel, A. Leiter and W. E. L. Spiess, *J. Food Eng.*, 2014, **141**, 44–50.

[166] J. Barrett, *Int. J. Biochem. Cell Biol.*, 2001, **33**, 105–117.

[167] M. I. Gibson, *Polym. Chem.*, 2010, **1**, 1141.

[168] A. Millo, Y. Raichlin and A. Katzir, *Appl. Spectrosc*, 2005, **59**, 460–466.

[169] R. L. Walker, K. Searles, J. A. Willard and R. R. H. Michelsen, *J. Chem. Phys.*, 2013, **139**, 244703.

[170] F. Mallamace, M. Broccio, C. Corsaro, A. Faraone, D. Majolino, V. Venuti, L. Liu, C.-Y. Mou and S.-H. Chen, *Proc. Natl. Acad. Sci. U.S.A.*, 2007, **104**, 424–428.

[171] M. Bar-Dolev, Y. Celik, J. S. Wettlaufer, P. L. Davies and I. Braslavsky, *J R Soc Interface*, 2012, **9**, 3249–3259.

[172] J. G. Dodd and L. K. DeNoyer, *Curve-Fitting: Modeling Spectra*, John Wiley & Sons, Ltd, Chichester, UK, 2006.

[173] F. Perakis, L. D. Marco, A. Shalit, F. Tang, Z. R. Kann, T. D. Kühne, R. Torre, M. Bonn and Y. Nagata, *Chem. Rev.*, 2016, **116**, 7590–7607.

[174] N. Kitadai, T. Sawai, R. Tonoue, S. Nakashima, M. Katsura and K. Fukushi, *J Solution Chem*, 2014, **43**, 1055–1077.

[175] K. Ohno, M. Okimura, N. Akai and Y. Katsumoto, *Phys Chem Chem Phys*, 2005, **7**, 3005–3014.

[176] Y. Maréchal, *J. Mol. Struct.*, 2011, **1004**, 146–155.

[177] J. D. Smith, C. D. Cappa, K. R. Wilson, R. C. Cohen, P. L. Geissler and R. J. Saykally, *Proc. Natl. Acad. Sci. U.S.A.*, 2005, **102**, 14171–14174.

[178] L. Pereira, S. F. Gheda and P. J. A. Ribeiro-Claro, *Int. J. Carbohydr.*, 2013, **2013**, 1–7.

[179] P. Pudney, T. M. Hancewicz, D. G. Cunningham and C. Gray, *Food Hydrocoll*, 2003, **17**, 345–353.

[180] P. D. A. Pudney, T. M. Hancewicz and D. G. Cunningham, *Spectroscopy*, 2002, **16**, 217–225.